Università degli Studi di Milano

PhD course in Physics, Astrophysics and Applied Physics

On the Lense-Thirring effect in accreting black hole systems

Supervisor:
Prof. Giuseppe Lodato

Ph.D. Candidate:
Alessia Franchini
Matr. R11040
cycle XXX

Director of the Ph.D. School:
Prof. Francesco Ragusa

Academic Year 2014 - 2017

Final examination:

November, 2017
Università degli Studi di Milano, Dipartimento di Fisica, Milano, Italy

Commission of the final examination:

External Members:

Prof. Andrew King, University of Leicester, Leicester, UK
Prof. Luciano Burderi, Università di Cagliari, Cagliari, Italy

Internal Member:

Prof. Giuseppe Lodato, Università degli Studi di Milano, Milano, Italy

Referees:

Dr. Chris Nixon, University of Leicester, Leicester, UK
Dr. Adam Ingram, University of Amsterdam, Amsterdam, Netherlands

MIUR subjects:

FIS/05 Astronomia e Astrofisica

PACS:

97.10.Gz Accretion and accretion discs
97.60.Lf Black holes in stellar evolution
04.25.dg Black hole binaries
97.80.Jp X-ray binary stars

Contents

Part I
Introduction

Chapter 1

Black Holes

The existence of black holes (BHs) is a natural prediction of Einstein's theory of general relativity (GR). The gravitational field of black holes is strong enough to prevent light from escaping and to distort the space and the flow of time around them. The modern view that black holes are the unavoidable end result of the evolution of massive stars arose from the theoretical work of Chandrasekhar, Landau and others in the first half of the 20th century. In 1963 extremely luminous distant objects were discovered and called quasars. Their discovery was quickly associated to the presence of very massive black holes (Lynden-Bell, 1969).

Quasars belong to a class of galaxies known as active galactic nuclei (AGN). What makes these galaxies "active" is the emission of staggering amounts of energy from their cores across the whole electromagnetic spectrum, from radio to X-rays. Moreover, the luminosities of AGN fluctuate on very short timescales, within days or even minutes (Bloom et al., 2011). These fluctuations and the finite velocity of light set an upper limit to the size of the emitting region. For these reasons we know that nuclei of some active galaxies responsible for the X-ray emission have a size $\lesssim 0.001$ pc, i.e. are at least 1 billion times smaller than the host galaxy. Astronomers had thus to explain how a luminosity of hundred of times that of an entire galaxy could be emitted from a volume billions of times smaller. The answer is the release of gravitational energy from matter falling towards a central black hole. Black holes in AGN would need to be enormous ($\sim 10^6 - 10^9 M_\odot$) in order to produce the luminosities of quasars. To distinguish these objects from stellar mass black holes left behind supernova explosions ($\sim 1-100 M_\odot$), the term "supermassive black hole" (SMBH) was coined.

In this Chapter we give an introduction to black hole maths and physics and the basics of gas accretion onto these compact objects.

1.1 Black hole maths

1.1.1 Schwarzschild metric

The proper description of the immediate vicinity of a black hole involves the use of Einstein's GR. In this theory the spacetime is assumed to be a 4-dimensional Lorentzian manifold. Schwarzschild (1916) described the spacetime outside a spherically symmetric body. This spherically symmetric vacuum solution to Einstein's equations is the Schwarzschild metric

$$ds^2 = -\left(1 - \frac{2GM}{c^2 r}\right) dt^2 + \left(1 - \frac{2GM}{c^2 r}\right)^{-1} dr^2 + r^2 d\Omega^2 \,. \tag{1.1}$$

where s is the distance between two points in this spacetime and t, r, Ω are the time coordinate, the radial coordinate and the solid angle respectively. M is a free parameter, that can be interpreted as the conventional Newtonian mass that we would measure by studying orbits at large distances from the gravitating source. This is the unique spherically symmetric solution because of Birkhoff theorem. Note that as $M \to 0$ we recover the Minkowski flat spacetime, which is to be expected. The metric becomes Minkowskian as $r \to \infty$, this property is known as "asymptotic flatness". The gravitational interaction reduces to Newtonian gravity, with a static potential

$$\phi = -\frac{GM}{r}\,. \tag{1.2}$$

It is interesting to note that the metric is static. However, we did not require that the source itself is static; it could be a collapsing star, as long as the collapse is symmetric. The metric coefficients become infinite at $r = 0$ and $r = 2GM/c^2$. It can be shown (Kruskal, 1960) that the second singularity corresponds to the event horizon. The location of this event horizon is called the Schwarzschild radius:

$$r_{\rm S} = \frac{2GM}{c^2} \simeq 3\left(\frac{M}{M_\odot}\right)\,{\rm km}\,. \tag{1.3}$$

The other is a curvature singularity, but it is screened by the event horizon and thus it is inaccessible from our Universe.

1.1.2 Kerr metric

The assumption of spherical symmetry, that is fundamental in order to write the Schwarzschild solution, can be relaxed to axial symmetry which is more appropriate for rotating black holes. The metric describing the spacetime outside a rotating axially symmetric body is the Kerr metric, which in Boyer-Lindquist coordinate is

$$ds^2 = -c^2\left(1 - \frac{2R_{\rm g}r}{\rho^2}\right)dt^2 + \frac{\rho^2}{\Delta}dr^2 + \rho^2 d\theta^2 + \sin^2\theta\left(r^2 + a^2R_{\rm g}^2 + \frac{2R_{\rm g}ra^2R_{\rm g}^2\sin^2\theta}{\rho^2}\right)d\phi^2 + \tag{1.4}$$

$$- \frac{4R_{\rm g}raR_{\rm g}\sin^2\theta}{\rho^2}c\,dt\,d\phi \tag{1.5}$$

where $\Delta = r^2 - 2R_{\rm g}r + a^2R_{\rm g}^2$, $\rho^2 = r^2 + a^2R_{\rm g}^2\cos^2\theta$ and $R_{\rm g} = GM/c^2$ is the gravitational radius.

The metric has two free parameters, M and a. It is straightforward to obtain the Schwarzschild metric if $a = 0$ and the Minkowski spacetime if $r \to \infty$. The parameter a is related to the total angular momentum of the spacetime $\mathbf{J}$

$$\mathbf{J} = a\frac{GM^2}{c}\hat{\mathbf{J}} \tag{1.6}$$

where $\hat{\mathbf{J}}$ is a unit vector along the $\theta = 0$ direction. This metric describes the spacetime structure around a rotating black hole, where the dimensionless parameter a is commonly

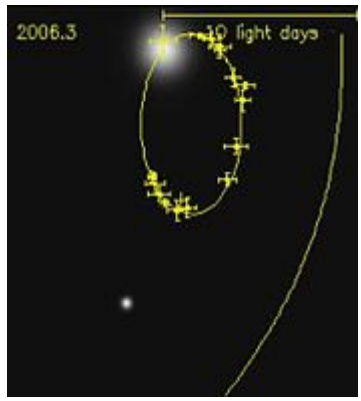

Figure 1.1: Orbit of the S-2 star around Sgr A*. Screenshot from a video created by the European Southern Observatory.

called the"spin". Singularities seem to appear at both $\Delta = 0$ and $\rho^2 = 0$. There are two radii at which Δ vanishes, given by

$$r_{\pm} = R_{\rm g} \pm \sqrt{R_{\rm g}^2(1-a^2)}\,. \tag{1.7}$$

Both radii are null surfaces that turn out to be event horizons. This restrict the values of the dimensionless spin to the range $0 \leq |a| \leq 1$.

1.2 Black hole physics

Mathematically, as we described so far, black holes are very simple object characterized by three parameters : mass, spin and charge. However, the latter is not relevant in an astrophysical context since if a black hole has a charge it attracts all the matter with opposite charge and eventually becomes neutral.

The measurements of the mass and spin of these object is all but straightforward. Especially probing the quiescent majority of SMBHs is an extremely difficult task. The first fundamental reason for investigating SMBHs is that they offer an exclusive opportunity to test GR. For instance the infrared and millimeter observation of the SMBH Sgr A* in the Milky Way centre, when coupled together, provide a strong evidence of the existence of black hole horizon (Broderick et al., 2009). Besides, the study of the orbits of S-stars around the central black hole, see Fig. 1.1, allowed both the mass of Sgr A* ($M = (4.5 \pm 0.4) \times 10^6 M_{\odot}$) and its distance ($D = 8.4 \pm 0.4$ kpc) to be estimated with very high precision (Ghez et al., 2008).

Also, SMBHs are believed to play a fundamental role in the growth and evolution of their host galaxies. In particular, there are scaling relations between the SMBH parameters and the properties of the host galaxy, such as the standard $M - \sigma$ relation, where σ is the bulge velocity dispersion (Ferrarese & Merritt, 2000). This relation might hold because the accretion of gas onto the SMBH can lead to strong outflows that regulate star formation through either energy or momentum deposition (King, 2003; King et al., 2005). If this is actually what happens, then studying SMBH growth becomes a very important task that allows other aspects of astrophysics to be understood. Accreting black holes have been detected as quasars in the optical waveband also at the very high redshifts

probed at present day (recently redshifts $z \gtrsim 7$ have been reached). This means that they have begun to grow at extremely high redshifts, namely $z > 10$. Soltan (1982) investigated quasar masses assuming that radiatively efficient accretion of gas onto massive black holes is the ultimate source of energy produced by quasars. If the growth occurred via Eddington-limited (see Section 1.2.1 below) gas accretion, the seed black hole mass must have been quite large, above $10^4 M_\odot$ (Volonteri & Rees, 2005).

Observations of AGN up to $z \sim 6$ (Fan et al., 2004, 2006) indicate that supermassive black holes with mass up to $10^9 M_\odot$ were already in place when the Universe was only 10^9 years old. This implies that the accretion rate at which these black hole grow is very high, namely $1 M_\odot$/yr. Such accretion rates, especially when the black hole is still low in mass, can be highly super-Eddington, unless the efficiency of conversion of mass into luminosity is very low, which requires very low spins (see below).

In order to address this issue several models have been proposed (Eisenstein & Loeb, 1995; Koushiappas et al., 2004; Lodato & Natarajan, 2006, 2007). In particular Lodato & Natarajan (2006) describe the formation of massive black hole seeds through gas cooling in primordial haloes via the growth of gravitational instabilities. Other scenarios of seed formation involve Population III stellar remnants (Madau & Rees, 2001), runaway collisions in a cluster directly producing an Intermediate Mass Black Hole (IMBH) (Devecchi & Volonteri, 2009) or direct collapse of large mass of primordial gas (Loeb & Rasio, 1994; Mayer et al., 2010; Begelman et al., 2008).

The spin parameter is essential in this context. SMBH can grow rapidly without violating the Eddington limit if the black hole has low spin and thus low radiative accretion efficiency. The black hole spin can be in general misaligned with respect to the angular momentum of the accreting gas surrounding it. This results in a coupling between the two momenta known as the Lense-Thirring effect or "frame-dragging" (Lense & Thirring, 1918). The astrophysical evidence of this effect could come from its influence on tilted accretion discs around rotating black holes, which we discuss in Chapter 3. Bardeen & Petterson (1975) showed how this effect might lead to a gradual transition of the accretion disc inner parts into the orbital plane of the black hole. If the black hole spin aligns quickly with the angular momentum of the accretion flow, then every randomly oriented accretion event would spin up the black hole preventing fast accretion. King & Pringle (2006) investigated the condition of counter-alignment between the spin and the angular momentum of the accretion flow due to the Bardeen-Petterson effect (Bardeen & Petterson, 1975). They showed that black holes can grow rapidly if they acquire most of the mass in a sequence of randomly oriented accretion events with smaller angular momenta compared to the black hole angular momentum. Furthermore the black hole has an angular momentum comparable with the last accretion episode. This means that the accretion can be chaotic and occur on a scale of the order of the disc size.

Accretion of gas onto black holes is the most efficient mechanism that converts matter into energy. The investigation of this complex physical mechanism, in terms of both radiative emission and mechanical outflow, is crucial in order to understand the observations of these accreting sources. Interestingly all the accreting sources show variability on different timescales. For instance, AGN emission varies on secular timescales while galactic X-ray binaries (XBs) show very fast variability, such as Quasi-Periodic Oscillations (QPOs), and state changes on human accessible timescales (see Chapter 6). One of the most interesting phenomena related to SMBH accretion are Tidal Disruption Events (TDEs), which show characteristic flares that last on timescales of months to years (Rees, 1988) and are investigated in details in Chapter 4.

1.2.1 Eddington limit

There is a limit on the accretion luminosity that can be reached by an accreting source. Consider a steady spherically symmetrical accretion. We assume the accreting material to be mainly hydrogen and to be fully ionized. Under these circumstances, the radiation exerts a force mainly on the free electrons through Thomson scattering, since the scattering cross-section for protons is smaller.

If S is the radiant energy flux ($\mathrm{erg\,s^{-1}cm^{-2}}$) and $\sigma_{\mathrm{T}} = 6.7 \times 10^{-25}\mathrm{cm}^2$ is the Thomson cross section, then the outward radial force on each electron $\sigma_{\mathrm{T}} S/c$ equals the rate at which it absorbs momentum. The attractive electrostatic Coulomb force between electrons and protons means that, as they move out, the electrons drag the protons with them. The radiation pushes out electron-proton pairs against the total gravitational force $GM(m_{\mathrm{p}} + m_{\mathrm{e}})/r^2 \sim GMm_{\mathrm{p}}/r^2$. If the luminosity of the accreting source is L ($\mathrm{erg\,s^{-1}}$), we have $S = L/4\pi r^2$ by spherical symmetry, so the net inward force on an electron-proton pair is

$$F_{\mathrm{tot}} = \left(GMm_{\mathrm{p}} - \frac{L\sigma_{\mathrm{T}}}{4\pi c} \right) \frac{1}{r^2} \,. \tag{1.8}$$

There is a limiting luminosity for which this expression vanishes, the Eddington limit,

$$L_{\mathrm{Edd}} = 4\pi GMm_{\mathrm{p}}c/\sigma_T \simeq 10^{44} M_6 \,\mathrm{erg\,s^{-1}} \tag{1.9}$$

where $M = 10^6 M_6 M_\odot$ is the mass of the black hole. For luminosities larger than L_{Edd}, radiation pressure throws the gas out. Thus if $F_{\mathrm{tot}} > 0$ the gas is thrown out and if $F_{\mathrm{tot}} < 0$ the gas will be accreted onto the black hole. Note that this limit holds when the previous assumptions are made, in general there could be super-Eddington accretion in black hole systems.

1.2.2 Tidal force

A tidal force is a difference in the strength of gravity between two points. The gravitational field of the Moon produces a tidal force across the diameter of the Earth, that causes the Earth to deform, giving rise to ocean tides. If the tidal force is stronger, which is the case for the gravitational field of BHs and SMBHs, than a given body's internal gravity (cohesiveness), the body will be disrupted.

The minimum distance to which a body (in our case this can be thought of as a star) can approach the black hole without being torn apart by tidal forces is the "tidal radius" (Hills, 1975). We consider a star with mass M_* and radius R_* in hydrostatic equilibrium at distance r_{t} from a supermassive black hole with mass M. In order to determine the tidal radius consider the various forces acting on the star per unit mass. This is subject to the gravitational tide of the BH across the star, assuming $r_{\mathrm{t}} \gg R_*$,

$$F_{\mathrm{T}} \simeq \frac{\partial}{\partial r} \left(\frac{GM}{r^2} \right) \Bigg|_{r_{\mathrm{t}}} R_* = \frac{GM}{r_{\mathrm{t}}^3} R_* \tag{1.10}$$

and to the gravitational force of the star

$$F_{\mathrm{G}} = \frac{GM_*}{R_*^2} \,. \tag{1.11}$$

These are both forces per unit mass. In order to obtain the tidal radius we have to require that the gravitational force and the tidal force balance each other out $F_{\rm T} = F_{\rm G}$ obtaining

$$r_{\rm t} = \left(\frac{M}{M_*}\right)^{1/3} R_* \gg R_* \,. \tag{1.12}$$

Essentially $r_{\rm t}$ is the distance from the hole at which $M/r_{\rm t}^3$ equals the mean internal density of the passing star. Since the horizon of a Schwarzschild (i.e. non-spinning) black hole grows linearly with the mass M, while the tidal radius grows with $M^{1/3}$, there is a critical mass known as the Hills mass:

$$M_{\rm Hills} = 1.1 \times 10^8 M_\odot r_*^{3/2} m_*^{-1/2} \tag{1.13}$$

above which the star would be swallowed by the horizon prior to the tidal disruption. Here we defined $m_* = M/M_\odot$ and $r_* = R/R_\odot$. Thus the event does not emit any electromagnetic signal that can be detected, although gravitational wave signals can still be detected.

1.3 Gas accretion

In general the gas that accretes onto the central object has a non zero angular momentum and this breaks spherical symmetry. Each fluid element has an angular momentum per unit mass l and so it is subjected to a centrifugal force per unit mass $v^2/R = l^2/R^3$, where v is the velocity that depends on the radial coordinate. In order to accrete onto the central object, every fluid element must get rid of its angular momentum. The accretion disc provides a useful tool to accomplish this.

Fluid elements conserve their specific angular momentum, thus we can compare the centrifugal force with the gravitational one for each element. At small radii the centrifugal force overcomes the gravitational one, while for $R \to \infty$ the opposite occurs. We define the circularization radius as the radius at which centrifugal balance is achieved

$$r_{\rm c} = \frac{l^2}{GM} \,. \tag{1.14}$$

We will see that this is the radius at which debris orbits circularize after a TDE. We will also shown that this value can be achieved from the conservation of angular momentum during the TDE that feeds the accretion disc. Fluid rotation squeezes the matter that will form a disc around the central object. Fluid elements falling towards the centre will initially be in eccentric orbits around the central object, but rapidly lose energy through shocks and dissipation and settle down in the minimum energy orbit for a given angular momentum, i.e. a circular orbit.

1.3.1 Angular momentum transport and accretion

The shear between adjacent layers of the disc redistributes the angular momentum: it slows down material lying in the inner regions and spins up the outer regions, leading to the spread of the disc. This process allows accretion of gas onto the central object.

Let us consider a simple approximate argument to show how, in a Keplerian disc, angular momentum exchange leads to accretion rather than to a simple spreading. Consider

two parts of the disc at radii R_1 and R_2 respectively, with $R_2 \gg R_1$. Assume that this fluid elements exchange a given amount of angular momentum

$$\Delta J = \Delta M_1 (GMR_1)^{1/2} = \Delta M_2 (GMR_2)^{1/2} \,. \tag{1.15}$$

This quantity is lost by the matter in the inner regions and gained by the outermost material. Since $R_2 \gg R_1$ we have $\Delta M_1 \gg \Delta M_2$, thus the amount of matter that accretes onto the central object is very large compared to the fraction that is carried towards outer radii. An infinitesimal fraction of material is pushed away carrying a finite amount of angular momentum to allow accretion of the inner regions of the disc onto M.

Since the disc mass is of the order of the disrupted star ($\approx M_\odot$) while the black hole is supermassive ($M \gg 10^5 M_\odot$), we can neglect the disc self-gravity and consider the gas orbits to be Keplerian to a first order approximation. Thus, the specific energy of a fluid element on a circular orbit in a gravitational potential of a point mass M is

$$e = \frac{1}{2} v^2 + \phi = -\frac{GM}{2R} \,. \tag{1.16}$$

Thus a fluid element that moves from a large distance ($e \approx 0$) to a smaller radius R has lost part of its energy. It has to maintain half of the potential energy gain from infinity in order to keep moving on circular orbit. The remaining $\Delta E_{\rm diss} = GM/2R$ is dissipated by viscous processes.

If we assume that the disc extends to infinity, we have that the total disc luminosity is given by

$$L_{\rm disc} = \frac{1}{2} \frac{GM\dot{M}}{R_{\rm in}} \tag{1.17}$$

where $\dot{M}$ is the accretion rate and $R_{\rm in}$ is the disc inner radius (we discuss this relation for the luminosity later in section (2.2.7)).

The disc inner radius is essentially the last stable orbit for a Kerr black hole

$$R_{\rm in} = f(a) GM/c^2 = f(a)\, 1.5 \times 10^{11}\, M_6 \,{\rm cm} \,, \tag{1.18}$$

with

$$f(a) = 3 + z_2 \mp (3 - z_1)^{1/2} (3 + z_1 + 2\, z_2)^{1/2} \,, \tag{1.19}$$

where

$$z_1 = 1 + (1 - a^2)^{1/3} \left[(1 + a)^{1/3} + (1 - a)^{1/3} \right] \,, \tag{1.20}$$

and

$$z_2 = (3\, a^2 + z_1^2)^{1/2} \tag{1.21}$$

The two signs refer to infalling particles with angular momentum either aligned or counter-aligned with respect to the spin direction. The innermost stable circular orbit (ISCO) for a Schwarzschild black hole ($a = 0$) is $R_{\rm in} = 6GM/c^2$ while for an extreme Kerr black hole ($a = 1$) it is located at $R_{\rm in} = GM/c^2$ for prograde orbits and $R_{\rm in} = 9GM/c^2$ for retrograde orbits (see Fig. 1.2).

For a Schwarzschild black hole $R_{\rm in} = 3R_{\rm S} = 6GM/c^2$, so according to 1.17 the disc luminosity is $L_{\rm disc} = (1/12)\dot{M}c^2$. Thus the efficiency in conversion of energy into light

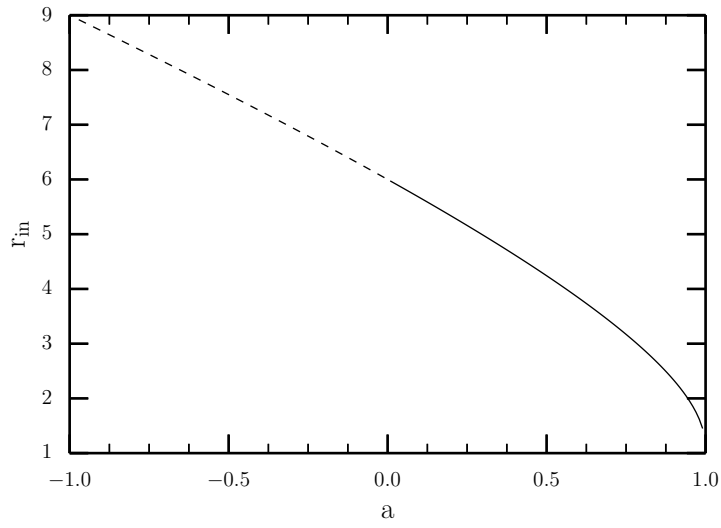

Figure 1.2: Radius of the innermost stable circular orbit in units of the gravitational radius $R_{\rm g} = GM/c^2$ both for prograde (straight-line) and retrograde orbits (dashed-line).

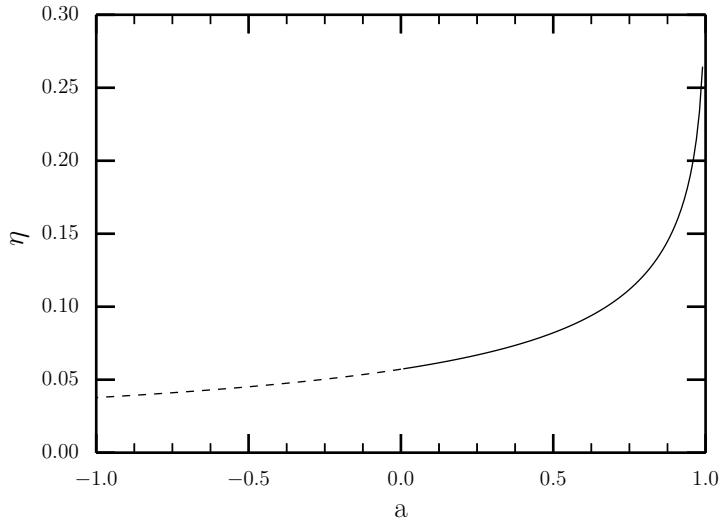

Figure 1.3: Accretion efficiency as a function of the hole spin a. The straight line stands for a prograde disc, while the dashed line stands for a retrograde one.

emission is very high. For a rotating Kerr black hole the efficiency is even higher (about 50%) because the radius of the last stable orbit is closer to the black hole.

Since for a black hole the radius does not refer to a hard surface but only to a region into which matter falls without escaping, the majority of the accretion energy might disappear into the black hole and simply add to its mass, rather than be radiated. This is parametrized by the accretion efficiency η, a dimensionless function of the black hole spin only. The accretion luminosity is then

$$L_{\rm acc} = \eta \dot{M} c^2 \,. \tag{1.22}$$

The accretion efficiency establishes how fast the black hole will grow and depends only on the hole spin value a. It can be obtained from the expression of the energy of a particle in the Kerr effective potential (Bardeen et al., 1972). Note that, while Eq. (1.22) is valid in general, Eq. (1.17) has been inferred in the Newtonian limit assuming that the disc extends to infinity. Massive black holes are stable and therefore can power an AGN by accretion as long as there is supply of gas from which energy can be extracted with sufficiently high efficiency.

In order to discuss the efficiency of energy extraction we need to consider that the metric describing the spacetime outside a black hole is the Kerr metric. Since the Kerr metric coefficients are independent of t and ϕ, the energy and angular momentum of a particle moving in the Kerr metric are conserved. From the calculation of both e and l (energy and angular momentum per unit mass), substituting them in the Kerr metric, we obtain the effective potential for motion in the equatorial plane

$$V_{\rm eff}(R) = -\frac{GM}{R} + \frac{l^2}{2R^2} + \frac{1}{2}\left(1-e^2\right)\left(1+\frac{a^2}{R^2}\right) - \frac{GM}{R^3}\left(l-ae\right)^2 \,. \tag{1.23}$$

The most important class of orbits are the circular ones in the equatorial plane. For a circular orbit at some radius R , $dR/d\tau$ (where τ is the proper time defined by the metric) must vanish both instantaneously and at all subsequent times. The general equation of motion in this potential then gives the conditions $V_{\rm eff}(R) = 0$ and $V'_{\rm eff}(R) = 0$. These equations can be solve simultaneously for e and l. The expression for the particle energy E (for details see Bardeen et al. (1972)) is

$$E(r) = mc^2 \frac{r^{3/2} - 2r^{1/2} \pm a}{r^{3/4}\left(r^{3/2} - 3r^{1/2} \pm 2a\right)^{1/2}} \tag{1.24}$$

where we defined r as the radial coordinate R in units of the gravitational radius $R_{\rm g} = GM/c^2$. The upper sign refers to particles orbiting in the same sense as the rotation of the hole, while the lower sign occurs for counter-rotating particles. An analogous expression can be obtained for L. The last stable orbit corresponds to a maximum efficiency of energy extraction

$$\eta(a) = 1 - \frac{E(r_{\rm in})}{mc^2} = 1 - \frac{f^{3/2} - 2f^{1/2} \pm a}{f^{3/4}\left(f^{3/2} - 3f^{1/2} \pm 2a\right)^{1/2}} \tag{1.25}$$

or approximately 50% for a particle co-rotating with a hole having the maximum allowed spin $a = 1$ (see Fig. 1.3).

When a particle falls into a black hole, all the available gravitational potential energy is released outside. In accretion discs the material cannot fall into the black hole without

dissipating its binding energy, so the efficiency must be given by the binding energy per unit mass at the last stable orbit, and this exceeds 6% even for a non-rotating black hole. Thus, in a disc efficiency presents no problem, provided only that a suitable source of viscosity exist to ensure that material falls in.

Chapter 2

Accretion disc physics

In general the gas accreting onto a black hole has non-zero angular momentum and therefore orbits any central massive object rather than simply falling onto it. The test particle trajectories are not closed ellipses since nearby stars or gas self-gravity causes perturbation in the Keplerian potential. These trajectories intersect each other creating gas shocks that result in dissipation of orbital energy through heating and radiation. Since angular momentum must be conserved the gas settles into lowest energy orbits and since in general it does not have all the same specific angular momentum it does form a disc rather than a ring.

In this Chapter we give a general description of accretion discs in order to understand the evolution of the systems under investigation. Even though the aim of this thesis is to describe the evolution of warped accretion disc, we also discuss the properties of flat discs that are valid in general (Lodato, 2008). In section 2.3 we present the warped disc scenario in details.

2.1 Accretion disc formation

Accretion discs in high energy astrophysics are often related to compact objects, such as white dwarfs, neutron stars and black holes. They can be found in a variety of astrophysical environments. For instance, protostellar discs around stars are thought to be the birthplace of planets. AGN are surrounded by wide accretion discs that have been detected through observations of water masers emission (Miyoshi et al., 1995; Greenhill et al., 1996).

Accretion discs can form around stars as a consequence of the gravitational collapse of the molecular cloud in which the star is forming that has a non zero initial angular momentum. They form also around black holes from energy dissipation and circularization of gas that is initially in elliptical orbits around the compact object. This gas might originate from the stellar debris after a TDE, in which the star is disrupted by the tidal force of a black hole. Another mechanism to form an accretion disc occurs in Low Mass X-ray Binaries (LMXBs) where the companion star fills in its Roche lobe causing part of its material to flow towards the black hole and form an accretion disc.

In general, without rotation the gas would sink down to the black hole without forming an accretion disc. A small amount of angular momentum prevents such falling, allowing the gas to sink down only to a minimum distance from the centre. This distance is the circularization radius, defined in Chapter 1 , and depends only on the mass of the central object M and on the angular momentum per unit mass of the gas l : $r_{\rm c} = l^2/GM$.

For instance, this distance is about twice the tidal radius $r_{\rm t}$ for a typical TDE. The disc will extend from the circularization radius down to the innermost circular orbit (ISCO),

that depends only on the black hole spin value. The inner parts of the disc will be more strongly affected by the Lense-Thirring torque than the outer layers. This difference will lead to the formation of a warp that will be discussed in details in section 2.3.

2.2 Accretion disc structure and dynamics

Accretion disc are usually assumed to be geometrically thin. The typical scale for the disc thickness H is set by the disc temperature T, as will be described below. The disc temperature varies considerably, even within individual discs.

In general, accretion discs have a large surface and thus they can cool down fast through radiation. This implies that the temperature and the pressure of the disc can reach low values rapidly and thus are not able to support the disc against gravity unless the disc is flat, thus if $H/R \ll 1$ where R is the radial distance.

2.2.1 Thin disc approximation

Requiring that $H/R \ll 1$ is equivalent to requiring the sound speed c_s to be much smaller than the rotational velocity v_ϕ. Moreover, assuming that accretion takes place on a long timescale, the radial velocity v_R turns out to be smaller than both the sound speed and the rotational speed. Thus in thin accretion discs we have the ordering: $v_\mathrm{R} \ll c_\mathrm{s} \ll v_\phi$. We now treat the thin disc approximation according to which most of the equations we are going to use can be integrated in the vertical direction. Thus rather than dealing with quantities per unit volume (such as the density ρ), we deal with quantities per unit surface (such as the surface density Σ) instead. When volume quantities are needed (for example the viscosity ν), these will generally be understood as vertically averaged.

As we will see in section 2.3, equations for the propagation of a warp inside the accretion disc become simpler in this approximation (Papaloizou & Lin, 1995). However, for instance, accretion discs formed after TDEs around supermassive black holes are expected to be geometrically thick rather than thin. We will discuss also the corrections due to the disc being thick later on in the thesis.

2.2.2 Gas dynamics of viscous disc

The evolution of accretion discs can be described by the basic equations of viscous fluid dynamics: the continuity and the Navier-Stokes equations. Given the geometry of the problem, we use cylindrical coordinates centred on the central object and assume that to the first order the disc is axisymmetric, therefore no disc quantity depends on the azimuthal angle ϕ. Consider a disc with surface density $\Sigma(R,t)$. The continuity equation, integrated in the vertical direction, reads:

$$\frac{\partial \Sigma}{\partial t} + \frac{1}{R}\frac{\partial}{\partial R}(R\Sigma v_\mathrm{R}) = 0 \tag{2.1}$$

To determine the velocity $\mathbf{v}$, we use the Navier-Stokes equation:

$$\frac{\partial \mathbf{v}}{\partial t} + (\mathbf{v}\cdot\nabla)\mathbf{v} = -\frac{1}{\rho}(\nabla P - \nabla\cdot\sigma) - \nabla\Phi \tag{2.2}$$

where σ is the stress tensor that describes the effect of viscous forces, P is the pressure, ρ is the density and Φ is the gravitational potential.

The left hand side is the acceleration with the second term describing the momentum convected into the fluid by velocity gradients. On the right hand side we find the various forces acting on the fluid: pressure, viscous forces and gravity.

Since in most cases the disc mass can be neglected with respect to the central object mass, gravity is dominated by the latter. So the gravitational potential is simply given, to a first order approximation, by

$$\Phi = -\frac{GM}{r} \tag{2.3}$$

where r is the spherical radius $r^2 = z^2 + R^2$, with z being the coordinate in the vertical direction. The gravitational force is directed in the radial direction, and is given by:

$$-\nabla\Phi = -\frac{GM}{r^2}\hat{\mathbf{r}}\,. \tag{2.4}$$

As a first approach, the stress tensor can be assumed to be that given by the classical shear viscosity. Thus the only non vanishing component of σ in a circular shearing flow is

$$\sigma_{R\phi} = \rho\nu R\frac{d\Omega}{dR} \tag{2.5}$$

where $R\,d\Omega/dR$ is the rate of strain and $\Omega = v_\phi/R$ is the angular velocity and we have introduced the kinematic viscosity ν, which has the dimensions of length times velocity.

2.2.3 Centrifugal balance in the radial direction

In Eq. (2.2) the first term, $\partial v_{\rm R}/\partial t$, is negligible with respect to the second term, which gives rise to the centrifugal term $-v_\phi^2/R$. On the right hand side, the viscous term vanishes and the pressure term can be obtained using the equation of state. For a barotropic gas, since its pressure depends only on its density, the sound speed is simply defined as $c_{\rm s}^2 = dP/d\rho$.

If $c_{\rm s} \ll v_\phi$, the only term on the right hand side of (2.2) able to balance the centrifugal force is therefore the radial component of the gravitational force. To the first order, thus neglecting the pressure forces in the radial direction, we have the centrifugal balance:

$$\frac{v_\phi^2}{R} \simeq \frac{d\Phi}{dR} = \frac{GM}{R^2} = \frac{v_{\rm K}^2}{R} \tag{2.6}$$

where we used the fact that in the thin disc approximation $r \sim R$. The rotational velocity $v_\phi^2 = v_{\rm K}^2$ is then given by (2.6). Therefore, the angular velocity is

$$\Omega^2 = \frac{GM}{R^3} \tag{2.7}$$

which is a restatement of Kepler's third law. Therefore discs that do obey these relations are called Keplerian discs. Note that a Keplerian disc is strongly shearing in the radial direction, since Ω has a relatively strong decrease with R.

2.2.4 Hydrostatic equilibrium in the vertical direction

We now consider the vertical component of the Navier-Stokes equations (2.2). Since the velocity in the vertical direction is very small, the left hand side of the equation becomes negligible. The viscous force vanishes as well, since the only non-zero component of the stress is in the $R\phi$ direction. Thus we are left with just two terms to balance: gravitational force and pressure force in the vertical direction. The Navier-Stokes equation in the vertical direction becomes

$$\frac{1}{\rho}\frac{\partial P}{\partial z} = -\frac{d\Phi}{dz}\,. \tag{2.8}$$

The vertical component of gravity is

$$-\frac{GM}{r^2}\hat{z} \sim -\frac{GM}{r^2}\tan\delta \sim -\frac{GM}{R^2}\frac{z}{R} \tag{2.9}$$

where δ is the longitudinal angle above the disc and the approximation is valid for small z. The equation for the hydrostatic balance is then

$$\frac{c_{\rm s}^2}{\rho}\frac{\partial \rho}{\partial z} = -\frac{GMz}{R^3} = -\Omega^2 z \tag{2.10}$$

solving which we obtain the vertical density profile, which turns out to be a Gaussian

$$\rho(z) = \rho_0 e^{-z^2/2H^2} \tag{2.11}$$

where ρ_0 is the mid-plane density and

$$H = \frac{c_{\rm s}}{\Omega} = R\frac{c_{\rm s}}{v_\phi}\,. \tag{2.12}$$

Thus the surface density is given by

$$\Sigma = \int_{-\infty}^{+\infty} \rho dz = \int_{-\infty}^{+\infty} \rho_0 e^{-z^2/2H^2} dz = (2\pi)^{1/2}\rho_0 H\,. \tag{2.13}$$

The disc aspect ratio is then

$$\frac{H}{R} = \frac{c_{\rm s}}{v_{\rm K}}\,, \tag{2.14}$$

which then demonstrates that requiring that the disc is geometrically thin is equivalent to requiring that the disc rotation is highly supersonic. The speed of sound is given by

$$c_{\rm s}^2 = P/\rho \tag{2.15}$$

where in general the pressure P is the sum of gas and radiation pressures:

$$P = \frac{\rho k_{\rm B} T_{\rm c}}{\mu m_{\rm p}} + \frac{4\sigma_{\rm SB}}{3c}T_{\rm c}^4\,. \tag{2.16}$$

Here $\sigma_{\rm SB}$ is the Stefan-Boltzmann constant and we have assumed that the temperature T is close to the central value $T_{\rm c}$. We discuss the last approximation in section (2.2.7).

We have considered non-self gravitating disc. A complete treatment on the effect of gravitational instabilities can be found in Kratter & Lodato (2016) for protostellar discs and in Lodato & Pringle (2007).

2.2.5 The α-prescription

The nature of viscosity in accretion discs has been debated for decades in the scientific community. It is now commonly known, by means of hydrodynamical simulations, that accretion disc are turbulent and the transport occurs because of fluctuations associated with turbulence. While in non turbulent flows the exchange of angular momentum occurs through collisions between individual gas particles, in turbulent flows the mixture of fluid elements enhances the transport of angular momentum. Turbulence might arise from magneto-hydrodynamical instabilities in the accretion disc, in particular the magneto-rotational instability (MRI)(Balbus & Hawley, 1991). Let us consider a vertical weak magnetic field in a well-ionized plasma. In this configuration, the magnetic field lines are frozen within the disc. If now we perturb two fluid elements with a small radial displacement the magnetic field would tend to bring them back to the original configuration. Due to the shear in the disc, the inner fluid element coupled to the field moves azimuthally faster than an outer one. Magnetic tension along the field line then acts to remove angular momentum from the inner element, and add angular momentum to the outer one. This causes further radial displacement, leading to an instability.

Shakura & Sunyaev (1973) provided an estimate of the magnitude of viscosity using a very simple argument. The stress tensor has the physical dimension of a pressure, that is a density times the square of a velocity. The simplest assumption is then to take the stress tensor to be just proportional to the vertically integrated pressure $\Sigma c_{\rm s}^2$:

$$T_{{\rm R}\phi} = \frac{d\ln\Omega}{d\ln R}\alpha\Sigma c_{\rm s}^2\,, \tag{2.17}$$

where $d\ln\Omega/d\ln R = -3/2$ for a Keplerian disc, and where α is the proportionality factor between the stress tensor and the pressure. Assuming that the turbulence in the disc is isotropic and subsonic, Shakura & Sunyaev (1973) introduced a prescription for the kinematic viscosity ν given by

$$\nu = \alpha c_{\rm s} H\,. \tag{2.18}$$

The magnitude of the turbulent viscosity is given roughly by $\nu \sim v_{\rm t} l$, where l is the typical size of the largest eddies in the turbulent pattern and where $v_{\rm t}$ is the typical turbulent velocity. It is unlikely that the turbulence is highly supersonic since otherwise it would easily be dissipated through shocks. We thus have $v_{\rm t} \lesssim c_{\rm s}$. An upper limit to the size of the largest eddies l is obviously given by the disc thickness H (if we consider an isotropic viscosity). These two upper limits, taken together, clearly imply that $\alpha < 1$. It is important to point out that this is not a theory of viscosity in accretion discs. It is a simple parametrization based on dimensional analysis and on the fact that it is natural to assume that to a first approach the local stresses are proportional to the local rate of strain. This parametrization allows to put all the unknowns on the viscosity in this parameter α.

Non-local mechanisms of angular momentum transport may exist and for these the simple linear proportionality in Eq. (2.17) does not hold any longer. For instance, disc instabilities may play a crutial role in substaining turbulence and provinding a source of energy and angular momentum transport in accretion discs. The two main instabilities are the MRI and the gravitational instability (GI) (Lodato, 2007). The condition for the MRI to take place, in the regime of ideal magnetohydrodynamics (MHD), is that $\partial\Omega^2/\partial R < 0$, which is generally satisfied in accretion disc, provided that the gas is

perfectly coupled with the magnetic field. The gravitational instability might take place when $M_{\rm disc}/M \gtrsim H/R$. Especially in the colder outer parts, the disc self-gravity might affect its behaviour due to the propagation of density waves which lead to the formation of spirals. These waves are expected to provide a non negligible contribution to the angular momentum transport. In some cases the instability is strong enough that the disc might also fragment producing bound clumps. The investigation of the dynamics of self-gravitating discs is crutial to understand the processes that lead to the feeding of young stars and supermassive black holes in AGN. Furthermore, Coughlin & Nixon (2015) recently demonstrated numerically that the streams of the debris from a tidally disrupted star can be gravitationally unstable and form bound clumps. The accretion of these clumps causes a fluctuation of the late-time fallback rate.

In order to investigate in more detail the transport of angular momentum through non-local processes in accretion discs, large scale numerical simulation needs to be performed.

2.2.6 Angular momentum conservation

The azimuthal component of Navier-Stokes equation, integrated in the vertical direction, is

$$\frac{\partial}{\partial t}\left(\Sigma R v_\phi\right) + \frac{1}{R}\frac{\partial}{\partial R}\left(R v_\phi \Sigma v_{\rm R} R\right) = \frac{1}{R}\frac{\partial}{\partial R}\left(R^2 T_{R\phi}\right) \tag{2.19}$$

in which $T_{R\phi}$ is the vertically integrated stress tensor between adjacent layers. The right hand side term is the torque exerted by viscous forces while the left hand side term is the Lagrangian derivative of the angular momentum per unit mass. Combining equation (2.19) with the continuity equation (2.1), the angular momentum conservation equation becomes:

$$\frac{\Sigma\partial(\Omega R^2)}{\partial t} + \Sigma v_{\rm R}\frac{\partial(\Omega R^2)}{\partial R} = \frac{1}{R}\frac{\partial}{\partial R}\left(T_{R\phi}R^2\right) \tag{2.20}$$

Equation (2.17) then reads

$$T_{R\phi} = -\frac{3}{2}\alpha\Sigma c_{\rm s}^2 = -\frac{3}{2}\nu\Sigma\frac{c_{\rm s}}{H} \tag{2.21}$$

where the second equality is obtained using the α-prescription (2.18). From Eq. (2.20) we can obtain the radial velocity

$$v_{\rm R} = \frac{\frac{\partial}{\partial R}\left(\nu\Sigma R^3\Omega'\right)}{R\Sigma\frac{\partial}{\partial R}\left(R v_\phi\right)} \tag{2.22}$$

which can be inserted back into the continuity equation to give:

$$\frac{\partial\Sigma}{\partial t} = -\frac{1}{R}\frac{\partial}{\partial R}\left[\frac{1}{(R^2\Omega)'}\frac{\partial}{\partial R}\left(\nu\Sigma R^3\Omega'\right)\right]. \tag{2.23}$$

The above equation (2.23) is one of the key ingredient in accretion discs theory. It is a diffusion equation for the surface density of the disc, whose temporal evolution is determined only by the kinematic viscosity ν.

In stationary conditions ($d/dt = 0$), $v_{\rm R} < 0$ and thus the matter is moving inward. We can then define the accretion rate as $\dot{M} = -2\pi\Sigma v_{\rm R} R = \text{const}$ and use equation(2.20) to obtain

$$\dot{M}\Omega R^2 + 2\pi T_{R\phi} R^2 \equiv \dot{J} \tag{2.24}$$

where the first term represents the amount of angular momentum transported by the accreting matter. The forces that are leading to the angular momentum transport in a rotating system are also inducing an energy flow equal to $G(R) = -2\pi R^2 T_{R\phi}$. In Keplerian discs Ω increases inward and $T_{R\phi} < 0$, thus the energy flow is directed outwards.

The flux of angular momentum becomes, considering the definition (2.17),

$$\dot{J} = \dot{M}\Omega R^2 - 3\pi\nu\Sigma R^2\Omega = R^2\Omega(\dot{M} - 3\pi\nu\Sigma) \tag{2.25}$$

The value of the flux of angular momentum can be obtained from the so called 'no torque boundary condition'. Let us suppose that our disc extends all the way down to the surface $R = R_{\rm in}$ of the central object. In a realistic situation, the central object must rotate more slowly than the break-up speed at its equator, i.e. with angular velocity $\Omega_{\rm in} < \Omega(R_{\rm in})$. In this case the angular velocity of the disc material remains Keplerian and thus increases inwards, until it begins to decrease to the value $\Omega_{\rm in}$ in a 'boundary layer' of radial extent b. Thus there exists a radius $R = R_{\rm in} + b$ at which $d\Omega/dR = 0$. At this radius, the viscous torque vanishes due to the presence of a boundary layer where the disc connects to the central object.

For the thin disc approximation described above, we have that $b \ll R_{\rm in}$. Thus the angular momentum flux becomes $\dot{J} = \dot{M}\Omega(R_{\rm in})R_{\rm in}^2$. Inserting this into equation (2.25), we obtain

$$\dot{M}\left[1 - \left(\frac{R_{\rm in}}{R}\right)^{1/2}\right] = 3\pi\nu\Sigma\,. \tag{2.26}$$

At large radii, $R \gg R_{\rm in}$, the surface density and the viscosity satisfy the following simple relation:

$$\dot{M} = 3\pi\nu\Sigma \tag{2.27}$$

that is, surface density and viscosity are inversely proportional.

We note that, since a black hole does not have a 'hard surface' at $R_{\rm in}$, the 'no torque boundary condition' might not be necessary. However, numerical simulations performed by Shafee et al. (2008) have shown that, in the steady state, the specific angular momentum profile of the accreting magnetized gas (around a non-spinning black hole) at the ISCO deviates by only 2% from the standard thin disc model, which takes into account the no torque boundary condition (Novikov & Thorne, 1973).

2.2.7 Disc energetics

In losing their angular momentum the particles in the disc also lose their gravitational energy due to viscous processes. Part of the gravitational energy leads to an increase in the kinetic energy of rotation while the rest is converted into thermal energy. This energy is radiated from the surface of the disc since it cannot heat up the disc in a stationary configuration.

The power produced by the torque $G(R)$ exerted on an annulus of radial extension ΔR per unit radial interval is

$$-\frac{\partial G}{\partial R}\Omega = -\left(\frac{\partial}{\partial R}(G\Omega) - G\Omega'\right) \tag{2.28}$$

The matter at R loses its energy due to two contribution. The first is related to energy transport by means of viscosity and it vanishes when integrated on the disc surface except for the energy transported out of the disc boundaries (so it does not give any contribution to the energy radiated from the disc surface). The second is the energy dissipation caused by viscous forces. We can define the dissipated power per unit area from the disc surfaces as

$$D(R) = \frac{-G(R)\Omega'}{2\pi R} = \nu\Sigma\left(R\Omega'\right)^2 . \tag{2.29}$$

In a steady, Keplerian disc by using (2.26) we obtain

$$D(R) = \frac{3GM\dot{M}}{4\pi R^3}\left[1 - \left(\frac{R_{\rm in}}{R}\right)^{1/2}\right] . \tag{2.30}$$

Hence the energy flux through the faces of a steady thin disc is independent of viscosity. This result comes from the fact that we were able to use conservation laws to eliminate ν. However, clearly, the other disc properties (e.g. Σ, $v_{\rm R}$, etc.) do depend on the viscosity. The energy flux decreases near the last stable orbit and the maximum of $D(R)$ is reached at $R = 1.36R_{\rm in}$ (Shakura & Sunyaev, 1973). Since the energy transport is radiative, the energy flux in the vertical direction is:

$$F(z) = -\frac{16\sigma_{SB}T^3}{3\kappa_R\rho}\frac{dT}{dz} , \tag{2.31}$$

where κ_R is the Rosseland mean opacity. Integrating this equation in the vertical direction and defining the optical depth $\tau = \rho\kappa_R H \simeq \kappa_R\Sigma$ we obtain the relation between the energy flux and the disc temperature:

$$F(H) - F(0) = -\frac{4\sigma_{SB}}{3\tau}(T^4 - T_{\rm c}^4) \tag{2.32}$$

where the ratio between the central temperature $T_{\rm c}$ and the temperature at which radiation is emitted T is of the order of $\tau^{1/4}$. If the accretion disc is optically thick ($\tau \gg 1$) we have $T_{\rm c} \gg T$, the energy flux at $z = 0$ is negligible and thus we can write

$$F(H) = \frac{4\sigma_{SB}}{3\tau}T_{\rm c}^4 = \frac{D(R)}{2} , \tag{2.33}$$

where we divide by a factor 2 because the disc has two sides, obtaining the expression for the power per unit surface dissipated by the disc.

If we assume that the disc extends to infinity, we have that the disc luminosity is

$$L_{\rm disc} = \int_{R_{\rm in}}^{\infty} 2\pi R\, D(R)\, dR = \frac{1}{2}\frac{GM\dot{M}}{R_{\rm in}} \tag{2.34}$$

where in the last expression we have substituted the expression (2.30). Note that the luminosity is only half of the potential energy lost by the accreting matter, the remaining half being needed to keep the disc in Keplerian rotation at $R_{\rm in}$.

The energy dissipated by an annulus of width ΔR, far from the inner boundary is given by

$$2\pi R\, D(R)\Delta R = \frac{3GM\dot{M}}{2R^2}\Delta R\,. \tag{2.35}$$

We know that $(GM\dot{M}/2R^2)\Delta R$ comes from the release of gravitational binding energy. The extra energy is provided by the energy transported from the inner disc and indeed it can be shown that the energy transport term in equation (2.28) provides just the right amount of energy.

If all the dissipated power (cfr. Eq. 2.30) is radiated away at R as thermal black body emission we can write the expression for the energy density of radiation ϵ

$$\epsilon = bT_{\rm c}^4 = 4\frac{\sigma_{SB}}{c}T_{\rm c}^4 = \frac{1}{c}3\tau D(R) = 3\frac{D(R)}{c}\Sigma\kappa_R\,. \tag{2.36}$$

Shakura & Sunyaev (1973) divide the disc in three main regions depending on the radial distance from the central object:

- region (a) radiation pressure dominated with $c_{\rm s}^2 = \epsilon/3\rho$. In this region, photon scattering onto free electrons plays the main role. Thus the opacity is $\kappa_{\rm R} \simeq \kappa_{\rm T}$, with $\kappa_{\rm T} = \sigma_{\rm T}/m_{\rm p}$ being the opacity for Thomson scattering;
- region (b) gas pressure dominated with $c_{\rm s}^2 = k_{\rm B}T/m_{\rm p}$. Electron scattering gives still the main contribution to the opacity;
- region (c) still gas pressure dominated with $c_{\rm s}^2 = k_{\rm B}T/m_{\rm p}$ and the opacity determined by free-free absorption and other mechanisms, thus $\kappa_R \simeq \kappa_{\rm ff}$.

Within the region of maximal energy flux $R < 1.36R_{\rm in}$ the radiation pressure dominates.

According to the standard Shakura & Sunyaev (1973) picture, the stress tensor is proportional to the total (gas plus radiation) pressure. However this results in both thermal (Sunyaev & Shakura, 1975) and inflow (Lightman & Eardley, 1974) instability. In general, thermal instabilities have faster growth rates compared to the inflow modes. Region (a) can be stabilized by considering the stress tensor as given by only the sound speed of the gas $c_{\rm s_g}^2 = k_{\rm B}T/m_{\rm p}$ rather then the whole sound speed $c_{\rm s}$ that includes also the radiation pressure contribution. The same holds for the dissipated power and the energy density radiated per unit surface (2.36):

$$\epsilon = 3\frac{D(R)}{c}\Sigma\kappa_R = \frac{27}{8}\frac{\alpha\kappa_R}{c}\Sigma^2 c_{\rm s_g}^2\,\Omega \tag{2.37}$$

where we have substituted the expression (2.29) for $D(R)$ and we have considered a Keplerian accretion disc.

2.2.8 Disc thickness

We can derive a simple and very important result for the disc thickness H within regions dominated by radiation pressure from the disc energetics. Neglecting gas pressure and combining equations (2.15), (2.16) and (2.30) we get

$$c_{\rm s}^2 = \frac{3GM\dot{M}\tau}{8\pi R^3\rho c}\left[1 - \left(\frac{R_{\rm in}}{R}\right)^{1/2}\right]\,. \tag{2.38}$$

Since the opacity in such a region is dominated by electron scattering, we have $\tau = \Sigma\sigma_{\rm T}/m_{\rm p} = (2\pi)^{1/2}\rho H\sigma_T/m_{\rm p}$. Inserting this into the equation above and eliminating the speed of sound through Eq. (2.12) we obtain

$$H = (2\pi)^{1/2}\frac{3\sigma_T\dot{M}}{8\pi m_{\rm p}c}\left[1-\left(\frac{R_{\rm in}}{R}\right)^{1/2}\right]. \tag{2.39}$$

Hence, the scale-height of radiation pressure supported disc regions is essentially independent of R: this really results from the fact that the radiation pressure force $\sim T_{\rm c}^4 \sim M\dot{M}R^{-3}$ is balancing the z-component of gravity $\propto MHR^{-3}$.

Radiation pressure limits the accretion luminosity of any object to the Eddington value that we have derived in Section 1.2.1. From Equation (1.22), this means that there is a critical accretion rate $\dot{M}_{\rm crit}$:

$$\dot{M}_{\rm crit} = \frac{L_{\rm Edd}}{\eta c^2} = \frac{4\pi GMm_{\rm p}c}{\eta\sigma_T c^2} = 4\times10^{-13}\left(\frac{\eta}{0.1}\right)^{-1} M_6 M_\odot {\rm yr}^{-1}. \tag{2.40}$$

In terms of the critical Eddington accretion rate value, the disc thickness (2.39) becomes

$$H = \frac{3}{2\eta}(2\pi)^{1/2}\frac{GM}{c^2}\frac{\dot{M}}{\dot{M}_{\rm crit}}\left[1-\left(\frac{R_{\rm in}}{R}\right)^{1/2}\right] \approx \frac{R_{\rm g}}{\eta}\frac{\dot{M}}{\dot{M}_{\rm crit}} \tag{2.41}$$

In the outer regions, where $R \gg R_{\rm in}$ the disc thickness does not depend on the radius but only on the flux of accreting matter.

2.2.9 Discs around black holes

Initially, we consider the disc inner radius to be the last stable orbit of a Schwarzschild black hole because we want to be able to compare our results to those obtained by Shakura & Sunyaev (1973). Thus for now $r_{\rm in} = 3r_{\rm S}$ is the disc inner radius.

Since we assumed the stress tensor to be given by the gas sound speed, the surface density depends on the disc temperature. Thus we need to find a relation for the temperature. Matching equation (2.37) with the general expression for the radiated energy density (2.36) we find that

$$T_{\rm c} = \left(\frac{27\kappa_R k_B}{32\sigma_{\rm SB}m_{\rm p}}\right)^{1/3}\Omega^{1/3}\alpha^{1/3}\Sigma^{2/3} \tag{2.42}$$

The surface density is defined by $\Sigma = (2\pi)^{1/2}\rho H$, where $\rho = \epsilon/3c_{\rm s}^2$ is the density in the radiation pressure dominated region and ϵ is given by Eq. (2.37). Then the surface density reads:

$$\Sigma = \frac{8}{9(2\pi)^{1/2}}\frac{m_{\rm p}}{\alpha k_{\rm B}\kappa_{\rm R}T_{\rm c}}H\Omega. \tag{2.43}$$

Substituting (2.42) in (2.43) we obtain the following relation for the matter surface density

$$\Sigma = 0.86\,\alpha^{-4/5}\,\dot{m}^{3/5}M_6^{1/5}r^{-3/5}\left[1-\left(\frac{r_{\rm in}}{r}\right)^{1/2}\right]^{3/5}{\rm g\,cm^{-2}} \tag{2.44}$$

The numerical value is obtained defining the following dimensionless quantities: $M_6 = M/10^6 M_\odot$, $\dot{m} = \dot{M}/\dot{M}_{\rm crit}$ and $r = R/R_{\rm g}$, with $r_{\rm in} = 3 \times 10^{11} M_6$ cm and we have considered $\kappa_{\rm R} \simeq \kappa_{\rm T} = \sigma_{\rm T}/m_{\rm p}$.

The temperature at the midplane of the disc is then given by (2.42)

$$T_{\rm c} = 3 \times 10^3 \, \alpha^{-1/5} \dot{m}^{2/5} M_6^{-1/5} r^{-9/10} \left[1 - \left(\frac{r_{\rm in}}{r}\right)^{1/2}\right]^{2/5} \, {\rm K} \tag{2.45}$$

The energy density then becomes

$$\epsilon = \frac{8}{\pi} \frac{c}{\kappa_R} \frac{\Omega}{\alpha} = 1.3 \times 10^{10} \, \alpha^{-1} M_6^{-1} r^{-3/2} \, {\rm erg} \, . \tag{2.46}$$

The result for the energy density (2.46) is the same that Shakura & Sunyaev (1973) have obtained if we consider their dimensionless quantities. Results for both the surface density and the disc temperature are slightly different because we have considered the stress tensor given by (2.17) with $c_{\rm s}^2 = c_{\rm s_g}^2$, neglecting the contribution of the radiation pressure to the speed of sound. However we can see that the orders of magnitude are the same (see Eq. (2.44) and (2.45)).

The behaviour of an accretion disc surrounding a Kerr black hole is similar to that of a Schwarzschild black hole except for the value of the innermost stable orbit radius, which causes some changes in the scale values of the quantities of interest inferred in the previous section. However the radial dependences are the same as the one for non-rotating black holes.

For a Kerr rotating black hole the radius of the last stable orbit, and so the disc inner edge $r_{\rm in}$ is given by (1.18). It is useful to write the aspect ratio H/R as a function of the radius so that we can evaluate the thin disc approximation. Dividing (2.41) by R we get

$$\frac{H}{R} = \frac{3}{2} (2\pi)^{1/2} \, \eta^{-1} \left(\frac{1}{r}\right) \dot{m} \left[1 - \left(\frac{r_{\rm in}}{r}\right)^{1/2}\right] \tag{2.47}$$

where the accretion efficiency is $\eta = \eta(a)$. Deriving we find that the aspect ratio reaches its maximum at $x \equiv r/r_{\rm in} = 2.25$ at which

$$\left.\frac{H}{R}\right|_{\rm max} = 0.557 \, \eta^{-1} f^{-1} \dot{m} \tag{2.48}$$

From Eq. (2.47) we can see that very close to the black hole the disc becomes thick and the thin disc approximation is no longer valid. This equation shows also that at accretion rates approaching the critical value (2.40), the thin disc approximation must break down near the central object. We can see that the thin disc approximation will also fail if $T_{\rm c}$ becomes very large, for example when the cooling mechanism is inefficient, so that the temperature of the disc greatly exceeds the black body temperature $T(R)$.

Similarly, it is useful to evaluate the ratio $c_{\rm s}/c$ in terms of the quantities of interest. In the radiation pressure dominated region we have

$$\frac{c_{\rm s}}{c} = \frac{3}{8\pi} (2\pi)^{1/2} \frac{\kappa_R}{c^2} \dot{M} \Omega \left[1 - \left(\frac{r_{\rm in}}{r}\right)^{1/2}\right] \tag{2.49}$$

$$= \frac{3}{2} (2\pi)^{1/2} \eta^{-1} \dot{m} \, r^{-3/2} \left[1 - \left(\frac{r_{\rm in}}{r}\right)^{1/2}\right] \tag{2.50}$$

which reaches its maximum $c_s/c \simeq 0.74$ at $x \equiv r/r_{in} = 1.78$ (for $a = 0.9$ and $\eta = 0.15$). In this way we ensured that the speed of sound is always smaller compared to the speed of light.

2.2.10 Thick discs

So far we discussed the properties of geometrically thin accretion discs with $H \ll R$. While this theory is well understood, the theory describing accretion discs with $H \sim R$ is not as complete and understood. In thin disc theory the radial pressure gradients are neglected and the vertical pressure balance is solved separately. This can be done as long as the disc is geometrically thin but this approximation may be violated in the innermost regions of accretion discs around black holes and neutron stars (see Eq. 2.47). For instance, the accretion disc formed after a TDE is expected to be geometrically thick since the initial mass accretion rate is well above the Eddington threshold.

Abramowicz et al. (1988) developed a model for slim accretion discs with $\dot{M} \simeq \dot{M}_{crit}$ taking into account additional cooling due to general relativistic Roche lobe overflow and the advection of heat. In particular, in a slim disc configuration, the additional term $v_R dv_R/dr$ and the horizontal pressure gradient $\rho^{-1} dP/dr$ need to be included in the Navier-Stokes equation (i.e. Eq. 2.2). Furthermore the advective horizontal heat flux $v_R T dS/dr$ is added to the energy equation.

Sądowski et al. (2011) developed a 2-D model for slim disc in which radial and vertical structures are coupled and then compared their model with the general relativistic version of the Shakura & Sunyaev (1973) model for thin discs (Novikov & Thorne, 1973). They found that for lower accretion rate ($0.1\dot{M}_{crit}$) the disc is radiatively efficient and therefore the flux profile coincides with the Novikov & Thorne solutions, while for higher accretion rates ($1.0\dot{M}_{crit}$) advection becomes important and the emission departs from the Novikov & Thorne profile.

Strubbe & Quataert (2009) developed a model for TDE accretion discs describing both the super-Eddington and the sub-Eddington regime. In the first phase the time it takes for photons to diffuse out of the disc is longer than the viscous time, so the disc is thick and advective, while at later times the accretion drops below the Eddington limit and the disc can cool by radiative diffusion. They neglect gas pressure and assume the stress tensor to be proportional to the radiation pressure. Including the radial entropy gradient in the energy equation and after some calculations the inferred disc aspect ratio is

$$\frac{H}{R} = \frac{3}{4}\,\eta^{-1}\dot{m}\,r^{-1} f(r) \left[\frac{1}{2} + \left[\frac{1}{4} + 6\,f(r)\left(\frac{\dot{m}}{\eta}\right)^2 \left(\frac{1}{r}\right)^2\right]^{1/2}\right]^{-1} \tag{2.51}$$

where $f(r) = (1 - (r_{in}/r)^{1/2})$ (r is the radius in units of R_g), $\dot{m} = \dot{M}/\dot{M}_{crit}$ and η is the accretion efficiency. A slightly modified version of this model will be used later in Chapter 5 to describe an accretion disc formed after a TDE by a SMBH.

2.2.11 Timescales

It is worth to briefly report and compare the timescales over which accretion discs form and evolve. First of all we have the dynamical timescale, which is simply related to the

angular velocity Ω by

$$t_{\rm dyn} = \frac{1}{\Omega}\,. \tag{2.52}$$

This is roughly the time needed to reach centrifugal equilibrium. For a Keplerian disc $\Omega = (GM/R^3)^{1/2}$, thus the dynamical time scales as $R^{3/2}$: the inner region of the disc moves faster than the outer one.

The second important timescale is the vertical timescale, needed to reach hydrostatic balance in the vertical direction. This is given by the sound crossing time across the disc thickness H

$$t_{\rm z} = \frac{H}{c_{\rm s}} = \Omega^{-1}\,. \tag{2.53}$$

This is of the same order of the dynamical timescale. In order to keep the gas at the top surface of the disc on top, the fluid elements need to receive an upward force, provided by pressure, that has to be effective on the short orbital timescale.

The third timescale is the thermal timescale $t_{\rm th}$, which is the time needed for the disc to change its thermal structure and its temperature. In general, there will be a cooling timescale $t_{\rm cool}$ that is set by the specific cooling processes in the disc, and a heating timescale $t_{\rm heat}$ determined by energy release due to accretion. In thermal equilibrium these two timescales are equal. The heating timescale is defined as the ratio between the heat content at a given radius and the power produced by accretion. Thus

$$t_{\rm th} = \frac{\Sigma c_{\rm s}^2/(\gamma(\gamma-1))}{\nu\Sigma(R\Omega')^2} \sim \frac{1}{\alpha\Omega}\,. \tag{2.54}$$

where γ is the ratio of the specific heats. Since $\alpha < 1$, the thermal timescale is longer than the dynamical one.

Finally the viscous timescale sets the time for the evolution of the surface density. This timescale is given by

$$t_\nu = \frac{R^2}{\nu} = \left(\frac{H}{R}\right)^{-2} \frac{1}{\alpha\Omega}\,. \tag{2.55}$$

We can see that the centrifugal balance in the radial direction and the hydrostatic balance in the vertical direction are very rapidly achieved, while the disc temperature evolves on a longer timescale, and on an even longer timescale one can see some evolution in the disc surface density profile.

2.3 Warped discs

In general the gas that orbits a black hole might have angular momentum in different directions and thus might settle into a warped disc. For instance, the disc formed by a tidally disrupted star might end up being warped. In general, there are many effects that lead to the formation of a warp in the accretion disc.

At distances of the order of $\approx 10 - 10^2 R_{\rm S}$ (with $R_{\rm S}$ being the Schwarzschild radius) from the black hole the most likely cause of warping is due to relativistic effects. For instance, the Lense-Thirring precession (dragging of inertial frames) might induce a warp in the disc (Bardeen & Petterson, 1975). The rate of precession is proportional to R^{-3}

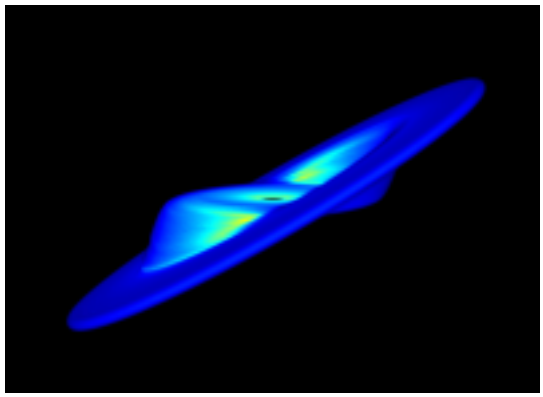

Figure 2.1: 3D structure of the warped accretion disc from 20 million particles SPH simulation performed by Lodato & Price (2010) using the PHANTOM code (Price et al., 2017). The disc inner regions lie in the equatorial plane while outer regions are inclined with respect to it.

(Kumar & Pringle, 1985), thus, since a faster precession implies an enhanced viscous dissipation, the inner parts of the disc tend to align the direction of their specific angular momentum with that of the black hole, while outside the typical warp radius $R_{\rm W} \approx 10^2 R_{\rm S}$ the disc keeps its original misalignment. The warp radius is defined as the radius where the warp diffusion timescale $t_{\nu_2} = R^2/\nu_2$, where ν_2 is the vertical shear viscosity that we defined later in this Section, equals the local forced precession rate $\Omega_{\rm p} = \omega_{\rm p}/R^3$ (Scheuer & Feiler, 1996):

$$R_{\rm W} = \frac{\omega_{\rm p}}{\nu_2}\,. \tag{2.56}$$

The disc is aligned at $R \ll R_{\rm W}$ and becomes misaligned at $R \gg R_{\rm W}$. Thus, an accretion disc becomes warped when the angular momentum direction changes with radius within the disc itself.

Fig. 2.1 shows the results obtained by Lodato & Price (2010) using very high resolution (up to 20 million particles) Smoothed Particle Hydrodynamics (SPH) simulations of a warped accretion disc. In order to induce a warp in the disc, the orbit of each particle is then tilted. Lodato & Price (2010) showed that there is very good agreement between numerical simulations and the analytic theory of warped discs in the diffusive regime.

While for a disc that lies entirely in the equatorial plane the evolution is described by means of a one-dimensional viscosity that transfers the angular momentum radially, in a warped disc the communication of angular momentum is three-dimensional. In particular, a planar disc has only the azimuthal shear acting to remove angular momentum and allowing accretion while in a warped disc there is a second 'vertical' type of shear and so the rate of orbital shear is $R\partial\Omega/\partial R\mathbf{l} + R\Omega\partial\mathbf{l}/\partial R$ (Ogilvie & Latter, 2013). The vertical viscosity is induced by horizontal (radial) pressure gradients caused by the misalignment of adjacent disc rings. The extra physics in a warped disc is thus the presence of a second component of the orbital shear that leads to the presence of an oscillatory pressure gradient in the fluid. In a nearly Keplerian disc the resonance of the forcing epicyclic frequency with the orbital frequency induces a torque driven by pressure resulting in the launch of a pressure wave.

The first self-consistent investigation on warped discs, in the regime $H/R \lesssim \alpha \ll 1$,

was performed by Papaloizou & Pringle (1983). They derived the linearized equation for angular momentum conservation first neglecting then taking into account the internal fluid dynamics. Pringle (1992) improved the previous work deriving a general equation of motion using only conservation laws that do not require to assume that the disc tilt is $\ll H/R$. However this work does not offer any insight on the viscosity values. Ogilvie (1999) then performed a systematic analysis starting from three dimensional fluid equations and derived a full equation that describes the evolution of a warped disc. They also determined the viscosity coefficients (azimuthal and vertical) as functions of the warp amplitude confirming the previous result of Papaloizou & Pringle (1983) obtained in the linear regime: azimuthal coefficient $\alpha_1 = \alpha$ and vertical one $\alpha_2 = 1/(2\alpha)$.

In this section we consider warps and their propagation in accretion discs. We briefly illustrate the case of a sufficiently viscous and thin disc where the warp propagates in a diffusive way ($\alpha \gtrsim H/R$) and we discuss in more details the opposite regime in which the disc is thick enough so that the warp propagates as a wave ($\alpha \lesssim H/R$). It is worthwhile to study both regimes in order to have an entire picture of the possible behaviours of warped accretion discs. For a detailed overview on warp propagation see Nixon & King (2016).

The more suitable way to describe a warp is to adopt a set of cylindrical coordinates with the Euler angles. Thus an annulus is described by (R, ϕ, z) and by the angles $\beta(R,t)$ and $\gamma(R,t)$. Let β be the tilt angle (the angle between the radial direction and the plane of the warped part of the disc) and γ be the twist angle, thus we can write the angular momentum unit vector in the following form

$$\mathbf{l} = (\cos\gamma \sin\beta, \sin\gamma \sin\beta, \cos\beta)\,. \tag{2.57}$$

The warp amplitude is defined as

$$\psi = R\left|\frac{\partial\beta}{\partial R}\right| = R\left|\frac{\partial \mathbf{l}}{\partial R}\right| \tag{2.58}$$

where the second expression holds for small values of β. Indeed we have $z = R\tan\beta \simeq R\beta$ for small β values and so $\partial z/\partial R \sim R\partial\beta/\partial R = \psi$.

2.3.1 Diffusive regime

In the regime where the viscous damping dominates over pressure forces, the warp propagates diffusively within the accretion disc. The equation of motion in the diffusive case are well understood in both linear and non linear regimes.

We now consider a Keplerian geometrically thin rotating disc with angular velocity $\Omega(R)$, surface density $\Sigma(R)$ and angular momentum density $\mathbf{L}(R)$. The direction of the angular momentum is defined by the unit vector $\mathbf{l}(R) = \mathbf{L}(R)/L(R)$. The disc is warped whenever the angular momentum direction changes with radius.

Following Papaloizou & Pringle (1983), we take the tilt of each annulus to be small so that we can write $\mathbf{l} = (l_\mathrm{x}, l_\mathrm{y}, 1)$ where $l_\mathrm{x}, l_\mathrm{y} \ll 1$. The continuity equation is not affected by the small tilt and thus is given by Eq. (2.1). By assumption $\partial\mathbf{l}/\partial t \ll \Omega\mathbf{l}$, thus the local density of angular momentum can be written as $\Sigma R^2\Omega\mathbf{l}$. The equation of conservation of angular momentum for an annulus of width ΔR at a radius R is

$$\frac{\partial}{\partial t}\left(\Sigma 2\pi R^3 \Delta R \Omega \mathbf{l}\right) = \left(\Sigma 2\pi R^3 v_{\rm R} \Delta R \Omega \mathbf{l}\right)_R - \left(\Sigma 2\pi R^3 v_{\rm R} \Delta R \Omega \mathbf{l}\right)_{R+\Delta R} + \\ + \mathbf{G}\left(R+\Delta R\right) - \mathbf{G}\left(R\right) + \mathbf{T} \quad (2.59)$$

where $\mathbf{G}(R,t)$ is the three-dimensional internal viscous torque exerted by one annulus onto its neighbours and $\mathbf{T}$ is the external torque that gives rise to the precession of the warp. For the time being, we neglect this external torque.

In local cylindrical coordinates (R,ϕ,z) we have the (R,ϕ) component of the viscous torque that is proportional to $R\,d\Omega/dR$ and independent of the azimuthal angle and the component (R,z) that is $\partial v_z/\partial R$ and has a $\cos\phi$ dependence. The (R,ϕ) component gives a contribution in the local direction of $\mathbf{l}$ that is $\mathbf{G}_1 = 2\pi\nu_1\Sigma R^2 d\Omega/dR$ (i.e. the standard viscous torque in a flat disc). By considering neighbouring annuli with directions $\mathbf{l}$ and $\mathbf{l}+\mathbf{\Delta l}$, the (R,z) component gives a contribution in the direction of $\Delta\mathbf{l}$ equal to $\mathbf{G}_2 = 2\pi R\frac{1}{2}\nu_2\Sigma R^2\Omega\partial\mathbf{l}/\partial R$, where the factor $1/2$ comes from the azimuthal average of $\cos^2\phi$. In order to derive the full angular momentum equation we let ΔR go to zero in equation (2.59) obtaining:

$$\frac{\partial}{\partial t}(\Sigma R^2\Omega\mathbf{l}) + \frac{1}{R}\frac{\partial}{\partial R}(Rv_R\Sigma R^2\Omega\mathbf{l}) = \frac{1}{R}\frac{\partial}{\partial R}(\nu_1\Sigma R^3\Omega'\mathbf{l}) + \frac{1}{R}\frac{\partial}{\partial R}(\frac{1}{2}\nu_2\Sigma R^3\Omega\frac{\partial\mathbf{l}}{\partial R}) \quad (2.60)$$

We assume the disc to be geometrically thin at each radius in the direction of $\mathbf{l}$. Taking the dot product of equation (2.60) with $\mathbf{l}$ and recalling that $\mathbf{l}\cdot\partial\mathbf{l}/\partial R = -\left|\partial\mathbf{l}/\partial R\right|^2$ we obtain the following expression for the radial velocity (Pringle, 1992)

$$v_{\rm R} = \frac{\frac{\partial}{\partial R}(\nu_1\Sigma R^3\Omega') - \frac{1}{2}\nu_2\Sigma R^3\Omega\left|\frac{\partial\mathbf{l}}{\partial R}\right|^2}{\Sigma R\frac{\partial}{\partial R}(R^2\Omega)} \quad (2.61)$$

Thus the radial velocity of a warped disc is smaller (more negative) than that of a flat disc. This implies an enhancement in the accretion rate.

Substituting this last expression in the continuity equation (2.1) we obtain

$$\frac{\partial\Sigma}{\partial t} = -\frac{1}{R}\frac{\partial}{\partial R}\left[\frac{\frac{\partial}{\partial R}(\nu_1\Sigma R^3\Omega')}{\frac{\partial}{\partial R}(R^2\Omega)}\right] + \frac{1}{R}\frac{\partial}{\partial R}\left[\frac{\frac{1}{2}\nu_2\Sigma R^3\Omega\left|\frac{\partial\mathbf{l}}{\partial R}\right|^2}{\frac{\partial}{\partial R}(R^2\Omega)}\right]. \quad (2.62)$$

The physical meaning of the two terms on the right hand side of Eq. (2.62) is the following. If the disc is flat, $\partial\mathbf{l}/\partial R = 0$ and the equation reduces to the standard accretion disc evolution equation. Thus the first is a diffusive term, i.e a term proportional to the second derivative of the angular momentum. The second term on the right hand side is an advective term with inwards flow velocity proportional to $\nu_2|\partial\mathbf{l}/\partial R|^2$.

There is also a third component of the internal torque (Papaloizou & Pringle, 1983; Ogilvie, 1999) $\mathbf{G}_3 = 2\pi R\nu_3\Sigma R^2\Omega\mathbf{l}\times\partial\mathbf{l}/\partial R$ that does not lead to a diffusive behaviour but causes a ring to precess if it is inclined with respect to its neighbours. This last term does not have a component in the direction of $\mathbf{l}$ meaning that it causes neighbouring rings to change their planes while it does not lead to any flux of mass or angular momentum. Its viscosity coefficient is smaller than ν_2 by a factor $\approx\alpha$, therefore it is often neglected. However, in the case concerning inviscid non-Keplerian discs, this is the only non-zero internal torque (Ogilvie, 1999).

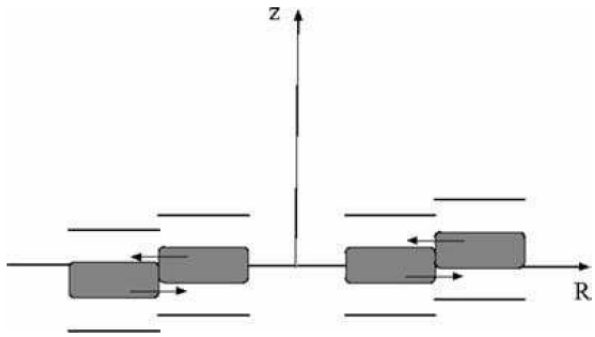

Figure 2.2: Schematic view of warped disc. The shaded areas indicate regions of higher pressure. The arrows indicate the direction of the pressure gradient induced by the warp. As a fluid element orbits around the centre, it feels an oscillating radial pressure gradient, whose amplitude is a linear function of the height z. (from Lodato & Pringle 2007)

2.3.1.1 The $\alpha_2 - \alpha$ relation

Lodato & Pringle (2007) have introduced a simple, physical model to describe the diffusive evolution of a warp in geometrically thin, viscous discs. This model essentially reproduces the more rigorous analysis of Papaloizou & Pringle (1983). The evolution of a warp is controlled essentially by hydrodynamical processes within the disc itself. The main point is that a warp, coupled with vertical stratification in a thin disc, induces a horizontal pressure gradient which depends on vertical height z (see Fig. 2.2).

As a fluid element orbits around the centre, it feels an oscillating radial pressure gradient, whose amplitude is a linear function of the height z, that vanishes along the line of nodes where there is no instantaneous pressure gradient. This horizontal pressure gradient oscillates with the orbital frequency Ω. For a Keplerian disc this forcing term is resonant with the epicyclic motion, since the epicyclic frequency is $\kappa = \Omega$. Hence the presence of the warp excites strong horizontal epicyclic motion within the disc. Thus the radial velocity field takes the approximate form

$$v_R = v_\perp \left(\frac{z}{H}\right) \cos\phi = v_\perp \left(\frac{z}{H}\right) \cos\Omega t \tag{2.63}$$

where ϕ is the azimuthal angle in the disc and $v_\perp$ denotes the induced horizontal velocity (induced by the radial pressure gradient) in the radial direction at the disc surfaces $z = \pm H$. The radial velocity depends on the fluid element position in the disc: if $\phi = \pi/2$, the radial velocity vanishes and so there is no horizontal oscillation motion.

The magnitude of the induced pressure gradient is given roughly by

$$\frac{\partial p}{\partial R} \sim \frac{\partial p}{\partial z}\psi \sim \frac{p\psi}{H} \tag{2.64}$$

We let $x(t)$ be the radial displacement of a disc particle at the disc surface relative to an unperturbed disc particle on a circular orbit, this implies that

$$x(t) = \left(\frac{v_\perp}{\Omega}\right) \sin\Omega t\,. \tag{2.65}$$

Then a disc particle at position $x(t)$ is subject to three forces: a restoring force which gives rise to the epicyclic oscillations, a damping force due to some form of viscous dissipation, and a pressure force caused by the warp with amplitude given by Eq. (2.64). Thus the radial component of the equation of motion is, using (2.14), (2.15) and the driven acceleration given by $(1/\rho)dp/dR$,

$$\ddot{x} + \frac{\dot{x}}{\tau} + \Omega^2 x = R\Omega^2 \left(\frac{\psi H}{R}\right) \cos \Omega t \tag{2.66}$$

where we have introduced a damping timescale τ, that describes the viscous damping of the horizontal shear motion induced by the warp. (Note that this horizontal motion is shearing in the vertical direction).

The horizontal shear motion is damped by a kinematic viscosity ν_z on a timescale $\tau \sim R^2/\nu_z$. If we assume that the viscosity is isotropic, so that $\nu_z = \nu_1$ where we have indicated $\nu = \nu_1$ the standard disc viscosity, we have

$$\tau \sim \frac{H^2}{\nu_1} = \frac{1}{\alpha\Omega}\,. \tag{2.67}$$

Note that assuming the isotropic viscosity means that each component of the shear (horizontal and vertical) is damped at the same average rates but this does not imply that the effective viscosity coefficients are isotropic (Nixon et al., 2016).

Now we look after a solution of the equation of motion in the form $x(t) = a \sin \Omega t$, where a is the amplitude of the horizontal motions at the disc surface. Substituting in Eq. (2.66) we find that

$$a = \psi H(\Omega\tau) \tag{2.68}$$

that corresponds to a horizontal velocity of $v_\perp = \dot{x} = a\Omega = \psi c_s(\Omega\tau)$.

The amplitude of the vertical shear is then

$$S = \frac{dv_R}{dz} = \frac{\Omega a}{H} = \Omega^2 \tau \psi \tag{2.69}$$

If we make the further assumption that the horizontal shear is damped by an isotropic viscosity with magnitude measured with the α-prescription, then

$$a \sim \frac{\psi}{\alpha} H \tag{2.70}$$

and the horizontal velocity is given by $v_\perp \simeq c_s\psi/\alpha$. So the amplitude of the vertical shear will be $S \simeq \Omega\psi/\alpha$.

Now, the coefficient ν_2 acts formally on the radial derivative of the vertical component of the velocity, since it dissipates the warp. The dissipation actually comes about because of damping of the resonantly induced horizontal shear motion that communicates the warp between different radii. The viscosity ν_z causes a decrease in the variation of v_R with z and so produces a damping of the oscillatory motion. If there is no more oscillatory motion, the warp is dissipated, thus dv_z/dR decreases. We need to relate these two processes; the rate at which the energy is dissipated in the two processes must be the same. Thus we have

$$\nu_2 \left\langle \frac{dv_z}{dR} \right\rangle^2 = \nu_z \left\langle \frac{dv_R}{dz} \right\rangle^2 \tag{2.71}$$

In a warped disc $v_z = \psi R\Omega$ and so $dv_z/dR = \psi\Omega$ that gives

$$\nu_2 = \nu_z(\Omega\tau)^2 = \Omega H^2(\Omega\tau) \tag{2.72}$$

With the α-prescription we can write equivalently the dissipation coefficient $\alpha_2 = \Omega\tau$. If the damping timescale is given by (2.67) we finally recover the desired scaling of ν_2 with α in the linear case

$$\frac{\nu_2}{\nu_1} \sim \frac{1}{\alpha^2} \tag{2.73}$$

It is worth noticing that this result is somewhat counterintuitive since it implies that the damping of the warp occurs more rapidly when the viscosity is smaller. This comes about because a small value of isotropic viscosity (small α) permits a large resonant velocity $v_R \propto 1/\alpha$. The dissipation rate depends on $\nu v_R^2 \propto 1/\alpha$, and so increase as α decreases. It is evident that the analysis must break down at some stage as $\alpha \to 0$.

2.3.1.2 External torque by spinning black holes

If we consider an accretion disc around a spinning black hole with a misaligned angular momentum, the disc undergoes Lense-Thirring precession (see Chapter 3). This effect induces a warp in the disc structure. The disc then achieves a steady state on a timescale t_{ν_2}. The Bardeen-Petterson effect (Bardeen & Petterson, 1975) leads to alignment between the black hole and the disc angular momentum on a given timescale $t_{\rm align}$.

We now consider a black hole with angular momentum $\mathbf{J}_{\rm h}$ surrounded by a Keplerian accretion disc with surface density Σ and specific momentum density $\mathbf{L}(R,t) = \Sigma R^2\Omega\mathbf{l}(R,t)$. We now consider the warp at $R_{\rm W} \gg R_{\rm S}$ (Lodato & Pringle, 2006), thus we can treat the black hole as a point mass and use Newtonian dynamics to treat our system. The equation for conservation of specific angular momentum in the disc is

$$\begin{aligned}\frac{\partial\mathbf{L}}{\partial t} = &\frac{3}{R}\frac{\partial}{\partial R}\left[\frac{R^{1/2}}{\Sigma}\frac{\partial}{\partial R}(\nu_1 R^{1/2}\Sigma)\mathbf{L}\right] + \frac{1}{R}\frac{\partial}{\partial R}\left(\frac{1}{2}\nu_2 R|\mathbf{L}|\frac{\partial\mathbf{l}}{\partial R}\right)\\ &+ \frac{1}{R}\frac{\partial}{\partial R}\left\{\left[\nu_2 R^2\left|\frac{\partial\mathbf{l}}{\partial R}\right|^2 - \frac{3}{2}\nu_1\right]\mathbf{L}\right\}\end{aligned} \tag{2.74}$$

where the first two terms are diffusive (proportional to $\partial^2\mathbf{l}/\partial R^2$), the third is advective (proportional to $\partial\mathbf{l}/\partial R$) and we used the formalism of Pringle (1992). Note that this equations evolve both the disc tilt and the surface density profile.

Papaloizou & Pringle (1983) have shown that in the linear approximation, corresponding to small warp angles, the ratio between the two coefficients of viscosity is $\nu_2/\nu_1 = 1/(2\alpha^2)$ (see section 2.3.1.1). Therefore, since $\alpha < 1$, the stress associated with warp propagation is much larger than the viscous stress.

In order to study the Lense-Thirring precession we have to include in Eq. (2.74) the external torque that the black hole exerts on the disc (Kumar & Pringle, 1985)

$$\frac{\partial\mathbf{L}}{\partial t}\,|_{\rm LT} = \mathbf{\Omega}_{\rm p}(R) \times \mathbf{L}(R) \tag{2.75}$$

where $\mathbf{\Omega}_{\rm p} = \omega_{\rm p}/R^3 = 2G\mathbf{J}_{\rm h}/(c^2R^3)$ is the precession rate for $R \gg R_{\rm S}$. Since the torque on the black hole is perpendicular to its angular momentum (torque components are in

the $x-y$ plane), the modulus of $\mathbf{J}_{\rm h}$ is constant with time. The only effects of the relative torques are to make the black hole spin change direction or precess (y-component) and affect alignment (x-component).

Accretion induced changes in the black hole spin occur on a longer timescale compared with that of the disc-induced change in spin direction because warp propagation typically occurs faster than mass propagation.

2.3.1.3 Steady state solution

The steady state solution of the angular momentum conservation equation (2.74) is

$$W = K \exp\left[-2(1-i)\left(\frac{\omega_{\rm p}}{\nu_2 R}\right)^{1/2}\right] \tag{2.76}$$

where we used the complex variable $W = l_{\rm x} + i l_{\rm y}$ to make the calculations. Therefore we see that for $R \to \infty$ the variable W tends to a constant value K, thus we have a flat inclined disc. If $R \to 0$ also $W \to 0$ and then we have a flat disc perpendicular to the axis of the black hole.

Since the Lense-Thirring precession rate is proportional to R^{-3} the main contribution comes from annuli within or just beyond the warp. Scheuer & Feiler (1996) derived the alignment timescale

$$t_{\rm align} = \left(\frac{acM}{2\nu_2 G}\right)^{1/2} \frac{1}{\pi \Sigma_\infty} \tag{2.77}$$

It is useful to rewrite this result in terms of the accretion rate. At large radii we have $\dot{M} = 3\pi\nu_1\Sigma_\infty$, substituting Σ_∞ in Eq. (2.77) with some manipulations we have

$$t_{\rm align} = 3a\frac{\nu_1}{\nu_2}\frac{M}{\dot{M}}\left(\frac{R_{\rm S}}{R_{\rm W}}\right)^{1/2} \tag{2.78}$$

Since $R_{\rm S}/R_{\rm W} \ll 1$, the alignment time is always shorter than the accretion time $M/\dot{M}$. This is consistent with the estimate given by Lodato & Pringle (2006). Thus while the warp propagates in the disc, the change in disc angular momentum (at the warp radius) is equal to the change in the black hole angular momentum during the alignment.

2.3.2 The bending waves regime

In the regime where the disc thickness is large compared to the viscosity coefficient α, the warp propagates as a wave within the disc (Papaloizou & Lin, 1995). The equation of motion in this wave-like case are only understood in the linear regime. The non linear investigation requires modelling the disc with little dissipation and thus high resolution numerical simulations.

Let us consider an accretion disc around a Kerr black hole. The steady Lense-Thirring torque causes each ring to precess at a rate that depends on the radius of the ring, resulting in a rapid twisting of the disc. If the disc is able to communicate the warp disturbances efficiently, it might be able to resist the differential precession by establishing an internal torque. This can be arranged so that the net torque on each ring is such as to produce a single, uniform precession rate.

The concomitant dissipation changes the total angular momentum of the disc, tending to bring it into alignment with the plane of rotation of the black hole. The oscillatory

torque in this regime drives a bending wave in the disc. The net effect of the steady (external) and oscillatory (internal) torques determines whether an initially coplanar disc will acquire a tilt over time or whether an initially inclined disc will evolve towards coplanarity.

We consider small amplitude warps that can be treated as linear perturbations of the fluid equation in a geometrically thin, non-self-gravitating disc in an external gravitational potential $\Phi(R,z)$ that is axisymmetric but not necessarily spherically symmetric. We suppose that the disc is nearly Keplerian in the sense that

$$\left|\frac{\kappa^2-\Omega^2}{\Omega^2}\right| \lesssim \frac{H}{R} \tag{2.79}$$

where κ is the epicyclic frequency, and

$$\left|\frac{\Omega_{\rm z}^2-\Omega^2}{\Omega^2}\right| \lesssim \frac{H}{R} \tag{2.80}$$

where $\Omega_{\rm z}$ is the vertical oscillation frequency. The three characteristic frequencies of motion are respectively

$$\begin{aligned} \Omega^2 &= \left(\frac{1}{R}\frac{d\Phi}{dR}\right)_{z=0} \\ \kappa^2 &= 4\Omega^2 + 2\Omega R\frac{d\Omega}{dR} \\ \Omega_{\rm z}^2 &= \left(\frac{\partial^2\Phi}{\partial z^2}\right)_{z=0} \end{aligned} \tag{2.81}$$

The linear dynamics of wave-like discs was first investigated by Papaloizou & Lin (1995). The linearized equations for the wave propagation within the accretion disc were derived also by Demianski & Ivanov (1997); Lubow & Ogilvie (2000) and read

$$\Sigma R^2\Omega\frac{\partial \mathbf{l}}{\partial t} = \frac{1}{R}\frac{\partial \mathbf{G}}{\partial R} + \mathbf{T} \tag{2.82}$$

$$\frac{\partial \mathbf{G}}{\partial t} + \left(\frac{\kappa^2-\Omega^2}{\Omega^2}\right)\frac{\Omega}{2}\mathbf{e_z}\times\mathbf{G} + \alpha\Omega\mathbf{G} = \Sigma R^3\Omega\frac{c_{\rm s}^2}{4}\frac{\partial \mathbf{l}}{\partial R} \tag{2.83}$$

where $\mathbf{T}(R,t)$ is the external torque density acting on the disc and $\mathbf{G}(R,t)$ is the internal torque. Equation (2.82) contains the horizontal component of the angular momentum conservation equation, including the external torque

$$\mathbf{T} = -\Sigma R^2\Omega\left(\frac{\Omega_{\rm z}^2-\Omega^2}{\Omega^2}\right)\frac{\Omega}{2}\mathbf{e_z}\times\mathbf{l}\,. \tag{2.84}$$

This torque arises from the lack of spherical symmetry in the black hole gravitational potential and therefore from the difference between the orbital and the vertical frequency. It is zero if the disc is Keplerian (thus $\Omega=\Omega_{\rm z}$) and there are no external effects.

The second term on the left hand side of (2.83) shows that the internal torque is mediated by horizontal epicyclic motion that are driven near resonance by horizontal pressure gradients in the warped disc. This term is zero for a precisely Keplerian disc. These stresses, together with the external torque, are responsible for the propagation of bending waves. The term proportional to α tends to dissipate the waves through an

exponential factor on a timescale $\sim 1/(\alpha\Omega)$. The horizontal motion is proportional to z and is therefore subject to strong viscous dissipation, which is the dominant channel of damping of the bending waves. Besides, equation (2.82) was derived assuming that the surface density profile does not change with time and that the radial velocity is zero. Thus these equation do not take into account neither mass diffusion nor angular momentum advection.

We can also write the above equation in the complex domain, considering the variables $W = W_{\rm x} + iW_{\rm y}$ and $G = G_{\rm x} + iG_{\rm y}$,

$$\Sigma R^2 \left[\frac{\partial W}{\partial t} + \left(\frac{\Omega_{\rm z}^2 - \Omega^2}{\Omega^2} \right) i \frac{\Omega}{2} W \right] = \frac{1}{R} \frac{\partial G}{\partial R} \tag{2.85}$$

$$\frac{\partial G}{\partial t} + \left(\frac{\kappa^2 - \Omega^2}{\Omega^2} \right) i \frac{\Omega}{2} G + \alpha\Omega G = \Sigma R^3 \Omega \frac{c_{\rm s}^2}{4} \frac{\partial W}{\partial R} \tag{2.86}$$

where $W(R,t) = \beta(R,t)\exp[i\gamma(R,t)]$ represents the tilt of the disc at each radius with β being the amplitude of the local tilt and γ the azimuthal angle (related to the twist). Note that we can use complex variables because these equations refer to the simple case in which $l_{\rm z} \approx 1$, therefore the only components we are interested in are $l_{\rm x}$ and $l_{\rm y}$.

Equations (2.85) and (2.86) are valid when the quantities W and G are sufficiently small and vary on a length scale longer than the typical disc scale height H and on a time scale long compared to the dynamical one (Ω^{-1}).

The equation of motion for a wave in the case in which the disc is Keplerian, thus $\Omega = \Omega_{\rm z} = \kappa$, and nearly inviscid are (Lubow et al., 2002)

$$\Sigma R^3 \Omega \frac{\partial \mathbf{l}}{\partial t} = \frac{\partial \mathbf{G}}{\partial R} \tag{2.87}$$

$$\frac{\partial \mathbf{G}}{\partial t} + \alpha\Omega\mathbf{G} = \Sigma R^3 \Omega \frac{c_{\rm s}^2}{4} \frac{\partial \mathbf{l}}{\partial R} \tag{2.88}$$

There are two dynamical degrees of freedom in the system described by the above equations. One is the tilting of the disc at each radius according to the tilt vector $\mathbf{l}$. The other is the horizontal motions described by $\mathbf{G}$, which cause eccentric distortions of the disc that are proportional to z.

2.3.2.1 The dispersion relation

In order to find out how fast this waves propagate in the disc we have to look for the dispersion relation (Nelson & Papaloizou, 2000). In the absence of viscosity the dispersion relation for a wave-like solution of (2.85) and (2.86), with rapidly varying phase factor is

$$\left[\omega - \left(\frac{\Omega^2 - \Omega_{\rm z}^2}{2\Omega} \right) \right] \left[\omega - \left(\frac{\Omega^2 - \kappa^2}{2\Omega} \right) \right] = \frac{1}{4} k^2 \Omega^2 H^2 \tag{2.89}$$

where k is the wavenumber. Neglecting the external torque and the non-keplerian term, taking the time derivative of the second equation (2.88) and substituting the (2.87) we obtain the relation

$$\frac{\partial^2 \mathbf{G}}{\partial t^2} + \alpha\Omega \frac{\partial \mathbf{G}}{\partial t} = \frac{c_{\rm s}^2}{4} \frac{\partial^2 \mathbf{G}}{\partial R^2} \tag{2.90}$$

If we write $G(R,t) \propto e^{i(kR+\omega t)}$ and calculate the derivative, we obtain the dispersion relation

$$\omega^2 - i\alpha\Omega\omega = \frac{c_s^2 k^2}{4} \tag{2.91}$$

which is (2.89) for a Keplerian disc. Therefore

$$\omega = \frac{1}{2}\left[i\alpha\Omega \pm (c_s^2 k^2 - \alpha^2\Omega^2)^{1/2}\right] \tag{2.92}$$

This shows that, for an exactly Keplerian disc ($\kappa = \Omega_z = \Omega$) with $\alpha = 0$, the warp propagates as a non-dispersive wave with wave speed $H\Omega/2 = c_s/2$. The presence of nodal and/or apsidal precession introduces dispersion and forbids propagation of frequencies between $(\Omega^2 - \Omega_z^2)/2\Omega$ and $(\Omega^2 - \kappa^2)/2\Omega$ (see Lubow et al. (2002) for details).

When $\alpha \gtrsim Hk$ we see that ω is purely imaginary and wave-like propagation no longer occurs. The propagation becomes purely diffusive in the limit $|\omega| \ll \alpha\Omega$, in which case we obtain

$$\frac{\omega}{i\alpha\Omega} = \left(\frac{c_s k}{2\alpha\Omega}\right)^2 \ll 1 \tag{2.93}$$

This pure diffusion occurs when $\alpha \gg \frac{1}{2}Hk = \pi\frac{H}{\lambda} \simeq \frac{H}{R}$ for the largest wavelength (result obtained by Lodato & Pringle (2007)). The boundary between the purely diffusive and the purely wave-like propagation regimes is not a sharp one. We take the transition between the two regimes to occur when the real and imaginary parts of ω are equal, thus when $\omega_R = \omega_I$. Thus the critical value of the viscosity is

$$\alpha_c = \frac{1}{2}Hk\,. \tag{2.94}$$

The warp propagation in the disc can lead either to local or global bending of the disc itself. The critical factor that distinguish the two scenarios is the wavelength λ of the perturbation. If $H \ll \lambda < R$ the disc warps while for longer wavelengths the disc tilts as a whole. This has been observed in the simulations performed by Nixon & Pringle (2010) that reproduced the response of a protostellar accretion disc to a warp induced in the outer regions by a stellar flyby. The warp propagates inwards towards a critical radius at which $\lambda(R) = R$. At this critical radius the warp wave is reflected and within it the disc is uniformly tilted by the warp. Indeed in the inner regions the perturbation wavelength is greater than the disc size and thus the warp cannot be communicated efficiently. However, since the angular momentum is communicated, the disc inner regions tilt without warping.

2.3.2.2 Timescales for warp propagation

In warped wave-like accretion discs there is also the possibility that the disc responds to the warping disturbances by precessing as a rigid body, meaning that all its annuli precess with the same frequency around the central object. In principle this occurs if the wavelength of the perturbation is larger than the disc outer radius. However also the timescale for the warp propagation inside the disc must be taken into account. The time needed by the warp to propagate inside the disc, which coincides approximately with the

time after which the disc reaches its stationary state. This timescale comes directly from the dispersion relation inferred above

$$t_{\rm wave} = \frac{2R}{c_{\rm s}}\,. \tag{2.95}$$

The ratio between the warp propagation timescale and the viscous timescale is

$$\frac{t_{\rm wave}}{t_\nu} = \frac{2R}{c_{\rm s}}\frac{\nu}{R^2} = 2\alpha\frac{H}{R}\,. \tag{2.96}$$

If the disc is thin the sound crossing time (2.95) is shorter than the viscous one, thus Σ can be assumed as a time constant during the warp propagation. If we refer to a thick disc, we cannot make this assumption, thus we have to consider the time evolution of the surface density.

In order for the disc to be able to achieve global precession we need the wave to damp non-locally ($\alpha \ll H/R$) and the warp propagation to be faster than any precession induced in the disc. We are going to discuss the rigid precession criterion in more details later on in the thesis.

2.3.2.3 Steady shape of a warped disc around a Kerr black hole

We now investigate the steady shape of an accretion disc around a Kerr black hole following Lubow et al. (2002). The orbital, epicyclic and vertical frequency can be inferred from the Kerr metric (Kato, 1990).

$$\begin{aligned} \Omega &= \frac{c^3}{GM}\frac{1}{r^{3/2}+a} \\ \zeta = \left(\frac{\Omega^2-\Omega_{\rm z}^2}{\Omega^2}\right) &= \pm 4ar^{-3/2} - 3a^2r^{-2} \\ \eta = \left(\frac{\Omega^2-\kappa^2}{\Omega^2}\right) &= 6r^{-1} \mp 8ar^{-3/2} + 3a^2r^{-2} \end{aligned} \tag{2.97}$$

where r is the radius in unit of the gravitational radius GM/c^2 and a is the dimensionless hole angular momentum, which is $-1 < a < 1$.

To a first approximation, i.e. considering only the first terms in Eqs. (2.97) and the dispersion relation (2.89) with $\omega = 0$ (thus $G(R,t) \propto e^{ikR}$ does not depend on time), we obtain the radial wavelength associated with the steady wave-like shape of a prograde disc around a Kerr black hole

$$\frac{\lambda}{H} \approx \frac{\pi r^{5/4}}{(6a)^{1/2}}\,. \tag{2.98}$$

The wavelength (2.98) is shorter for more rapidly rotating black holes, and decreases as the marginally stable circular orbit is approached, but is always at least a few times the disc thickness. This suggest that the wave-like solutions are physical and might be described with some confidence by theories of long-wavelength bending waves.

A description of the steady wave-like shape can be achieved by setting the time derivatives in Eq. (2.85) and (2.86) to zero. This results in a second-order ordinary differential equation for the tilt variable $W(R,t)$

$$\frac{d}{dR}\left[\frac{\Sigma R^3\Omega^4 H^2}{\Omega^2-\kappa^2+2i\alpha\Omega^2}\frac{dW}{dR}\right]+\Sigma R^3(\Omega^2-\Omega_{\rm z}^2)W=0 \tag{2.99}$$

We then take the first order approximation of equations (2.97), use the radial coordinate in unit of GM/c^2 and neglect the imaginary part because we are interested in solutions in the real domain (thus with no twist, since $W(r)=\beta(r)e^{i\gamma}$, where β is the warp angle and γ the twist angle). The only way to find an analytic solution in the real domain is to set $\alpha=0$, i.e. to consider an inviscid disc. This approximation can be done if the disc is geometrically thin, so that $\alpha\lesssim H/R\ll 1$.

We would like to express Eq. (2.99) in terms of dimensionless variables. We use therefore the following parametrization for the surface density and the disc aspect ratio respectively: $\Sigma=\Sigma_0 r^{-p}$, $H=H_0 r^{-q+\frac{3}{2}}$, where Σ_0 and H_0 are evaluated at $R_0=GM/c^2$. Thus

$$\frac{d}{dr}\left[r^{4-2q-p}\frac{dW}{dr}\right]+k_* r^{-3/2-p}W=0 \tag{2.100}$$

where we have isolated all physical parameters in $k_*=24a\,(H_0/R_0)^{-2}$. We can see that this latter parameter depends on the black hole spin and on the disc aspect ratio evaluated at the scale radius.

We define the quantities

$$\hat{\alpha}=4-2q-p \tag{2.101}$$

$$\hat{\beta}=-p-3/2 \tag{2.102}$$

so that Eq. (2.100) reads

$$\hat{\alpha}r^{\hat{\alpha}-1}\frac{dW}{dr}+r^{\hat{\alpha}}\frac{d^2W}{dr^2}+k_* r^{\hat{\beta}}W=0\,. \tag{2.103}$$

Making the following substitutions

$$W(r)=r^{\frac{1}{2}(1-\hat{\alpha})}y(r)=r^{-\hat{\gamma}}y(r) \tag{2.104}$$

$$r=z^{\frac{2}{2-\hat{\alpha}+\hat{\beta}}}=z^{1/\hat{\delta}}\,. \tag{2.105}$$

Eq. (2.103) becomes

$$\psi^2\frac{d^2y}{d\psi^2}+\psi\frac{dy}{d\psi}+\left[-\left(\frac{\hat{\gamma}}{\hat{\delta}}\right)^2+\psi^2\right]y=0\,. \tag{2.106}$$

where we defined $\psi=z\sqrt{k_*}/\hat{\delta}$. This is a Bessel differential equation. The solutions to this equation define Bessel functions $J_{[\hat{\gamma}/\hat{\delta}]}(\psi)$ and $Y_{[\hat{\gamma}/\hat{\delta}]}(\psi)$, which are called Bessel function of first and second kind. The solution can be written as a linear combination of Bessel functions

$$y(\psi)=C_1 J_{[\hat{\gamma}/\hat{\delta}]}(\psi)+C_2 Y_{[\hat{\gamma}/\hat{\delta}]}(\psi) \tag{2.107}$$

where C_1, C_2 are constants.

Thus the solution of Eq. (2.100) is

$$W(r) = r^{\frac{1}{2}(3-2q-p)} \left[J_{\left[\frac{p+2q-3}{2q-\frac{7}{2}}\right]} \left(\frac{2\sqrt{k_*} r^{\frac{1}{2}(2q-7/2)}}{2q-\frac{7}{2}} \right) + Y_{\left[\frac{p+2q-3}{2q-\frac{7}{2}}\right]} \left(\frac{2\sqrt{k_*} r^{\frac{1}{2}(2q-7/2)}}{2q-\frac{7}{2}} \right) \right] \tag{2.108}$$

Bessel functions of the first kind are finite at $r = 0$ for all real values of $\nu = \hat{\gamma}/\hat{\delta}$, while Bessel function of the second kind are singular in $r = 0$. The Bessel functions of the first kind can be determined using an infinite power series expansion and Bessel functions of the second kind can be expressed in terms of those of the first kind as follows

$$Y_\nu(\psi) = \frac{J_\nu(\psi)\cos(\nu\pi) - J_{-\nu}(\psi)}{\sin(\nu\pi)} \tag{2.109}$$

At $\psi \ll 1$ the second Bessel function is dominant and the tilt tends to a constant value W_∞. At small radii $\psi \gg 1$ the following approximation based upon asymptotic expansions can be used

$$J_\nu(\psi) = \left(\frac{2}{\pi\psi}\right)^{1/2} \left[C_1 \cos\left(\psi - \frac{\nu\pi}{2} - \frac{\pi}{4}\right) - C_2 \sin\left(\psi - \frac{\nu\pi}{2} - \frac{\pi}{4}\right) \right] . \tag{2.110}$$

Thus Bessel function are oscillatory and the oscillation amplitude is given by

$$W \propto \left(r^{\frac{1}{2}(2q-\frac{7}{2})} \right)^{-1/2} r^{\frac{1}{2}(p+2q-3)} \propto r^{1/8} (\Sigma H)^{-1/2} . \tag{2.111}$$

When the amplitude is independent from radius ($p + q - 5/4 = 0$), the tilt reduces to

$$W = \left(\frac{2}{\pi}\right)^{1/2} [C_1 \sin(r) - C_2 \cos(r)] \tag{2.112}$$

exactly. While the constant C_2 is fixed by the tilt at large radius, the constant C_1 depends on the inner boundary condition. If it is such that the torque vanishes at $R_{\rm in}$, then $dW/dR = 0$ there, meaning that the tilt is a constant (non-zero) function of radius. In the special case of constant amplitude, the solution is

$$W = W_\infty \frac{\cos(r_{\rm in} - r)}{\cos(r_{\rm in})} \tag{2.113}$$

provided that $\cos(r_{\rm in}) \neq 0$. This solution can be understood as a standing wave that is a superposition of ingoing and outgoing bending waves with zero phase velocity but non-zero group velocity. The condition of vanishing torque at the inner boundary reflects ingoing bending waves.

It is worth noticing that in the previous calculation the viscosity has always been modelled using the α-prescription (Shakura & Sunyaev, 1973). This implies that both the vertical and horizontal shear are damped at the same rate by viscous dissipation. However this does not imply that we assumed the effective viscosities (ν_1, ν_2, ν_3) to be isotropic. The internal structure of the warp itself implies that these coefficients have different values that depend on the shear and warp amplitude. If both α and the warp

are small, ν_2 is significantly stronger because of the resonance between disc orbits and forcing in a warp (Nixon & King, 2016). If angular momentum transport is affected by turbulence associated to the MRI within the disc, then it is likely that the strong radial shear, governed by ν_1, would lead to an anisotropic turbulence (Pringle, 1992). Since the radial shear is secular while the vertical shear is oscillatory, the angular momentum transport process is different in each case.

The viscosity assumption is the same in both the diffusive and the bending wave regime. The damping of propagating warp waves can be identified with the ν_2 torque since the physics of both torques is the same. The viscous damping controls the resonant response to radial pressure gradients. When pressure dominates over viscosity then the disc responds by propagating the warp as a wave that damps through α. In the opposite scenario the wave is damped locally and diffuses within the disc.

Note that the oscillatory behaviour depends on the relative sign of nodal and apsidal precession (different for prograde and retrograde discs). The same derivation for the binary potential has been done by Facchini et al. (2013).

Chapter 3

Lense-Thirring rigid precession

Since this thesis contains work on the Lense-Thirring (LT) precession in two different context, the first concerning an accretion disc formed after the tidal disruption of a star (Part II) and the second accretion discs in Low Mass X-ray Binaries (LMXBs) (Part III), it is fundamental to present a general analysis on the global precession of a warped disc around a Kerr black hole. Under certain circumstances that I am going to discuss later on in this Chapter, the warping disturbances are propagated so efficiently that the disc becomes able to precess as a rigid body around the black hole. This means that all the disc annuli precess with the same frequency rather than with their own local LT frequency. We define the precession rate that originates from the LT effect and then calculate the rate of global precession of the disc.

From an observational point of view, the signature of this global precession in a TDE disc is a quasi-periodic behaviour in the light curve caused by the consequent precession of the jet associated with the event (Stone & Loeb, 2012; Shen & Matzner, 2014; Lei et al., 2013). If this is actually the case, then some insight on the values of the black hole parameters can be obtained by measuring the precession period. In the LMXBs case the LT precession of the disc can be associated with type-C QPOs as we will see in the third part of this thesis.

3.1 Global precession frequency

We know that the external torque due to Lense-Thirring precession is $\mathbf{T}(R) = \mathbf{\Omega}_{\rm LT}(R) \times \mathbf{L}(R)$ (see Eq. 2.84), where $\mathbf{\Omega}_{\rm LT}$ is the local precession rate and $\mathbf{L}(R)$ is the angular momentum of the disc (Lodato & Pringle, 2006). The expression for $\Omega_{\rm LT}$ will be specified later in Section 3.3.

In cartesian coordinates, let $\mathbf{\Omega}_{\rm LT}$ define the z-axis and consider an element of the disc with angular momentum $\mathbf{L}$ which is not parallel to the black hole spin. Each such annulus feels a torque $\mathbf{T}(R)$ that induces precession around the z-axis. Integrating over all these torques to get the total torque exerted on the disc by the black hole, we conclude that the total torque can only have components in the (x, y)-plane (King et al., 2005). We can write the scalar equation for the external torque

$$T(R) = \Omega_{\rm LT}(R) L(R)\,. \tag{3.1}$$

where the misaligned component of the disc angular momentum is

$$L(R) = \Sigma R^2 \Omega \sqrt{l_{\rm x}^2 + l_{\rm y}^2} \tag{3.2}$$

We now assume that the warp amplitude is small, therefore $l_{\rm x}, l_{\rm y} \ll 1$ and $l_{\rm z} \approx 1$. Integrating Equation (3.1) between the inner and the outer edge of the disc we get:

$$T_{\rm tot} = \int_{R_{\rm in}}^{R_{\rm out}} T(R) 2\pi R \, dR = \int_{R_{\rm in}}^{R_{\rm out}} \Omega_{\rm LT}(R) L(R) 2\pi R \, dR \, . \tag{3.3}$$

If each of the disc annuli precess with the same frequency, i.e. if the disc globally precess, the misaligned component of the angular momentum rotates in the (x, y)-plane with frequency $\Omega_{\rm p}$. Therefore, the torque experienced by the whole disc due to external LT precession is

$$T_{\rm tot} = \frac{dL_{\rm tot}}{dt} = \Omega_{\rm p} L_{\rm tot} \tag{3.4}$$

where we can define the total disc angular momentum as

$$L_{\rm tot} \simeq \int_{R_{\rm in}}^{R_{\rm out}} L(R) 2\pi R \, dR \, , \tag{3.5}$$

appropriate for small amplitude warps. Thus, the global precession frequency is (Lodato & Facchini, 2013a)

$$\Omega_{\rm p} = \frac{\int_{R_{\rm in}}^{R_{\rm out}} \Omega_{\rm LT}(R) L(R) 2\pi R \, dR}{\int_{R_{\rm in}}^{R_{\rm out}} L(R) 2\pi R \, dR} \tag{3.6}$$

In the case of an accretion disc around a Kerr black hole, the surface density profile in the radiation dominated region is (see Eq. 2.44)

$$\Sigma(R) = \Sigma_0 \, R^{-p} f^p \, . \tag{3.7}$$

where $f = (1 - (R_{\rm in}/R)^{1/2})$ with $p = 3/5$. The coefficient Σ_0 depends on the viscosity α, the accretion rate and the black hole mass.

The underlying assumption in taking Eq. (3.7) as the surface density profile for the whole disc is that the disc under investigation is not very wide and we can consider it to lie within region a) (Shakura & Sunyaev, 1973). This happens to be the case in TDE accretion discs that are indeed expected to be narrow.

3.2 Global precession criterion

So far we have assumed that the disc globally precesses around the black hole. However, simulations and analytical studies have shown that often the disc does not precess as a rigid body but in general shows differential precession and, if the misalignment is large, can even tear apart in discrete rings which then precess with their local precession frequencies (e.g. Larwood et al., 1996; Lodato & Price, 2010; Nixon et al., 2012, 2013; Facchini et al., 2013; Doğan et al., 2015; Nealon et al., 2015). In general, differential precession occurs when the local precession is faster than the wave communication. When this occurs, each of the disc annuli precesses with its own frequency and eventually gets aligned to the plane perpendicular to the spin of the black hole. Krolik & Hawley (2015) showed through simulations that a time-steady transition can be achieved between an inner disc region aligned with the equatorial plane and an outer region orbiting in a different plane.

Papaloizou & Lin (1995), Larwood et al. (1996) and Fragile & Anninos (2005) have shown that the most stringent condition for a disc to globally precess is that the local precession period ($t_{\rm p}(R) = 2\pi/\Omega_{\rm LT}(R)$) at any radius is longer than the sound crossing time $t_{\rm wave}$, of the warp disturbance across the disc.

As an alternative it can be required that the global precession period is longer than the wave travel time. In the following sections, we investigate both criteria in order to establish which one works best using numerical ring code simulations.

3.2.1 Local criterion

For a wavelike disc subject to an external torque driving precession, the warp propagation timescale throughout the whole disc is given by (Lubow et al., 2002)

$$t_{\rm wave} = \int_{R_{\rm in}}^{R_{\rm out}} \frac{2\,dR}{c_{\rm s}}\,. \tag{3.8}$$

In order to rigidly precess we require the disc to be able to communicate any induced warping disturbance on a timescale at least as fast as those disturbances can grow, ensuring that it efficiently communicates the warp. Furthermore, to warp a disc each ring needs to tilt by at least $\sim H$. Geometrically, each of the disc annuli has to precess by a fraction $\sim H/R$ of a full period in order for them to reach a unique precession angle and thus lead to the global precession of the disc. Therefore, thicker discs must precess further to establish a warp. The criterion would then need to depend explicitly also on H/R. From this ansatz we construct the local criterion for global precession of wavelike warped discs as

$$k\frac{H}{R}t_{\rm p}(R) \gtrsim t_{\rm wave}\,. \tag{3.9}$$

The condition (3.9) needs to hold at all radii inside the disc itself. The dependence on the aspect ratio is not straightforward. Performing several numerical simulations, classified based on the value of H/R, we found that a linear relation between the two timescales exists in each group. However, the slope of the line that separates the global precession region from the differential precession one does change linearly with the disc aspect ratio.

Since in general the precession period is an increasing function of radius and for most discs the aspect ratio increases with radius as well, the most stringent condition is given by Eq. (3.9) with the right hand side to be evaluated at the disc inner radius. The exact value of the constant k of order unity needs to be determined from simulations. We assumed a pure power law profile for both the surface density and the sound speed, respectively $\Sigma = \Sigma_0\, r^{-p}$ and $c_{\rm s} = c_{\rm s,0}\, r^{-q}$ (where $r = R/R_{\rm g}$). We then tested the criterion in (3.9) performing simulations with a ring code spanning the parameter space. The disc rigid precession can be identified by looking at the oscillatory behaviour of the x-component of the disc angular momentum with time for different radii inside the disc and also at the shape and behaviour of the disc tilt and twist (see Section 3.3.1 for details).

The code used to test the rigid precession criterion in (3.9), is a one dimensional grid code based on a leapfrog algorithm (the same used by Franchini et al. 2016). This ring code solves the linearized equation for the warp propagation within the disc in the bending waves regime in both time and space domain (i.e. Eqs. 2.82 and 2.83). The disc is discretized into a set of thin annuli, each of which can be tilted and can interact with the other via pressure and viscous forces. The equations are then solved by means of a

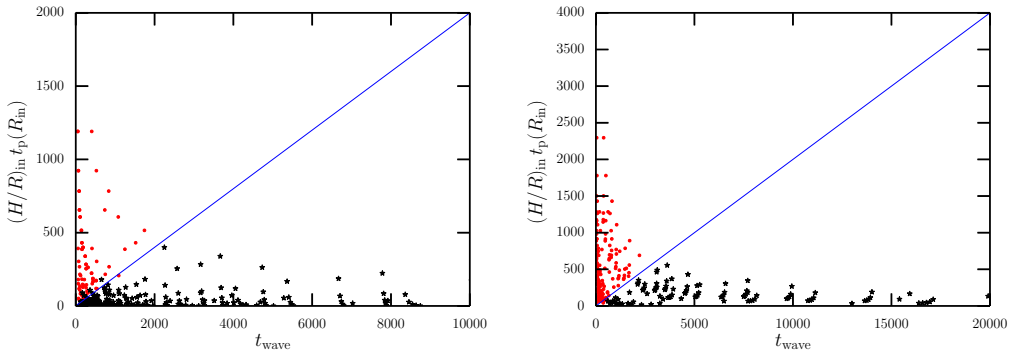

Figure 3.1: Left hand side of Eq. (3.9) evaluated at the inner radius against wave propagation timescale for prograde (left panel) and retrograde (right panel) orbits. The blue line has a $1/k$ slope, with $k = 5$ for both the prograde and retrograde case. The red dots represent the cases in which we see the rigid precession of the disc while the black stars are related to differential precession of the disc annuli.

leapfrog algorithm requiring that at the disc boundaries the internal torque G is zero. This code is a modified version of the code used by Lodato & Facchini (2013a). In the linear regime it has proved to recover full 3D SPH simulations (e.g. Facchini et al., 2013; Nealon et al., 2015). In order to to probe a large enough portion of the parameter space, I performed several simulations varying the values of some of the system parameters to find both rigidly and differentially precessing accretion discs.

The only fixed values are the viscosity parameter and the slope of the surface density profile, fixed at $\alpha = 0.01$ and $p = 3/5$ respectively. The spin varies from 0.2 and 0.99, the disc aspect ration lies in the range $0.05 \leq H/R \leq 0.5$, the outer radius varies from 10 to $40R_{\rm g}$ and the slope of the sound speed profile ranges between 0.5 and 1.5.

In Figure 3.1 we plot the results of the simulations performed exploring the parameter space for both prograde and retrograde orbits. The red dots represent the cases in which the disc precess rigidly while the black stars represent those showing differential precession. The red dots do lie above the blue line (i.e. in the region where $k\, H/R\, t_{\rm p}(r) \geq t_{\rm wave}$) while the black stars lie below it (i.e. in the region in which the condition (3.9) is not satisfied). This means that the condition that has to hold in order for the disc to precess as a rigid body is actually given by (3.9) with $k \simeq 5$. We compared the two quantities involved in the criterion by evaluating the left hand side of Eq. (3.9) at the inner radius.

Note that, in general, the wider the disc, the longer it takes for the warp wave to propagate inside it. Thus a larger radial extent leads to a longer $t_{\rm wave}$ that eventually becomes large enough to prevent the rigid precession of the disc.

3.2.2 Global criterion

Another criterion for establishing the condition under which the disc is able to rigidly precess requires the global precession period to be longer than the wave travel time:

$$k\, t_{\rm p} \gtrsim t_{\rm wave}\,. \tag{3.10}$$

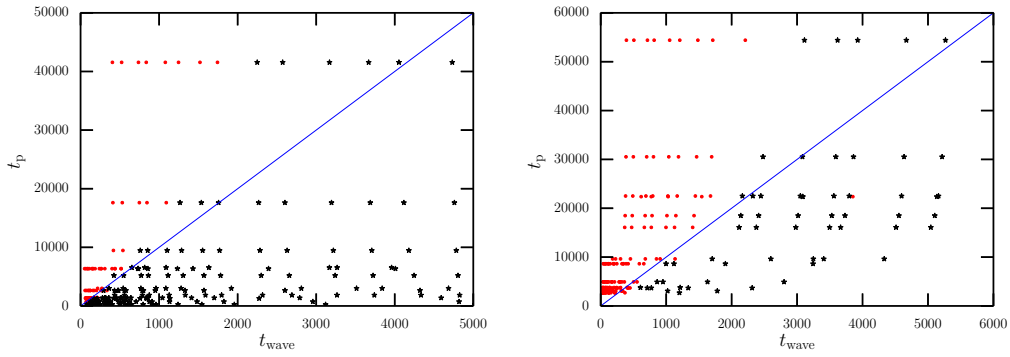

Figure 3.2: Right hand side of Eq. (3.10) evaluated at the inner radius against wave propagation timescale for prograde (left panel) and retrograde (right panel) orbits. The blue line has a $1/k$ slope, with $k = 0.1$ for both cases. The red dots represent the cases in which we see the rigid precession of the disc while the black stars are related to differential precession of the disc annuli.

This criterion naively assumes that the disc is already precessing rigidly. The results of the ring code simulations are shown in Figure 3.2. It is hard to determine a constant k that works for both the prograde and retrograde case. In Figure 3.2 the blue line has a $k = 0.1$ slope but there are non rigidly precessing discs that lie in the wrong region of the plot. The global condition (3.10) represents a necessary but not sufficient requirement in order to have global precession. If this condition is satisfied the disc might precess as a whole but this is not guaranteed to occur.

A much more systematic analysis is required in order to establish which criterion works best. However, at least for the Lense-Thirring precession, we can see that the local criterion gives the same result for both prograde and retrograde orbits and k is of order unity while the global criterion would require the warp propagation timescale to be an order of magnitude shorter than the global precession period in order for the disc to rigidly precess.

3.3 Precession frequencies from different gravitational potentials

The exact form of the orbital and vertical oscillation frequencies can be inferred from the Kerr metric (Kato, 1990; Lubow et al., 2002). Approximations can be obtained considering the gravomagnetic force per unit mass experienced by the fluid in the vicinity of a rotating black hole to the lowest post-Newtonian order. This results in two terms that can be added to either the Newtonian potential (from now on this is indicated with N) or to the Einstein potential (indicated with E) (Nelson & Papaloizou, 2000). It is particularly useful to study the approximated forms since we would like to compare our results with SPH simulations. These are Newtonian codes, thus we need to infer our numerical results under the same approximation.

The Kerr metric gives the following exact expressions for the orbital, apsidal and nodal

frequencies (Kato, 1990):

$$\begin{aligned} \Omega &= \frac{c^3}{GM}\frac{1}{r^{3/2}+a} \\ \eta &= 6r^{-1} \mp 8ar^{-3/2} + 3a^2r^{-2} \\ \zeta &= \pm 4ar^{-3/2} - 3a^2r^{-2} \end{aligned} \tag{3.11}$$

where $r = R/R_{\rm g}$, $R_{\rm g} = GM/c^2$, $-1 < a < 1$ is the dimensionless hole angular momentum ($a < 0$ for retrograde orbits) and η and ζ are defined in (2.97). For a prograde disc with $a > 0$ we have the ordering $\kappa < \Omega_{\rm z} < \Omega$ at any r, where the epicyclic frequency κ is defined in (2.81).

From equations (3.11), matching (2.84) with (3.1) and substituting (3.2), we obtain the following expression for the local Lense-Thirring precession frequency in the linear regime

$$\Omega_{\rm LT} = \frac{\Omega\zeta}{2} = \frac{1}{2}\frac{c^3}{GM}\frac{1}{r^{3/2}+a}(4ar^{-3/2} - 3a^2r^{-2}) \tag{3.12}$$

where we can recover (for $r \gg a$) the r^{-3} dependence to the first order approximation. This is appropriate if the disc is radially extended while it is only approximate for a narrow disc.

The above expression for the local precession frequency is valid only for small amplitude warps since the torque in Eq. 2.84 was inferred under the linear approximation. From the Kerr metric, the vertical frequency $\Omega_{\rm z}$ can be inferred exactly for small amplitude oscillations around the equatorial plane (Kato, 1990). In the weak field limit (i.e. for $\Omega_{\rm z} \simeq \Omega$), the torque 2.84 can be rewritten as

$$\mathbf{T} \simeq \frac{(\Omega - \Omega_{\rm z})\,2\Omega}{\Omega^2}\frac{\Omega}{2}\mathbf{e}_{\rm z} \times \mathbf{L} = \mathbf{\Omega}_{\rm p} \times \mathbf{L} \tag{3.13}$$

where one can identify the precession frequency with $\mathbf{\Omega}_{\rm p} = (\Omega - \Omega_{\rm z})\mathbf{e}_{\rm z}$. Therefore, in the weak field limit, Eq. (3.12) coincides with the expression that we will use later in Chapter 7 (i.e. Eq. 7.1).

Substituting Eq. (3.12) in Eq. (3.6) we obtain the correct form of the rigid precession frequency:

$$\Omega_{\rm p} = \frac{1}{2}\frac{c^3}{GM}\frac{\int_{r_{\rm in}}^{r_{\rm out}} \frac{r^{3-p}f^p}{(r^{3/2}+a)^2}\zeta dr}{\int_{r_{\rm in}}^{r_{\rm out}} \frac{r^{3-p}f^p}{(r^{3/2}+a)}dr}\,. \tag{3.14}$$

In 3D the nodal precession can be directly induced using the description of the Lense-Thirring precession adopted by Nelson & Papaloizou (2000) with the Newtonian potential, while the apsidal precession arises from the use of the Einstein potential instead of the Newtonian one (Nealon et al., 2015). Nelson & Papaloizou (2000) define the gravomagnetic force per unit mass experienced by the disc in the vicinity of a rotating black hole as

$$\mathbf{v} \times \mathbf{h} = \frac{2S\left(\mathbf{v} \times \hat{\mathbf{k}}\right)}{R^3} + \frac{6Sz\,(\mathbf{r} \times \mathbf{v})}{R^5} \tag{3.15}$$

where $S = a(GM)^2/c^3$, $\hat{\mathbf{k}}$ is the direction of the black hole angular momentum, $\mathbf{v}$ is the velocity of the fluid element and $\mathbf{r}$ is the coordinate vector. This is the gravomagnetic force that gives rise to the Lense-Thirring precession, which in turn leads to alignment of the disc angular momentum with the black hole spin. For linear disturbances at large radii, the velocity can be replaced by the unperturbed Keplerian velocity $v_\phi = \sqrt{GM/R}$. The term (3.15) can be considered to arise from an effective potential such that

$$\mathbf{v} \times \mathbf{h} = -\nabla \Phi_{\rm grav} \tag{3.16}$$

with

$$\Phi_{\rm grav} = \frac{4S\sqrt{GM}}{5R^{5/2}} - \frac{3Sz^2\sqrt{GM}}{R^{9/2}}\,. \tag{3.17}$$

Using the Newtonian potential Φ together with the LT corrections $\Phi_{\rm N} = \Phi + \Phi_{\rm grav}$, the orbital, apsidal and nodal frequency read

$$\begin{aligned} \Omega_{\rm N} &= \frac{c^3}{GM}\left(r^{-3} - 2ar^{-9/2}\right)^{1/2} \\ \eta_{\rm N} &= -\frac{3a}{2r^{3/2} - 4a} \\ \zeta_{\rm N} &= \frac{3a}{2r^{3/2} - 4a} \end{aligned} \tag{3.18}$$

where the radius is in units of the gravitational radius $r = R/R_{\rm g}$.

We can now compute the rigid precession frequency resulting from the use of $\Phi_{\rm N}$ in order to compare the analytical results with the SPH 3D simulations. By writing the local LT precession frequency as $\Omega_{\rm LT} = \Omega_{\rm N}\zeta_{\rm N}/2$ in Eq. (3.6), we obtain:

$$\Omega_{\rm p,N} = \frac{1}{2}\frac{c^3}{GM}\frac{\int_{r_{\rm in}}^{r_{\rm out}} r^{3-p} f^p (r^{-3} - 2ar^{-9/2})\zeta_{\rm N} dr}{\int_{r_{\rm in}}^{r_{\rm out}} r^{3-p} f^p (r^{-3} - 2ar^{-9/2})^{1/2} dr}\,. \tag{3.19}$$

Nelson & Papaloizou (2000) introduced also the Einstein potential which constitutes an alternative to the standard Newtonian potential. This potential treats the central object as a sphere of uniform density of finite size to prevent the gravitational force from becoming infinite as the radius decreases. In this case the gravitational force per unit mass outside the sphere was taken to be

$$-\nabla \Phi_{\rm E} = -\frac{GM}{R^3}\left(1 + \frac{6R_{\rm g}}{R}\right)\,. \tag{3.20}$$

Using the potential $\Phi_{\rm E} + \Phi_{\rm grav}$, the orbital, apsidal and nodal frequency read

$$\begin{aligned} \Omega_{\rm E} &= \frac{c^3}{GM}\left(r^{-3} + 6r^{-4} - 2ar^{-9/2}\right)^{1/2} \\ \eta_{\rm E} &= \frac{1}{2}\frac{\left(6r^{-4} - 3ar^{-9/2}\right)}{\left(r^{-3} + 6r^{-4} - 2ar^{-9/2}\right)^{1/2}} \\ \zeta_{\rm E} &= \frac{3ar^{-9/2}}{\left(r^{-3} + 6r^{-4} - 2ar^{-9/2}\right)^{1/2}}\,. \end{aligned} \tag{3.21}$$

The advantage of using the Einstein potential is that it results in the correct apsidal precession at large distances from the black hole. The comparison of the apsidal precession

rates $\eta_{\rm E}$ and $\eta_{\rm N}$ shows that the effects of Einstein precession remain relatively more important further away from the black hole. It is worth noticing that the two apsidal precession rates have opposite signs. Nelson & Papaloizou (2000) showed that using the Einstein potential leads to changes in the numerical results, in particular on the way in which the disc undergoes the transition between the plane occupied by the inner disc and that occupied by the outer disc.

By writing the local LT precession frequency as $\Omega_{\rm LT} = \Omega_{\rm E}\zeta_{\rm E}/2$ in Eq. (3.6) we obtain the rigid precession frequency:

$$\Omega_{\rm p,E} = \frac{1}{2}\frac{c^3}{GM}\frac{\int_{r_{\rm in}}^{r_{\rm out}} r^{3-p} f^p (r^{-3} + 6r^{-4} - 2ar^{-9/2})\zeta_{\rm E} dr}{\int_{r_{\rm in}}^{r_{\rm out}} r^{3-p} f^p (r^{-3} + 6r^{-4} - 2ar^{-9/2})^{1/2} dr}\,. \tag{3.22}$$

It is worth noticing that, in general, the precession is due to the forcing torque at the inner edge of the disc $\Omega_{\rm LT}(r_{\rm in})$ and that, since the majority of angular momentum of the disc lies in the outer region because $M \propto R^{2-p}$, the larger the outer radius the longer the precession period. To the first order approximation, the orbital frequency has the same dependence on the radius in all cases listed above while the apsidal frequency η (defined by Eq. 2.97) take different values. Figure 3.3 shows the comparison of the apsidal and nodal frequency respectively for different values of the black hole spin, obtained using the Kerr metric (Kato, 1990; Lubow et al., 2002) (LOP) and the relativistic corrections with either the Newtonian or the Einstein potential.

The outer radius of the disc depends on the system under investigation, for instance TDE discs and discs in LMXBs have very different outer radii as we will see. Once the outer radius and the black hole mass are fixed, we can evaluate the precession period as a function of the black hole spin. Choosing an outer radius of about $50R_{\rm g}$ and a black hole with $M = 10^6 M_\odot$, we find that while the Lubow et al. (2002) and the Einstein approach are in good agreement in terms of the precession period for several spin values, the Nelson & Papaloizou (2000) corrections with Newtonian potential approach tends to give slightly longer precession periods.

By looking at the dispersion relation for wave like solutions with rapidly varying phase factor in the absence of viscosity, i.e. Eq. (2.89), the case $\omega = 0$ is of some interest, as it relates to steady warped discs (Lubow et al., 2002). The dispersion relation indicates an oscillatory behaviour of the spatial structure of the warp with radial wavenumber given by

$$k^2 H^2 = \frac{\left(\Omega^2 - \Omega_{\rm z}^2\right)\left(\Omega^2 - \kappa^2\right)}{\Omega^2 \Omega_{\rm z}^2}\,. \tag{3.23}$$

When the nodal and apsidal frequencies have opposite signs, a steady warp is spatially evanescent. The comparison between the left and right panels of Fig. 3.3 shows that while the presence of the Einstein potential gives the same sign of nodal and apsidal precession in agreement with the frequencies inferred from the Kerr metric (Kato, 1990), using $\Phi_{\rm N}$ results in opposite sign of the precession frequencies. Nelson & Papaloizou (2000) found that the Einstein precession gives rise to many wave-like tilt oscillations which might be interpreted as inward propagating bending waves excited in the transition region between the aligned inner part of the disc and the misaligned outer part. This phenomenon has been predicted by Ivanov & Illarionov (1997) and then confirmed analytically by Nelson & Papaloizou (2000). Note that solutions with many oscillations in the inner disc appear in the linear theory. While Nelson & Papaloizou (2000) were not able to find tilt oscillations

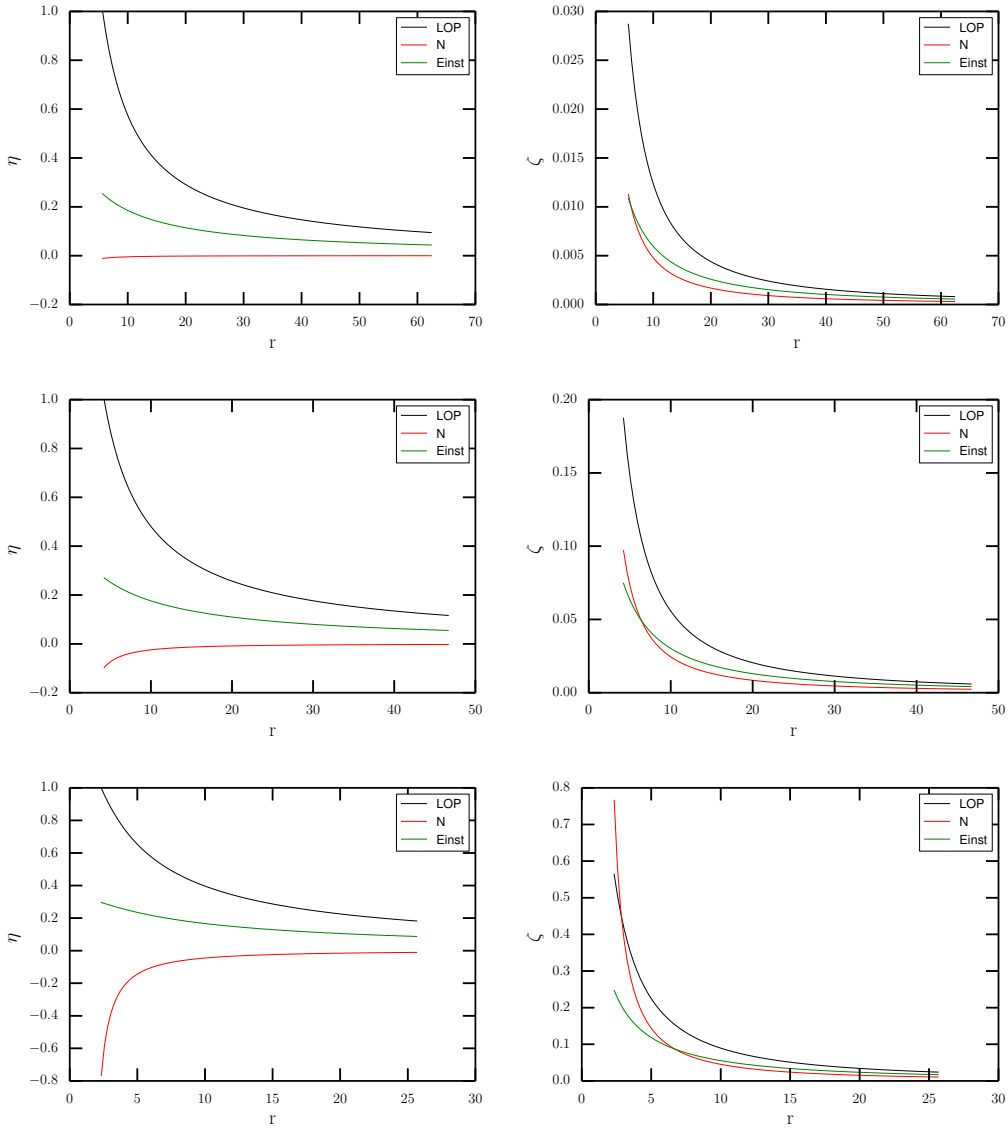

Figure 3.3: Apsidal (left panels) and nodal (right panels) precession frequency as a function of the radius for three values of the black hole spin (from top to bottom panels): $a = 0.1$, 0.5, 0.9 respectively. The black lines show results obtained using the Kerr metric (LOP), the red lines show the results obtained using $\Phi_{\rm N}$ (indicated with N) and the green lines refer to the Einstein potential (indicated with E).

in their hydrodynamical simulations (they found Bardeen-Petterson alignment instead), Nealon et al. (2015) used the Einstein potential in 3D SPH simulations, recovering the disc radial tilt oscillations.

Radial tilt oscillations are claimed to be seen also in GRMHD simulations (Fragile et al., 2007; Liska et al., 2017). Fragile et al. (2007) performed global numerical simulations of tilted accretion discs including GR effects and magnetorotational turbulence as the primary source of angular momentum transport. In particular, Liska et al. (2017) showed that thick tilted accretion discs around rapidly spinning black holes launch relativistic jets that propagate along the disc rotation axis and precess with the accretion disc.

Grid-based and SPH codes have their own advantages and disadvantages, depending on the type of system that one needs to reproduce with the simulations. MHD grid-based codes have the advantage of generating selfconsistently the viscous dissipation through the MRI rather than introducing the artificial viscosity as in SPH codes (see Section B.3). However, a fundamental difference is that in grid-based codes angular momentum conservation can only be achieved by using a grid matched to the geometry of the system. This means that angular momentum is conserved only when the flow is aligned with the grid. Sorathia et al. (2013a) performed numerical simulations of inclined disc using a grid code. Among other results, they showed that the fluid total angular momentum is never exactly conserved.

The fundamental idea of SPH simulations is discretising fluid quantities onto particles of fixed mass that move with the fluid velocity with the aim of solving the equations of fluid dynamics. Thus the resolution of the method follows the mass rather than the volume as in grid-based codes. Furthermore the mass will be an exactly conserved quantity. In SPH the equations of motions are derived from the Lagrangian, therefore the symmetries in the Lagrangian will be reflected as conservation properties in the equations of motion: Galilean covariance, exact conservation of linear and angular momentum, energy and entropy (Price, 2012). SPH codes are found to be better at resolving dense structures. This makes the SPH approach more suitable for studying, for instance, star formation since a grid-based code requires adaptive mesh refinement (AMR) which results in an additional computational cost. Since in SPH codes the conservation of angular momentum is independent of geometry, in order to perform numerical simulations of warped accretion discs it is much more convenient to use SPH instead of grid-based codes. Lodato & Price (2010) obtained a detailed proof of predictions from the α-disc theory and this was possible since the orbital dynamics is the same regardless of the inclination of the orbital plane and also since the only source of angular momentum dissipation is explicitly added as a viscosity term, very well controlled by a switch (see Appendix B for details).

3.3.1 Simulations

For the above reasons, we investigate rigid precession of tilted accretion discs using the SPH code PHANTOM (see Appendix B for details). In this code the relativistic corrections due to the Lense-Thirring effect with both Newtonian and Einstein potential (i.e., Eqs. (3.17) and (3.20)) are implemented.

The ring code results are in perfect agreement with the analytical estimate for both potentials. We ran SPH simulations in order to compare the results with both the ring code and the analytical estimate. We present here the results obtained using $\Phi_{\rm N}$ (Nelson & Papaloizou, 2000). The disc extends from $r_{\rm in} = 10$ to $r_{\rm out} = 50$ in units of $R_{\rm g}$, has an aspect ratio $H/R = 0.1$, the disc viscosity is $\alpha = 0.01$ and it is inclined with

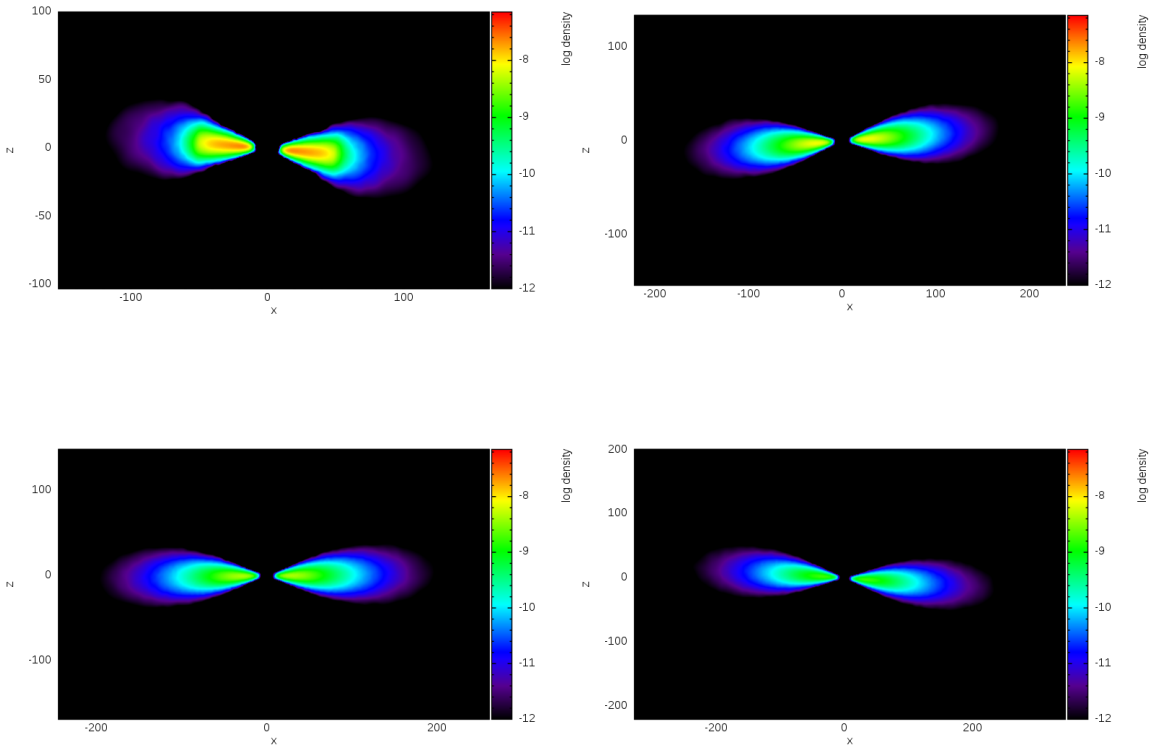

Figure 3.4: Cross section view of the disc initially inclined by 5° with respect to the black hole spin (the spin axis is vertical with respect to the page, i.e. along the z-axis). The colour scale shows the density. The four panels show snapshots at four different times during a precession cycle. Note that the disc spreads with time due to viscosity.

respect to the black hole spin by 5°. The black hole has a mass of $10^6 M_\odot$, although both simulations are re-scalable with the mass, and a spin $a = 0.9$. We chose a sound speed profile $c_s = c_{s,0} r^{-1/2}$ and a surface density profile $\Sigma = \Sigma_0 r^{-3/5}(1-(r_{in}/r)^{1/2})$. Note that we are in the bending waves regime since we chose values such that $\alpha \lesssim H/R$ through the whole disc.

Fig. 3.4 shows four snapshots of the cross section view of the disc initially inclined at 5° with respect to the black hole spin. The colour scale shows the density. The upper left panel shows the disc initial configuration, the upper right panel is the disc after half a precession cycle, the lower left panel shows the configuration at two thirds of a cycle and finally the lower right panel shows the disc after a full precession cycle (which is the same as the initial one). The density in the disc decreases with time because of mass accretion onto the black hole.

Fig. 3.5 shows the tilt and twist profile respectively as a function of the radius at three different times from the SPH (left panels) and ring code (right panels) simulation. The upper panel shows the initial condition, the middle and lower ones after half and a

full precession cycle respectively.

In order to have rigid precession of the whole accretion disc the tilt (see Eq. (2.57)) needs to be a given function of the radius, since the disc is warped by the LT effect, that decreases with time due to viscosity

$$\beta(R,t) = A(t)\beta_0(R) \tag{3.24}$$

while the twist can be described by a given function of radius that shifts with time at the global precession rate $\Omega_{\rm p}$

$$\gamma(R,t) = \gamma_0(R) + \Omega_{\rm p} t\,. \tag{3.25}$$

We can see that this is exactly what is shown in both left and right panels of Fig. 3.5. It is worth noticing that in the ring code we did not include mass accretion when calculating the Σ profile. This is indeed a limit of the ring code as it is at the moment, however we are working in order to fix this and also to allow radial expansion of the disc caused by viscous processes in order to be able to obtain more informations about the dynamics of warped accretion discs from the ring code.

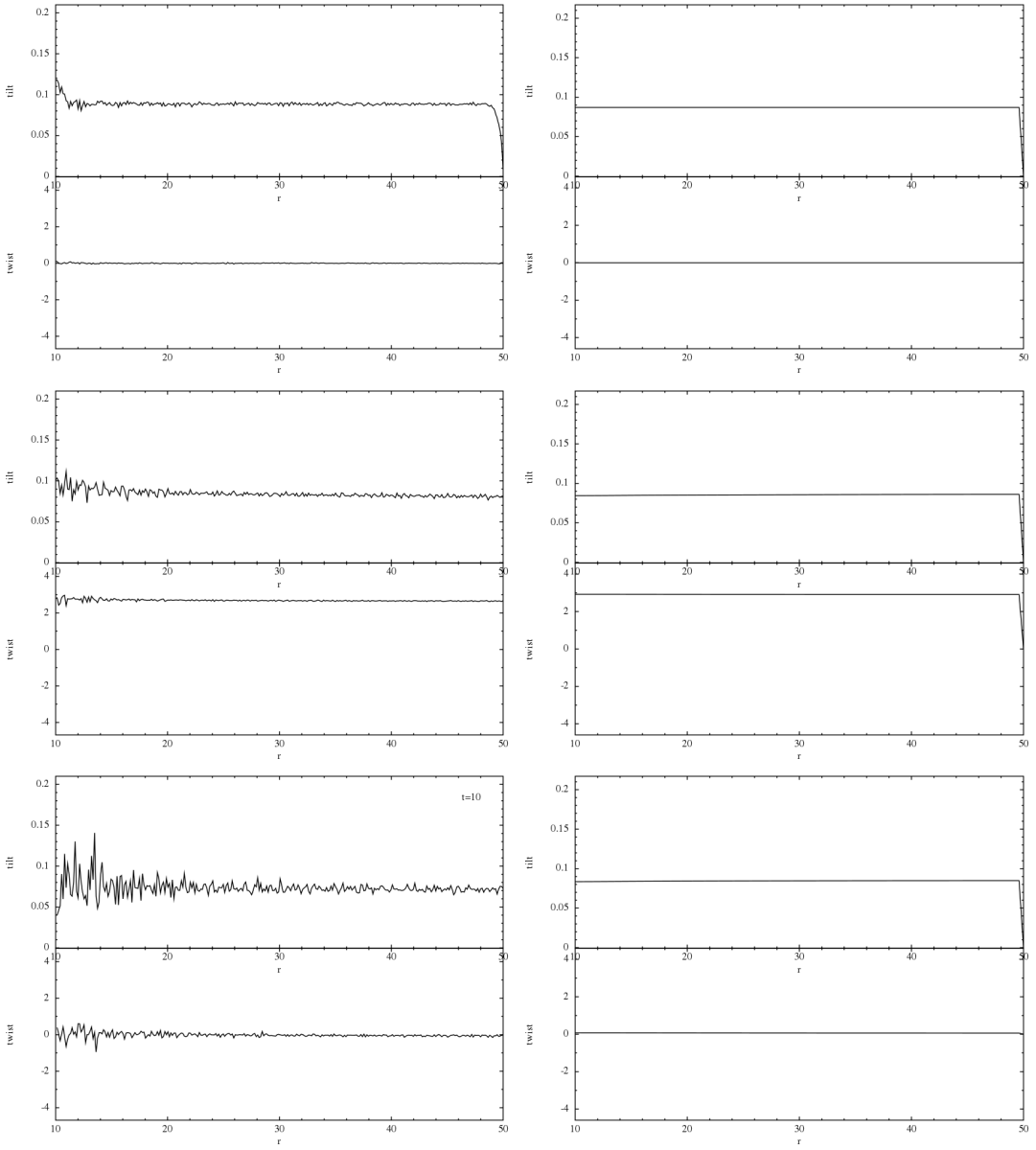

Figure 3.5: Tilt and twist of the accretion disc from SPH simulation analysis (left panels) and from the ring code (right panels). The upper panel shows the initial condition at $t = 0$, the middle one shows the disc after half a precession cycle at $t = 10^5$ and the lower panel after a full precession cycle at $t = 2 \times 10^5$ in code units.

Part II

Relativistic precession in Tidal Disruption Events

Chapter 4

Tidal Disruption Events

Observations of the copious amount of radiation that is emitted when SMBHs accrete gas from their immediate vicinity can be studied in order to obtain constraints on the black hole parameters: mass and spin. Studies of quasar and AGN populations at redshifts $z > 2$ led to the well known inference that black holes lurking in the centres of relatively quiescent galaxies should be widespread. The best diagnostic of a black hole presence would be some observation that cannot be explained in any other way. A candidate is the distinctive manifestations of tidal capture and disruption of stars.

Tidal Disruption Events (TDEs) show detectable characteristic flares that last on timescales of months to years (Rees, 1988). They do offer a unique opportunity to probe the nuclei of otherwise quiescent galaxies with not enough gas in their centre to cause strong emission. Tidal capture or disruption of stars was first explored in the 1970s (Frank, 1978) as a possible way of fuelling AGN. The outcome of these studies was that tidal disruption could not supply a quasar-level fuelling rate unless the stellar concentration around the black hole is so high that other processes, such as stellar collisions, would supervene and release still more gas. The process has still become interesting from an observational point of view. As the number of surrounding stars and their motions are known to a good degree, the capture rate by the putative central black hole can be estimated (Magorrian & Tremaine, 1999; Wang & Merritt, 2004; van Velzen & Farrar, 2014; Stone & Metzger, 2016); the question that arises is whether the apparent quiescence of the nuclei of these galaxies is compatible with a SMBH presence. The answer depends on what happens to the debris of each disrupted star.

A tidal disruption event occurs whenever a star wanders close enough to the black hole to be torn apart by its tidal force. This might be the case if the star is perturbed onto an almost radial trajectory as a consequence of an encounter with another star or another massive object. Depending on the mass of the disrupted star, part of its debris gets ejected and a fraction remains bound to the black hole. The bound fraction is then accreted onto the black hole normally producing a non-stationary characteristic flare of soft X-ray radiation (Esquej et al., 2008; Saxton et al., 2012, 2015; Komossa, 2015).

4.1 Observations

Roughly seventy TDEs have been discovered over the last two decades through dedicated surveys at various wavelengths. The relatively small number of candidates makes it difficult to resolve theoretical uncertainties concerning their rates, their super-Eddington accretion phase and the period during which dissipation in shocks allows an accretion disc to form.

The emission can occur over a wide range of the electromagnetic spectrum, from X-rays to radio waves, because it is produced by a high-energy jet of particles that might happen to point almost exactly in our line of sight. The high energy emission is thought to be caused by inverse Compton up-scattering of the accretion disc photons, photons from within the jet itself and photons from the structure external to the accretion disc. By contrast, the UV-optical radiation of tidal disruption events is usually associated with thermal emission from the accretion disc made of stellar debris that forms around the black hole.

The first sky survey in the UV was performed by the *GALEX* satellite. Three UV flares had been observed by the *GALEX* satellite (Gezari et al., 2006, 2008, 2009).

One of the first events detected in the optical is known as PS1-10jh and has been found with the *Pan-STARRS* survey (Gezari et al., 2012). Flares from quiescent galaxies with very high luminosity matching the predictions of TDEs theory have been detected during the *ROSAT* X-ray survey. Four main events have been detected from the galaxies NGC 5905 Komossa & Bade (1999), RXJ1242-1119 (Komossa & Greiner, 1999), RXJ1624+7554 (Grupe et al., 1999) and RXJ1420+5334 (Greiner et al., 2000). The first two events have the best covered long term X-ray lightcurve (Komossa et al., 2004).

All such flares have been associated to TDEs because of their extremely high brightness (close to the Eddington limit, see section 1.2.1), their duration and the decay of the light curve roughly proportional to $t^{-5/3}$, which is taken as a signature of a TDE, as we will see later on.

Using archival Sloan Digital Sky Survey (SDSS) multi-epoch imaging data, van Velzen et al. (2011) have searched for the tidal disruption of stars by supermassive black holes in non-active galaxies. Two candidate events have been identified with flares in the optical range of the electromagnetic spectrum. These two candidates are much more luminous in the optical than predicted (Strubbe & Quataert, 2009).

The *Swift* satellite led to a breakthrough in the field of TDEs. Its discovery of the first event that launched a relativistic jet, Swift J164449.3+573451 (hereafter Sw J1644+57) (Bloom et al., 2011; Burrows et al., 2011; Zauderer et al., 2011), has triggered many theoretical studies on the formation of radio jets, and this event has now the best covered light curve of any TDE to date (Komossa, 2015). Subsequently, Cenko et al. (2012) have discovered a second jetted TDE, Swift J2058.4+0516.

The X-ray *Swift* transient Sw J1644+57 is the clearest TDE candidate so far. It was originally detected as a long duration gamma-ray burst at redshift $z = 0.3543$ by the *Swift* satellite at a time $t_0 = 28$ March 2011. Given the longevity and flaring of the X-ray afterglow, it was quickly realized that the high energy emission was different than usually observed in GRBs. It was then suggested that Sw J1644+57 could be analogous to a scale-down version of a blazar (the class of most variable AGN with SMBHs) impulsively fed by a solar mass star. The fundamental difference between this event and the ones discovered previously is both its high energy emission and the fact that it has been also detected in the radio (Zauderer et al., 2011), indicating that the emission might come from a jet pointing in our direction. There are basically two lines of evidence that suggest an accreting black hole origin for this unusual event (Bloom et al., 2011). Firstly, the astrometric coincidence of the associated X-ray, optical, infrared and radio transient with the light centroid of the putative host galaxy is strongly indicative of a positional connection to a SMBH. Besides, the observed X-ray variability is consistent with that of an accreting black hole.

Zauderer et al. (2013) presented continued multi-frequency radio observation of the

relativistic tidal disruption event Sw J1644+57 extending to $t \approx 600$ days. The data were obtained with the *JVLA* and *AMI Large Array*.

More recently, similar X-ray events have been detected with *Chandra* and *XMM-Newton*. The *Swift* satellite provided follow-ups of several of these events that showed the correct decay in the X-rays allowing the luminosity evolution to be constrained.

The All-Sky Automated Survey for SuperNovae (ASAS-SN), a long-term project to monitor the sky looking for supernovae (Shappee et al., 2014), detected 4 TDE candidates: ASASSN-14ae (Holoien et al., 2014), ASASSN-14li (Holoien et al., 2016a), ASASSN-15lh (Leloudas et al., 2016) and ASASSN-15oi (Holoien et al., 2016b). ASASSN-14ae and ASASSN-15lh event have been classified as optical/UV TDEs in the literature, while ASASSN-14li is more likely to fall in the X-ray TDE category (Auchettl et al., 2017). A follow-up of the last source ASASSN-15oi was performed also with *Swift* and indicates that this is an optical/UV TDE (Holoien et al., 2016b). However, it faded significantly more rapidly than other optically discovered TDEs. A weak X-ray emission was detected but it decayed much more rapidly than the optical/UV emission.

TDEs might occur in AGN as well and the rates of stellar disruption are expected to be quite high. However it is difficult to identify such events from other processes in the permanently bright accretion disc. Besides, it is more difficult to uniquely associate any particular flare in classical AGN with a TDE since the processes within the accretion disc might cause high-amplitude variability. Jetted TDEs are a powerful tool for probing the formation and early evolution of radio jets. They also might explain related issues like the cause of the radio-quiet radio-loud dichotomy in AGN (Komossa, 2015).

Another important effect for AGN is the non-thermal emission. Thermal emission spans almost the entire electromagnetic spectrum. About the origin of the non-thermal component there can be the emission from the disc corona. Accretion disc coronae are believed to account for X-ray emission (Liang 1977; Galeev et al. 1979; White & Holt 1982; Begelman et al. 1983; Czerny & King 1989a,b; Różańska et al. 2015 and references therein). It is postulated that the hot medium responsible for the soft-X-ray emission forms a corona above the inner parts of the accretion disc. This corona is assumed to be optically thick in many models depending on the investigated sources. Torricelli-Ciamponi et al. (2005) assumed the observed emission to be due to a population of relativistic, non-thermal electrons (e.g. produced in a flare) injected at the top of an accretion disc magnetic loop. While electrons stream along magnetic field lines their energy distribution evolves in time essentially because of inverse Compton and synchrotron losses. The corresponding time-dependent emission due, in the X-ray energy range, to the inverse Compton mechanism, has been computed. We do not know yet whether this disc region does exists or not in TDE discs. This is an interesting idea to study, since it will lead to a more deep understanding of AGNs high energy non-thermal emission.

It is important to investigate these transients in order to understand the general behaviour of processes involving black holes and their surroundings. The most important aspect of TDEs is that they might be our only probe to obtain a large sample of dormant black holes, including possible IMBHs in globular clusters and dwarf galaxies (Donato et al., 2014). Since X-rays trace the very vicinity of the black hole, TDEs can also probe relativistic effects such as precession around a Kerr black hole. Besides, they also allow us to study accretion physics at high rates and close to the last stable orbit offering also an opportunity to gain indirect black hole parameter estimates.

Note that, for black holes with masses $M \gtrsim 10^8 M_\odot$ (i.e. close to Hills mass), the tidal disruption radius lies inside the Schwarzschild radius, hence a TDE survey that covers

a sample of galaxies with a wide enough central black hole mass range is sensitive to whether supermassive black holes have an event horizon. Theoretical estimates of SMBH spins depend sensitively on the extent to which SMBHs grow by accretion or mergers. Given the large sample of observed TDEs expected in the near future and the wide range of predicted SMBH spins, it is important to determine the extent to which TDE rates depend on SMBH spin. The greater the spin dependence, the more tightly observed TDEs will be able to constrain the distribution of SMBH spins.

4.1.1 Rate of stellar disruptions

Many different processes can contribute to the observed rates of tidal disruption. The most important is the collisional two-body relaxation of stars into the 'loss-cone', the region where orbital pericentres $r_{\rm p}$ lie inside the tidal radius $r_{\rm t}$ (Alexander, 2012). The two-body relaxation process causes stars to diffuse in the loss-cone at a very low rate. Exactly how frequently a star enters this 'zone of vulnerability' depends on the stellar velocity distribution. In a simpler case when the velocities are isotropic at $r_{\rm h} = GM/\sigma^2$ (radius within which the black hole dominates the dynamics, with σ being the velocity dispersion of the host galaxy), the frequency at which a solar-type star would pass within a distance $r_{\rm p} \ll r_{\rm h}$ is (Rees, 1988)

$$\dot{N} \approx 10^{-4} M_6^{4/3} \left(\frac{N_*}{10^5 {\rm pc}^{-3}}\right) \left(\frac{\sigma}{100\,{\rm km\,s}^{-1}}\right)^{-1} \left(\frac{r_{\rm p}}{r_{\rm t}}\right) {\rm yr}^{-1} \tag{4.1}$$

where N_* is the stellar density and σ is the stellar velocity dispersion. Thus tidal disruption events are rare: they are expected to occur roughly once every $10^4 - 10^5$ years per galaxy.

The rate of stellar disruption inferred from X-ray, UV (Gezari et al., 2008) and optical (van Velzen & Farrar, 2014) observations is $\sim 10^{-5}{\rm yr}^{-1}{\rm gal}^{-1}$. These rates are roughly an order of magnitude lower than the ones predicted theoretically. The explanation for this discrepancy might reside in selection effects, poor statistics and the possible influence of dust or photoelectric extinction (Stone & Metzger, 2016).

Magorrian & Tremaine (1999) studied the stellar disruption rates in detailed dynamical models of real galaxies, taking into account the refilling of the loss-cone of stars on destructible orbits by two-body relaxation and tidal forces in non-spherical galaxies. The lack of symmetry causes the loss-cone to be replaced by a 'loss wedge'. In a steady state, this wedge feeds stars to the black hole at a rate that is almost always faster (roughly a factor 2) compared to the rate obtained for spherical galaxies. This is because galaxies with a high degree of axisymmetry host a significant fraction of stars that pass very close to the center and have low angular momentum (stars on centrophilic). While stars on centrophobic orbits (i.e. in spherical galaxies) are expected to plunge into the black hole with pericentres well within the tidal radius, stars on these ultraclose orbits are expected to 'pancake' (Rees, 1988). The highest disruption rates (one star per 10^4 yr) occur in faint ($L \lesssim 10^{10} L_\odot$) galaxies, which have steep central density cusps. More luminous galaxies are less dense and have much longer relaxation times and more massive black holes, thus tidal flares occur much less frequently (Magorrian & Tremaine, 1999). Therefore only in the faintest galaxies and for loosely bound orbits the diffusion is strong enough to keep the loss-cone full.

Also Wang & Merritt (2004) compute rates of tidal disruption of stars by supermassive black holes in galactic nuclei. They found that in galaxies with steep nuclear density profiles, which dominate the overall event rate, the disruption frequency varies inversely

with assumed black hole mass. Also, using downwardly revised black hole masses from the $M-\sigma$ relation implied a total rate per unit volume that is an order of magnitude larger than previous studies.

These works concluded also that the lowest mass galaxies hosting black holes dominate the TDEs rate. The reason is that the number of small galaxies is larger, the correlation between the SMBH mass and central stellar density is negative and the TDE rate is higher for lower SMBH masses in 'cuspy' galaxies. However, the detected TDE rate depends also on how the luminosity of the flare in a given waveband scales with the SMBH mass.

Strubbe & Quataert (2009) predicted detection rates for Panoramic Survey Telescope and Rapid Response System (Pan-STARRS), the Palomar Transient Factory (PTF) and the Large Synoptic Survey Telescope (LSST) of around hundreds or thousand of events per year.

Stone & Metzger (2016) updated the previous theoretical estimates using the most recent $M-\sigma$ relation and a much larger sample of galaxy surface brightness profiles. They conclude that the largest uncertainty in the TDE rate estimate is that the occupation fraction of SMBHs in low mass galaxies is badly constrained. Thus the discrepancy between the theoretical and the observational disruption rate is still unsolved.

4.2 Hydrodynamics of TDE

We know the basic hydrodynamics of TDEs under some approximations. In particular, the main feature of these kind of events is a powerful flare produced during the event with peak accretion rate up to two orders of magnitude above the Eddington limit, decaying with time as $t^{-5/3}$ (Rees, 1988; Phinney, 1989; Evans & Kochanek, 1989).

Tidal disruption occurs when the pericentre radius $r_{\rm p}$ of the star, assumed to be in a roughly parabolic orbit around a black hole, becomes as small as the tidal radius (Eq. 1.12)

$$r_{\rm t} \simeq 0.3\, M_6^{1/3} (R_*/R_\odot)(M_*/M_\odot)^{-1/3}\,{\rm AU} \tag{4.2}$$

where M_6 indicates the black hole mass in units of $10^6 M_\odot$. This estimate assumed that the gravitational field of the black hole is that of a Newtonian point particle, which should only be valid for $r_{\rm t} \gg r_{\rm S}$, where $r_{\rm S}$ is given by (1.3). One should be very careful in using this estimate at the event horizon. In a proper general relativistic treatment (Kesden, 2012), the spacetime of a spinning black hole is described by the Kerr metric (1.5). In this case the upper limit on the mass of the black hole for a tidal disruption event to occur (see Eq. 1.13) becomes $\approx 10^9 M_\odot$.

Complete disruption requires $r_{\rm p} \lesssim r_{\rm t}$. For $r_{\rm p}$ larger than the tidal radius, a star could lose its outer layers, but the dense interior would survive (Guillochon & Ramirez-Ruiz, 2013). For a range of still larger values of $r_{\rm p}$ a solar-type star loses no material, but gets so distorted during the flyby that the subsequent material dissipation (when it readjusts) might exceed its incoming kinetic energy $M_*\sigma^2/2$. Energy conservation thus implies that the star would thereafter be on an orbit bound to the black hole.

Thus, the outcome of a TDE depends on the penetration factor $\beta = r_{\rm t}/r_{\rm p}$. This determines how deeply the star plunges into the black hole gravitational potential well. In order to tidally disrupt the star we require $\beta \gtrsim 1$.

A simple way to consider the process is by treating the interaction between the star and the black hole under the impulse approximation (Lodato et al., 2009), that assumes that the interaction occurs in a very small time-span as the star gets close to the pericentre.

This is only approximate for the parabolic orbit case considered here, but the qualitative behaviour is correct.

We assume that there is no spread in kinetic energy between different stellar debris. All the orbits have the same velocity until they reach the pericentre distance. We consider the case in which the stellar radius is very small compared to the pericentre radius, $R_* \ll r_\mathrm{p}$, which is appropriate for stellar disruption by SMBHs. The fact that $r_\mathrm{p} \gg r_\mathrm{S}$ allows to use the Keplerian potential to a first order approximation. The motion of the star is a straight line until it reaches the pericentre, at which point it is subject to a short impulse that deflects the various fluid elements, each of them individually conserving their own specific energy.

Until it reaches the pericentre the structure of the star is essentially unchanged and it keeps its original radial density profile and its initial size. As Evans & Kochanek (1989) pointed out, the spread of specific energy the star has reached just before the impulse is simply given by the different depths at which the various fluid elements lie within the black hole potential well because they all share the same velocity, thus the same kinetic energy. Since the centre of mass follows a trajectory with zero binding energy, the stellar material located deeper in the potential well that is moving with the same velocity at the point of disruption has a binding energy per unit mass equal to the difference between its potential energy per unit mass and that of the centre of mass of the star (Rees, 1988). The impulse occur instantaneously and therefore does not modify the kinetic energy of the fluid elements but imparts some degree of rotation in the star, with $\Omega \approx (2GM/r_\mathrm{p}^3)^{1/2}$.

The above assumptions allow to estimate the expected energy spread

$$\Delta\epsilon = \frac{\epsilon(r_\mathrm{t} - R_*) - \epsilon(r_\mathrm{t} + R_*)}{2} = \left.\frac{\partial\epsilon}{\partial R}\right|_{r_\mathrm{t}} R_* = \frac{GM}{r_\mathrm{t}^2} R_* = \frac{GM_*}{R_*}\left(\frac{M}{M_*}\right)^{1/3}. \tag{4.3}$$

We thus expect energy distribution to extend roughly between $-\Delta\epsilon$ and $\Delta\epsilon$. Note that this does not depend on the single fluid element. Note that we are using $\beta = 1$ and we have computed the expected energy spread at the tidal radius. It can be shown that this spread does not change much with the penetration factor (Guillochon & Ramirez-Ruiz, 2013; Kobayashi et al., 2012). The spread in Eq. (4.3) can greatly exceed the star binding energy $E_\mathrm{b} = GM_*/R_*$

$$\frac{\Delta\epsilon}{E_\mathrm{b}} = \frac{GM}{r_\mathrm{t}^2}\frac{R_*^2}{GM_*} = \left(\frac{M}{M_*}\right)^{1/3} = 100 \tag{4.4}$$

where the last equation holds for a $10^6 M_\odot$ black hole.

If we consider a solar-type star ($m_* = M_*/M_\odot = 1$, $x_* = R_*/R_\odot = 1$) on an initial parabolic orbit with pericentre r_p, after tidal disruption roughly half of the stellar mass becomes gravitationally bound to the black hole with specific binding energy (4.3). Newtonian orbits with specific binding energy $\Delta\epsilon$ have orbital period

$$t = 2\pi GM(2\Delta\epsilon)^{-3/2} \tag{4.5}$$

implying that the debris return to pericentre after a time

$$t_\mathrm{min} = \frac{2\pi GM}{(2\Delta\epsilon)^{3/2}} = \frac{\pi}{2^{1/2}}\left(\frac{r_\mathrm{t}}{R_*}\right)^{3/2}\left(\frac{r_\mathrm{t}^3}{GM}\right)^{1/2} \approx 0.11\, M_6^{1/2} m_*^{-1} {x_*}^{3/2}\,\mathrm{yr} \tag{4.6}$$

after tidal disruption (Lodato & Rossi, 2011). This means that for a few years there would be a steady stream of material returning for the first time to the vicinity of $r_{\rm t}$. In a Newtonian potential the debris follow elliptical orbits differing in semimajor axis but sharing the same pericentre and latus rectum. Since the pericentre radius is very close to the Schwarzschild radius, the relativistic (Einstein) precession of the latus rectum is enough to lead to stream-stream collisions and therefore to strong shocks (Evans & Kochanek, 1989; Cannizzo et al., 1990). These shocks convert kinetic energy into radiation pressure at peak temperatures $\sim 10^7$ K. The timescale needed to radiate away the excess energy of the debris is

$$t_{\rm rad} \approx \frac{GMM_*}{4r_{\rm t}L_{\rm Edd}} \approx 4M_6^{-1/3}m_*^{4/3}x_*^{-1}{\rm yr}\,. \tag{4.7}$$

There are three possible scenarios that need to be considered. The accretion rate might be i) so high that the material is drained from the disc almost immediately as it circularizes, ii) slower than circularization but faster than the radiation time so the material accretes in a thick disc iii) or even slower than radiation so the disc ends up to be thin (Ulmer, 1999). We expect the debris streams to circularize on a timescale of the order of the fallback time and form a gaseous torus in the vicinity of the black hole. Once a near-equilibrium torus is formed, the material will spread out into a viscous accretion disc (Lynden-Bell & Pringle, 1974). Since the accretion rate from the stream is super-Eddington in the early phases, the disc is expected to be hot, thus geometrically thick, and radiation pressure dominated (since it is also expected to be narrow).

The disc viscous time is

$$t_\nu = \frac{R^2}{\nu} = \frac{1}{\alpha}\left(\frac{H}{R}\right)^{-2}\left(\frac{8r_{\rm p}^3}{GM}\right)^{1/2} = 0.052\left(\frac{H}{R}\right)^{-2} m_*^{-1/2}x_*^{3/2}\,{\rm d}\,. \tag{4.8}$$

This is much shorter than the timescale at which the material falls back to the pericentre radius. In the early phase, the accretion rate onto the black hole is thus the same as the rate at which the disc is fed from the fallback material. At very late times ($t \gtrsim 100$ yrs after the event, e.g. Ulmer 1999) the viscous time becomes long enough so that the accretion rate is controlled by viscous processes rather than by the disc feeding.

For non-spinning black holes, Hayasaki et al. (2013) and Bonnerot et al. (2016) have demonstrated through hydrodynamical simulations that the gas debris circularize on a few orbital timescale because relativistic precession causes the stream to self-cross, forming either a thin disc at the circularization radius, or an extended thick torus depending on the cooling efficiency.

The simulations by Hayasaki et al. (2013) show that although the post-Newtonian potential does not accurately model the precession of nearly circular orbits, by the time the post-Newtonian potential becomes significantly inaccurate, the debris streams have entered a regime of frequent orbit crossing, guaranteeing further rapid circularization. The post-Newtonian potential plays a central role in orbital circularization processes, because the motion of a particle in the Newtonian potential takes place in a closed path and therefore causes no orbit crossing.

Bonnerot et al. (2016) performed simulations with the SPH code PHANTOM using the Tejeda & Rosswog (2013) potential and confirmed that gas debris streams circularize on an orbital timescale because of stream-stream collisions owing to relativistic apsidal precession. Besides, higher eccentricities and/or deeper encounters lead to circularization on a faster timescale. They have also shown that if the internal energy deposited by

shocks during stream-stream collisions is radiated away almost immediately, the gas forms a narrow ring at the circularization radius that proceeds to accrete viscously at a super-Eddington rate and thus will increase its thickness under radiation pressure. The long term evolution of the debris stream under the presence of shocks and magnetic fields has been treated analytically by Bonnerot et al. (2017). They showed that shocks are likely to further shrink the orbit and magnetic stresses might lead to ballistic accretion. Furthermore they showed that if the excess thermal energy injected by shocks is not radiated away efficiently, the stream rapidly forms a thick structure.

4.2.1 TDE light curve

The light curve of a TDE is determined by the energy distribution of the bound debris. The simple theory by Rees (1988) is based on the assumption that the bound debris of the disrupted star follow Keplerian orbits with different periods depending on their depth within the black hole potential well. Thus the bound debris come back to the pericentre after a period t that is related to their specific energy (Lodato et al., 2009)

$$\epsilon = -\frac{1}{2}\left(\frac{2\pi GM}{t}\right)^{2/3} . \tag{4.9}$$

The mass distribution of specific energy corresponds, through Eq. (4.9), to a mass distribution of return times dM/dt. The next fundamental assumption is that once the bound material has come back to the pericentre it loses its energy and angular momentum on a time scale shorter than t, thus suddenly accreting onto the SMBH and giving rise to the flare. The mass distribution of return times is therefore effectively the mass accretion rate of the black hole during the event. During the formation of the accretion disc it is likely that the accretion rate differs from the fallback rate $\dot{M}_{\rm fb}$ (Shiokawa et al., 2015). If the viscous time is shorter compared to the circularization time, then the accretion rate is fixed by the fallback rate but the debris are accreted without forming any disc while if the two timescales are comparable, a disc is also formed (Bonnerot et al., 2016). If the star is on a parabolic orbit the debris are viscously accreted during the circularization process, thus it is reasonably to assume that $\dot{M} = \dot{M}_{\rm fb}$.

From Equation (4.9) the mass accretion rate is

$$\frac{dM}{dt} = \frac{dM}{d\epsilon}\frac{d\epsilon}{dt} = \frac{(2\pi GM)^{2/3}}{3}\frac{dM}{d\epsilon}t^{-5/3} \tag{4.10}$$

In order to obtain the $t^{-5/3}$ light curve, we have to make another fundamental assumption that the energy distribution is uniform.

We consider the case in which the stellar radius is much smaller than the pericentre radius. Since we assumed that the star is disrupted from a parabolic orbit, the energy distribution will be centred on zero and distributed between $-\Delta\epsilon$ and $\Delta\epsilon$, with $\Delta\epsilon$ given by (4.3).

Since the material at lower energies contributes to the accretion rate at later times we expect that if the star is more centrally condensed the flare should start with a relative longer delay and therefore the light curve would be shallower. Indeed, the lack of matter at larger energies leads to a shorter return time while the abundance of mass at lower energies leads to the opposite (Lodato et al., 2009).

We expect the energy distribution to flatten at the lowest energies and therefore the light curve to approach a $t^{-5/3}$ profile at late times. In simulations the star is often

considered as a simple polytropic sphere ($P = K\rho^{\gamma}$) with some index and the quantities of interest are calculated solving the Lane-Emden equation. At pericentre the star is already quite distorted with respect to its initial configuration and in particular it has somewhat expanded. This occurs because while in isolation the star is in hydrostatic equilibrium between its pressure and its self-gravity, as it approaches the black hole, the tidal field effectively acts as to reduce the stellar gravity, making pressure forces unbalanced and therefore 'inflating' the star. The effect would be more significant for small polytropic index γ. This reflects the fact that the radius of a polytrope with small γ is more sensitive to the effective gravity.

Lodato et al. (2009) showed two important results. First, even when $\beta = 1$ and the spin-up of the star is expected to approach the break-up velocity, equation (4.3) gives a good estimate for the total energy spread. Secondly, the energy distribution $dM/d\epsilon$ within the bound matter depends on the internal structure of the star. In particular it is constant only for an idealized incompressible star ($\gamma \gg 1$). In general the resulting fallback accretion rate departs from the $t^{-5/3}$ power-law behaviour during the first few months, resulting in a smaller peak fallback rate.

If the distribution in energy $dM/d\epsilon$ is flat, then the fallback accretion rate is given by (Rees, 1988)

$$\dot{M}_{\rm fb} = \dot{M}_{\rm p} \left(\frac{t}{t_{\rm min}} \right)^{-5/3} . \tag{4.11}$$

where $\dot{M}_{\rm p}$ is the peak accretion rate

$$\dot{M}_{\rm p} = \frac{1}{3} \frac{M_*}{t_{\rm min}} \approx 1.9 \times 10^{26} M_6^{-1/2} m_*^2 x_*^{-3/2} \, {\rm g \, s^{-1}} . \tag{4.12}$$

This is roughly two orders of magnitude above the Eddington threshold, assuming a radiative efficiency $\eta = 0.1$. In reality this power-law evolution is expected to occur at late times, while initially the light curve shows a smooth rise to the peak, the details of which depend on the internal structure of the disrupted star (Lodato et al., 2009). Also this behaviour has been sometimes observed (Gezari et al., 2009, 2012).

The ratio between the peak fallback accretion rate and the Eddington rate is $\propto M^{-3/2}$, so the fallback rate is expected to be only marginally super-Eddington for a $10^7 M_\odot$ black hole. The mass accretion rate can exceed the Eddington limit for days to months after disruption likely producing a mass overflow. After super-Eddington phase the emission is dominated by a thermal component from the accretion disc, which also photoionizes the unbound stellar debris, producing broad emission lines. The thermal disc emission has been investigated by Lodato & Rossi (2011). They showed that, after a few months, optical and UV light curves scale as $t^{-5/12}$, and are thus substantially flatter than the $t^{-5/3}$ behaviour, which is a prerogative of the bolometric light curve only.

Coughlin & Nixon (2015) recently showed through numerical simulations that the stream of tidally stripped debris can be gravitationally unstable and fragment into bound clumps. These clumps are accreted at discrete times causing fluctuations in the fallback rate around the $t^{-5/3}$ average.

More than one year after disruption, the observed emission is dominated by the disc at all frequencies (Lodato & Rossi, 2011). The spectrum of an optically thick disc is approximately given by a superposition of black body spectra with temperature ranging from $T_{\rm out} = T(R_{\rm out})$ and $T_{\rm in} = T(R_{\rm in})$. Since the radial extent is expected to be small

for a TDE accretion disc, the range of disc temperatures is correspondingly small

$$\frac{T_{\rm in}}{T_{\rm out}} \simeq \left(\frac{R_{\rm out}}{R_{\rm in}}\right)^{3/4} \approx 30\, M_6^{-1/2}\,. \tag{4.13}$$

Suppose that the event is observed at a given wavelength $\nu_{\rm obs}$. Then the shape of the light curve is determined by the relative size of $T_{\rm obs}, T_{\rm in}$ and $T_{\rm out}$. When the disc is hotter, for relatively small observed frequency we have $T_{\rm obs} < T_{\rm out}$. In this case, the observed frequency lies in the Rayleigh-Jeans tail of the spectrum and thus the luminosity scales as $\nu L_\nu \propto T_{\rm d} \propto \dot{M}^{1/4} \propto t^{-5/12}$, where $T_{\rm d}$ is the disc effective temperature. When $T_{\rm out} < T_{\rm obs} < T_{\rm in}$, the emission at $\nu_{\rm obs}$ is dominated by the disc radii with $T(R) \approx T_{\rm obs}$. Since the emitting portion of the disc does not vary much with time, we expect a monochromatic luminosity proportional to $t^{-5/3}$ in this phase. At late times, $T_{\rm in} < T_{\rm obs}$ since the disc has cooled down significantly. The observed frequency lies in the Wien part of the spectrum and we should expect an exponentially declining monochromatic light curve.

In the optical and FUV, the light curve initially follows a $t^{-5/12}$ decline for several hundred years. Only in the X-rays the initial light curve is expected to show the standard $t^{-5/3}$ decline for a few years, before turning into an exponential decline.

Chapter 5

Measuring SMBH spins with Lense-Thirring precession of TDE discs

Based on the paper by **Alessia Franchini**, *Giuseppe Lodato and Stefano Facchini: "Lense-Thirring precession around supermassive black holes during tidal disruption events " published in Monthly Notices of the Royal Astronomical Society, 455, 1946-1956 (2016).*

In general black hole masses can be measured through dynamical studies of the orbital motion of individual stars and gas in galactic nuclei. This kind of measurement can be performed using Newtonian mechanics since the stars are far from the black hole. The estimate of the spin is much more challenging. The spin has no gravitational effects in the Newtonian theory, so it can be measured only by probing the space-time geometry close to the black hole. Tidal disruption events occurring at distances of only a few gravitational radii from the black hole offer just this opportunity.

Since the accretion disc forms very close to the black hole, general relativity effects must be taken into account. Stone & Loeb (2012) demonstrated that the Lense-Thirring precession around a spinning SMBH can produce significant time evolution of the disc angular momentum vector, since in general the initial orbit of the star is inclined with respect to the spinning black hole equatorial plane. For a thin disc it is expected that the Bardeen-Petterson effect (Bardeen & Petterson, 1975) induces a warp in the disc structure. Lei et al. (2013) argued that the precession of the jet is a possible consequence of this effect, providing an explanation for the Sw 1644+57 quasi-periodic modulation of the light curve. However the disc formed after a TDE is expected to be geometrically thick, as discussed in the previous chapter (Strubbe & Quataert, 2009; Ulmer, 1999). In this configuration the Bardeen-Petterson effect does not occur. Still, if the disc is narrow it can precess as a solid body rotating around the black hole, inducing the precession of the jet and thus the modulation in the light curve. This has now been seen in GRMHD numerical simulations (Liska et al., 2017). The warp induced by the Lense-Thirring precession can propagate either in the diffusive regime if $\alpha \gtrsim H/R$ (Pringle, 1992; Lodato & Price, 2010) or in the bending waves regime if $\alpha \lesssim H/R$ (Nelson & Papaloizou, 2000), α being the Shakura & Sunyaev (1973) viscosity, and H being the disc thickness. Since the disc formed after a TDE is expected to be geometrically thick we are in the second regime, thus the warp propagates as a wave with half the speed of sound inside the disc.

Shen & Matzner (2014) have reexamined this issue considering a disc spreading both inwards and outwards from the circularization radius and its precession as a solid body applying the model to Sw 1644+57.

A precessing disc might offer a novel way to measure spin in black hole systems, through timing observations. The prospects for an effective determination of the spin

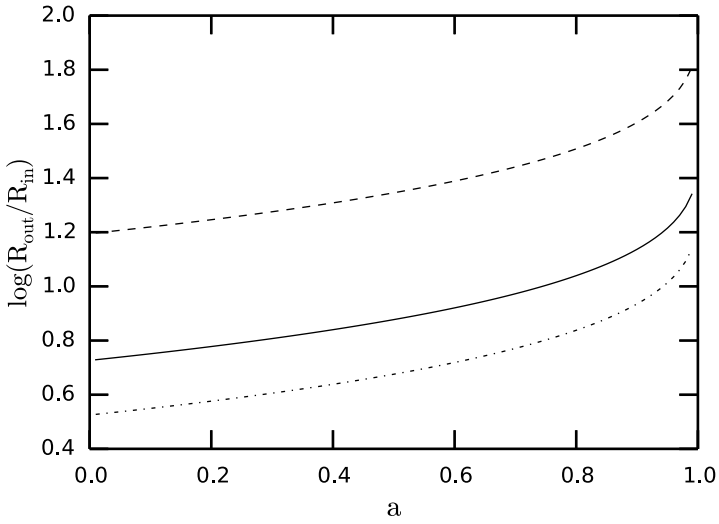

Figure 5.1: Disc extension as a function of the black hole spin a for different values of M_6. The dashed line refers to $M_6 = 1$, the solid one to $M_6 = 5$ and the dash-dotted one to $M_6 = 10$.

parameter in this way are encouraged by the successful application of such techniques to stellar mass black holes, through the analysis of type-C QPOs in Low Mass X-ray Binaries (e.g., Ingram et al. 2009; Motta et al. 2014b). This will be discussed later on in the thesis.

In this chapter I consider a simple model with a disc that extends from the circularization radius, that is about twice the tidal radius towards the Innermost Stable Circular Orbit (ISCO) around the supermassive black hole.

The outer radius of the disc is :

$$R_{\rm out} = 0.94\,{\rm AU}\,M_6^{1/3} \tag{5.1}$$

where in the last equality I assumed that the disrupted star is a solar type one, thus $m_* = x_* = 1$ and the penetration factor is $\beta = 1$.

In units of the gravitational radius the inner radius $r_{\rm in}$ is a function of the spin only, while the dimensionless outer radius depends only on the mass of the black hole, $r_{\rm out} = 94\,M_6^{-2/3}$.

The disc extension is then given by

$$\frac{r_{\rm out}}{r_{\rm in}} = 94\,\frac{1}{r_{\rm in}}\,M_6^{-2/3} \tag{5.2}$$

which takes into account the dependence of the disc extension on the black hole spin a and on the black hole mass through M_6.

Fig. 5.1 shows the extension of the disc as a function of the spin for different values of the black hole mass. From Fig. 5.1, we can see that for larger values of a, $r_{\rm in}$ decreases and thus the disc inner radius is closer to the black hole, thus the disc is wider, since the outer radius does not depend on the spin of the black hole but only on its mass. We can see that the ratio $r_{\rm out}/r_{\rm in}$ in the most massive case of $10^7 M_\odot$ is very small, from 3 to

roughly 10 depending on the spin value. The disc is then relatively narrow. For lower black hole masses the ratio between the outer and the inner radius ranges from ≈ 15 to ≈ 60.

5.1 A slim disc model for the disc structure

Accretion discs formed by stellar debris after a TDE are expected to be geometrically thick, meaning that the aspect ratio H/R approaches unity. During the super-Eddington phase, the time for photons to diffuse out of the disc is longer than the viscous time, thus the disc is thick and advective. Strubbe & Quataert (2009) derived a 'slim disc' model similar to the one of Abramowicz et al. (1988), which describes the structure of the disc in both the super and sub Eddington accretion regime. The gas pressure is negligible since the radiation pressure dominates the disc for at least a few years. Besides the disc formed after a TDE is so narrow that we can reasonably assume that it lies entirely within region a) according to the Shakura & Sunyaev (1973) picture. They assumed the stress tensor to be given by the radiation pressure, since numerical simulations have shown that the heating and cooling mechanisms balance each other and give a stable disc configuration, only slightly violating the thermal stability criterion, even in the radiation pressure dominated region (Hirose et al., 2009). Note that such a slim disc model has been often used in TDE modelling (Strubbe & Quataert, 2009; Stone & Loeb, 2012; Lodato & Rossi, 2011). A proper modelling should involve global MHD, GR simulations, but for the simple analytical analysis proposed in this work we deem this approximation as reasonable.

The vertically integrated heating and cooling rates are $2Hq^+ = 3GM\dot{M}/4\pi R^3$ and $2Hq^- = 8\sigma T^4/3\tau$. These relations form a quadratic equation that can be solved. Using dimensionless quantities defined in the previous sections, the slim disc aspect ratio becomes

$$\frac{H}{R} = \frac{3}{2}(2\pi)^{1/2}\,\eta^{-1}\dot{m}\,r^{-1}f(r)\,K(r)^{-1} \tag{5.3}$$

where K is the following function of radius r and spin a (Strubbe & Quataert, 2009):

$$K(r) = \frac{1}{2} + \left[\frac{1}{4} + 6\,f(r)\left(\frac{\dot{m}_{\rm fb}}{\eta}\right)^2\left(\frac{1}{r}\right)^2\right]^{1/2}. \tag{5.4}$$

This correction factor $K(r)$ takes into account the modified structure for a slim disc. Thus the disc thickness becomes $H \sim R$ during the super-Eddington phase and decreases as $t^{-5/3}$ afterwards.

The sound speed is then given by:

$$c_{\rm s} = \frac{3}{2}(2\pi)^{1/2}\,\eta^{-1}c\,\dot{m}_{\rm fb}\,r^{-3/2}f(r)\,K^{-1}(r). \tag{5.5}$$

The surface density dependency on the various quantities of interest is:

$$\Sigma = \Sigma_0 r^{-3/5} f^{3/5}(r)\,{\rm g\,cm^{-2}} \tag{5.6}$$

where Σ_0 is a constant that depends on $\dot{m} = \dot{M}/\dot{M}_{\rm Edd}$, M_6 and α, and $f(r) = 1-(r_{\rm in}/r)^{1/2}$.

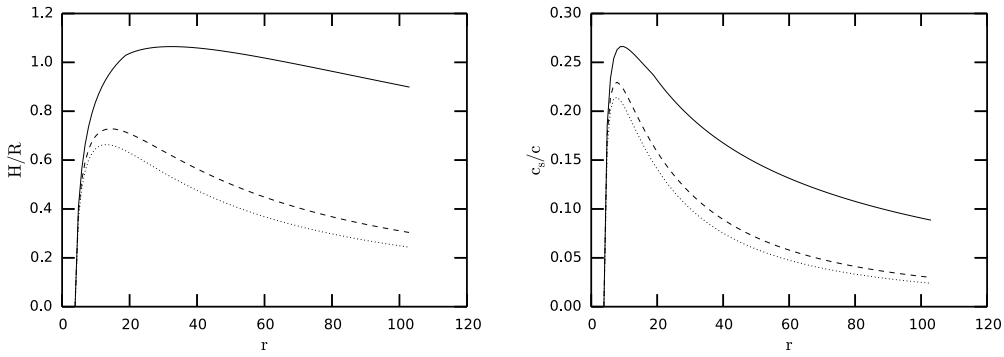

Figure 5.2: Disc ratio H/R (left panel) and sound speed c_s/c (right panel) as a function of the radius. The solid lines refer to the super-Eddington phase at a time $t_{\rm min}$. The dashed lines refer to the Eddington phase, reached after $2.6\,t_{\rm min}$ and the dotted lines refer to the sub-Eddington phase, after $3\,t_{\rm min}$. The curves refer to a black hole with $M_6 = 10$ and $a = 0.6$.

In order to describe the evolution of the disc we consider a viscosity given by the α-prescription by Shakura & Sunyaev (1973). We assume the stress tensor to be proportional to gas pressure only rather than to total pressure, in order to avoid the Lightman & Eardley (1974) instability. In our model the α-parameter is both constant in time and isotropic. This simple assumption is commonly taken in evolutionary models of discs in the literature, since it prevents computationally expensive simulations. In order to properly compute the viscous stress in discs simulations one would need to perform magnetohydrodynamic (MHD) calculations to treat the magneto-rotational instability (MRI) (e.g. Sorathia et al., 2013b). However the work presented here is a preliminary study with the aim to confirm the validity of the model, thus we consider the simple isotropic viscosity.

5.1.1 Super-Eddington phase

The viscous time in the disc is generally much shorter than the fallback time (see section 4.2), which would then imply that the stellar debris are immediately processed through the disc, such that the black hole accretion rate equals the fallback rate (Rees, 1988). In reality this might not happen for two different reasons. Firstly, disc accretion might start with a significant delay with respect to fallback. In this case most of the debris accumulate in a ring and only start accreting when fallback has faded significantly. In this case the accretion rate through the disc is dictated by viscous processes rather than by fallback (Cannizzo et al., 1990; Shen & Matzner, 2014). Numerical simulations of the disc formation process do not yet clarify the extent to which such a delay occurs (Bonnerot et al., 2016). Here, we thus assume that – if possible – the accretion rate does coincide with the fallback rate. Even in this case, however, if the fallback rate is super-Eddington, most of the debris might be expelled from the system in the form of an outflow. The dynamics of super-Eddington discs is complex and not well understood. While some models seem to imply that super-Eddington rates can be sustained with little mass outflow if the disc is radiatively inefficient (Ohsuga & Mineshige, 2007; McKinney et al., 2014), it is in general expected that super-Eddington rates will result in an outflow. The recent discovery

of pulsating ultra-luminous X-ray sources (ULXs) supports the models according which ULXs are beamed X-ray sources powered by super-Eddington accretion onto stellar mass compact objects (King et al., 2001; Begelman et al., 2006; King, 2009; Koliopanos et al., 2017).

Given a super-Eddington mass supply, the accretion disc is stable at large radii down to the radius at which the local energy release is close to the local Eddington and the excess mass is expelled in an outflow (Poutanen et al., 2007; King & Lasota, 2016). The local disc luminosity is $L_{\rm disc}(R) = GM\dot{M}(R)/2R$, while the Eddington limit is $L_{\rm Edd} = \eta \dot{M}_{\rm Edd} c^2$ and the efficiency can be written as $\eta = GM/(2R_{\rm in}c^2)$. In this work we make the simple and reasonable assumption that in order to keep each disc radius close to its local critical value ($L_{\rm disc}(R) = L_{\rm Edd}$), the outflow must ensure that the accretion rate decreases as

$$\dot{m} = \frac{r}{r_{\rm in}} \tag{5.7}$$

for radii smaller than

$$r_{\rm Edd} = \dot{m}_{\rm fb} r_{\rm in}, \tag{5.8}$$

which is a function of time. At large radii, the local disc luminosity is below Eddington even if the fallback rate is globally super-Eddington. We thus assume that $\dot{m} = \dot{m}_{\rm fb}$ for $r > r_{\rm Edd}$.

The evolution of the disc thickness for a typical choice of parameters as a function of time is shown in Fig. 5.2. The solid line refers to the super-Eddington phase and one can see that $H/R \sim 1$ and thus the disc is geometrically thick. The aspect ratio increases with radius until $r = r_{\rm Edd}$ while at larger radii it scales as $1/r$. The long dashed line refers to the Eddington phase while the dotted line refers to the sub-Eddington phase. The time at which the accretion rate is equal to the Eddington value can be inferred by requiring that $\dot{m}_{\rm fb} = 1$. This gives

$$t_{\rm Edd} = \left(\frac{\dot{M}_{\rm Edd}}{\dot{M}_{\rm p}} \right)^{-3/5} t_{\rm min}. \tag{5.9}$$

In Fig. 5.2 the three curves are obtained for a $10^7 M_\odot$ black hole, spinning with $a = 0.6$. For higher values of the black hole spin, the efficiency η increases slightly and thus the disc thickness is lower.

5.2 Global precession

In the previous section we have described the structure of an accretion disc formed after the tidal disruption of a star by a supermassive black hole. Since the initial stellar orbit is likely to be inclined with respect to the black hole equatorial plane, the disc angular momentum is in general misaligned with the black hole spin. We now focus on the evolution of such inclined disc.

The misalignment between the disc and the black hole spin generates a relativistic torque on the disc proportional to R^{-3} (see section 2.3). A faster precession implies an enhanced viscous dissipation, thus the inner disc tends to align with the equatorial plane while the outer regions keep the original misalignment. Additionally, under certain conditions the warped disc is expected to rigidly precess around the hole (e.g. Papaloizou & Lin, 1995; Fragile & Anninos, 2005; Fragile et al., 2007, see Section 3.2). Observationally, the only evidence we have of this phenomenon might be the early periodicity of

the light curve of the event Sw J1644+57 (e.g. Shen & Matzner, 2014). Here we aim to compute the precession period of a misaligned disc as a function of the black hole mass and spin, such that the observed periodicity in the light curve of TDEs may be used to infer fundamental properties of the central black hole.

5.2.1 Precession period

In this section we assume that the disc can rigidly precess. We have discussed the conditions for rigid precession in Section 3.2. We estimate the global precession frequency using the same procedure described in Section 3.1.

The Lense-Thirring frequency $\Omega_{\rm LT}(R)$ is the frequency at which an isolated ring of material would precess under the influence of the external torque $T(R)$ given by Eq. (2.84) . Assuming that the whole disc precesses with the same frequency $\Omega_{\rm p}$, this is given by

$$\Omega_{\rm p} = \frac{\int_{R_{\rm in}}^{R_{\rm out}} \Omega_{\rm LT}(R) L(R) 2\pi R\, dR}{\int_{R_{\rm in}}^{R_{\rm out}} L(R) 2\pi R\, dR}. \tag{5.10}$$

Having defined an expression for $\Sigma(R)$ with Eq. (5.6), we now need to derive an expression for $\Omega_{\rm LT}(R)$, in order to compute the precession frequency. We evaluate the external torque using the expression:

$$T(R) = \Sigma R^2 \Omega \left(\frac{\Omega_{\rm z}^2 - \Omega^2}{\Omega^2}\right) \frac{\Omega}{2} \tag{5.11}$$

where $\Omega_{\rm z}$ is the vertical oscillation frequency due to frame dragging. The angular and vertical frequencies derived from the Kerr metric are (Kato, 1990):

$$\Omega = \frac{c^3}{GM} \frac{1}{r^{3/2} + a}; \tag{5.12}$$

$$\left(\frac{\Omega^2 - \Omega_{\rm z}^2}{\Omega^2}\right) = 4ar^{-3/2} - 3a^2 r^{-2}, \tag{5.13}$$

where $-1 < a < 1$ is the dimensionless hole angular momentum ($a < 0$ for a retrograde disc).

For $r \gg 1$, we have

$$\Omega \simeq \frac{c^3}{GM} \frac{1}{r^{3/2}}, \tag{5.14}$$

From (5.12) and (5.13), we obtain the following expression for the local precession frequency, in units of the gravitational radius:

$$\Omega_{\rm LT}(r) = \frac{1}{2} \frac{c^3}{GM} \frac{1}{r^{3/2} + a} (4ar^{-3/2} - 3a^2 r^{-2}), \tag{5.15}$$

which, for $r \gg 1$, gives the usual r^{-3} dependence:

$$\Omega_{\rm LT} \simeq 2a \frac{c^3}{GM} r^{-3}. \tag{5.16}$$

Fig. 5.3 shows the dependence of the global precession period $T = 2\pi/\Omega_{\rm p}$ on the black hole spin for three different values of the hole mass. The solid lines represent the estimate of the precession period obtained from numerical integration of (5.10), including all the

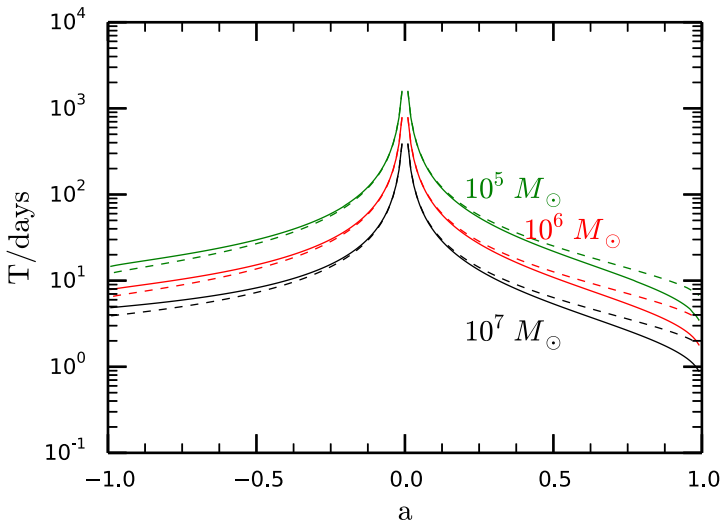

Figure 5.3: Dependence of the global precession period on a for a prograde and a retrograde disc. The dashed lines show the same period using the first order approximated forms Eq. (5.14) and (5.16). This results refer to $M_6 = 0.1$ (green lines), $M_6 = 1$ (red lines) and $M_6 = 10$ (black lines).

terms of the expressions of the Keplerian and vertical frequency (5.12) and (5.13). The dashed lines indicate the same result where we have considered only the dominant term in the limit of $r \gg 1$ in the same equations (Eq. 5.14 and 5.16). The difference between the two cases becomes relevant at high spin values, where the difference in the precession period can be as large as a factor of 2, whereas it is negligible at low spin values.

If the black hole has a large spin, the disc is wider than for low spin values (see Fig. 5.1) and has therefore a larger angular momentum. However, since the inner radius is closer to the hole, the torque that generates the precession is stronger. The combined effect is that the precession frequency $\Omega_{\rm p}$ is larger. In this case, the period is short enough to be detectable at the beginning of a TDE ($\sim 1 - 20$ days).

5.3 Time dependent calculations

In this section we consider the evolution of the disc with time to check that rigid precession does occur and how it evolves with time. The accretion rate is super-Eddington at the beginning and decreases as $t^{-5/3}$. This decrease with time implies a decrease of the ratio H/R (see Eq. (5.3)). When H/R drops below the value of the disc viscosity α, the warp propagates inside the disc in a diffusive way (Papaloizou & Pringle, 1983; Pringle, 1992; Lodato & Price, 2010). At this point the accretion flow is susceptible to the Bardeen-Petterson effect (Bardeen & Petterson, 1975) that leads to alignment between the disc and the hole angular momentum.

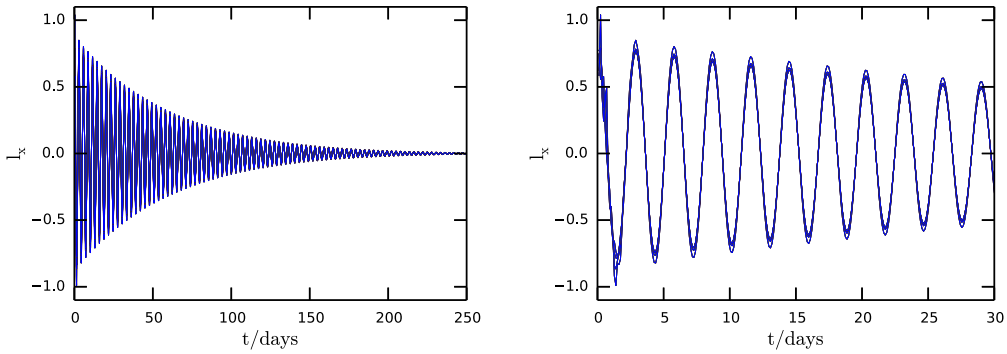

Figure 5.4: Evolution of the x-component of the disc angular momentum with time. The viscosity is $\alpha = 0.05$, the value of the hole spin is $a = 0.7$ and the mass $10^7 M_\odot$. The right panel is a detail of the left one. The different curves refer to different radii inside the disc. Although the amplitudes are slightly different, the period of the oscillations at different radii is the same.

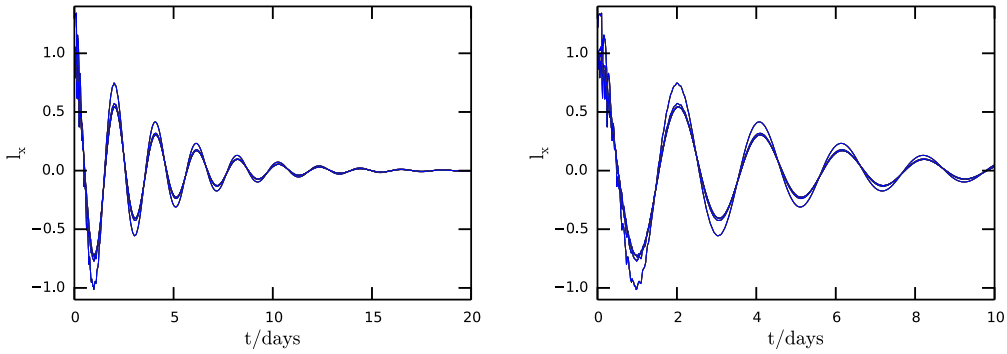

Figure 5.5: Evolution of the x-component of the disc angular momentum with time. The viscosity is $\alpha = 0.05$, the value of the hole spin is $a = 0.9$ and the mass $10^6 M_\odot$. The right panel is a detail of the left one. The different curves refer to different radii inside the disc. Although the amplitudes are slightly different, the period of the oscillations at different radii is the same.

5.3.1 Warp propagation in bending waves regime

The disc formed after a tidal disruption event is expected to be thick (see upper panel in Fig. 5.2) enough that $H/R \gtrsim \alpha$ and the warp caused by the Lense-Thirring effect propagates in the bending waves regime (Papaloizou & Pringle, 1983). Its propagation is described by the following linearised equations (Papaloizou & Lin, 1995; Lubow & Ogilvie, 2000):

$$\Sigma R^2 \Omega \frac{\partial \mathbf{l}}{\partial t} = \frac{1}{R}\frac{\partial \mathbf{G}}{\partial R} + \mathbf{T} \tag{5.17}$$

$$\frac{\partial \mathbf{G}}{\partial t} + \left(\frac{\kappa^2 - \Omega^2}{\Omega^2}\right)\frac{\Omega}{2}\mathbf{e_z} \times \mathbf{G} + \alpha\Omega\mathbf{G} = \Sigma R^3 \Omega \frac{c_s^2}{4}\frac{\partial \mathbf{l}}{\partial R} \tag{5.18}$$

where $\mathbf{T}(R,t)$ is the external torque density acting on the disc, that arises from a lack of spherical symmetry in the potential, and $\mathbf{G}(R,t)$ is the internal torque. Equation (5.17) represents the horizontal component of the angular momentum conservation equation, including the external torque. The term on the right side of equation (5.18) depends on the speed of sound c_s which changes with time since it depends on $\dot{m}(t)$, see Eq. 5.5. Both equation are valid if one requires the deviation from the Keplerian potential to be small, i.e., $|\kappa^2 - \Omega^2| \lesssim \delta\Omega^2$ and $|\Omega_z^2 - \Omega^2| \lesssim \delta\Omega^2$ where $\delta = H/R$ (Foucart & Lai, 2014).

Note that the above equations, being linear, do not treat the possibility of shocks in the disc. The small warps produced in the case considered here (see below) do not produce supersonic shear and thus are not expected to develop shocks. During the disc formation phase (Shiokawa et al., 2015; Bonnerot et al., 2016) shocks might develop. However, here we treat the disc dynamics after the initial circularization phase.

The equations were derived in the case of isotropic viscosity $\nu = \alpha c_s H$. Pringle (1992) pointed out that the viscosity may be significantly anisotropic due to the different types of shear present in a warped disc. In general the viscosity parameter α in Eq. (5.18) can be different from that responsible for the radial transfer of mass and angular momentum. Azimuthal shear is secular where gas particles drift further apart, whereas vertical shear is oscillatory and thus should induce less dissipation. However, if the velocity spectrum of the turbulence is predominantly on scales $< H$ then it is likely to act similarly in each direction. Recently, Nixon (2015) explored models for a disc that is tilted and forced to precess by the radiation warping instability, to see what constraints can be provided on the internal communication of angular momentum in a warped disc.

We used a numerical grid code in order to solve the above equations in both space and time domain. In our code we used the radius R as the only spatial variable of the system. We therefore discretized the disc into a set of thin annuli, each of which can be tilted and interacts with the others via pressure and viscous forces. We wrote the bending waves equations in terms of dimensionless quantities and then we solved them using the leapfrog algorithm. This code is an modified version of the code used by Lodato & Facchini (2013a). In the linear regime it has proved to recover full 3D SPH simulations (e.g. Facchini et al., 2013; Nealon et al., 2015).

5.3.2 Results

We performed simulations choosing the values of the black hole parameters mass and spin referring to the observed period of the event Sw J1644+57. This tidal disruption event has an observed period of $T = 2.7$ days and the quasi-periodicity of the light curve lasts

approximately 10 days (Lei et al., 2013). Based on Fig. 5.3, we see that a period of 2.7 d can be reproduced with $a = 0.7$ for $M = 10^7 M_\odot$ and $a = 0.9$ for $M = 10^6 M_\odot$. We have performed simulations also for $M < 10^6 M_\odot$.

The evolution of the disc with time is shown in Figs. 5.4 and 5.5 for the two masses, respectively. The four curves refer to four different radii inside the disc at which the angular momentum is evaluated. As one can easily see, the amplitude changes slightly with radius but the curves have exactly the same period, implying that rigid precession is indeed occurring. The values of the rigid precession period computed numerically agree well with the expected value, 2.7 d.

As one can see (Figs. 5.4 and 5.5) the amplitude of the oscillation decreases steadily with time and the disc eventually aligns with the black hole. The most notable difference between the two cases shown is that while for $M = 10^7 M_\odot$ alignment occurs after several months, for $M = 10^6 M_\odot$ it only takes a few days to align for the same value of α. We will discuss the alignment process in details below.

We conclude that if we want to apply this model to Swift J1644, where some periodicity is observed only within the first 10 days, we would disfavour a high SMBH mass, unless α is significantly larger than 0.05. Similarly a value of M below $10^6 M_\odot$ is disfavoured since it would require an almost maximally spinning black hole. In particular, a 2.7 d period can be reproduced only for an extremely high value of a if $M < 5\,10^5 M_\odot$ (see the green lines in Fig. 5.3).

Fig. 5.6 shows the tilt β (defined as the misalignment between the spin and the local disc angular momentum) as a function of the radius for the case $M = 10^6 M_\odot$, $a = 0.6$ and $\alpha = 0.05$ (top) and 0.5 (bottom), respectively. The first thing to notice is that while the disc is rigidly precessing, it maintains a small warp (β is a function of the radius), which is necessary to balance the external torque. Note that the disc turns out to be (slightly) more misaligned in the inner regions than in the outer regions. This is not unexpected. As shown by Lubow et al. (2002), the radial profile of beta depends on the relative signs of the nodal and apsidal precession frequencies. While, for example, in the case of a circumbinary disc, the tidal torque produces a monotonically increasing tilt, in the case of Lense-Thirring precession the tilt function is not monotonic and can show regions where the disc warps away from alignment.

On a timescale much longer than the precession time, the disc slowly aligns. Comparing the two panels of Fig. 5.6 we note that the alignment time scales inversely with α and is thus proportional to the viscous timescale.

5.4 Alignment

In general the mechanisms that are likely to lead to alignment are at least two. The first one can be the cooling of the disc, as a consequence of the reduction of the accretion rate (given by Eq. 4.11). As the disc cools, it naturally becomes thinner. Eventually the disc will transit to a regime where the warp propagation becomes diffusive ($\alpha \geq H/R$). In this regime there is no rigid precession and the disc rapidly aligns with the black hole spin. This is the case considered by Stone & Loeb (2012) (SL), who calculate the associated alignment timescale as

$$t_{\rm thin} = t_{\rm min} \alpha^{-3/5} \left[5\, f(r) \frac{M_*}{\dot{M}_{\rm Edd} t_{\rm min}} \frac{1}{r} \right]^{3/5} \tag{5.19}$$

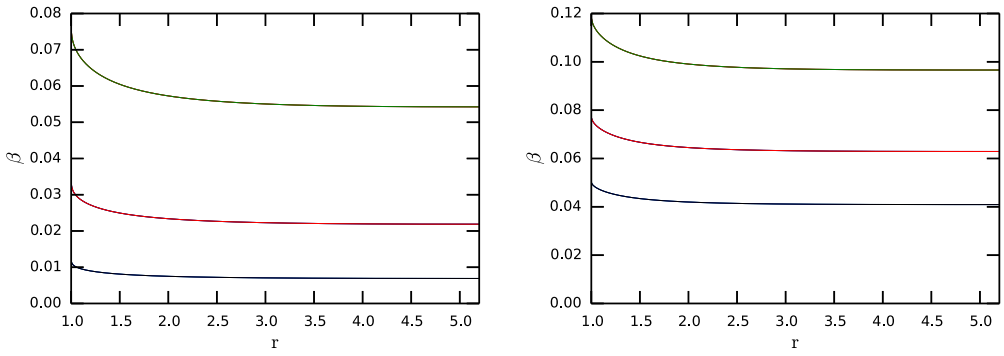

Figure 5.6: Shape of the tilt β inside the disc as a function of radius. Both panel refers to a black hole with $M = 10^6 M_\odot$ and $a = 0.6$. The left panel was obtained taking $\alpha = 0.05$. The green, red and black lines refer to the shape after roughly 290, 350 and 405 days. The right panel was obtained with $\alpha = 0.5$. The green, black, red and black lines refer to roughly 29, 35 and 40.5 days.

where $t_{\rm min}$ is the time after which the debris return to the pericentre (Eq. 4.6). The alignment timescale in this case is $\propto \alpha^{-3/5}$, while we have just seen (Fig. 5.6) that at least for the case $M = 10^6 M_\odot$, $a = 0.6$ our results indicate that $t_{\rm align} \propto \alpha^{-1}$.

The second possible mechanism is provided by the presence of the natural disc viscosity that damps the oscillations at a rate inversely proportional to the viscosity ($t_{\rm align} \propto \alpha^{-1}$). Thus if the viscosity is higher, the warp is dissipated on a shorter timescale.

We investigate under which condition one process dominates over the other by running several simulations with different values of α and of the black hole parameters. In general one may expect that since for low spin values the inner disc radius is larger, the torque exerted on the disc is weaker and rigid precession is expected to last on a longer timescale. The mass of the black hole changes the disc radial extent, thus we investigate for each values of the spin both values $10^6 M_\odot$ and $10^7 M_\odot$.

Different values of the black hole spin correspond to different magnitude of the torque and also to different evolutions of the oscillations of the disc tilt in time, as can be seen by the comparison of the two panels of Fig. 5.7. Both show the evolution of the x-component of the disc angular momentum with time, they differ only by the spin value, which is $a = 0.2$ and $a = 0.6$ respectively. We note two things. Firstly, as expected, for larger a the alignment is faster. Secondly, since the shape of the decay with time is different we might argue that the process that leads to alignment is not the same in the two cases.

We investigate which process is more likely to occur by computing $t_{\rm align}$ for each simulation and checking its dependence on α. In the cases like the one shown in the lower panel of Fig. 5.7, where an exponential decay with time of the x-component of the disc angular momentum is evident, we fitted the specific angular momentum curve with an exponential function

$$l = l_0 e^{-t/t_{\rm align}} \tag{5.20}$$

and then extracted the alignment timescale. For cases similar to the one shown in the upper panel of Fig. 5.7, where the shape of the decay is not exponential, rather than fitting equation (5.20) to the decay function, in order to have a direct comparison with

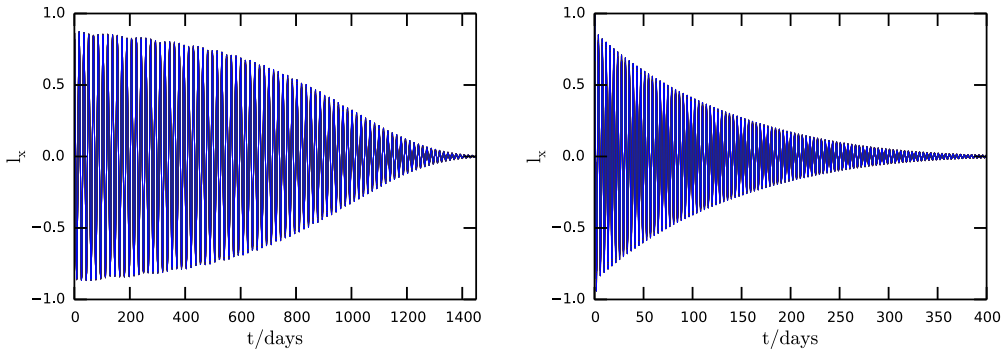

Figure 5.7: Evolution of the x-component of the disc angular momentum with time. The viscosity is $\alpha = 0.05$, the value of the mass is $10^7 M_\odot$, while the value of the spin is $a = 0.2$ for the left panel and $a = 0.6$ for the right panel.

the exponential case, we have computed the alignment timescale evaluating the time after which the angular momentum value is reduced by the same factor as in the exponential case, that is by $1/e$.

A sample of our results is shown in Fig. 5.8. The top panels refer to a case of moderate spin ($a = 0.6$) for the two cases $M = 10^6 M_\odot$ (left) and $M = 10^7 M_\odot$ (right). We see that the alignment time computed from the simulation is one to two orders of magnitude smaller than that predicted by SL (black line). Also, in this cases, $t_{\rm align}$ scales exactly as α^{-1}. We conclude that viscous alignment occurs much before the disc becomes thin enough to move into the diffusive regime.

The situation becomes less clear for low spins ($a = 0.2$) as shown in the bottom panel of Fig. 5.8. Here, the prediction by SL is much closer to the observed value. Additionally, the scaling of $t_{\rm align}$ with α becomes less evident (as shown by the red lines, that indicate a representative α^{-1} scaling).

A closer inspection of the bottom right panel of Fig. 5.8 reveals something interesting. While for larger values of α ($\alpha > 0.2$) $t_{\rm align} \propto \alpha^{-1}$, for $\alpha < 0.2$ we have $t_{\rm align} \propto \alpha^{-3/5}$, as evident in the fit shown in Fig. 5.9, where we have fitted $t_{\rm align}(\alpha)$ as a broken power law.

For each value of the black hole mass and spin, we have fitted a function of the form:

$$t_{\rm align} = t_0 \alpha^{-s} \tag{5.21}$$

to the simulation data, with t_0 and s as free parameters. The resulting value of s as a function of a for different M are shown in Fig. 5.10.

We clearly see two regimes: for $a \gtrsim 0.4$ we obtain $s = 1$ independently of M, this indicating a viscous origin for the alignment mechanism. For $a \leq 0.4$, s is smaller than 1. For high M it is very close to 3/5, indicating cooling as the main alignment mechanism. Values of s intermediate between 3/5 and 1 generally indicate cases similar to the one in Fig. 5.10, where $t_{\rm align}(\alpha)$ is a broken power-law, such that for large α the disc aligns viscously, while for low α it aligns due to cooling.

Recently it has also been suggested that jets can play a role in the alignment process. (Polko & McKinney, 2017) invesigated whether a disc aligns due to the jet or to the Lense-Thirring torque, finding that in some cases alignment can occur due to the jet torque before the LT torque becomes dominant.

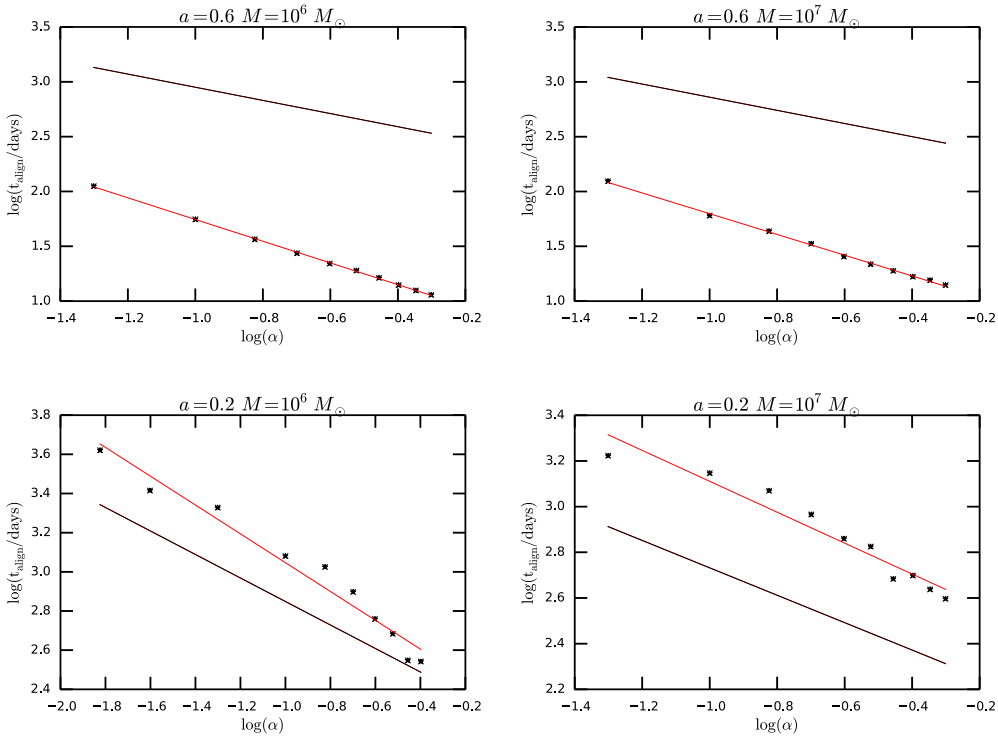

Figure 5.8: The different panels show the alignment timescale (in days) as a function of the viscosity parameter α for different couples of values of the black hole parameters: mass and spin. The black and red lines are representative curves $t_{\rm align} \propto \alpha^{-s}$ with $s = 0.6$ (SL) and $s = 1$ respectively. The stars are the values obtained from the simulations. Note that the normalization of the black and red line here is arbitrary. The simulations are consistent with the fact that disc tends to align on the shorter timescale.

5.4.1 Viscous alignment timescale calculations

As shown above, the disc viscosity leads to alignment, at least for spin values $a \gtrsim 0.4$. This occurs because it acts on the shearing motions inside the disc leading to energy dissipation. Bate et al. (2000) evaluated the amount of kinetic energy dissipated by the disc viscosity and the energy dissipation rate. Then from the ratio between these two quantities the alignment timescale can be inferred. In terms of the viscous time, this is

$$t_{\rm align} \sim t_{\rm Bate} = \frac{1}{\alpha}\left(\frac{H}{R}\right)^2 \frac{\Omega}{\Omega_{\rm p}^2}\,. \tag{5.22}$$

This result has been obtained referring to circumbinary discs, thus for relatively thin discs with a pure power law profile of H/R.

A more precise analysis has been performed by Foucart & Lai (2014) (FL). They argued that the damping rate of the global precession is

$$\gamma = \frac{1}{t_{\rm align}} = \frac{\int_{R_{\rm in}}^{R_{\rm out}} dx \frac{4\alpha G_\phi^2}{\Sigma c_{\rm s}^2 x^3}}{\int_{R_{\rm in}}^{R_{\rm out}} dx \Sigma x^3 \Omega} \tag{5.23}$$

where G_ϕ is the internal stress in the disc given by

$$G_\phi(r) = \int_{r_{\rm in}}^{r} dx \Sigma x^3 \Omega(\Omega_{\rm p} - Z\Omega)\,. \tag{5.24}$$

where Z is the nodal precession

$$Z(r) = \frac{\Omega^2 - \Omega_{\rm z}^2}{2\Omega^2}\,. \tag{5.25}$$

Eq. (5.24) represents the difference between the total torque exerted by the black hole on the disc and that required in order to keep the global precession of the disc. This difference is due to the fact that the finite viscosity α twists the disc by an angle $\phi = \arctan(l_y/l_x)$, thus creating a non-zero torque on the plane defined by the hole angular momentum and that of the disc. Using our one-dimensional code, we evaluated the twist angle as a function of the disc radius calculated at a fixed time for each value of α, and thus calculated the expected $t_{\rm align}$ based on FL.

The comparison between the results obtained with the FL method and those calculated with our code is shown in Fig. 5.11 where we can see that there is very good agreement.

This approach is equivalent to that of Bate et al. (2000), except for a shape factor ξ that depends on the profiles of $G(R)$ and $\Sigma(R)$. Considering the profiles in Eq. (5.6) and (5.3) and assuming $\dot{m} = 1$, we indeed find:

$$t_{\rm damp} = \frac{1}{4}\, t_{\rm Bate}\, \xi, \tag{5.26}$$

where ξ is the shape factor that lies in the range $1 \leq \xi \leq 8$ and the timescale $t_{\rm Bate}$ is evaluated at the disc outer radius $R_{\rm out}$.

5.5 Conclusions

In this work, we have developed a simple model for rigid disc precession in tidal disruption events. We have assumed that the disc can be modelled as a standard α-disc dominated by

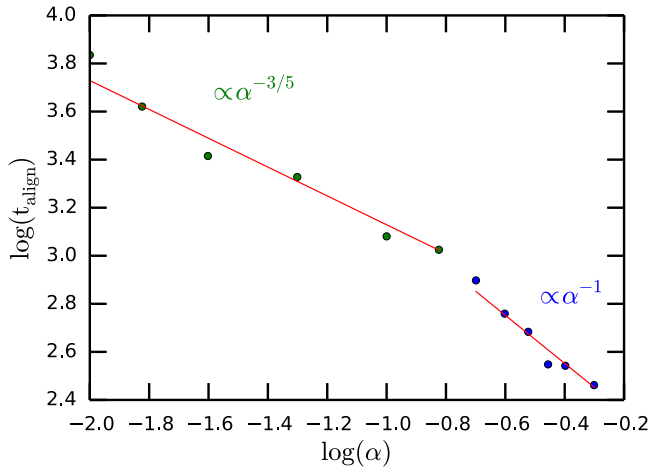

Figure 5.9: Alignment timescale behaviour as a function of the viscosity parameter α for a black hole with $a = 0.2$ and $M = 10^7 M_\odot$. For low viscosity values the timescale follows the prediction of SL, while for higher values it decreases with α^{-1}.

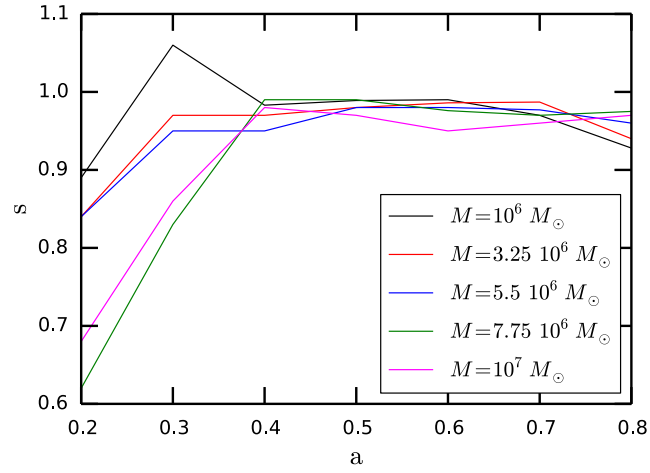

Figure 5.10: Values of the slope parameter as a function of the black hole spin a for different values of the black hole mass. For most spin values the parameter is $s = 1$ almost independently on the mass.

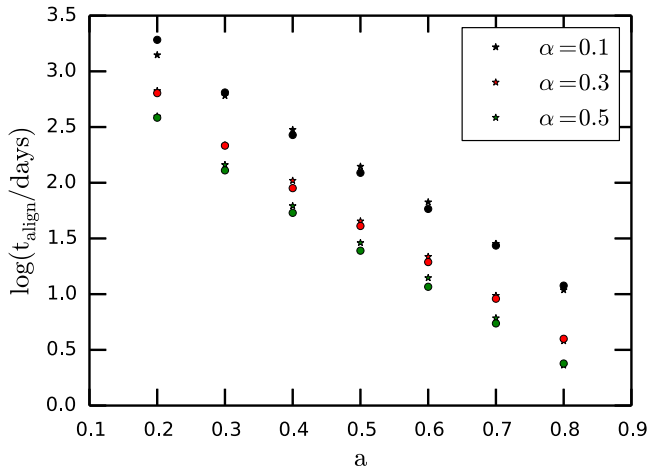

Figure 5.11: Comparison between the alignment timescales (in days) obtained with the one-dimensional code and those calculated with the FL method. The latter are represented by dots while the star values are those computed with our code. We choose a black hole with $M = 10^7 M_\odot$.

radiation pressure. We have thus computed the expected precession period as a function of the main system parameters. We find periods of the order of a few days up to a few weeks, with smaller black hole spins and masses giving rise to longer periods.

We have then compared our analytical expectations against time dependent simulations, where the disc is modelled as a series of interacting rings, applicable to small misalignments. We have thus confirmed that, initially, a TDE disc can globally precess across the whole parameter range applicable to TDE, with precession periods matching closely the expectations of the analytical model. On a longer timescale, however, the system evolves towards alignment. For a given precession period, a smaller black hole mass implies a faster alignment timescale, because in this case the radial extent of the disc is larger and warp communication less effective.

Periodic modulation of a TDE signal has rarely been observed, with a tentative detection of a 2.7 d period decaying after ≈ 10 days in the case of Swift J1644 (Lei et al., 2013). If we interpret this signal as arising from the Lense-Thirring precession of the disc, we would thus conclude that the black hole mass should be close to $5\ 10^5 - 10^6 M_\odot$, with a moderate spin value of $a \approx 0.6$. A smaller black hole mass would not produce such a small precession period, while a larger black hole mass would result in many more precession cycles than observed.

We have also investigated the mechanism responsible for alignment. SL have proposed that alignment is associated with disc cooling, which brings the disc into the diffusive warp propagation regime, where the Bardeen-Petterson effect occurs. In this case, the alignment timescale is expected to scale with viscosity as $\alpha^{-3/5}$. We have shown that such process is responsible for alignment only in a small region of the parameter space, for large black hole masses, low spins and low α values. For most of the cases considered, viscous dissipation of the warp is the leading alignment process, resulting in $t_{\rm align} \propto \alpha^{-1}$.

Indeed, a theoretical calculation of the alignment timescale using the viscous dissipation model by FL is in very good agreement with our time-dependent calculations.

However, the FL model is generally difficult to apply, since it requires a detailed knowledge of the disc shape and in particular of the twist, which is generally not known from observations. The simpler estimate of $t_{\rm align}$ by Bate et al. (2000) (Eq. (5.22)), which links the alignment timescale to the disc aspect ratio, Keplerian frequency and global precession rate evaluated at the outer disc edge, provides a good first order approximation to the actual alignment time, accurate to within a factor of a few.

This model can be used in conjunction with future TDE observations that show an early quasi-periodicity, in order to derive the main system parameters, such as the black hole mass and especially its spin.

Part II

Relativistic precession in Low Mass X-ray Binaries

Chapter 6

Low Mass X-ray Binaries

X-ray binaries (XRB) are double systems composed by a compact object, either a black hole (BH) or a neutron star (NS), that is accreting matter from a companion star by means of an accretion disc through either Roche-lobe overflow or strong stellar wind by the companion (e.g. Cyg X-1). In the first case, the onset takes place when the binary shrinks (due to the loss in angular momentum) so that the envelope of the companion expands filling the Roche-lobe. In either cases the gas forms an accretion disc around the compact object.

The majority of BH XRBs are transient systems (King et al., 1996), meaning that they alternate long quiescent periods with short ($\sim$ weeks to years, e. g. GRS 1915+105) outbursts showing variability on human accessible timescales (from milliseconds to years). During quiescence they are generally faint ($10^{-9} - 10^{-8} L_{\rm Edd}$) while the count rate increases by several orders of magnitude during an outburst (reaching X-ray luminosities of $0.1 - 1\, L_{\rm Edd}$ or above, e.g. GRS 1915+105 and V404 Cyg). the transient systems is called Low Mass X-ray Binary (LMXB) if the companion is a faint star with mass less than $1 M_{\odot}$ belonging to an older stellar population compared to that of High Mass X-ray Binaries.

During their outbursts they show large increases in luminosity (occasionally reaching or even exceeding the Eddington limit) and remarkable variations in their spectral and fast variability properties (Belloni et al., 2011; Belloni & Motta, 2016). The different states are defined based on the spectral properties of the source and on the inspection of the power density spectra (PDS), where changes in the fast time variability can be clearly observed. The most remarkable features detected in the PDS are narrow peaks known as quasi-periodic oscillations (QPOs), whose centroid frequency are thought to be associated with time scales in the accretion flow. The detailed classification of these features will be given in Section 6.4. The origin of QPOs is still under debate and several models have been proposed to explain their existence (see e. g. Motta 2016 for a review). However, it is commonly accepted that most QPOs originate in the vicinity of the black hole potentially offering an insight on the properties and motion of matter in a strong gravitational field.

6.1 Outburst mechanism

The mechanism that is believed to trigger the outburst in dwarf novae and LMXBs is the 'disc instability' or 'hydrogen ionization instability' (Lasota, 2001; Done et al., 2007). This involves both the disc thermal and viscous instability, which evolve on timescales $t_{\rm th}$ and t_{ν} respectively. The variations of T on scales $t_{\rm th}$ are much more rapid than

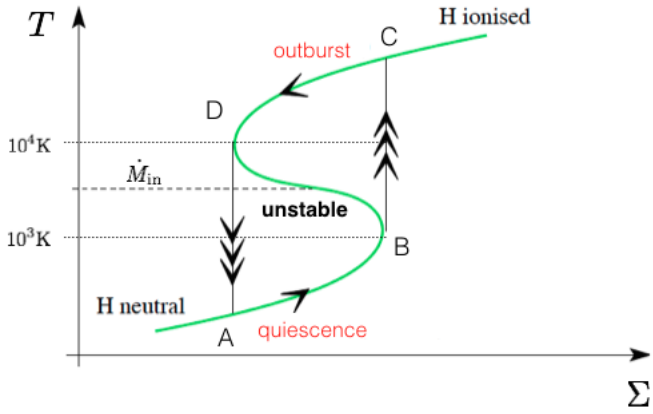

Figure 6.1: Hydrogen ionization instability. This shows the S-shaped relation between the disc temperature T and surface density Σ, at a given radius. The cycle ABCD is covered counterclockwise by the disc.

the variations in Σ on t_ν. The disc is unstable if $\partial T/\partial\Sigma < 0$, meaning that a small perturbation tends to increase the mismatch between the heating and cooling rate (Frank et al., 1992). This occurs at temperatures close to the hydrogen ionization temperature $T_{\rm H} \sim 6500$ K. Around $T_{\rm H}$ a temperature increase leads to significant increase of the disc opacity which prevents the dissipation of the radiation causing a further increase in T. In general the relation between T and Σ is S-shaped composed by an unstable central branch near $T = T_{\rm H}$ lying between two stable branches at lower and higher temperatures (see Figure 6.1).

The quiescent disc is being fed through mass transfer from the companion at a given accretion rate, $\dot{M}_{\rm in}$. The disc density increases and the disc heats up eventually triggering the H ionization instability. This corresponds to point B in Fig. 6.1. At this stage the disc needs to move to the closest stable branch of the S-curve, thus it jumps from point B to point C significantly increasing its temperature and starting the outburst. This increased mass accretion rate is maintained until the outer disc temperature drops below $T_{\rm H}$. This triggers a cooling wave that brings back the disc to quiescence (lower branch of the S-curve).

The inner disc in black hole X-ray binary systems is extremely luminous, meaning that irradiation might become important as well. The disc can thus remain hot even at large radii (van Paradijs, 1996) and stay in the upper branch. By heating the outer disc regions, X-ray irradiation prevents the propagation of the cooling wave that would switch off the outburst. The peak accretion rate is thus much higher than the mass transfer rate by the companion so the disc is drained by viscous accretion (King & Ritter, 1998). The accretion rate then becomes low enough so that irradiation cannot prevent the cooling front from propagating. Eventually, the irradiation plays no role and the cooling wave switches off the outburst on a local thermal timescale (Lasota, 2001).

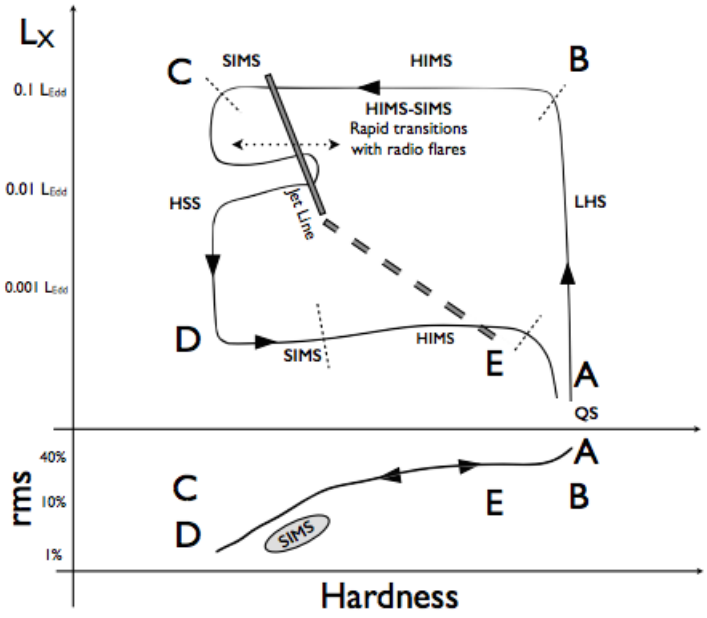

Figure 6.2: Stylized Hardness-Intensity Diagram (HID) and Hardness-Rms Diagram (HRD, see Section 6.3.1) for a black hole XRB outburst, with labels indicating the radio properties of the source. (Belloni & Motta, 2016).

6.2 Hardness Intensity Diagram (HID) and state changes

The changes in the spectral variability can be described through the Hardness-Intensity Diagram (HID) (Homan et al., 2001; Belloni et al., 2011; Belloni & Motta, 2016), where hysteresis loops can be identified (Miyamoto et al., 1992) and different branches of a q-shaped track roughly correspond to different spectra/timing states. The HID is both source and instrument dependent and can be used to describe the fast time variability properties of BHBs. Most active BH LMXBs show four main different states: the Low Hard State (LHS), High Soft State (HSS), Hard Intermediate State (HIMS) and Soft Intermediate State (SIMS). These states are shown in Figure 6.2 as branches of a q-shaped diagram traced counterclockwise by the source. In this diagram the total count rate is plotted as a function of the spectral hardness (ratio of observed counts in two energy bands, hard and soft).

Fig. 6.2 upper panel shows the HID path with a clear hysteresis cycle. The two vertical branches (A to B and C to D) corresponds roughly to the LHS (right) and HSS (left) respectively that have been identified before the *RXTE* era. The right vertical branch is observed at the beginning and at the end of an outburst, never in the middle. This branch is not exactly vertical but softens as the flux increases instead. The left branch typically shows some excursion back to other states as well as intrinsic variability of the hard spectral component. The horizontal branches (B to C and D to E), identified as intermediate regions, correspond roughly to the HIMS and SIMS. The transition from the LHS to the HSS occurs along these two branches at two different flux levels. In the intermediate states the most dramatic changes in the timing properties are observed.

The LHS is reached at the beginning and at the end of an outburst. The energy spectrum is dominated by Comptonized emission and it is hard. This state is characterized by very high variability ($> 30\%$ in rms). In general, as the flux increases the total fractional variability decreases (see bottom panel in Fig. 6.2). This variability has the form of a broad-band noise made of a few components with characteristic frequencies that increase with luminosity.

After the LHS (and before returning to it after the whole outburst) usually the source experiences a transition to the HIMS, identified with the horizontal branches at high and low flux. Here the spectrum is softer with respect to the LHS and a thin accretion disc starts contributing to the X-ray emission above 2 keV. The fractional rms decreases to roughly 10% and the spectrum is dominated by a weak band-limited noise and a type-C QPO (also present in the LHS). The frequency of the QPO is anti-correlated with hardness and correlated with the photon index of the hard spectral component.

When both the hardness and fractional rms drop below a certain threshold, the source enters the SIMS and produces a spectrum similar to the one in the HIMS but with different timing characteristics and noise shape. Here type-B QPOs appear with a frequency (~ 6 Hz) that correlates with the hard X-ray flux (Motta et al., 2011). The fractional rms drops below 10%. The spectrum lacks the high energy cutoff observed in the HIMS. These intermediate states can be also identified by looking at the central part of the Rms-Intensity Diagram (RID) (Muñoz-Darias et al., 2011).

Leaving the SIMS the source goes to the HSS, identified by the leftmost branch in the HID. Here the thermal emission from an accretion disc dominates the spectrum and the variability is very low. In this state also low-frequency QPOs can be detected, identified with type-C QPOs.

A few sources have also shown an *anomalous* or ultra-luminous state (ULS), in which the luminosity is significantly higher with respect to the other states (see, e.g., Belloni 2010; Done & Kubota 2006; Motta et al. 2012). While the hard states are characterized by higher variability ($30 - 40\%$ rms in the LHS and $5 - 20\%$ rms in the intermediate states), the variability in the ULS and in the HSS is very low (around and below 5% rms, respectively).

Even though the basic states and their properties can be defined for all systems, not all transients show a regular evolution pattern through such states. Intermediate minor transition between states can be observed. In some sources the initial LHS is so fast that it is not observed while some other sources never leave the LHS. Other sources reach the HIMS but without showing a transition to the soft part of the diagram (Capitanio et al., 2009; Motta & Belloni, 2010). The level at which the LHS to HIMS transition takes place can vary in different outburst of the same source, but it is always higher than the reverse transition (Maccarone & Coppi, 2003; Dunn et al., 2010). One important transition is the one between the two intermediate states since it appears to be associated to the launch of relativistic jets (Fender et al., 2009).

6.3 X-ray Energy spectra of XRBs

The change in the spectral properties during a source outburst can be explained by the so-called *truncated disc model* (Ichimaru, 1977; Esin et al., 1997; Poutanen et al., 1997; Done et al., 2007; Ingram et al., 2016). In the hard states the geometrically thin, optically thick accretion disc (Shakura & Sunyaev, 1973) is truncated at a radius significantly larger than the ISCO. The disc is filled in with an inner hot, geometrically thick, accretion flow.

As the accretion rate increases to make the source brighter, the truncation radius moves closer to the black hole. The inner flow is thus cooled by comparatively cool disc photons, leading the spectrum to soften and the disc contribution to become important in the spectrum. The ratio of the electrons power over that of the seed photons illuminating them $L_{\rm h}/L_{\rm s}$ determines the energy balance between heating and cooling and therefore constitutes a fundamental parameter to understand thermal Compton scattering since it sets the electron temperature.

At low luminosities, the inner optically thick disc is replaced by the hot flow probably due to evaporation (Meyer & Meyer-Hofmeister, 1994; Mayer & Pringle, 2007). Since there are few photons from the disc illuminating the flow, Compton cooling of the electrons (due to the relatively cold photons) in the vicinity of the black hole is not very efficient compared to the heating from the collisions with protons. Therefore, in the LHS ($L_{\rm h}/L_{\rm s} \gg 1$), the spectrum is dominated by a hard power-law tail with photon index $\Gamma < 2$ that breaks at low and high energies, produced via Compton up-scattering of the few seed photons from the outer disc by the cloud of hot electrons (Haardt & Maraschi, 1993; Sunyaev & Titarchuk, 1980; Done et al., 2007).

The spectrum often shows a high energy cutoff that has been seen to move to lower energies as the flux increases in a couple of sources (GX 339-4 and GRO J1655-40). In a few sources a hot thermal disc has been detected, suggesting that the inner disc radius could be always close to the innermost stable orbit (Saito et al., 2007; Kubota & Done, 2004). Sometimes also a non-thermal component is present in the spectrum, associated with the synchrotron radio jet. The low and high energy cutoff in the spectrum are associated with the seed photon temperature and the electron temperature respectively.

As the source brightens, the flow becomes optically thick and gradually collapses into a Shakura-Sunyaev disc that reaches the ISCO in the HSS. The decrease in the disc truncation radius leads to softer spectra ($\Gamma \sim 2$), to higher frequencies in the PDS and to faster jets as well. In the intermediate states the spectrum shows the contributions from both the accretion disc and the Comptonized emission. This means that the characteristics of the spectra come from both the hard component and the component typical of the soft states. These types of spectra are usually observed during the HIMS and SIMS. In GX 339-4 (Motta et al., 2009) and GRO J1655-40 (Joinet et al., 2008) the energy cutoff is observed to suddenly increase again in the HIMS reaching its maximum in the SIMS.

In the HSS the accretion disc is believed to have reached the innermost stable circular orbit and this leads to dramatic changes in both spectral and time domain. This includes also a significant decrease in the radio flux. Any remaining electrons which gain energy outside of the optically thick disc are subjected to a stronger Compton cooling leading to $L_{\rm h}/L_{\rm s} \leq 1$. The spectrum in the HSS is thus softer and Comptonized, characterized by a strong disc contribution and a soft tail with $\Gamma > 2$ extending beyond 500 keV (Gierliński et al., 1999). The hard component extending to higher energies is believed to be produced by Compton scattering on a non-thermal electron population.

As stated above, some source experiences an "ultra-luminous" state where the energy spectrum appears dominated by a soft disc component that allows to infer a high inner disc temperature associated to a small disc inner radius. The hard component is steep and faint.

Alternative geometries proposed so far have significant problems in matching the observed features of spectra in the hard states. Markoff et al. (2001) proposed a model where the hot electrons are located at the base of a jet. The hard X-rays and radio flux are produced via synchrotron emission from the high energy fraction of the non-thermal

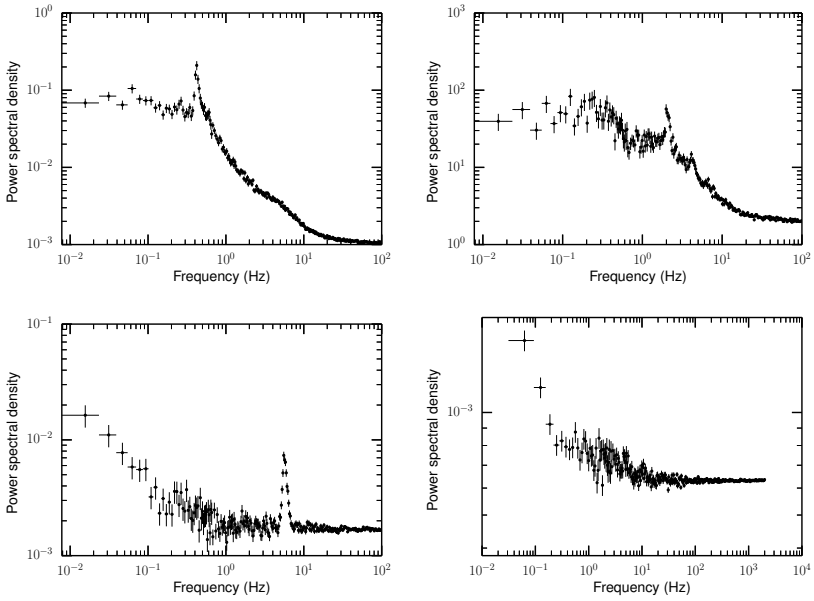

Figure 6.3: Power spectra in the low hard, hard intermediate, soft intermediate and high soft state respectively for the source GX 399-4.

electron population. However the high energy cutoff in the hard states is too sharp to be explained with synchrotron models (Zdziarski et al., 2003). Therefore (Markwardt & Swank, 2005) proposed a model where the X-rays are produced via Comptonization off thermal electrons at the base of the jet, while the radio emission comes from non-thermal electrons that are accelerated by the jet itself. This model is compatible with the truncated disc with some additional beaming of the hard X-rays (Belloni & Motta, 2016).

Fig. 6.3 shows four type of power density spectra in the four states experienced by the source GX 339-4 during an outburst: LHS, HIMS, SIMS and HSS respectively.

The first panel shows a type-C QPO in the PDS at around 0.4 Hz that is the typical frequency at which this type of QPOs appear in the LHS. The PDS in the second panel shows a type-C QPO as well, at around 2 Hz while the one in the third panel shows a type-B QPO at 5.7 Hz. The last panel shows a soft state PDS with very low variability level and a type-C QPO at 10.6 Hz that was detected by Franchini et al. (2017) (see Chapter 7).

From the evolution of the spectrum observed during the transition from the hard to the soft state it became clear that the different components are linked together, so that their frequencies all increase as the spectrum softens (van der Klis, 2004). The most obvious correlation is the one between the LF QPO and the low frequency break in the continuum noise power $\nu_{\rm b}$, below which the PDS is frequency independent (Done et al., 2007). These frequencies change such that $\nu_{\rm LF} \sim 5\nu_{\rm b}$ (Wijnands et al., 1999).

These findings support the truncated disc model. The existence of characteristic frequencies in the PDS shows that a particular radius is chosen by the variability and the fact that these frequencies experience shifts shows that this radius must also move, as predicted by the truncated disc/hot inner flow models. The truncated disc model has

several characteristic frequencies. The lowest is usually associated to the viscous timescale of the inner edge of the thin disc. This acts as a filter for slow fluctuations in the mass accretion rate and suppress any faster one owing to the inability of the disc to respond to them (Done et al., 2007; Ingram et al., 2009). The break frequency $\nu_{\rm b}$ sweeps from 0.03 to 0.2 Hz if the thin disc inner radius decreases from $20R_{\rm g}$ to $6R_{\rm g}$ during the transition from the hard to the soft state. Thus by measuring the frequency of the break in the continuum noise power, the inner edge of the truncated disc can be inferred.

Another possibility is to determine the disc truncation radius using the low frequency QPO. This is correlated to the frequency of a bump sometimes present in the spectrum at higher frequencies. Even if this bump is not observed, the detection of the LF QPO allows to place tighter constraints on the disc radius.

These two independent methods to infer the inner edge of the truncated disc using the frequencies contained in the PDS give the same result that is quantitatively as predicted by the changing geometry model for spectral transition with the disc reaching the ISCO in the soft state.

The truncated disc model can also explain the changes in the shape of the PDS. According to this model all the fluctuations produced at the truncation radius have to propagate through the inner hot accretion flow. Thus the truncation radius produces a spectrum of fluctuations that are further modulated when they propagate into the inner flow. In particular the viscous time at the inner edge of the accretion flow (i.e. the ISCO) acts as a low pass filter at a frequency $\nu_{\rm max}$ The observed power spectrum is then a result of the spectrum of the intrinsic fluctuations multiplied by that of the low pass filter. This filtering fixes a maximum frequency $\nu_{\rm max} \sim 5$ Hz above which the power spectrum is constant, as seen in the data (Done et al., 2007).

6.3.1 Rms as a tracer for different spectral states

The amount of variability (rms) is a very useful observable that is seen to vary along the outburst because the relative contribution of each spectral component depends on the accretion rate. Variability is mainly associated with the hard component rather than the thin accretion disc.

The lower panel of Fig. 6.2 shows the Hardness Rms Diagram (HRD) where the fractional rms variability integrated over a broad range of frequencies is plotted against the hardness (Belloni, 2010). The HRD constitutes a powerful tool for the study of the outburst evolution of transient XRBs in general, especially BH X-ray binaries. The fundamental property that becomes clear in this diagram is a positive correlation between hardness and rms observed across the whole outburst. Unlike the HID, this diagram does not show any hysteresis cycle. The majority of the points follow a correlation over a single line from the softest points with variability $< 5\%$ to the hardest points exceeding 30%. Sources that display an hysteresis loop in the HID do not show it in the HRD where the correlation is the same for both the upper and lower branch.

The LHS is characterized by a flat and soft (rms decreasing with energy) spectrum. Flat rms spectra can be explained considering that variability arises from variations in the normalization of one single spectral component. The soft part is investigated by looking at the variations in the spectral shape of the component. A considerable change in the shape of the rms spectra is observed along the HIMS. This hardens as the system approaches the soft states on a fast timescale. Hard rms spectra are observed in soft states.

The rms is also a good tracker for LFQPOs (see Section 6.4). Plotting this variable versus the centroid frequency of a QPO from the same observation allows to distinguish between different types of QPOs, which generally form distinct groups in an rms versus frequency plot.

In order to better understand the relation between the QPOs and accretion states, the rms can be plotted against the source intensity (counts/s) in the so called Rms-Intensity diagram (RID) (Muñoz-Darias et al., 2011). The RIDs from BH sources show hysteresis loops below a certain luminosity and a high rate horizontal branch above this threshold. Muñoz-Darias et al. (2011) followed several outbursts of the source GX 339-4 and traced the correspondent RID. The location of the spectral states is rather precise in this diagram. At the beginning and at the end of all outbursts, in correspondence of the LHS, the rms increases with the count rate forming the so-called 'hard line'. The rms then starts to decrease while the flux is still increasing and the system leaves the hard line. Then a sudden increase in luminosity is observed but at almost constant rms. Muñoz-Darias et al. (2011) associated this increase to an optically thick accretion disc with a low variability level. The central part of the RID identifies the two intermediate states (HIMS and SIMS) where the total fractional rms decreases. In the soft state the observation follow a soft branch that is very different from the hard line showing a variability level lower than $\sim 5\%$ and much more scatter.

6.3.2 Emission at longer wavelengths

X-ray binaries emit in a very broad range of energies, from the radio to hard X-rays and sometimes even γ-rays (Fender & Muñoz-Darias, 2016). Observations of accreting stellar mass black holes at longer wavelengths have led to the discovery of other processes such as relativistic jets. Relativistic jets in X-ray binaries have been observed in the infrared and radio bands. The radio emission offers insights on the synchrotron radiation related to relativistic jets (Fender et al., 2010) while in the IR, optical and UV bands the thermal emission from the companion star and from the disc outer parts can be observed (Homan et al., 2005; Russell et al., 2006; Migliari et al., 2007).

The properties of the observed radio emission correlates with the position of the source in the HID. During quiescence a weak flat spectrum radio emission is observed. When the source brightens in the LHS, the radio luminosity increases as well while the radio spectrum remains flat. In a few sources a compact radio jet has been detected in this state. The radio luminosity of these jets shows a strong, non-linear correlation with the X-ray luminosity (Gallo et al., 2003).

A breakdown in the correlation between radio-IR and X-ray flux marks the transition from the LHS to the HIMS (Fender et al., 2004; Homan et al., 2005). The spectrum becomes more an more dominated by an optically thick accretion disc and the radio emission shows non-monotonic variations (Fender et al., 2004). As the source moves along the HIMS approaching the SIMS, the radio emission decreases, the radio spectrum steepens (Fender et al., 2004) and a radio jet is detected around the time of the transition (Fender et al., 2009) (marked by the 'jet line').

During the HSS no radio emission that can be traced back to the central source has been detected so far. Outflows in the form of winds can be observed. At high luminosity, multiple transitions to the SIMS/HIMS and back might occur (Belloni, 2005; Casella et al., 2004; Belloni, 2010; Fender & Belloni, 2012). The observations are consistent with the presence of weaker radio flares corresponding to these transitions (Brocksopp et al., 2002; Casella et al., 2004). When the source moves back towards the hard part of the

HID the radio emission becomes detectable again but at a higher hardness value than the one at which it disappeared during the first horizontal branch.

Since the accretion disc contributes to the flux in the IR and optical, estimating the jet contribution for establishing a correlation is all but straightforward. In GX 339-4 a correlation between the IR and X-ray flux has been found in the LHS, ending with the transition to the HIMS. The study of several different sources led to the conclusion that there is a correlation between the fluxes in different bands extending from quiescence to bright LHS, similar to that observed in the radio band.

6.4 Quasi-Periodic Oscillations (QPOs)

QPOs have been detected basically in every kind of accreting sources such as CVs, ULXs and AGN. Since they are detected in the X-rays, the reasonable assumption is that they are produced very close to the central compact object, thus they offer insights on the behaviour of matter in a strong gravitational field. These features are normally associated with different spectral states, thus they can give a hint on the underlying physical conditions that produce these states.

6.4.1 Classification

QPOs are usually divided in two groups based on their frequency: low frequency and high frequency (LFQPOs and HFQPOs, respectively). LFQPOs have frequencies typically varying from a few mHz up to ~ 30 Hz and are further divided into three types - type-A, type-B and type-C - based on their properties (e.g. peak frequency, width, energy dependence and phase lags) and on the associated broad band noise in the PDS (shape and total variability level, Wijnands et al. 1999, Casella et al. 2005, Motta et al. 2011).

Fig. 6.4 shows an example of LFQPOs in the PDS of the very well sampled accreting black hole candidate GX 339-4.

Type-A

Type-A QPOs are the less common kind of QPOs in BH X-ray binaries. According to the classification of Homan & Belloni (2005), they are commonly found in the SIMS. However, more recent works (Belloni et al., 2011; Motta, 2016; Belloni & Motta, 2016) placed this type of QPOs in the HSS, since they typically appear at total fractional rms below 5% in BHBs. They usually appear close in time to a type-B QPO (see next Section). They are characterized by a weak (few percent rms) and broad ($\nu/\Delta\nu \leq 3$) peak around $6 - 8$ Hz without subharmonics or harmonics of the second or higher order. A very low amplitude red noise is usually associated with a type-A QPO. Since the number of detection is pretty low, it is difficult to find an explanation for these kind of QPOs. There is only one model that attempts to describe the origin of type-A QPOs. This is based on the accretion ejection instability and its interaction with Rossby waves (Tagger & Pellat, 1999). The Rossby waves instability can arise if there is an asymmetric bump in the inverse potential vorticity (Lovelace et al., 1999). In the presence of a large scale vertical magnetic field, which is to be expected in some accretion discs around Kerr black holes, Tagger & Pellat (1999) found that the condition for the instability is violated. The magnetic Rossby wave instability predicts outflows of energy and angular momentum via Alfven waves from the disc corona vortices. The outflows from rotating vortices are thought to constitute an explanation of QPOs according to this model.

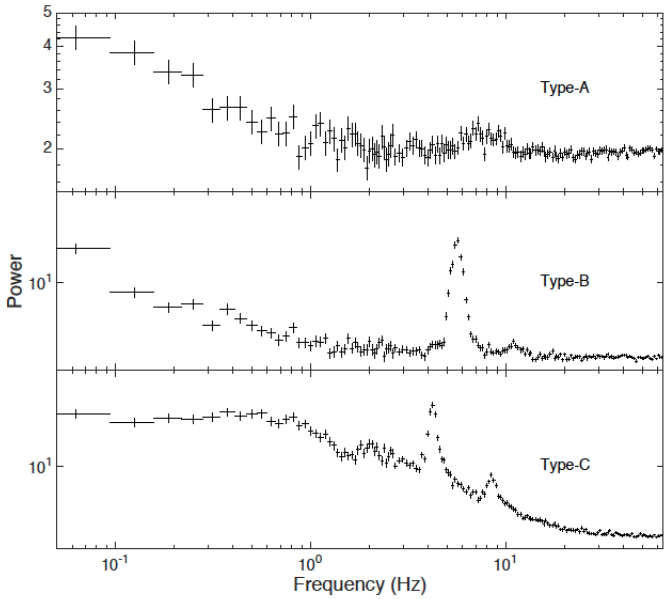

Figure 6.4: The upper, middle and lower panel show type-A, type-B and type-C QPOs respectively of the accreting source GX 339-4. Taken from Motta et al. (2011).

Type-B

Type-B are only seen in the SIMS (which is defined by their presence, Belloni & Motta 2016). They are characterized by a relatively strong (4% rms or higher) and narrow ($\nu/\Delta\nu \geq 6$) peak around 6 Hz (Motta et al., 2015). This type of QPOs might appear with a weak second harmonic and a subharmonic peak which can have a higher amplitude and lower FWHM than the first peak in a few cases (Casella et al., 2004). Type-B QPOs in BH XRBs have been associated with relativistic jets during the transition from the hard to the soft state (Fender et al., 2009). Furthermore, Motta et al. (2015) have shown that the intrinsic power of type-B QPOs is higher for sources with an accretion disc slightly inclined with respect to the line of sight. This supports the theory according to which they are associated with the launch of jets since there is no obvious mechanism that would be stronger for face on sources.

Type-C

The third type of LFQPOs are the most relevant QPOs for the work presented in this thesis. Type-C QPOs can be detected essentially in any spectra/timing state (including the ULS, Motta 2016), even though they are strongest in the LHS and HIMS. They are characterized by a strong (up to 20% rms), narrow ($\nu/\Delta\nu \geq 3$, but often much larger) and variable peak (its frequency and amplitude varying by few orders of magnitude, depending on the source, during an outburst; see, e.g., Motta et al. 2015) superposed on a flat-top noise that steepens above a frequency comparable to the centroid frequency of the QPO. Type-C QPOs appear at low frequencies (from a few mHz up to tenths of Hz Motta et al. 2011) in the hard state where the disc is thought to be truncated at a large radius (tens

to hundreds of R_g). They increase in frequency during the transition from the hard to the soft state, reaching their maximum in the HSS, where they show frequencies up to 30 Hz (Motta et al. 2014b, Motta et al. 2014a). Often they are detected together with a subharmonic, a second and even third harmonic peak. The rms of the QPO together with the flat top noise can reach up to 40%. Several models have been proposed to explain type-C QPOs, either based on instabilities in the accretion flow or on geometrical effects (see Section 6.5).

Titarchuk & Fiorito (2004) proposed a model based on the existence of a bounded compact coronal region. The existence of this region is a natural consequence of the adjustment of the Keplerian disc flow to the innermost sub-Keplerian boundary conditions near the central object and ultimately leads to the formation of a transition layer (TL) between the adjustment radius and the innermost boundary. In the TL model for the corona, the type-C QPO is related to the transition layer normal (i.e. a "breathing" mode) mode magneto-acoustic oscillation frequency.

Another model to explain both type-C QPOs and the associated broad band noise was developed by Cabanac et al. (2010). The corona oscillates due to the propagation of magneto-acoustic waves. This causes a modulation of the Comptonization efficiency on embedded photons that should produce the type-C through resonance effect and the noise.

Tagger & Pellat (1999) proposed the accretion ejection instability (AEI) as a model to explain LFQPOs. This is a spiral instability of the disc which is driven by the presence of a magnetic of moderate (of the order of equipartition with the gas thermal pressure) amplitude. It belongs to the same class as galactic spirals, driven by self-gravity or the Papaloizou-Pringle (Papaloizou & Pringle, 1985) instability, driven by pressure forces. Tagger & Pellat (1999) showed that the instability can be fed by coupling between the spiral and a Rossby wave at its corotation radius (the radius where the wave rotates at the same velocity as the gas) due to differential rotation. The Rossby wave stores the energy and angular momentum it extracts from the disc at corotation. This exchange makes the perturbation unstable and maintains the instability. According to the model based on the AEI, type-C QPOs are produced in the non-relativistic regime where the RWI does not play any significant role (Varnière & Tagger, 2002; Varnière et al., 2012). Varnière & Tagger (2002) also explained the turnover in the correlation between the disc inner radius and the LFQPO frequency by taking into account relativistic effects.

Ingram et al. (2009) proposed a model based on relativistic precession of a radially extended portion of the hot inner accretion flow that produces a modulation of the X-ray flux. This model is discussed below in Section 6.5.

HFQPOs

The first high frequency QPO in a BH XRB was detected in the bright system GRS 1915+105 at around 67 Hz in the *RXTE* data (Morgan et al., 1997). HFQPOs are fairly rare in BH binaries (while they are commonly observed in NS systems, where they are referred to as kHz QPOs, see van der Klis 2006) and have been detected only in a few sources (Belloni et al., 2012). Only in the source GRS J1655-40 two simultaneous, therefore different high-frequency QPOs have been detected and called lower and upper HFQPO respectively (Strohmayer, 2001; Motta et al., 2014b). HFQPOs seem to appear preferentially in the HSS and in the ULS, even though observational biases could be at play because of the low number of detections currently available. They appear almost

only at high accretion rate but their properties can vary significantly even when all other observables do not change (Motta, 2016). HFQPOs can be seen as either single or double peaks with a typical fractional rms of 0.5-6% increasing steeply with energy. Quality factors (ratio between centroid frequency and FWHM of the QPO peak) are around 5 for the lower peak and 10 for the upper (Motta, 2016).

There are at least three models that aim to describe the origin of HFQPOs.

According to the warped disc model by Kato (2004b, 2005b) HFQPOs are disc oscillations excited by a resonant process. They superpose on the disc oscillations that might have resonant interaction with the disc at specific radii through non-linear coupling with the warp. Kato (2004a) explained HFQPOs in a pair with frequency ratio close to $2:3$ using this model. Kato (2005b) extended the model to precessing discs around rotating compact objects while spin-induced perturbations were included by Kato (2005a).

Abramowicz & Kluźniak (2001); Kluzniak & Abramowicz (2001) proposed the nonlinear resonance model based on non linear 1:2,1:3 and 2:3 resonances between the vertical and radial epicyclic motions. Abramowicz et al. (2004) then proposed the Keplerian nonlinear resonance model that assumes the resonance to occur between the radial epicyclic frequency and orbital frequency. These models successfully explain black hole QPOs with frequency ratio 2:3 or 1:2. Since the resonance occur at a specific radius, the QPO frequencies are expected to either remain constant or to jump from one resonance to another according to this model.

The third model, which is the one that we consider in this thesis, is the Relativistic Precession Model (RPM), described in Section 6.5.

6.5 Modelling type-C and HF QPOs

The truncated disc model (Ichimaru, 1977; Esin et al., 1997; Poutanen et al., 1997) requires a geometrically thin accretion disc (Shakura & Sunyaev, 1973) truncated at some radius filled in with an inner hot accretion flow that is able to rigidly precess around the compact object spin axis. According to this model type-C QPOs are produced by the Lense-Thirring precession of a radially extended region of the hot inner accretion flow that produces a modulation of the X-ray flux due to several processes (Ingram et al., 2009). Since the flow has an optical depth $\tau \sim 1$, there can be weak projected area effects. The flow can also self-occult causing a dip in the flux when the flow is aligned with the line of sight. Another important effect is the variation in the number of seed photons from the outer Shakura-Sunyaev disc which gives a maximum flux when the misalignment between the flow and the disc reaches its maximum. Relativistic beaming can also contribute to the modulation of the X-ray flux (Schnittman et al., 2006).

These effects would give stronger modulation for either larger inclination angles or higher optical depths. Indeed, the maximum QPO rms strength increases with inclination and with the mass accretion rate.

The associated broad-band noise would be produced by variations in the accretion rate from the outer regions. These variations propagate towards the central object producing a modulation in the inner regions as well modulating also the radiation. This modulation depends on the inclination (Ingram & van der Klis, 2013).

Figure 6.5 shows the geometry described by the truncated disc model (Ingram et al., 2009). The grey inner accretion flow is expected to rigidly precesses around the black hole spin axis producing the QPO while the outer thin disc keeps its alignment with the binary companion.

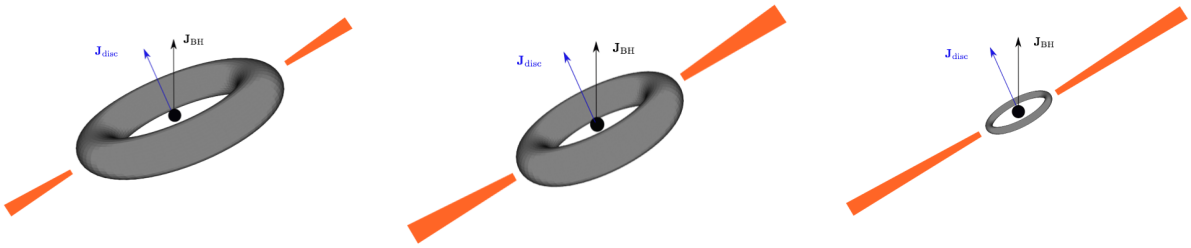

Figure 6.5: Schematic view of the geometry described by the truncated disc model in the LHS (left panel), SIMS and HIMS (middle panel) and HSS (right panel). The inner geometrically thick accretion flow (grey with blue angular momentum) precesses around the black hole angular momentum vector $\mathbf{J}_{\rm BH}$ while the outer disc (orange) keeps the alignment with the binary companion. The flow extends from the ISCO to the truncation radius which moves inward during the transition from the hard to the soft state.

The QPO frequency is a weighted average of the free precession frequencies at the various radii (see Eq. 3.6). However, for the disc to precess rigidly, its radial extent must be narrow (tens of $R_{\rm g}$) (Lodato & Facchini, 2013b; Franchini et al., 2016; Nixon et al., 2016). In particular, in the HSS, where the accretion disc inner radius is expected to be close to or coincident with the innermost stable circular orbit (ISCO, e.g. Dunn et al. 2010), the inner hot (geometrically thick) accretion flow is expected to be extremely narrow (its outer radius determined by the inner thin disc truncation radius). Therefore, its precession frequency is reasonably well described by that of a test particle orbiting at the ISCO. In the HSS and in particular close to the ISCO, a good approximation to this rigid precession model is offered by the RPM (Ingram & Motta, 2014).

The RPM has been originally proposed by Stella & Vietri (1998); Stella et al. (1999) and was recently revisited by Motta et al. (2014b,a); Ingram & Motta (2014), to explain three types of QPOs: type-C QPOs, the lower and the upper HFQPOs. In the RPM, the centroid frequency of three different types of QPOs is associated with the frequencies of a test particle orbiting a spinning black hole, as predicted by the theory of General Relativity. The Lense-Thirring (LT) frequency is associated with the type-C QPO, the periastron precession frequency with the lower HFQPO and the orbital motion corresponds to the upper HFQPO. The RPM predicts that the expected values of these frequencies depend solely on the fundamental parameters of the BH, i.e. mass and spin, and on the radius at which the particle motion occurs (i.e. where the QPOs are produced). Based on this fact, once a type-C QPO and two HFQPOs are observed simultaneously, a precise measurement of the fundamental parameters of the black hole, spin and mass can be inferred (Motta et al., 2014b). The spin can also be measured when only two simultaneous QPOs of the relevant types are detected and an independent mass measurement, for instance determined dynamically, is available (Motta et al., 2014a). If the mass is unknown, the RPM still allows to place limits on the mass and spin of the black hole (see Ingram & Motta 2014 and Chapter 7).

Chapter 7

Constraining black hole spins using type-C QPOs in soft states

Based on the paper by **Alessia Franchini**, *Sara Elisa Motta and Giuseppe Lodato: "Constraining black hole spins with low-frequency quasi-periodic oscillations in soft states " published in Monthly Notices of the Royal Astronomical Society, 467, 145-154 (2017).*

The measurement of the black hole fundamental parameters - mass and spin - is a major issue in astrophysics. While the mass can be estimated through often complex dynamical studies, the spin can only be inferred in an indirect way. In the HSS measurements of the spins can be obtained through X-ray spectroscopy by modelling the thermal disc emission in the spectrum (McClintock et al., 2011, 2014; Steiner et al., 2010, 2011, 2012). In the hard and intermediate states, the spin is instead measured by modelling the disc reflection spectrum, in particular by modelling the effects of the spin on the Iron-Kα line emission (Miller, 2007; Reynolds, 2013). Both methods rely upon identifying the inner radius of the accretion disc with the ISCO. In addition, for the spectral continuum method, one must also know the mass of the black hole, the inclination of the accretion disc (generally assumed equal to the inclination of the binary system) with respect to the line of sight and the distance to the binary. For these reasons, such methods are often affected by large systematic errors and in a few cases they have led to inconsistent values of the black hole spin when used on the same source (e.g. Shafee et al. 2006). The RPM is based only on measurements that can be inferred through very precise X-ray timing measurements (i.e. the precision of the measurement of a QPO centroid frequency is only limited by the time resolution of the data used, which is usually extremely high). Therefore, the RPM can be used to estimate black hole spins and masses independently from other methods.

In this work we applied the RPM to QPOs detected in the HSS, i.e. produced close or at the ISCO, in order to place limits on the black hole spin of a number of sources by making reasonable assumptions on the mass, when this is not known *a priori*.

7.1 Observations and data analysis

Based on Motta et al. (2015) we analyzed *RXTE*/Proportional Counter Array (PCA) archival observations of 12 transient BHBs showing QPOs. We selected those sources that showed a standard HSS among the 14 sources considered by Motta et al. (2015). We did also include observations in the ULS for those sources that showed this kind of state during their outbursts, i.e. GRO J1655-40 and 4U 1630-47. We excluded *Swift* J1753.5-0127 since it has not shown a HSS in the *RXTE* era (Soleri et al., 2013), and

XTE J1720-318, which did not show QPOs during the outburst observed by *RXTE*. We looked for QPOs in the HSS and in the ULS, where they are thought to be produced at or close to the ISCO (see Motta et al. 2012, Motta et al. 2015). We have also analyzed all the observations in the *RXTE* catalogue in the HSS and ULS that have not been included in Motta et al. (2014b,a, 2015). Then we added also the QPOs found in previous works.

We computed the PDS using a custom software under IDL in the total and hard energy band ($\sim 2-37$ keV, absolute channels 0-64, and $\sim 6-37$ keV, absolute channels 14-64, respectively). Since QPOs typically show a hard spectrum (Sobolewska & Życki, 2006) by producing the PDS using only hard photons we maximize the chances of detecting faint signals. The intrinsic variability of these signals could be diluted by the non-variable seed photons from the outer geometrically thin accretion disc, which dominates in the soft states and emits mostly below 6 keV. Since the efficiency of the PCA drops dramatically above ∼30 keV and the variability coming above this energy is mostly Poisson noise, we did not consider the photons above channel 64. In addition, in the HSS the energy spectrum is typically very steep, with very little or no signal above ∼20 keV. In a few cases we could not produce PDS in the hard band since the data modes did not allow it, therefore we only analyzed the total energy band PDS (channel 0-64 if available, otherwise channels 0-249). We used 16 s-long intervals and a Nyquist frequency of 2048 Hz to produce the single PDS and then combined them to get the averaged PDS. The PDS were then normalized following Leahy et al. (1983) and converted to square fractional rms (Belloni & Hasinger, 1990). We measured the integrated fractional rms (i.e. the rms from the entire PDS) in the 2-15 keV band and between 0.1 and 64 Hz. From now on, if not otherwise stated, by rms we refer to the integrated fractional rms.

We then inspected all the PDS selecting only those where we detect one or more narrow peaks and fitted them using the standard XSPEC fitting package with a one-to-one energy-frequency conversion and a unity response matrix. Following Belloni et al. (2002), we fitted the noise components with a number of broad Lorentzians and the QPOs with narrow Lorentzians [1]. A constant component was added to take into account the contribution of the Poisson noise. We estimated the statistical significance of these peaks and excluded all features with single trial significance below 3σ. We then considered also the number of trials in the calculation of the significance and we discarded all the peaks that resulted not significant after this analysis. We rejected also the peaks with quality factor (i.e. the ratio between centroid frequency and FWHM of the QPO peak frequency) $Q < 2$. Since in the HSS both type-C QPOs and HFQPOs can be seen, we classified the QPOs we found following Motta et al. (2011) and Motta et al. (2012).

7.2 The relativistic precession model: constraining the spin

The fundamental frequencies of a particle orbiting a spinning black hole are the Lense-Thirring precession frequency $\nu_{\rm LT}$, the periastron precession frequency $\nu_{\rm per}$ and the orbital frequency ν_ϕ. These are given by (from lowest to highest frequency):

$$\nu_{\rm LT} = \nu_\phi \left[1 - \left(1 \mp 4ar^{-3/2} + 3a^2r^{-2}\right)^{1/2}\right] \tag{7.1}$$

$$\nu_{\rm per} = \nu_\phi \left[1 - \left(1 - 6r^{-1} \pm 8ar^{-3/2} - 3a^2r^{-2}\right)^{1/2}\right] \tag{7.2}$$

[1] Type-C QPOs sometimes show significant harmonic content especially in the hard states. However, a single Lorentzian is always enough to fit type-C QPOs in the HSS.

$$\nu_\phi = \pm \frac{c^3}{2\pi GM} \frac{1}{r^{3/2} \pm a} \tag{7.3}$$

where r is the radius (in units of the gravitational radius $R_g = GM/c^2$) at which the frequencies are produced, a is the dimensionless black hole spin parameter, and M is the black hole mass. The signs refer to prograde and retrograde orbits, respectively.

According to the RPM, type-C QPOs are associated with the Lense-Thirring precession frequency, the lower HFQPO to the periastron precession frequency and the upper HFQPO to the orbital frequency. Under the hypothesis that when observed simultaneously, these frequencies are produced at the same radius r, the equations above - linking the black hole parameters (spin and mass) to the QPO centroid frequencies - form a system of three equations in six variables: $(a, M, r, \nu_\phi, \nu_{\rm per}, \nu_{\rm LT})$. Therefore, when a type-C QPO and two HFQPOs are detected simultaneously, the RPM system of equations can be exactly solved, obtaining precise values for a, M and r (Motta et al., 2014a,b).

In this work we assume that the highest frequency type-C QPO detected in the HSS or ULS for each source corresponds to the Lense-Thirring precession frequency of a test particle orbiting the black hole at the ISCO. The radius of the ISCO ($r_{\rm ISCO}$), as predicted by the theory of General Relativity, is only a function of the black hole dimensionless spin parameter (see, e.g., Stella & Vietri 1998). Therefore, substituting the expression of $r_{\rm ISCO}$ into the equations above, allows us to obtain equations that only depend on M and a. This implies that, if either the mass or the spin are known, one can obtain an estimate of the other parameter detecting just one QPO produced at the ISCO and using the related RPM equation evaluated at the ISCO. While black hole spin measurements can be obtained only indirectly and are often affected by large uncertainties, black hole masses can be inferred through dynamical studies. The literature includes to date mass measurements for a few tens of compact object in binary systems, including several stellar mass black holes. We can thus make reasonable assumptions on the mass range spanned by the black holes hosted in the systems of our sample. This means that, even without a dynamically determined black holes mass, we are able to place limits on the black hole spin using the RPM. In principle, this could be done with any QPO relevant for the RPM (type-C QPO, upper or lower HFQPO). However, type-C QPOs are much more common and easier to detect than HFQPOs and can be detected in basically all spectra/timing states (Motta, 2016), including the HSS and ULS.

In order to place limits on the spin in the cases where a dynamical black hole mass is not available, we choose a conservative range of masses: $3 - 20 M_\odot$ (Casares & Jonker, 2014). The lowest dynamically confirmed stellar mass black hole is GRO J1655-40, with $M = 5.4 M_\odot$ (Beer & Podsiadlowski, 2002). In a similar way, the upper limit is based on the fact that the heaviest dynamically confirmed stellar mass black hole in a Galactic binary system is the one in GRS J1915+105 (Reid et al., 2014), with a black hole of $12.4 M_\odot$. There is no evidence for heavier stellar mass black holes (even though a binary with two $30 M_\odot$ black holes has been recently detected through gravitational wave emission Abbott et al. 2016), therefore we assumed a conservative upper limit on the mass of $20 M_\odot$.

We explore the range between 3 and ~ 150 Hz for the LT frequency. The lower limit is chosen based on the observational evidence that all BHBs show type-C QPOs reaching at least 3 Hz (Motta et al., 2015). Indeed, it is worth noticing that a type-C QPO produced around an almost maximally spinning black hole (e.g. $a = 0.98$ obtained for GRO J1655-40 using spectroscopic methods) should have a frequency well above 100 Hz.

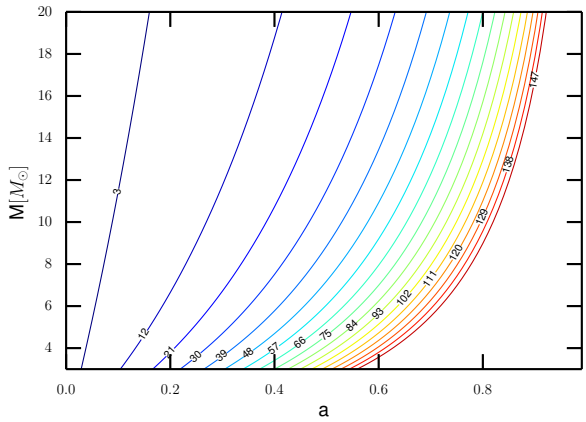

Figure 7.1: Couples of mass-spin values that give the LT precession frequency. The numbers are the frequencies evaluated in Hz. Each line is obtained numerically solving Eq. 7.1 assuming a frequency range from 3 to 147 Hz.

Since in principle a type-C QPO these high could be detected, we choose a wider range of frequencies to explore this possibility and in order to guarantee an unbiased analysis.

GRS J1915+105 shows HFQPOs around 67 Hz (Morgan et al., 1997) while the other sources show this type of QPOs above 150 Hz. Therefore we assumed the periastron precession frequency (and orbital frequency, coincident with the periastron precession frequency at the ISCO) to be strictly above 50 Hz and to reach 350 Hz tops since this is the highest observed HFQPO so far (Strohmayer, 2001; Belloni et al., 2012). We stress that, according to the RPM, it is possible to distinguish type-C QPOs from the HFQPO associated to either orbital or periastron motion since there is no mass-spin combination that gives the same frequency for both motions.

In Figure 7.1 we show the Lense-Thirring precession frequency $\nu_{\rm LT}$ evaluated at $r_{\rm ISCO}$ for every mass and spin couple within the ranges $3M_\odot < M < 20M_\odot$ and $0 < a < 1$ (i.e. we considered only prograde orbits). Note that for clarity we only show Lense-Thirring frequencies spaced by 9 Hz. For comparison, we also show in Fig. 7.2 the periastron precession frequencies at $r_{\rm ISCO}$ with the same spin and mass ranges.

In order to place limits on the spin value, we selected the highest frequency type-C QPO for each source (considering both the QPOs we found in this work and the QPOs reported in Motta et al. 2012, 2014b,a, 2015) and then solved Eq. (7.1) for the spin a after substituting the expression of $r_{\rm ISCO}$.

7.3 Results

7.3.1 QPO Classification

Plotting the total integrated fractional rms versus the centroid frequency of a QPO is a useful method for distinguishing different types of QPOs, which in a rms vs frequency plot are known to generally form different, well defined groups (see e.g. Casella et al. 2005, Kalamkar et al. 2011, Motta et al. 2012). In particular, type-C QPOs are known

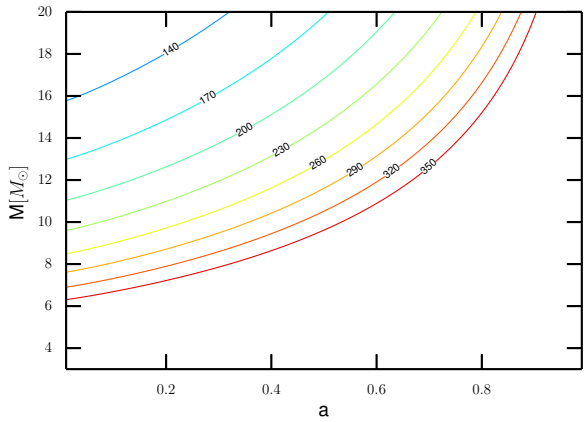

Figure 7.2: Couples of mass-spin values that give the periastron precession frequency. The exactly same plot is obtained considering the orbital frequency at the ISCO. Indeed, at the ISCO there is no radial oscillation in the frequency, thus $\nu_{\rm per} = \nu_\phi$. The numbers are the frequencies evaluated in Hz. Each line is obtained numerically solving Eq. 7.2 assuming a frequency range from 50 to 350 Hz.

to correlate well with the rms, forming a curved track in a frequency versus rms plane with rms decreasing for increasing frequency and breaking at ∼10 Hz (see Figure 7.3). The slope is always steeper for the high-frequency half of the correlation track (see, e.g., Motta et al. 2012 for the case of GRO J1655-40). HFQPOs, instead, form a different group of points at significantly higher frequencies and rms comparable to that of type-C QPOs found in the soft state, i.e. $\sim 1 - 5\%$ rms.

In Fig. 7.3, we plot the integrated fractional rms versus the centroid frequency of the QPOs for each source of our sample. We see that for most sources the QPO centroid frequency correlates well with the rms, forming the expected curved track. In the plot we mark with black dots the QPOs reported in Motta et al. (2012, 2014b,a, 2015) and with red stars the type-C QPOs found in this work.

Figure 7.4 shows a selection of PDS containing a type-C QPO detected in the HSS and in the ULS. From upper left to bottom panel, the PDS come from GX 339-4, 4U 1543-47 and GRO J1655-40 respectively. The first two QPOs are characterized by a strong and narrow peak at frequencies of the order of 10 Hz. The third is a small though significant (3.96 σ, single trial) peak at 27.5 Hz.

We report in Table 7.1 the properties of the new QPOs detected in this work: the ObsID, the centroid frequency, the quality factor and the integrated fractional rms.

Note that the total fractional rms measured for the observation where a given QPO was detected is always $\leq 5\%$, which shows that all these QPOs were detected in soft states. As noted elsewhere, this implies that the inner disc radius is close or coincident to the ISCO and the RPM can be applied to obtain a constrain on the spin of the central black hole.

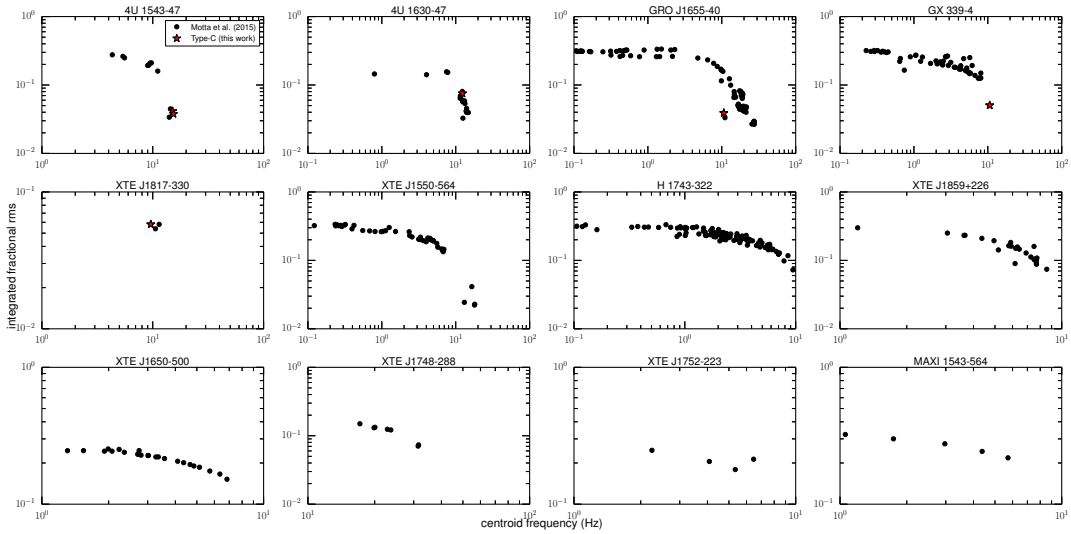

Figure 7.3: Integrated fractional rms versus QPO centroid frequency. Each point corresponds to a single *RXTE* observation. Each panel refers to a single source of our sample.

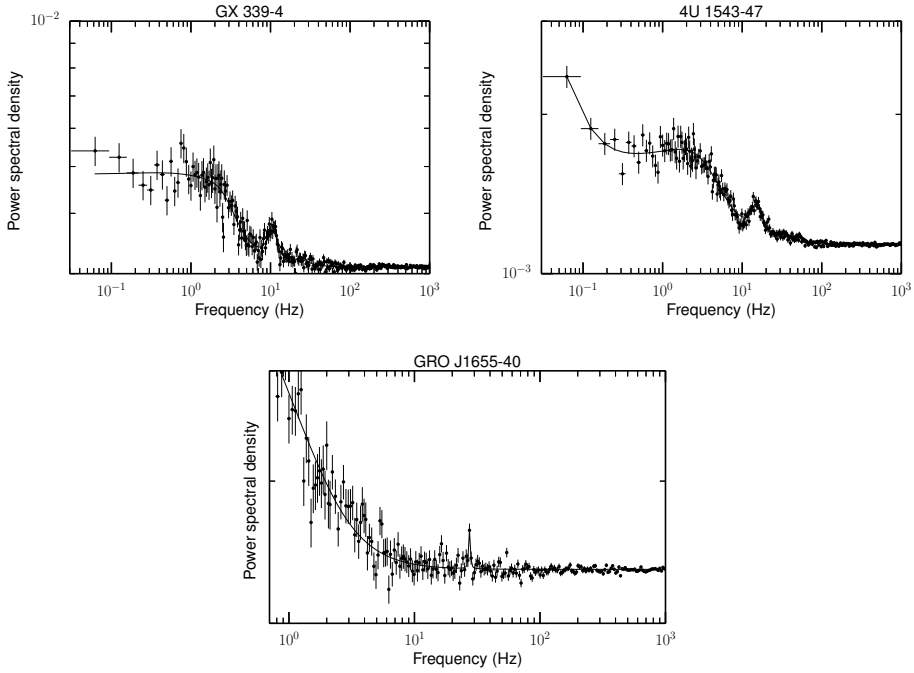

Figure 7.4: Upper panel: PDS obtained from observation 92085-01-02-03 of the source GX 339-4 during its outburst in 2007. The type-C QPO found at 10.6 Hz is clearly visible. Middle panel: PDS obtained from observation 70133-01-01-00 of the source 4U 1543-47. The type-C QPO found at 15.4 Hz is clearly visible. Lower panel: PDS obtained from observation 91702-01-17-10 of the source GRO J1655-40. There is a small but significant peak at roughly 30 Hz. This is the highest type-C QPO detected for this source.

ObsID	ν (Hz)	Q	rms
GX 339-4			
92085-01-02-03	10.59	3.46	0.05
4U 1630-47			
70417-01-09-00	12.3	2.15	0.033
4U 1543-47			
70133-01-01-00	15.37	2.57	0.042
70133-01-05-00	15.0	3.75	0.046
XTE J1817-330			
91110-02-32-00	9.6	2.93	0.057
GRO J1655-40			
10255-01-05-00	10.7	2.7	0.011

Table 7.1: Properties of the QPOs found in this work divided by source. For each QPO the first column contains the ObsID, the second is the centroid frequency, the third is the quality factor Q and the last one is the integrated fractional rms.

7.3.2 Evidence of QPOs in the soft state

It has been shown that for two sources in our sample, GRO J1655-40 and XTE J1550-564 (see Saito et al. 2007 for GRO J1655-40 and Kubota & Done 2004 for XTE J1550-564), the accretion disc inner radius remains constant for most of the HSS, providing a strong evidence for the accretion disc having reached the ISCO (see also Steiner et al. 2011, Motta et al. 2014b, Plant et al. 2014). It is worth noticing that the QPOs in the HSS of these two sources stand out in terms of very low total fractional rms and high Q factor (see Table 7.2). Given the behavior of the sources of our sample (and of transient black hole X-ray binaries in general) in the HIDs, it is reasonable to assume that the inner disc radius does indeed reach the ISCO any time a source is observed in the HSS, which is basically the same assumption used for the spin measurements based on spectroscopy (see e.g. McClintock et al. 2014 and references therein). Since the type-C QPOs detected in the ULS have frequencies very close to those observed in the HSS (see e.g. Motta et al. 2012), we extended this assumption also to the ULS. However we decided not to place upper limits using type-C QPOs in the ULS since they might be underestimated if the QPO was not produced at the ISCO. We describe in Section 7.3.3 the uncertainty in the spin estimate produced by using this assumption.

If the highest type-C QPO is detected in the HSS, we can assume that it was produced at the ISCO and thus place a lower and an upper limit on the spin assuming a lower and an upper limit for the mass. For those sources for which we did not detect a type-C QPO in the soft state, we can still use the highest frequency type-C QPO detected in other states to place a conservative lower limit to the spin assuming a lower limit for the mass since these QPOs probably corresponded to radii larger than the ISCO. In these cases an upper limit on the spin would be incorrect given our assumptions.

Fig. 7.5 shows the HIDs of the 5 sources that showed type-C QPOs in the HSS. The red dots represent the observations of the newly detected QPOs. By looking at these diagrams and at the rms values in Table 7.1 it is clear that the type-C QPOs in GX 339-4, 4U 1543-47 and XTE J1817-330 were detected in soft states. Instead the type-C QPOs in GRO J1655-40 and 4U 1630-47 have been detected in the ULS. We can reasonably assume that also in this state the accretion disc inner radius reaches the ISCO since the

frequencies of type-C QPOs in the ULS are very similar to those detected in the HSS. In the 4U 1543-47 HID we marked with red dots the two different type-C QPOs we detected that slightly overlap one another.

7.3.3 Constraining the spin

We placed lower limits on the black hole spin for each source of our sample as described in Section 7.2. For the sources with the highest type-C QPO detected in the soft state we did also place an upper limit (assuming an upper limit on the mass). We summarize the results obtained applying the RPM to our sample in Table 7.2. In the first column are listed the source names and the second contains the Obs-ID of the highest detected type-C QPO. The third, fourth and fifth columns contain the highest type-C QPO frequency, the quality factor and the total fractional rms, respectively. The sixth column indicates whether the highest type-C QPO was detected in this or in previous works. The last two columns contain the state in which the highest type-C QPO was detected and the spin limits obtained respectively.

We would like to stress that we performed a systematic search for type-C QPOs in the HSS and ULS. For those sources where we did not detect any type-C QPO in these states we used the type-C QPOs reported in Motta et al. (2015).

For most of the sources of our sample there is no independent mass measurement, thus we assumed the mass to lie in the range $3 - 20 M_{\odot}$. In a few cases, however, we have better constraints on the black hole mass and thus on the spin value. The lower limit for the black hole mass in GX 339-4 is $6 M_{\odot}$ (Hynes et al., 2003; Muñoz-Darias et al., 2008). Thus we can place a stricter lower limit on the spin value: $a_{\rm lower} = 0.16$. Since we are assuming black hole masses up to $20 M_{\odot}$, the upper limit for the spin of GX 339-4 is $a_{\rm upper} = 0.38$.

For both GRO J1655-40 ($5.31 \pm 0.07\, M_{\odot}$ Motta et al. 2014b) and XTE J1550-564 ($9.1 \pm 0.6 M_{\odot}$ Orosz et al. 2011) we have a good independent mass measurement. Using these dynamically estimated mass values, we can narrow significantly the spin range of values for the two sources (see Table 7.2). The spin values found by Motta et al. (2014b,a) ($a = 0.290 \pm 0.003$ for GRO J1655-40 and $a = 0.34 \pm 0.01$ for XTE J1550-564) are, as expected, in good agreement with the range we inferred using the RPM with the highest type-C QPO at the ISCO.

As mentioned above, there might still be the possibility that, even in the soft state, the disc does not extend down to the ISCO, but somewhere close to it. In this case, the QPO frequency can still be related to the spin of the black hole, because we expect that the hot inner flow would have a finite and small radial extent so that it would precess as a rigid body (Ingram & Done, 2011; Franchini et al., 2016). Thus, we can assume that the hot inner flow extends from the ISCO to an outer radius $R_{\rm out}$, and then compute the spin value that would reproduce a given QPO frequency using, for example Eq. (1) in Ingram & Done (2011). In this way, we can thus estimate the associated change in the spin value obtained from the RPM model, as a function of $R_{\rm out}$. For instance, using the highest type-C QPO detected in GRO J1655-40 (i.e. 27.51 Hz) together with the mass estimate for this source, we can evaluate the uncertainty with respect to the value obtained using the RPM. The results in this case are shown in Figure 7.6. The x-axis is the ratio between the outer radius of the inner accretion flow and the ISCO and the y-axis is the relative change in the spin value. A similar result holds also for different QPO frequencies.

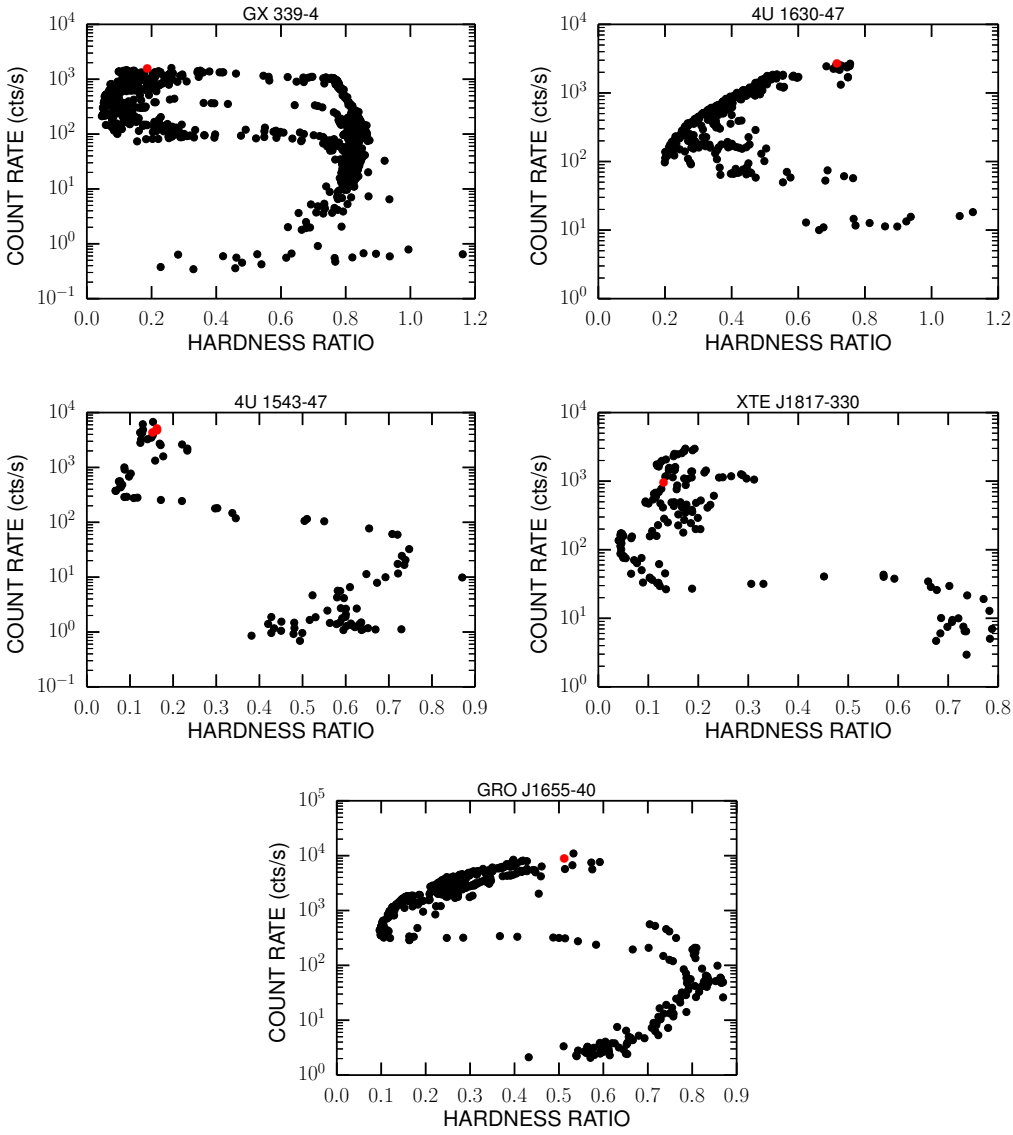

Figure 7.5: HID of the 5 sources with type-C QPOs in the HSS (GX 339-4, 4U 1630-47, 4U 1543-47, XTE J1817-330, GRO J1655-40). The red dots represent the observations that contain the type-C QPOs we found in this work. Note that the QPOs in GX 339-4, 4U 1543-47 and XTE J1817-330 were detected in soft states, while the ones in GRO J1655-40 and 4U 1630-47 were detected in the ULS. In the HID of 4U 1543-47 we marked the two different type-C QPOs we found with red dots.

Table 7.2: Spin limits inferred from the highest frequency type-C QPO at ISCO according to the RPM. Both limits are evaluated assuming a black hole mass in the range $3 - 20 M_{\odot}$. In the case of GX339-4 the lower limit corresponds to $6 M_{\odot}$. For XTE J1550-564 and GRO J1655-40 the limits correspond to the measured masses $9.1 \pm 0.6 M_{\odot}$ and $5.31 \pm 0.07 M_{\odot}$ respectively (Muñoz Darias et al., 2010; Motta et al., 2014a,b). The first column contains the name of the source, the second is the Obs-ID of the highest type-C QPO detected. The third, fourth and fifth columns contain the properties of the QPO, i.e. frequency and the Q factor, and the total fractional rms. The sixth column indicates whether the highest type-C QPO has been detected in this work or the previous ones. The seventh column indicates the state in which the QPO was detected and the last column contains the spin limits.

Target	Obs-ID	$\nu_{\rm max}$ (Hz)	Q	rms	New ?	state	spin limits
GX 339-4	92085-01-02-03	10.59 ± 0.18	3.46 ± 0.50	5.05 ± 0.03	yes	HSS	0.16 - 0.38
4U 1630-47	80117-01-07-01	14.80 ± 0.28	2.17 ± 0.27	9.5 ± 0.4	no	ULS	> 0.12
4U 1543-47	70133-01-01-00	15.37 ± 0.18	2.57 ± 0.27	4.2 ± 0.03	yes	HSS	0.13 - 0.47
XTE J1859+226	40124-01-14-00	8.56 ± 0.06	2.76 ± 0.18	12.4 ± 0.4	no	HIMS	> 0.07
XTE J1650-500	60113-01-13-02	6.84 ± 0.05	8.05 ± 1.23	20.8 ± 0.3	no	HIMS	> 0.06
XTE J1817-330	91110-02-32-00	9.6 ± 0.5	2.93 ± 0.82	5.7 ± 0.1	yes	HSS	0.08 - 0.36
XTE J1748-288	30171-02-01-00	31.55 ± 0.13	6.00 ± 0.42	10.2 ± 0.5	no	HIMS	> 0.23
XTE J1752-223	95360-01-11-00	6.46 ± 0.13	3.6 ± 1.1	23.4 ± 1.2	no	HIMS	> 0.06
XTE J1550-564	40401-01-48-00	18.10 ± 0.06	19 ± 4	6.2 ± 0.1	no	HSS	0.31 - 0.34
MAXI J1543-564	96371-02-02-01	5.72 ± 0.04	10.2 ± 1.4	27.3 ± 1.2	no	HIMS	> 0.05
H1743-322	80135-02-03-00	14.6 ± 0.2	12.6 ± 6.3	4.4 ± 0.2	no	ULS	> 0.12
GRO J1655-40	91702-01-17-01	27.51 ± 0.13	44 ± 21	2.7 ± 0.1	no	HSS	0.29 - 0.31

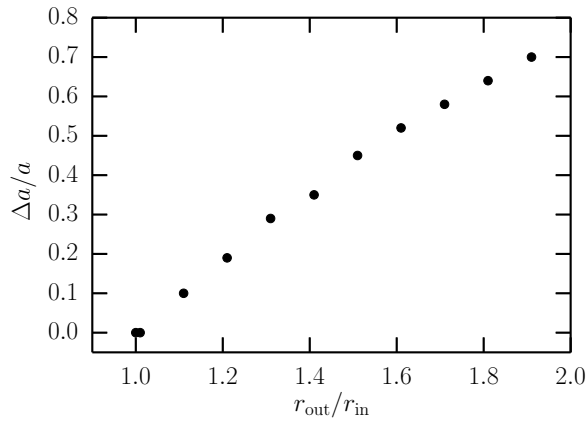

Figure 7.6: Relative change in the spin estimate assuming that the QPO is produced by an extended rigidly precessing structure (Ingram et al., 2009) rather than a test particle at ISCO, as a function of the radial extent of the precessing structure $r_{\rm out}/r_{\rm in}$, where $r_{\rm out}$ is the outer radius and $r_{\rm in} = r_{\rm ISCO}$ is the inner radius of the structure.

7.4 Discussion

We analyzed *RXTE* observations of 12 black hole transients that showed a soft state. We considered observations in the HSS and ULS of these sources. We then assumed that the highest frequency type-C QPO has been produced at the ISCO and applied the RPM in order to place limits on the spin value. This is done either using a known value of the black hole mass or assuming the mass in a reasonable range of values, decided *a priori* ($3 - 20 M_{\odot}$ in our case).

This method is based on the assumption that the inner disc truncation radius is constant and coincident with ISCO when a BHB is observed in the HSS or ULS. Demonstrating the coincidence of the inner disc truncation radius with ISCO is problematic and involves spectroscopic measurements that are generally affected by large uncertainties. Therefore, our assumption constitutes a relevant caveat. However, both observations and simulations provide strong evidence about the stability of the inner disc radius over time in disc-dominated states of BHBs (e.g. McClintock et al. 2014). Tanaka & Lewin (1995) showed that the inner radius is remarkably stable also if the thermal flux of the source steadily decreases on timescales of months by one or two orders of magnitude. Similar evidence for a constant inner disc radius in the soft state has been demonstrated for many sources (Done et al. 2007 and references therein, Plant et al. 2014, Plant et al. 2015). According to Tanaka & Lewin (1995), the constancy of the inner radius suggests that it is related to the ISCO. More recently Steiner et al. (2010) found another evidence of a non varying disc inner radius over time for the source LMC X-3, unaffected by the high variability of this source. Nevertheless, since we cannot be certain of the coincidence of the inner disc radius with ISCO for all the sources of our sample, excluded GRO J1655-40 and XTE J1550-564 (for which the coincidence has been demonstrated explicitly), we advice the reader to consider the inferred limits with caution.

The rigid precession of the inner accretion flow as an explanation of type-C QPOs has been supported by several studies (e.g. Ingram et al. 2009; Ingram & Motta 2014; Ingram et al. 2016). The rigid precession model tends asymptotically to the RPM for radii approaching the ISCO, therefore, given the stability of the disc inner radius in the soft state, the RPM represents a good approximation of the rigid precession for truncation radii (hence hot flow *outer* radii) very close to the ISCO (Ingram & Motta, 2014).

The approach we used in this work differs from that of Ingram & Motta (2014), which always requires that at least two QPOs are detected simultaneously (the type-C QPO and one HFQPO) in order to place an upper or lower limit on spin and mass, depending on the case considered. Here we assumed that the highest frequency type-C QPO is produced at the ISCO. Thus the RPM system of equations is reduced to just one equation (i.e. Eq. 7.1) that gives either a lower limit (if the highest type-C QPO was not detected in the HSS) or a range of spin values. The ranges are broad if there is no independent (e.g. dynamical) mass measurement available, or significantly narrower if the mass is known. The reason is that the uncertainty on the spin is completely dominated by the error on the mass (much larger than the error on the QPO centroid frequency).

In general, the two uncertainties that contribute to the error on the spin value are that on the black hole mass and the identification of the highest type-C QPO. In principle we can never be completely sure that the type-C QPO we assumed to be the highest is actually the highest ever produced by the source in the soft state. There is always the possibility that an even higher frequency type-C QPO has been produced and not detected. Using a type-C QPO that is not at the highest possible frequency for a given

source results in an underestimation of both upper and lower limit of the spin. In other words, when estimating the spin range from a type-C QPO that is not the highest in frequency, we would be following the wrong track in Fig. 7.1, that would be found to the left of the track corresponding to the actual highest frequency type-C QPO. This effect is larger for QPOs that are not detected in the HSS, therefore produced at a radius that is almost certainly larger than ISCO.

We note that the different tracks in Fig. 7.1 tend to lay closer to each other for high frequencies (i.e. above 80 Hz). Thus, the error on the spin estimate might still be dominated by that on the mass if the QPO frequency is very high. For instance, if the actual highest type-C QPO was produced at, 30 Hz instead of being detected at 21 Hz, the error that we commit on the spin estimate is of the order of a few percent.

7.4.1 Comparison with other methods

For some sources of our sample the spin has been also measured through X-ray spectroscopy by fitting the thermal disc emission or by modelling the disc reflection spectrum. Fig. 7.7 shows the spin measurements found in the literature obtained from X-ray spectroscopy versus the spin values we inferred from timing analysis in this work. The black line marks the position where the measurements should fall if there was perfect agreement between spectroscopy based measurements and timing based measurements. In two out of five sources (XTE J1550-564 and 4U 1543-47) the spin measurements obtained with spectroscopy and timing do agree. In particular, Morningstar & Miller (2014) obtained a spin value $a = 0.43^{+0.22}_{-0.31}$, in agreement with our values, for 4U 1543-47 using both the spectral continuum fitting method and the iron line fitting method simultaneously. Steiner et al. (2011) used data from the BHB XTE J1550-564 to model the continuum and to fit the iron line obtaining two different spin measurements, that combined resulted in a spin of $a = 0.49^{+0.13}_{-0.20}$ which is consistent with the spin range that we report (see Table 7.2).

For 4U 1630-47 King et al. (2014) measured the spin by fitting the continuum spectrum of the source, obtaining $a = 0.985^{+0.005}_{-0.014}$, which is in principle compatible with our lower limit (i.e. $a > 0.12$). For XTE J1752-223 and GX 339-4, spectroscopy returned high spin values using both continuum fitting and the reflection model (Reis et al., 2011; Miller et al., 2002; Reis et al., 2008). Reis et al. (2011) found an intermediate black hole spin $a = 0.52 \pm 0.11$ for XTE J1752-223 while for GX 339-4 an almost extreme spin value $a = 0.935 \pm 0.010$ has been inferred. For XTE J1752-223 we were able to place only a lower limit on the spin thus our findings are still consistent with the results obtained using spectroscopy. The spectroscopic estimate of the spin in GX 339-4 is not consistent with the range that we obtained using the RPM.

Motta et al. (2014b) measured with unprecedented precision the mass and spin of the black hole in GRO J1655-40 applying the RPM using the three QPOs that have been simultaneously observed (Motta et al., 2012; Strohmayer, 2001). They inferred a mass $M = 5.31 \pm 0.07 M_{\odot}$ and a spin value $a = 0.290 \pm 0.003$ that is, as expected, in good agreement with the range obtained in this work. Through spectroscopic studies, different, much higher, values of the spin have been inferred. By modelling the thermal spectral continuum Shafee et al. (2006) found a spin range $a = 0.65 - 0.75$. Reis et al. (2010) placed a lower limit $a = 0.9$ by fitting the strong reflection features in the spectrum and Miller et al. (2009) obtained a highly spinning black hole with $a = 0.94 - 0.98$ using the same method. Both the spectroscopic methods rely on the assumption that the inner edge of the disc always corresponds to the ISCO, which might not be a correct assumption in all

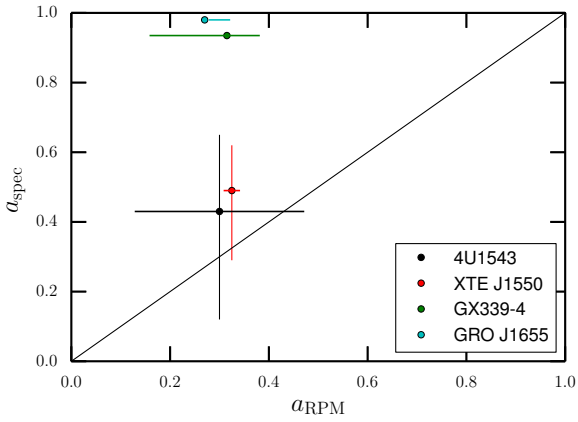

Figure 7.7: The horizontal lines represent the different ranges of spin values obtained in this work for each source. The black, red, green and cyan lines refer to 4U1543, XTE J1550, GX 339-4 and GRO J1655 respectively. On the y-axis the dots represent the values obtained using spectroscopic methods with the correspondent error bars. The black line represents the case $a_{\rm spec} = a_{\rm RPM}$.

spectral states of active black holes (see, e.g. Done et al. (2007)). Furthermore, in order to use the spectral continuum fitting method, one must also know the black hole mass, the inclination of the (inner) accretion disc with respect to the line of sight and the distance to the source. All these factors introduce large uncertainties and possibly significant biases in the spin measurement. For instance, as already noted by Motta et al. (2014a) in the case of GRO J1655-40, the disagreement between spin measurements inferred through different methods might be due to the high inclination of the inner accretion disc with respect to the outer disc (i.e. the orbital inclination) and to the line of sight. When such misalignment is not taken into account, the final spin measurement can be largely biased. The RPM method does not depend on any of these variables, and in the case where 3 QPOs are simultaneously detected, it allows to obtain self consistently the mass and spin of the black hole. The precision on the inferred parameters is only driven by the precision in the QPO frequencies measurement.

More spectroscopy-based and timing-based measurements of the spin are necessary to confirm the validity of the RPM method and to test its consistency with other methods. New generation satellites (such as eXTP Zhang et al. (2016)) will provide more and better data to test this and other methods for spin measurements.

Finally, as already noted by Motta et al. (2014b), we would like to stress that the RPM is a simplified model aimed at describing rather complex physical conditions, such as those encountered in the innermost disc regions around an accreting compact object. The RPM does not include yet a production mechanism for the QPO signals (but see Psaltis & Norman 2000 or Schnittman et al. 2006 for possible mechanisms), which remains an open question to be investigated in the future.

7.5 Summary and conclusions

In this work we placed limits on the value of the black hole spin for several black hole X-ray binaries through the sole use of X-ray timing. In particular we looked for type-C QPOs in the soft state for a number of sources selected based on the presence of type-C QPOs in their PDS, and then applied the RPM. This choice is justified by the fact that in the HSS the disc is expected to extend down or very close to the ISCO. As a consequence, the inner accretion flow is extremely narrow in this state and we assumed that its Lense-Thirring frequency can be well described by that of a test particle at the ISCO. According to the RPM, we associated the highest frequency type-C QPO with the Lense-Thirring precession frequency of a test particle at the ISCO. We then inferred lower spin limits for all the sources of our sample and upper limits for the ones that showed type-C QPOs in the HSS or ULS, assuming a reasonable range of black hole masses or using the actual mass value for those source where a dynamical mass measurement is available. We successfully applied the RPM to all the sources in our sample that showed type-C QPOs in the HSS or ULS.

Our results are in good agreement with those inferred using other spectroscopy-based methods (continuum fitting method and the K-α line modelling) only in two cases out of 5. Next generation satellites, characterized by a better sensitivity might help in solving the issue of spin measurements.

Chapter 8

Global precession in Low Mass X-ray Binaries

Based on the paper by Sara Elisa Motta, **Alessia Franchini**, *Giuseppe Lodato and Guglielmo Mastroserio: "On the different flavours of Lense-Thirring precession around accreting stellar mass black holes " accepted for publication in Monthly Notices of the Royal Astronomical Society.*

QPOs have been explained in terms of relativistic precession of either a single test particle orbiting the black hole (according to the RPM) or a geometrically thick accretion disc precessing as a rigid body. According to the rigid precession model (i.e. the truncated disc model) the type-C QPO is produced through the modulation of the X-ray flux coming from self-occultation, projected area and relativistic effects (Ingram & Done, 2012; Veledina et al., 2013; Ingram et al., 2016) that become stronger with inclination (Motta et al., 2015). This model also naturally explains why a coherent low frequency QPO can be observed even when the inner flow is thought to be radially wide (tens of $R_{\rm g}$). The aim of this work is to demonstrate that the test particle RPM is the limiting case of the rigid precession when the radial extent of the precessing flow is very small, and that solid lower limits to the black hole spin can be obtained by considering the test particle model alone. We also show that the global precession model naturally accounts for the range of frequencies observed for type-C QPOs without the need to invoke a truncation of the inner accretion flow before it reaches the innermost stable circular orbit. Finally, we show that, in order to maintain rigid precession, the thick accretion flow should be radially narrow, and that if it extends beyond $10 - 10^2$ gravitational radii it aligns with the black hole spin too fast to produce a coherent QPO.

8.1 Test particle versus rigid precession

In the Relativistic Precession Model by Stella & Vietri (1998), three observed QPO frequencies are associated with the Keplerian frequency, the periastron precession frequency and the nodal precession frequency related to the Lense-Thirring effect at a given radius in the disc. Motta et al. (2014a) showed that the equations describing these three frequencies, predicted by General Relativity, form a system of three equations for the three unknowns: M (the black hole mass), a (the dimensionless black hole spin parameter) and R (the radial location at which the QPOs are produced around the black hole). Such system of equations can be solved analytically if three QPOs of the correct type are observed simultaneously, or numerically when an independent measurement of the black hole mass is available (e.g. from dynamical spectro-photometric observations), together with two QPOs (see Motta et al. 2014a, Motta et al. 2014b, Ingram & Motta 2014).

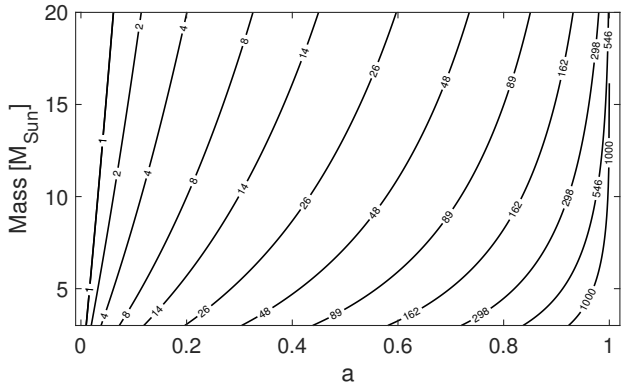

Figure 8.1: Mass-spin relation for different test-particle Lense-Thirring frequencies. Each line has been obtained assuming that the frequency is produced at the ISCO. The number on each line corresponds to the frequency considered in Hz.

In this work, we are especially concerned with the Lense-Thirring precession frequency (the *test particle precession frequency*) that is given by:

$$\nu_{\rm LT} = \pm \frac{c^3}{2\pi GM} \frac{1}{r^{3/2} \pm a} \left[1 - \left(1 \mp 4ar^{-3/2} + 3a^2 r^{-2} \right)^{1/2} \right], \tag{8.1}$$

where top and bottom signs refer to prograde or retrograde precession respectively, and where $r = R/R_{\rm g}$, with $R_{\rm g} = GM/c^2$. Figure 8.1 shows the contours of (prograde) $\nu_{\rm LT}$ in Hz computed by using Eq. (8.1) at the ISCO, as a function of mass and spin of the black hole. It is worth noticing that $\nu_{\rm LT}$ at the ISCO is of the order of ≈ 1000 Hz for maximally spinning black holes, with a weak dependence on the black hole mass.

A strong argument against the test particle precession model is that one expects any local disc feature, whose emission is responsible for the QPO, to be rapidly sheared out by differential rotation. The so-called *rigid precession model* (see e.g. Ingram et al. 2009) attempts to solve this problem by requiring that type-C QPOs are produced via the *global*, rigid precession of a toroidal structure, rather than being produced via precession of a single test particle. The global *rigid precession frequency* is given by (see e.g. Lodato & Facchini 2013a; Ingram & Done 2012):

$$\nu_{\rm p} = \frac{\int_{R_{\rm in}}^{R_{\rm out}} \nu_{\rm LT}(R) L(R) 2\pi R \, {\rm d}R}{\int_{R_{\rm in}}^{R_{\rm out}} L(R) 2\pi R \, {\rm d}R}, \tag{8.2}$$

where $R_{\rm in}$ and $R_{\rm out}$ are the inner and outer radii of the rigidly precessing thick disc, $L(R) = \Sigma(R)\Omega_{\rm K} R^2 \propto \Sigma(R) R^{1/2}$ is the specific angular momentum, $\Sigma(R)$ is the radial surface density and $\Omega_{\rm K}$ is given by the relativistic correction to the Keplerian angular velocity. Following Shakura & Sunyaev (1973), we will assume a surface density profile:

$$\Sigma(R) \propto R^{-p} \left(1 - \sqrt{\frac{R_{\rm in}}{R}} \right)^p, \tag{8.3}$$

where the index p varies between 0 and 1. The rigid precession frequency is sensitive to the shape of the surface density profile in the vicinity of the ISCO. In particular,

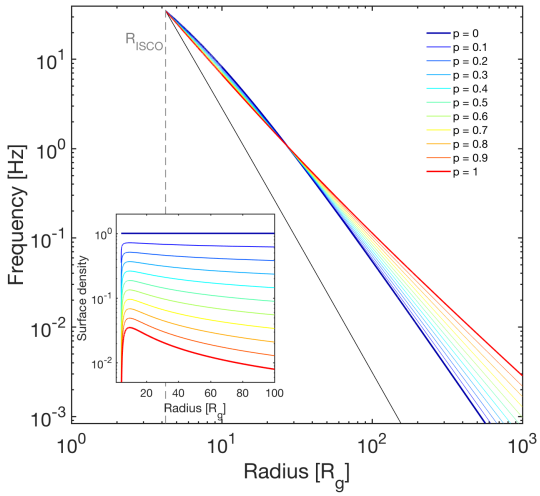

Figure 8.2: Lense-Thirring frequency for a test particle (black solid line) and rigid precession frequency (coloured lines) as a function of radius. The inset show the surface density profile for different values of p. In both panels different colours correspond to different values of p (see legend). The frequencies have been calculated for a 10 $M_\odot$ black hole with dimensionless spin parameter $a = 0.5$.

non-zero surface densities at the ISCO yield higher rigid precession frequencies, which is a natural consequence of the fact that $\nu_{\rm LT} \propto r^{-3}$. In order to avoid exceedingly high type-C QPO frequencies, Ingram et al. (2009) assumed a truncated surface density profile. This is not necessary if we assume a surface density profile in the form 8.3, which for p = 3/5 corresponds to a radiation pressure dominated Shakura and Sunyaev disc with stress tensor proportional to the gas pressure (Franchini et al., 2016). In this work we assume that the inner radius $R_{\rm in}$ of the thick disc *always* coincides with the ISCO, while the outer radius can in principle assume any value larger than $R_{\rm ISCO}$. Of course, the surface density profile given by Eq. 8.3 does not correspond to the form described in Shakura & Sunyaev (1973) if $p \neq 3/5$. However, provided that the profile tends to zero for $R \to R_{\rm ISCO}$, the rigid precession frequency yielded by Eq. 8.2 does not depend significantly on its specific form, as we will show below.

In Fig. 8.2 we show a comparison between the test particle precession frequency given by Eq. (8.1) and the rigid precession frequencies obtained through Eq. (8.2) for a 10 $M_\odot$ black hole with spin $a = 0.5$. The rigid precession frequency depends on the inner radius $R_{\rm in}$ and on the outer radius $R_{\rm out}$ of the thick disc. The test particle frequency depends only on the radius of the orbit that the test particle is following. For comparison, in the figure, this radius is the same $R_{\rm out}$ used to compute the global frequency. The rigid precession frequency depends on the choice of p (indicated with different colours in the plot) through the surface density profile, displayed in the figure inset. At large radii, values of p close to zero give a steeper relation between frequency and outer radius than values of p close to one. Note, however, that the dependence on p is generally weak, especially at large radii. The spread in frequency caused by p (shown in Fig. 8.2) is spin-dependent and reaches its maximum at radii smaller than $\approx 10 R_{\rm g}$ (note that the plot in Fig. 8.2 is in log-scale). This effect is better displayed in Fig. 8.3, where we plot

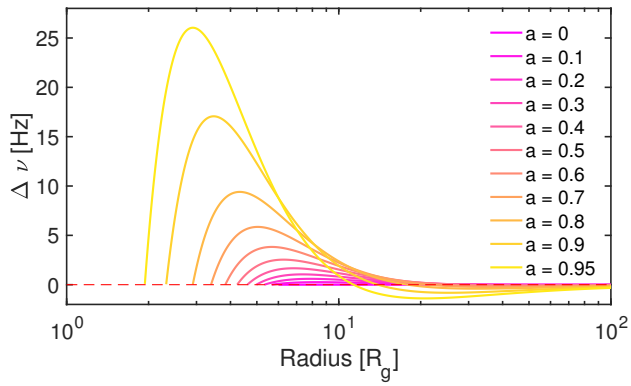

Figure 8.3: Maximum spread as a function of radius for rigid precession frequencies computed for variable spin (see legend) and a 10 $M_\odot$ black hole. The maximum frequency spread is calculated as the difference between the rigid precession frequencies computed for $p = 0$ and for $p = 1$.

the difference $\Delta\nu$ between the rigid precession frequencies calculated assuming $p = 0$ and $p = 1$, as a function of $R_{\rm out}$ for a 10 $M_\odot$ black hole. For spins lower than ≈ 0.7 the frequency difference remains smaller than ≈ 5 Hz, while it increases quickly to several tens of Hz for higher spins. Figure 8.4 shows a comparison between the rigid precession frequencies obtained for a $10M_\odot$ black hole with spin a = 0.5, calculated assuming the surface density profile given in Eq. 8.3, and the rigid precession frequencies obtained taking a surface density profile with the form $\Sigma(R) \propto R^{-p}(1 - \sqrt{R_{\rm in}/R})$. In both cases we assumed $p = 3/5$. The maximum difference in frequency using the two different profiles is smaller than 1 Hz at any radius. It can be shown (Franchini et al., 2016) that $p = 3/5$ is the most appropriate value for a radiation pressure dominated Shakura-Sunyaev disc, and thus for the thick discs that we consider here, with viscosity proportional to the gas pressure and opacity dominated by electron scattering. Unless otherwise specified, from now on we will assume $p = 3/5$.

8.2 Spin measurements from relativistic precession

As it is clear from Fig. 8.2, when the outer radius of the thick disc $R_{\rm out}$ approaches the ISCO (i.e. as the thick disc becomes more and more narrow), the rigid precession frequency asymptotically tends to the test particle frequency. Based on this property, in Franchini et al. (2017), we obtained lower limits (and a few upper limits) for the black hole spin by using the highest frequency type-C QPO detected in the soft state of the outburst of each source of our sample. We assumed that in this state the precessing thick disc is squeezed to a very narrow radial extent, such that we could substitute the (simpler) test particle frequency (Eq. 8.1) to the rigid precession frequency (Eq. 8.2) for $R \approx R_{\rm ISCO}$.

We noted, however, that the lower limits to the spins that we obtained were all significantly below the maximally spinning value $a \sim 1$ (the highest spin we obtained is $a = 0.47$ for the case of 4U 1543-47), despite the fact that the soft-state type-C QPOs that we detected in the HSS spanned a fairly large frequency range ($\sim$ 5-30 Hz). The origin of this

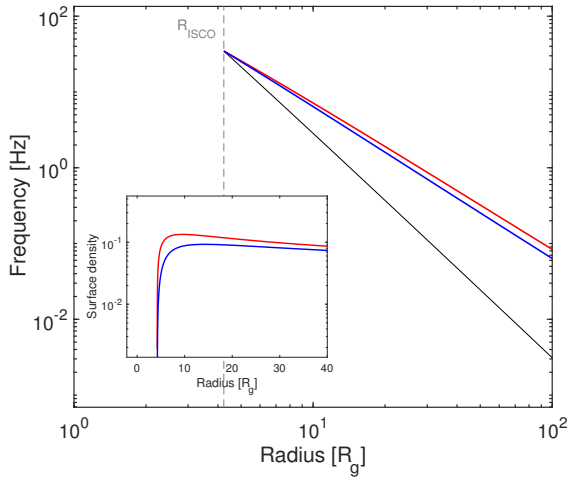

Figure 8.4: Rigid precession frequencies obtained for a $10M_{\odot}$ black hole, with spin a = 0.5, calculated assuming the surface density profile given in Eq. 8.3 (red line) and those obtained taking a surface density profile with the form $\Sigma(R) \propto R^{-p}(1-\sqrt{R_{\rm in}/R})$ (blue line). The inset shows the surface density profiles of the two cases,

trend can be deduced from Fig. 8.1, that shows that for black hole masses below $10M_{\odot}$, a spin estimate of $a \gtrsim 0.8$ would correspond to a QPO frequency above 500 Hz, much above the maximum frequency type-C QPOs observed so far ($\approx 30Hz$, see e.g.Motta et al. 2015). Similarly, Fig. 8.2 shows that for any given radius, the rigid precession frequency is higher than the test particle precession frequency by a factor that we empirically estimate to be $\sim R/R_{\rm ISCO}$. This implies that for a given mass, frequencies explained via simple test particle precession at ISCO will always require spins systematically lower than those explained in terms of global precession.

The spin distribution of stellar mass black holes is still largely unknown. Fragos & McClintock 2015 showed that a constant distribution of black hole spins (obtained through the fitting of the spectral continuum in outbursting black hole low-mass X-ray binaries, see, e.g., McClintock et al. 2011) can be obtained by assuming that the natal spin of the black hole in these systems is initially low, and then increases during the accretion phase. This would result in a roughly constant spin distribution, but requires a strong coupling between the core and the envelope of the progenitor star of the back hole (which has been observed only for red giant stars with mass up to $2M_{\odot}$). While Podsiadlowski et al. (2003) showed that a significant spin-up during the accretion phase is possible, King & Kolb (1999) ruled out this possibility by showing that the amount of accreted mass by the black hole would be too small to significantly change the spin.

Spin measurements obtained via fitting of the reflection features in the energy spectra from accreting black holes seem to indicate that the black hole spin distribution for black hole X-ray binaries might be skewed to high values (see, e.g., Reynolds 2013). It must be noted, however, that the spin measurements obtained through this method are typically affected by large uncertainties and, in a few cases, are also in contrast with the measurements obtained through other methods (see, e.g., Shafee et al. 2006 and Reis et al. 2010 for the case of GRO J1655-40). This makes it difficult to establish the spin

distribution underlying the measurements obtained so far.

There is still no obvious reason why certain spin values should be preferred, therefore the simplest assumption we can make is that the spin distribution is somewhat constant. Therefore, the dimensionless spin parameter of a stellar mass black hole can in principle take any value between 0 and 1. Based on this argument, it seems clear that the spin measurements/lower limits based on the test particle precession are conservative, especially if obtained from QPOs that are produced far from the ISCO (Franchini et al. 2017).

A finite disc radial extent results in lower global precession frequencies. Figure 8.5 shows contour plots of the rigid precession frequency computed as a function of the black hole mass and spin for different disc radial extents: from top to bottom $\Delta R = R_{\rm out} - R_{\rm in} =$ 0.1, 3, 5 and 10 $R_{\rm g}$. While for $\Delta R = 0.1 R_{\rm g}$ the plot is very similar to the test particle case (see Fig. 8.1), for wider thick discs the resulting frequencies rapidly decrease for a given mass-spin couple. We thus see that by allowing a modest radial extent of the thick disc we obtain Lense-Thirring frequencies that are consistent with the type-C QPOs frequencies typically observed around black hole X-ray binaries, with their maximum reaching up to ≈ 30 Hz when the thick disc is a few $R_{\rm g}$ wide (i.e. what we expect in the HSS). Allowing the thick disc to maintain a radial extent implies the entire spin range can be spanned in order to obtain frequencies typical of type-C QPOs in the HSS for a reasonable range of black hole masses ($\sim 3 - 20 M_{\odot}$). This essentially removes one of the limitations of the test particle model described above.

The spin measurement that can be obtained depends strongly on the thick disc actual radial size. In Figure 8.6 we plot the spin a obtained from the rigid precession model as a function of the radial extent of the thick disc, assuming a given observed type-C QPO frequency for different values of the black hole mass. The plots show that the test particle precession provides a solid lower limit to the black hole spin, while a stricter lower limit on the spin (or its actual value) could only be inferred knowing the radial extent of the thick disc. We note that for wider thick discs the inferred spin quickly saturates to 1 even assuming relatively low QPO frequencies, i.e., ∼5-15 Hz depending on the mass of the black hole (the higher the mass, the lower the frequency at which the spin saturates at 1). Such regions where the spin is equal to 1 for a variable ΔR correspond to fractions of the parameters space for which there is no solution given a particular frequency and ΔR. Again under the assumption that the spin distribution of stellar mass black holes is close to a constant in the 0 to 1 range, the above suggests that it is unlikely that the thick disc will have a radial extent ΔR larger than ∼5-10 $\rm R_g$ in the HSS.

8.3 Requirements for global rigid precession of the thick disc

The outer radius $R_{\rm out}$ of the thick disc only depends on the physical properties of the accretion flow, and changes depending on the accretion state of a source. Since, in general, the thick disc angular momentum is not aligned with the black hole spin, the disc undergoes precession due to the Lense-Thirring effect, which induces a precession rate proportional to R^{-3}. Thus, the innermost thick disc orbits are subject to a stronger torque and tend to align with the black hole spin while the outer parts keep the original misalignment. This leads to the formation of a warp in the thick disc. In a thick disc the warping disturbances propagate as waves with half the sound speed (Nelson & Papaloizou, 2000). Eventually, the thick disc becomes too wide for the warp to be communicated efficiently across it, and at this point rigid precession can no longer occur. Additionally, a very extended disc has the tendency to align with the black hole spin, again inhibiting

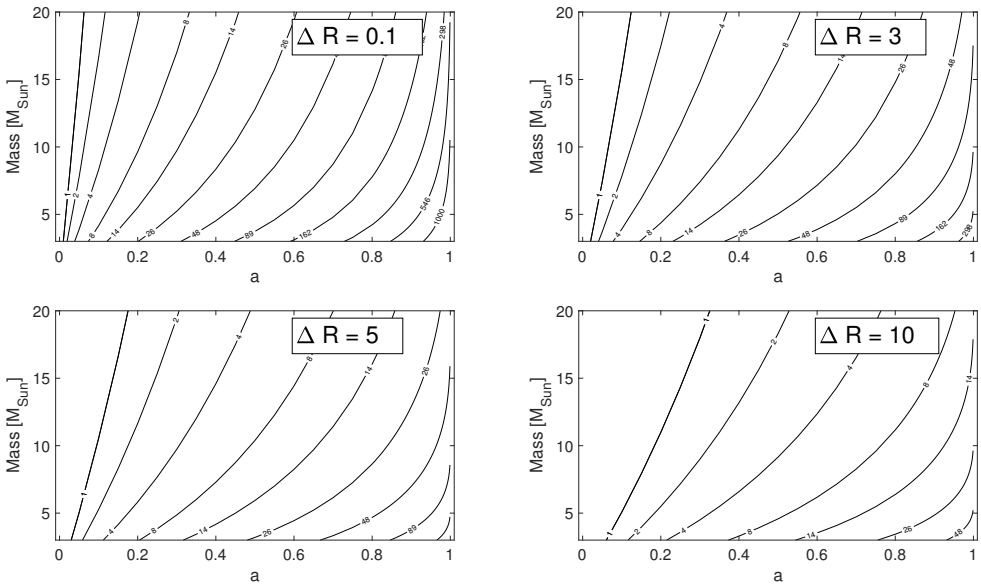

Figure 8.5: Mass-spin relation for different Lense-Thirring frequencies in the rigid precession model. Each line has been obtained assuming that the frequency is produced by a torus extending between $R_{\rm isco}$ and $R_{\rm out}$, with $R_{\rm out} - R_{\rm isco} = \Delta R$ (indicated in each plot). These relations have been obtained assuming the same density profile as in Fig. 8.3, with $p = 3/5$.

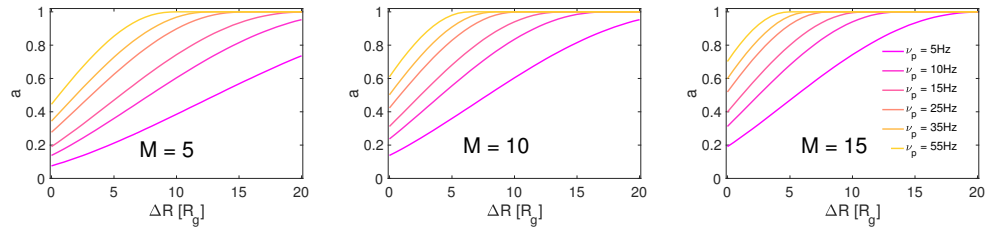

Figure 8.6: Spin inferred for a 5, 10 and 15 $M_\odot$ black hole, obtained assuming that a given frequency is produced by a thick disc with increasing $R_{\rm out} - R_{\rm isco} = \Delta R$. In each case, $\Delta R = 0$ corresponds to the test particle precession. The rigid precession frequencies have been computed assuming $p = 3/5$.

precession. Therefore, there exists a maximum radius $R_{\rm max}$ beyond which the thick disc cannot precess as a whole.

8.3.1 Rigid precession condition

Papaloizou & Lin (1995); Larwood et al. (1996); Fragile & Anninos (2005) have shown that the most stringent condition to maintain rigid precession is that the warp wave travels across the thick disc before a precession cycle is over (Larwood & Papaloizou, 1997). Therefore a simple criterion that needs to be satisfied in order to possibly have rigid precession is to require that the precession time scale $t_{\rm p} = 1/\nu_{\rm p}$ is longer than the sound crossing time scale from the inner to the outer radius of the thick disc ($t_{\rm wave}$). This *rigid precession condition* reads:

$$t_{\rm wave} \lesssim t_{\rm p}, \tag{8.4}$$

with

$$t_{\rm wave} = \int_{R_{\rm in}}^{R_{\rm out}} \frac{2dR}{c_{\rm s}(R)}. \tag{8.5}$$

The maximum outer radius that satisfies the criterion given in Eq. (8.4) corresponds to the maximum radial extent that a thick disc can have in order to be able to precess as a rigid body. This, of course, does not impose any limit on the actual size of the thick disc.

In order to solve Eq. (8.5) we considered a pure power law sound speed profile $c_{\rm s} = c_{\rm s,0} r^{-q}$, with $r = R/R_{\rm g}$. Since $H = c_{\rm s}/\Omega_{\rm K}$, the coefficient of the sound speed evaluated at the gravitational radius is $c_{\rm s,0} = c(H/R)_0$, where c is the speed of light. Solving Eq. (8.5), the wave propagation time scale becomes:

$$t_{\rm wave} = 2\frac{GM}{c^3}\left(\frac{H}{R}\right)^{-1}_{\rm ISCO} r_{\rm ISCO}^{1/2-q} \frac{1}{1+q}\left(r_{\rm out}^{1+q} - r_{\rm in}^{1+q}\right) \tag{8.6}$$

where $(H/R)_{\rm ISCO} = (H/R)_0\, r_{\rm ISCO}^{-q+1/2}$ is the disc aspect ratio at $R_{\rm ISCO}$, and where both $r_{\rm in}$ and $r_{\rm out}$ are expressed in units of $R_{\rm g}$ for convenience. Equation (8.6) implies that the larger the disc aspect ratio at the ISCO, the shorter the warp propagation time scale. Thus, thicker discs are more likely to precess as rigid bodies.

Figure 8.7 shows the precession time scale and the sound crossing time scale for the case of a black hole with $M = 10M_\odot$ and $a = 0.5$. The coloured solid lines show the rigid precession time scale $t_{\rm p}$ for different values of p, the same used in Fig. 8.2. The maximum outer radius that allows rigid precession $r_{\rm rigid}$ can be read off as the intersection of these lines with the black dashed line, that marks $t_{\rm wave}$ as defined above (Eq. 8.6), where we have assumed $q = 3/2$ and $(H/R)_{\rm ISCO} = 0.1$. Since the thick disc is expected to be entirely radiation pressure dominated, we choose $q = 3/2$ (Frank et al. 1992, Eq. 5.54). The aspect ratio at the ISCO, $(H/R)_{\rm ISCO}$, is proportional to $\dot{M}/\dot{M}_{\rm Edd}$ (Frank et al. 1992). Since the rigid precession condition is expected to be most relevant where the thick disc is radially very wide - e.g. in the LHS - we initially chose the value of $(H/R)_{\rm ISCO}$ by considering that in this state, the accretion rate is thought to be low, i.e. $\approx$1-10%$L_{\rm Edd}$ (Fender & Gallo 2014, Dunn et al. 2010), which implies $(H/R)_{\rm ISCO} \sim 0.1$. If the outer radius $r_{\rm out}$ of the thick disc is larger than $r_{\rm rigid}$, only the section of the thick disc with $r < r_{\rm rigid}$ will be able to precess rigidly. The outer part would not able to precess coherently with the inner section of the disc, and could arguably either undergo differential

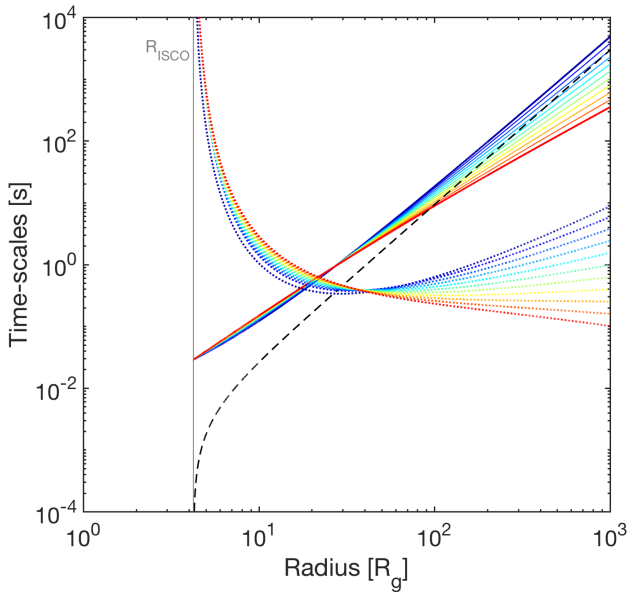

Figure 8.7: Precession time scales (coloured solid lines) compared with the the sound-crossing time scale (black dashed line) and the viscosity-related alignment time scale (dotted coloured lines). The solid coloured lines correspond to the precession time scales obtained from the precession frequency shown in Fig. 8.2. All the time scales have been calculated for a 10 $M_\odot$ black hole with dimensionless spin parameter $a = 0.5$, by assuming $(H/R)_{\rm ISCO} = 0.1$ and $q = 3/2$. Each colour corresponds to a different p as in Fig. 8.2.

precession (van den Eijnden et al. 2016), or break free from the (still precessing) inner flow (see e.g. Nealon et al. 2015).

The rigid precession condition depends on the spin of the black hole (while it is independent on the black hole mass), as it directly depends on the precession time scale, as well as on the disc aspect ratio. Since higher spins mean faster precession, higher spins will also correspond to smaller maximum precession radii $r_{\rm rigid}$. In Fig. 8.8 we show the behaviour of $r_{\rm rigid}$ (solid lines) as a function of the spin for different values of $(H/R)_{\rm ISCO}$, as obtained through Eq. (8.5) for a black hole with spin $a = 0.5$.

We see that while for low spins the precession time scale is long enough to allow rigid precession of very wide thick discs [1] ($r_{\rm out} \gtrsim 10^5 R_{\rm g}$), for very high spins the thick disc will be able to precess globally only as long as its outer radius is smaller than $\sim 10 R_{\rm g}$, especially for low aspect ratios. We must note, however, that in principle $\dot{M}/\dot{M}_{\rm Edd}$ and, consequently the aspect ratio (H/R), increase for increasing spin. For simplicity we have not considered this effect. However, given the above, the actual maximum precession radii given by Eq. (8.5) for a thick discs around a highly spinning black hole are likely larger than those shown in Fig. 8.8 (solid lines).

[1] Note that the entire accretion disc filling the Roche lobe around a stellar mass black hole in a binary system can be as large as $10^6 R_{\rm g}$, but it is typically smaller than this.

8.3.2 Condition for disc alignment

While the presence of misalignment between the black hole spin and the disc angular momentum leads to rigid precession, viscosity acts to dissipate the warp, leading to alignment of the disc angular momentum to the black hole spin. If alignment is achieved faster than one precession time, rigid precession can no longer occur. The disc viscosity damps precession at a rate inversely proportional to the viscosity parameter α ($t_{\rm align} \propto \alpha^{-1}$). An approximate expression for the damping rate $\gamma \approx t_{\rm align}^{-1}$, based on the estimate of the energy loss rate due to viscous dissipation in the disc, was proposed by Bate et al. (2000) for discs of constant thickness. Foucart & Lai (2014) gave a more accurate estimate of this time scale by computing the difference between the total torque exerted by the black hole on the disc and that required in order to keep global precession. The precession damping rate, and therefore the alignment time scale, are given by:

$$\gamma = \frac{1}{t_{\rm align}} = \frac{\int_{r_{\rm in}}^{r_{\rm out}} {\rm d}x \frac{4\alpha G_\phi^2}{\Sigma c_{\rm s}^2 x^3}}{\int_{r_{\rm in}}^{r_{\rm out}} {\rm d}x \Sigma x^3 \Omega_{\rm K}} \,. \tag{8.7}$$

The term G_ϕ is the internal stress in the disc and is defined as

$$G_\phi(r) = \int_{r_{\rm in}}^{r} dx \Sigma x^3 \Omega_{\rm K} (\Omega_{\rm p} - Z\Omega_{\rm K}) \,. \tag{8.8}$$

where Z is defined as $Z(r) = (\Omega_{\rm K}^2 - \Omega_{\rm z}^2)/(2\Omega_{\rm K}^2)$.

In these equations $\Omega_{\rm K}$ is the Keplerian orbital angular velocity, $\Omega_{\rm z}$ the vertical oscillation angular velocity and $\Omega_{\rm p} = 2\pi\nu_{\rm p}$ is the global precession angular velocity of the disc.

Similarly to the case of the rigid precession condition (Sec. 8.3), Eq. (8.7) implies that there is a maximum radius $r_{\rm align}$ beyond which the alignment time scale is faster than the precession time scale. When this happens, the disc aligns to the black hole spin before a complete precession cycle is over, effectively inhibiting continuous precession. Therefore, in order to maintain precession, we also need to require that the thick disc extends no further than $r_{\rm align}$. In Figure 8.7 we show the alignment time scales (coloured dotted lines) together with the precession time scales and the sound crossing time scale. Since $t_{\rm align}$ depends on the index p through the surface density profile Σ, each colour corresponds to a different choice of p (see legend in Fig. 8.2). The alignment time scale is shorter for higher black hole spins, which implies that $r_{\rm align}$ become smaller for increasing spin. As noted above in the case of the rigid precession condition, we are not considering the effects of the spin on H/R, which would likely make $r_{\rm align}$ larger than what obtained simply by solving Eq. (8.7), especially at high spins.

It is important to note that in the case of a black hole in a binary system, the companion star is feeding the compact object, providing a constant stream of misaligned material. This implies that even though the flow undergoes alignment due to frame dragging within one precession cycle, there is always more material coming in inclined with respect to the black hole equatorial plane, at least until the system eventually achieves global alignment, which may or may not take longer than the time it takes for the companion to evolve.

In a scenario where the alignment time scale is fairly short, precession would still occur, but only intermittently. In this context, the quality factor Q (defined as $Q = \nu_{\rm QPO}/FWHM_{\rm QPO}$, where $\nu_{\rm QPO}$ is the QPO centroid frequency and $FWHM_{\rm QPO}$ is the QPO full width half maximum) of the resulting QPO would then be approximately the number of precession cycles in an alignment time scale. Since by definition QPOs have

$Q > 2$, this means that we can impose a stricter constraint on $r_{\rm align}$, which is then obtained by requiring $t_{\rm align} > 2t_{\rm p}$.

In Figure 8.8, together with the maximum radius at which rigid precession is allowed by the global criterion (Eq. 8.4), we show the maximum radius at which rigid precession is permitted before alignment (indicated with dashed lines) as a function of the spin. We calculated such radii for variable aspect ratio $(H/R)_{\rm ISCO}$, assuming $\alpha = 0.01$ and $p = 3/5$. Interestingly, we see that the disc alignment condition given by Eq. (8.7) almost always dominates over the wave propagation condition given by Eq. (8.5), and therefore the maximum radius $r_{\rm max} = \min(r_{\rm rigid}, r_{\rm align})$ at which rigid precession can occur is basically always determined by the tendency of the disc to align with the black hole spin.

8.4 Discussion and Conclusions

We compared the test particle Lense-Thirring precession and the global rigid precession as mechanisms likely responsible for the presence of type-C QPOs in the light curve of accreting stellar mass black holes in binary systems. We showed that the global rigid precession of a radially extended thick disc (as opposed to the test particle precession) can produce QPO frequencies that match those of type-C QPOs typically observed in black hole binaries. This geometry is the same already proposed by other authors, in particular Ingram et al. (2009), who made the first explicit connection between the idea of rigid precession already observed in numerical simulations (e.g. Fragile et al. 2007, Liska et al. 2017) and the observed properties of type-C QPOs.

The geometry that we considered in this work consists of a thick disc whose inner radius is set by the ISCO. In agreement with the truncated disc model, the outer radius of the thick disc, instead, is set by the inner truncation radius of the thin disc concentric and surrounding it, and is always significantly larger than $R_{\rm ISCO}$ (i.e. the radial extent of the thick disc must never be negligible).

The surface density profile we assumed is a power-law with index p, with a correction at small radii, to satisfy the no-torque boundary condition $\Sigma = 0$ at $R = R_{\rm in}$ (Shakura & Sunyaev, 1973). The index p can be determined based on disc energetics arguments. In the case considered here, we assume that the disc is radiation pressure dominated with stress tensor proportional to the gas pressure only, in which case $p = 3/5$.

We showed that in order to match the observed type-C QPOs frequencies it is not necessary to assume that the thick accretion disc is truncated on the inside at a radius larger than the ISCO, contrary to what has been proposed by other authors (e.g., Ingram et al. 2009). Instead, we assumed that while in the HSS the thick accretion disc is significantly radially narrower than in the other states, its radial dimension should never become negligible. We showed that in order to both match the observed type-C QPOs frequencies and span the entire spin and mass range suitable for accreting stellar mass black holes the thick accretion disc must always maintain a non-negligible, though moderate, radial extent, i.e. between a few and $\approx 10R_{\rm g}$. Additionally, we confirmed that the test particle Lense-Thirring precession applied to the type-C QPOs observed in the HSS allows us to infer a solid lower limit to the black hole spin (see also Franchini et al. 2017).

The prediction that the thick disc should maintain a significant radial width is consistent with a well-known property of the PDS of accreting black hole binaries. PDS showing type-C QPOs can be modelled by multiple Lorentzians (see, e.g., Belloni et al. 2002). The lowest frequency Lorentzian is generally zero-centered and shows a break at a certain frequency $\nu_{\rm b}$, corresponding to the so-called *low-frequency break* in the flat-top

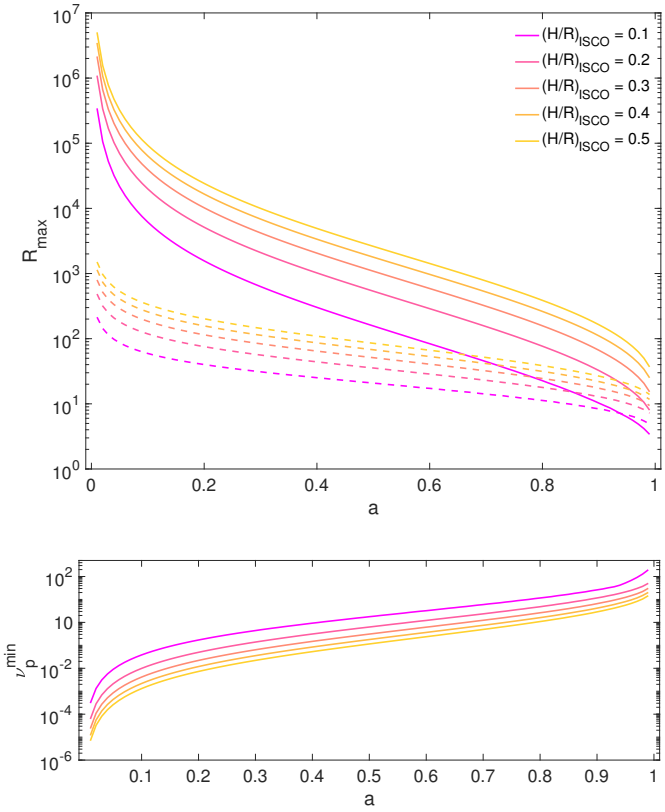

Figure 8.8: *Top panel:* Maximum precession radius $r_{\rm max}$ due to the rigid precession condition (i.e., $r_{\rm rigid}$, solid lines) or the alignment condition (i.e. $r_{\rm align}$, dashed lines) as a function of the spin and for variable $(H/R)_{\rm ISCO}$ ($p = 3/5$, $q = 3/2$, $\alpha = 0.01$). The relations displayed have been obtained through Eq. (8.5) and (8.7), respectively. The figure shows that the maximum radius at which global rigid precession is allowed is always determined by the tendency of the disc to align with the black hole spin. *Bottom panel:* corresponding minimum global precession frequency as a function of the spins. The colour coding is the same used in the top panel. Frequencies have been estimated assuming a black hole mass of $10 M_{\odot}$.

noise typically associated with type-C QPOs. The break frequency $\nu_{\rm b}$ is thought to be associated with the viscous time scale $t_\nu = (H/R)^{-2}(\alpha\Omega)^{-1}$ at the outer radius of the thick disc (see e.g. Done et al. 2007 and Ingram et al. 2009). This frequency is approximately ~ 0.01 Hz in the hard state and ~ 1 Hz in the soft state (see, e.g., Done et al. 2007) and roughly correspond to a few tens of $R_{\rm g}$ and a few $R_{\rm g}$, respectively, for a $10M_\odot$ black hole with spin $a = 0.5$ (assuming $\alpha = 0.01$ in the disc), in agreement with our predictions on the disc radial extent in the soft state.

We then studied the condition under which the thick disc can undergo global rigid precession around a spinning black hole. The two requirements that need to be satisfied in order for the thick disc to rigidly precess - and thus produce detectable QPOs - are the efficiency of warp propagation and reflection that allows global precession, together with a sufficiently long alignment time scale. The first requirement depends on the sound crossing time scale within the disc and guarantees that the warp is maintained. The second requirement depends on the presence of viscosity and ensures that each precession cycle is over before the disc aligns with the black hole spin. Both conditions depend on the mass and on the spin of the black hole, and on the disc aspect ratio. The condition based on the alignment time scale depends also on the viscosity parameter α. We have then calculated the maximum outer radius that a thick disc can have in order to maintain global rigid precession. Interestingly, comparing the maximum precession radii coming from the above conditions, we found that global rigid precession is always inhibited by the disc tendency to align with the spin rather than by the loss of connection between the different regions of the thick disc necessary for global rigid precession. In other words, beyond a certain radius $r_{\rm max}$ the disc aligns faster than it precesses. Since the global precession frequency decreases with increasing outer radius, this implies that, if type-C QPO are indeed due to global precession, for any given black hole mass there is a minimum allowed QPO frequency, that for a $10M_\odot$ black hole is in the range of $0 - 10^2$Hz (see Fig. 8.8, bottom panel). Since the vast majority of the known black hole LMXBs show QPOs below 1 Hz, this result essentially implies that none of such black holes can have a spin higher than $a \approx 0.6$.

We remind the reader that both the maximum precession radii given by the rigid precession condition and the maximum precession radii given by alignment are likely higher than the values obtained from Eq. (8.5) and Eq. (8.7) for high spin values. As a consequence, the minimum allowed precession frequency is lower than those shown in Fig. 8.8 (bottom panel), especially for high spins. Furthermore, we note that very recently Liska et al. (2017) have found evidence in a General Relativistic 3D MHD simulation that the jet can play a role in the alignment of the accretion flow. In particular, the presence of a jet might cause both the precession time scale and the alignment time scale to increase. Investigating further the effects of high spins on the disc dynamics is beyond the scope of this work, and further investigations are left to a future work.

The existence of a maximum radius at which global rigid precession can occur has consequences for the production of type-C QPOs in different accretion states. While in the HSS (and in the ULS) the radial extent to the thick disc is thought to be small, in the LHS the thick disc could be in principle several tens of $R_{\rm g}$ wide. As a consequence, the rigid precession conditions described above could significantly influence the properties of QPOs observed in this state. For instance, a QPO could show a loss in coherence if produced in a thick disc with $r_{\rm out} \sim r_{\rm max}$ with respect to those QPOs produced when $r_{\rm out} < r_{\rm max}$. This might explain type-C QPOs detected in active sources caught shortly after they left the quiescence and/or close to their return to it at the end of an outburst.

Such QPOs typically appear at frequencies lower than ~ 0.1 Hz and are in general broader and less coherent ($\nu_{\rm QPO}/FWHM_{\rm QPO} \approx 2$) than those observed at higher frequencies (typically $\nu_{\rm QPO}/FWHM_{\rm QPO} \gg 2$).

Chapter 9

Conclusions

In this Chapter I present the main conclusions and future perspectives of the study performed in this thesis on the Lense-Thirring effect in both tidal disruption events and low mass X-ray binaries.

X-ray satellites such as *Swift* and *RXTE* have provided a significant impetus to the field of these kind of transients. These satellites collected very good precision data in the time domain of transients. *Swift* is a multi-wavelength satellite dedicated to the study of gamma-ray bursts (GRBs) (Cummings et al., 2011). Furthermore this satellite has detected a modest numer of TDEs and has been used as follow-up for TDEs detected by other missions, providing very well sampled lightcurves. The *Swift* discovery of a couple of jetted TDE has led to a new and significant effort in trying to understand the underlying physics.

The *RXTE* satellite, launched in 1995, featured unprecedented time resolution in combination with moderate spectral resolution to explore variability in X-ray sources. Time scales from microseconds to months are covered in an instantaneous spectral range from 2 to 250 keV.

Both satellite provided a huge amount of very precise data allowing to perform timing studies of transients in such a way that we can use the data within theoretical models to estimate the values of the relevant parameters.

For what concerns the studies performed in this thesis on TDEs (see Chapter 5), the availability of very well sampled *Swift* X-ray lightcurves provides a possible test for our rigid precession model. For instance, a quasi-periodic behaviour was first identified in *Swift* J16449.3+573451 (Lei et al., 2013), even if its origin is still debated.

Similarly, the outbursts of several LMXBs (see Chapter 6) have been well sampled by *RXTE*/PCA. The high resolution of these data allowed to perform several timing studies, in particular the detection of hundreds of QPOs in the spectra of several sources.

TDE and LMXBs are both composed of accretion discs around black holes. The main difference resides in both the mass of the central object and the morphology of the surrounding accretion disc. Stars are torn apart typically by supermassive black holes lurking in the centre of galaxies, while X-ray binaries are stellar mass black holes accreting matter from a companion star.

The accretion disc formed after a TDE is geometrically thick and narrow. The debris are expected to circularize at a specific radius and then the disc spreads owing to viscosity. The material around the black hole in a LMXB, according to the truncated disc model, is expected to form a geometrically thick accretion flow embedded in a Shakura-Sunyaev thin accretion disc truncated at some radius. The truncation radius is not constant but instead moves further inwards as the accretion rate increases during an outburst. Even if the geometry involved in X-ray binaries is more complicated than the TDE discs one,

the inner accretion flow has basically the same characteristics of the thick disc. They are both expected to be hot, thus geometrically thick, and radially narrow. It is therefore reasonable to apply the rigid precession model to both these systems as we did in this thesis.

The main aim of this thesis was to infer the relevant parameters (mass and spin) of a black hole, either supermassive or stellar mass, from observables. While black hole masses can be measured with quite good precision through dynamical studies, the spin can only be inferred indirectly. In this context the study of the Lense-Thirring precession is extremely interesting, first because it is an effect predicted by General Relativity, secondly the rigid precession of the thick accretion disc present in both TDE and LMXB systems allows to infer, or at least constrain, the spin of two extreme scales of black hole masses: SMBH with $M \sim 10^6 - 10^8 M_\odot$ and stellar mass black holes with $M \sim 3 - 20 M_\odot$.

9.1 TDE discs

In Chapter 5, we have modelled the accretion disc formed after a TDE with a radiation pressure dominated slim disc (Strubbe & Quataert, 2009). We adopted a slim disc model because the peak accretion rate $\dot{M}_{\rm p}$ is highly super-Eddington and if the disc is radiatively inefficient it puffs up becoming geometrically thicker.

Since TDE accretion discs are expected to be radially narrow, we reasonably assumed that the entire disc is radiation pressure dominated. However in order to stabilize the innermost region (region a) in Shakura & Sunyaev 1973) against the Lightman-Eardley instability we chose the viscous tensor to be proportional to the gas pressure only. We also assumed that the viscosity can be parametrized using the α-prescription (Shakura & Sunyaev, 1973) with α being constant in time and isotropic. In the bending waves regime, since pressure dominates over viscosity the wave is damped locally through α.

We assumed that the accretion disc precesses as a whole around the supermassive black hole spin axis and we have computed the precession frequency spanning the entire range of black hole spins (both prograde and retrograde orbits) for different values of the black hole mass. We compared our analytical results with that inferred through a ring code that solves the linearized warp propagation equations in both time and space domain using a leapfrog algorithm, finding a perfect agreement. The precession periods obtained range from a few days to a few weeks with smaller spins and masses giving longer periods. These are human accessible timescales that can in principle result in observable quasi-periodic behaviours in the light curve of TDEs. This occurs, for example, if the jet is obscured by the precessing disc which might not be the case. The interactions between the jet and the disc need to be investigated in more details in order to draw this conclusion.

On longer timescales, however, the system evolves towards alignment. This can be due to two mechanism and we showed that the most likely is the presence of the disc viscosity that acts in order to dissipate the warp. The alignment is achieved when the quasi-periodicity shown in Figure 5.5 drops to zero. We evaluated the alignment timescale using the estimate given by Foucart & Lai (2014) and the results perfectly agree with the outcomes of the ring code simulations.

We noted that both the precession period and the alignment timescale depend on the black hole parameters mass and spin. Since in principle from the light curve we are able to estimate both timescales, we can solve the degeneracy inferring an estimate of the black hole mass and spin without making *a priori* assumptions on their value.

9.2 LMXB discs

In Chapter 7, we looked for type-C QPOs in the soft states of a sample of LMXBs that showed this kind of state during their outbursts covered by the *RXTE* satellite. In principle, the Relativistic Precession Model (RPM) can be used to infer indirectly both black hole mass and spin if a type-C QPO and two HFQPOs are detected simultaneously. These frequencies are associated to three frequencies of motion of a test-particle around a black hole: orbital, apsidal and nodal frequency. We used this model (as explained in Chapter 7) to place limits on the black hole spin detecting only the highest frequency type-C QPO produced in the soft state and assuming that it was produced at the ISCO. We considered a conservative range of black hole masses for the sources that did not have a dynamical measurement.

The assumption that in the soft state the inner disc truncation radius is $R_{\rm ISCO}$ constitutes a relevant caveat that needs to be investigated in more details through spectroscopic analysis. This assumption was justified given that the stability of the inner radius has been proven for GRO J1655-40 and XTE 1550-564 (Saito et al., 2007; Kubota & Done, 2004).

Since the RPM represents a very simplified model for the study of such complex systems, we then studied, in Chapter 8, the rigid precession model as a generalization of the RPM in LMXBs. In the soft states of these accreting sources the thick accretion flow is squeezed into a very narrow ring and therefore the RPM can be used as an approximation of the rigid precession of the entire flow to place limits on the black hole spin through the detection of type-C QPOs. However, in the other states the radial width of the accretion flow is not negligible. We then considered other two processes connected to the rigid precession of the thick disc: the condition that has to be satisfied in order for global precession to occur and the alignment process between the disc angular momentum and the black hole spin (which occurs when the warp in the disc is completely damped out by viscosity). We found that the maximum truncation radius is almost always determined by the alignment timescale. Beyond a certain radius, the disc aligns faster than it globally precess and this actually means that no QPO can be produced by a thick disc that is too wide.

9.3 Future perspectives

Future detections in X-rays will be useful to investigate relativistic effects and accretion physics near the last stable orbit. This will allow to deepen our understanding of the physical processes involved in both tidal disruption events and low mass X-ray binaries. Furthermore, since there have been quite a few developments in hydrodynamical simulations codes as well, the combination of observations, theoretical models and simulations allow us to deepen the knowledge of these and many other type of systems.

- Surveys at various wavelengths, such as SKA, LSST, Einstein Probe and ASAS-SN, will hopefully find more TDEs. The large number of new events together with well sampled lightcurves will enable us to test the existent models and to understand even more deeply the physics involved in tidal disruption events. For instance the origin of the quasi-periodicity detected in the early X-ray lightcurve of *Swift* J16449.3+573451 is still unknown, thus in principle it might not be due to the rigid precession of the TDE accretion disc. Upcoming and existing X-ray surveys are crucial in order to look for periodicity of the order of days in other TDE lightcurves

that will allow us to apply our theoretical model to infer the values of the black hole parameters.

On the theoretical side, the model we developed for TDE discs can be improved using 3D SPH simulations to see whether the disc is actually able to rigidly precess a few times before it has a chance to align. In Chapter 3 we compared the results obtained with PHANTOM with the outcomes of the ring code simulations in terms of rigid precession period. The aim of this study was to be able to see if the reflection of bending waves actually occurs in SPH simulations. This is crucial to allow the formation of a stationary warp wave and thus the disc annuli to be able to precess all with the same frequency. We already investigated the waves reflection in Chapter 3 using the ring code. However, by construction, this code assumes the perfect reflection of bending waves at the disc boundaries. We showed that this actually occurs in SPH simulations of discs extended from 10 to $50R_{\rm g}$.

We found a very good match using the Post-Newtonian potential (Nelson & Papaloizou, 2000) with an accretion disc extended from $10R_{\rm g}$ to $50R_{\rm g}$. However, for an accretion disc formed after a TDE, we do expect the disc to extend from the circularization radius ($\sim$ tens to a hundred $R_{\rm g}$) down to the last stable orbit. Whether the waves reflection occurs in a disc that extends down to the last stable orbit is not yet clear. This possibility will be tested using more hydrodynamical simulations in the future. If the inner disc radius is further in compared to $10R_{\rm g}$ then 3D effects might become important. The closer the material is to the black hole, the stronger the precession. If the precession is very strong the disc might respond to that in a nonlinear way, that cannot be captured by the ring code by construction, and this might lead to enhanced dissipation of the warp and eventually to rapid alignment.

Even though the reflection of bending waves at the disc boundaries occurs, the disc might still not be able to rigidly precess around the black hole. Indeed, we showed through ring code simulations (see Chapter 3) that, even when the warp is reflected by code's construction, the disc might still show differential precession rather than global precession. This means that the wave reflection has to be efficient in order to lead to the formation of a stationary wave that allows global precession. We investigated the criterion for rigid precession in Chapter 3 and we found a possible dependence on the aspect ratio in the local criterion (see Section 3.2). A deeper investigation of possible 3D effects in SPH simulations is very likely to improve the existing local criterion for rigid precession and is among the future perspectives of this thesis.

- The spin estimates are a very controversial topic in the X-ray binary community since there are different methods leading to opposite results. There are basically three methods that allow to place limits on the black hole spin, two are based on spectroscopy while the third one, the RPM, is based on kinematic motion of test particles around the black hole.

  The spectroscopic methods are based on modelling the continuum X-ray spectrum of the accretion disc (McClintock et al., 2011) or on the fitting of strong reflection features, particularly the Fe K-α line, observable in the spectra of accreting BH binaries (Miller, 2007; Reynolds, 2013). The reflection features come from Comptonized photons that are scattered back into the line of sight by the accretion disc.

  Both spectroscopic methods rely on the assumption that the inner edge of the accretion disc coincides with the ISCO in any spectral state, which might not be

the case in the hard state for instance. Besides, in order to use one of these methods the mass of the black hole needs to be measured first along with the inclination of the inner accretion disc and the distance to the source. All these factors introduce large uncertainties in the spin measurement. Since the RPM is based on timing properties of the accreting source, the method we used to place limits on the BH spin does not depend on any of the above quantities. Therefore the error in the spin estimate is given only by the sensitivity of the QPO frequency measurement.

However in order to either rule out one of the models or find consistent results between them, more data are certainly necessary. In particular, the detection of more HFQPOs will allow to better test the RPM and the possible inference of the truncation radius from the spectral properties of these sources will improve the rigid precession model.

In Chapter 8 we studied the rigid precession of the inner accretion flow in LMXBs. We did so considering only type-C QPOs produced by the Lense-Thirring precession of the misaligned accretion flow around the black hole. In principle there are two more frequencies associated with the motion of matter around a massive object: periastron precession and orbital motion. Both these frequencies are believed to produce QPOs according to the RPM (Ingram & Motta, 2014). It is not clear which is the global expression of these two frequencies for the entire accretion disc but it is our intention to investigate this aspect in more details in the future with the aim to improve the rigid precession model.

Appendices

Appendix A

Innermost Stable Spherical Orbit

Since the accretion disc formed after the tidal disruption of the star is in general tilted with respect to the BH spin, we have to consider as the disc inner radius, instead of the ISCO, the Innermost Stable Spherical Orbits (ISSO). The ISSO is the innermost stable orbit at constant radius but fixed non-zero inclination with respect to the BH equatorial plane.

A.1 The effect of the ISSO on Lense-Thirring rigid precession of TDE discs

We follow the formalism given in the Appendix of Stone et al. (2013) and define an inclination angle θ such that $C = \cos\theta$ and $\theta = 0$ corresponds to the equatorial prograde orbits. The generic ISSO is a root of the polynomial

$$S(r) = r^8 Z(r) + a^2(1-C^2)(a^2(1-C^2)Y(r) - 2r^4 X(r)) \tag{A.1.1}$$

with $X(r), Y(r), Z(r)$ auxiliary function of the black hole spin, radius and inclination angle (see Appendix A in Stone et al. 2013).

Figure A.1 shows that the innermost stable orbit increases with the inclination angle. It is smallest for prograde equatorial, larger for inclined prograde. The frame-dragging torque has a stabilizing effect on the orbits since it moves particles on equatorial circular orbits closer to the black hole. If the orbit is inclined, the LT torque is weaker and therefore the stable orbit is slightly outside the equatorial one.

For completeness we also evaluate the values of the global precession period as a function of the black hole spin (prograde orbits) for a $10^6 M_\odot$ black hole and for different values of the inclination angle between $\theta = 0$ to $\theta = \pi/2$. The results are shown in Fig. A.2.

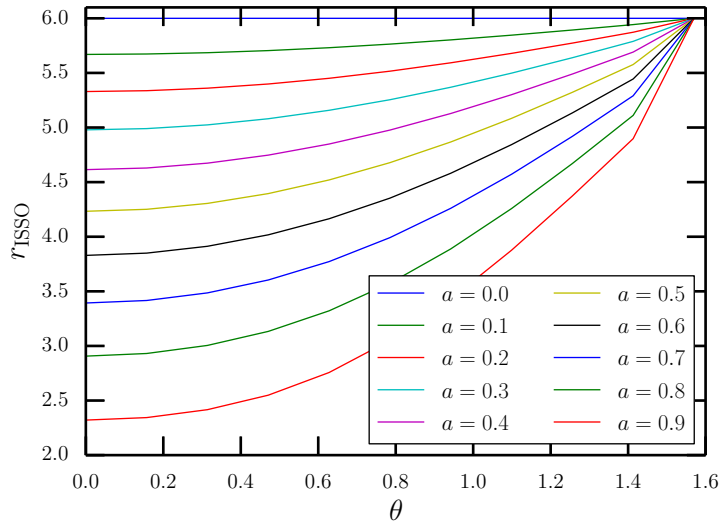

Figure A.1: Radius of the innermost stable spherical orbit as a function of the inclination angle for different values of the black hole spin value.

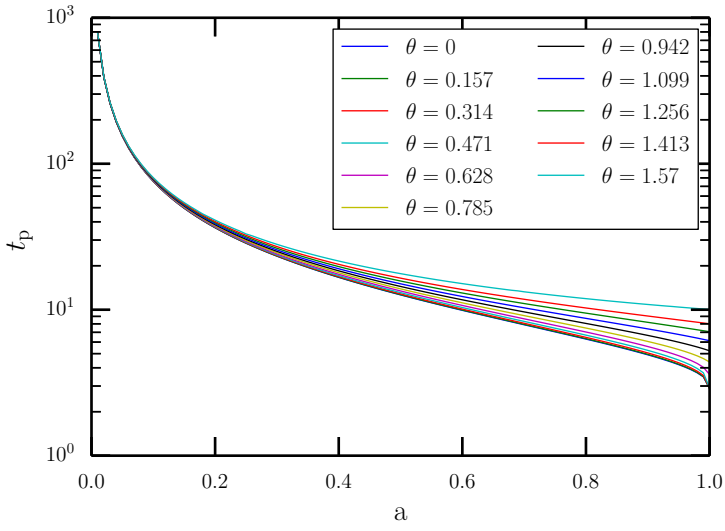

Figure A.2: Dependence of the global precession period on a for a prograde disc and different values of the inclination angle between $\theta = 0$ to $\theta = \pi/2$.

Appendix B

Smoothed Particle Hydrodynamics

In order to compare the outcomes of our analytical estimates with hydrodynamical simulations, we performed simulations using the code PHANTOM (Lodato & Price, 2010; Price et al., 2017). This has been developed by Dr. Daniel Price as an efficient SPH code optimized for studying several astrophysical problems. This is a low memory highly efficient smoothed particle hydrodynamics (SPH) code. SPH is a Lagrangian scheme for solving hydrodynamics equations in which fluid quantities and their derivatives are computed on a set of N particle that follow the fluid motion (Price, 2004; Monaghan, 2005). However, the fundamental axiom of SPH approach resides in the computation of the density from an arbitrary distribution of mass particles.

B.1 Density estimate

Figure B.1 shows three methods for computing the density from a point mass particle distribution. The first natural approach is to construct a mesh and divide the mass in each cell by the volume. However this leads to overestimated dense regions and underestimated sparse regions and also to a loss of accuracy, speed and consistency. The second approach, based on defining a local volume around the sampling point, leads to a very noisy estimate since the density would be sensitive to whether a distant particle on the edge of the volume is 'in' or 'out' of the estimate. This naturally leads to the idea that one should down-weight the contribution of neighbouring particles as their relative distance increases, resulting in a *smoothed* density estimate. In SPH the fluid is discretised into a set of 'particles' of mass $m_{\rm a}$ that move with the local fluid velocity $\mathbf{v}$. The density is then computed using a weighted summation over nearby particles

$$\rho_{\rm a} = \sum_{\rm b} m_{\rm b} W(|\mathbf{r}_{\rm a} - \mathbf{r}_{\rm b}|, h_{\rm a}) \tag{B.1.1}$$

where a and b are particle labels, W is the smoothing kernel (Monaghan, 1992; Price, 2004; Monaghan, 2005), h is the smoothing length and the sum is computed over neighbouring particles, meaning those within $R_{\rm kern}h$ with $R_{\rm kern}$ being the dimensionless cutoff radius of the smoothing kernel. The accuracy of the estimate in Eq. (B.1.1) resides in the choice of a sufficiently good smoothing kernel. The density thus depends only on the relative separation of the particles and is independent of their absolute position, of arbitrary rotations of the particle distribution and of time or history of particles.

The weighting should be positive, decreasing monotonically with the relative distance and should have smooth derivatives. Symmetry with respect to $(\mathbf{r}-\mathbf{r}')$ constitutes another fundamental requirement for a good smoothing kernel, together with a flat central portion

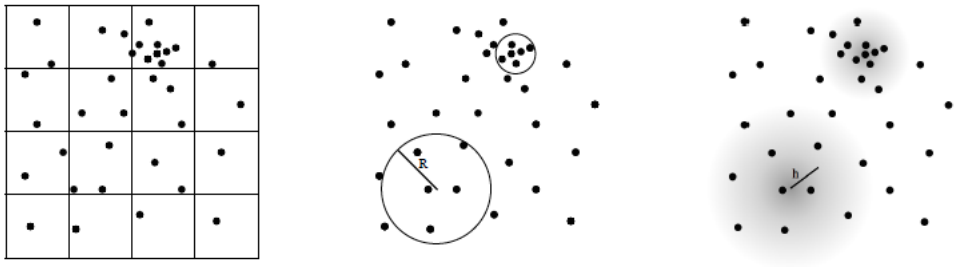

Figure B.1: Computing a continuous density field from a collection of point mass particles. The left panel shows particle-mesh methods while the middle one shows an alternative that consist into define a local volume around the sampling point. The right panel shows the approach adopted in SPH codes (Price, 2012).

so that the density estimate is not strongly affected by a small change in position of a near neighbour. A natural choice for the kernel is the Gaussian, although it is better to use a kernel with gaussian shape but truncated at a finite radius. This requirement is satisfied by the B-spline functions (Monaghan, 2005) such as the cubic and the quartic spline. Using these kernels allows to increase the number of neighbours without changing the smoothing length.

The smoothing length is defined as

$$h_{\rm a} = h_{\rm fac}\left(\frac{m_{\rm a}}{\rho_{\rm a}}\right)^{1/3} \tag{B.1.2}$$

where $h_{\rm fac}$ is a parameter specifying the smoothing length in units of the mean particle spacing $(m/\rho)^{1/3}$. This means that the resolution adapts to the local particle number density. Equations (B.1.1) and (B.1.2) can be solved simultaneously using standard root-finding methods such as Newton-Raphson (Price & Monaghan, 2007).

B.1.1 Neighbours search

The most computationally expensive process in any SPH code is finding neighbours. PHANTOM employs neighbour search for groups of particles. The results of this search are then cached into memory order and used to check for neighbours for individual particles in the group (Price et al., 2017). Following the method outlined by Gafton & Rosswog (2011) (known as the 'kd-tree' method), the particles are splitted recursively based on the center of mass and then the longest axis is bisected at each level. Then the tree is refined until it contains less than a certain number of particles $N_{\rm min}$ (this is called 'leaf node' and is 10 by default). The neighbour search is then performed once for each node, checking that the criterion

$$r^2_{\rm nm} < \left(s^2_{\rm m} + s^2_{\rm n} + R_{\rm kern}h^{\rm n}_{\rm max}\right)^2 , \tag{B.1.3}$$

where $r^2_{\rm nm}$ is the square of the separation between the node centres and s is the node size. Any node m satisfying this criterion that is not a leaf node has its children added

to the stack and the search continues. If node m is a leaf node then the list of particles it contains are added to the trial neighbour list, and the positions cached.

B.2 Equation of motion

The mass is an exactly conserved quantity since particles cannot lose, gain or diffuse mass. Furthermore, one of the key aspects of SPH is that the non-dissipative part of the numerical algorithm can be derived from the density by writing down the Lagrangian. The continuity equation can be written by taking the Lagrangian derivative of Eq. B.1.1

$$\frac{d\rho_{\rm a}}{dt} = \frac{1}{\Omega_{\rm a}} \sum_{\rm b} m_{\rm b} \left(\mathbf{v}_{\rm a} - \mathbf{v}_{\rm b}\right) \nabla_{\rm a} W_{\rm ab}(h_{\rm a}) \tag{B.2.1}$$

where $\Omega_{\rm a}$ is a term related to the gradient of the smoothing length $h_{\rm a}$ (Monaghan, 2002).

The equation of motion can be derived using the Euler-Lagrange equations with the first law of thermodynamics and the gradient of (B.1.1) (Price, 2012; Price & Federrath, 2010; Lodato & Price, 2010)

$$\frac{dv_{\rm a}}{dt} = -\sum_{\rm b} m_{\rm b} \left[\frac{P_{\rm a}}{\rho_{\rm a}^2} \nabla_{\rm a} W_{\rm ab}(h_{\rm a}) + \frac{P_{\rm b}}{\rho_{\rm b}^2} \nabla_{\rm a} W_{\rm ab}(h_{\rm b}) \right] \tag{B.2.2}$$

Note that both the total linear momentum and the angular momentum are exactly conserved quantities as a result of the antisymmetry in the kernel gradient. The conservation of these two quantities follows directly from the symmetries in the original Lagrangian and thus the SPH density estimate (Eq. B.1.1). The linear momentum is conserved because the Lagrangian and density estimate are invariant to translations, and angular momentum is conserved because they are invariant to rotations of the particle coordinates.

The energy equation can be derived as well from the Hamiltonian dynamics. It is important to point out that in SPH there is no difference in evolving either the thermal energy u, the total specific energy $e = 1/2v^2 + u$ or an entropy variable $K = P/\rho^\gamma$, except due to the timestepping algorithm. The evolution equation for the specific energy is

$$\frac{de_{\rm a}}{dt} = -\sum_{\rm b} m_{\rm b} \left[\frac{P_{\rm a}}{\Omega_{\rm a}\rho_{\rm a}^2} \mathbf{v}_{\rm b} \cdot \nabla_{\rm a} W_{\rm ab}(h_{\rm a}) + \frac{P_{\rm b}}{\Omega_{\rm b}\rho_{\rm b}^2} \mathbf{v}_{\rm a} \cdot \nabla_{\rm a} W_{\rm ab}(h_{\rm b}) \right] . \tag{B.2.3}$$

The total energy is exactly conserved in the SPH scheme as a natural consequence of the symmetry of the Lagrangian with respect to time as well as invariance under time translations.

B.2.1 Time integration

The equation of motion are integrated using a generalisation of the leapfrog scheme which is reversible in the case of both velocity dependent forces and derivatives which depend on the velocity field. The basic integrator is in the 'velocity Verlet' form (Verlet, 1967). According to this method the positions and velocities of particles are updated from time $t^{\rm n}$ to $t^{\rm n+1}$ according to

$$\mathbf{v}^{n+1/2} = \mathbf{v}^{n} + \frac{1}{2}\Delta t \mathbf{a}^{n}\,, \tag{B.2.4}$$

$$\mathbf{r}^{n+1/2} = \mathbf{r}^{n} + \Delta t \mathbf{v}^{n+1/2}\,, \tag{B.2.5}$$

$$\mathbf{a}^{n+1} = \mathbf{a}\left(\mathbf{r}^{n+1}\right)\,, \tag{B.2.6}$$

$$\mathbf{v}^{n+1} = \mathbf{v}^{n+1/2} + \frac{1}{2}\Delta t \mathbf{a}^{n+1} \tag{B.2.7}$$

where $\Delta t = t^{n+1} - t^{n}$. This algorithm preserves the Hamiltonian nature of the SPH scheme (Monaghan, 2005; Price, 2012). Both linear and angular momentum are exactly conserved and there is no long term energy drift and phase space volume is conserved.

In SPH this is complicated by velocity dependent terms in the acceleration from the shock capturing dissipation terms. However, the approach taken in PHANTOM is to notice that these terms are not usually dominant over the ones that depend on the position. In this case a first order prediction of the velocity is used

$$\mathbf{v}^{n+1/2} = \mathbf{v}^{n} + \frac{1}{2}\Delta t \mathbf{a}^{n}\,, \tag{B.2.8}$$

$$\mathbf{r}^{n+1/2} = \mathbf{r}^{n} + \Delta t \mathbf{v}^{n+1/2}\,, \tag{B.2.9}$$

$$\mathbf{v}^{*} = \mathbf{v}^{n+1/2} + \frac{1}{2}\Delta t \mathbf{a}^{n}\,, \tag{B.2.10}$$

$$\mathbf{a}^{n+1} = \mathbf{a}\left(\mathbf{r}^{n+1}, \mathbf{v}^{*}\right)\,, \tag{B.2.11}$$

$$\mathbf{v}^{n+1} = \mathbf{v}^{*} + \frac{1}{2}\Delta t \left(\mathbf{a}^{n+1} - \mathbf{a}^{n}\right)\,. \tag{B.2.12}$$

At the end of the step the code checks if the error in the first order prediction is less than some tollerance value $\epsilon = 10^{-2}$. If this is not satisfied the code computes again the accelerations until the error drops below ϵ.

The timestep is determined at the end of each step and it needs to be less than the Courant timestep (Lattanzio et al., 1986; Monaghan, 1997). For external forces, accelerations to SPH particles to/from sink particles and external forces with potentials defi

ned such that $\Phi \to 0$ when $r \to \infty$ different additional constraints on the timestep are applied. The timestep for a given particle is taken to be the minimum of all of the constraints.

B.3 Artificial viscosity in SPH

The artificial viscosity (AV) is introduced in SPH with the purpose to resolve shocks and prevent interpenetration of particles. In SPH simulations we assume that quantities are smoothed on the smoothing length, the smallest spatial scale, so discontinuities on this scale are not resolved by the numerical method. The usual approach is to broaden the shock over some smoothing lengths in order to deal with finite gradients and control the evolution by adding a dissipative term turned on only in the presence of shocks.

AV terms in SPH can be understood straightforwardly as numerical representations of second derivatives of the velocity and thus the AV acts as a Navier-Stokes physical viscosity. A general formulation of dissipative terms has been proposed by Monaghan

(1997), based on the analogy with Riemann solvers. The fundamental principle is that dissipative terms in conservative quantities involve jumps in those quantities, multiplied by eigenvalues that can be interpreted as signal velocities. The dissipative term for the specific momentum takes the form

$$\left(\frac{dv_{\rm a}}{dt}\right)_{\rm diss} = \sum_{\rm b} m_{\rm b} \frac{\alpha^{\rm AV} v_{\rm sig}\left(\mathbf{v}_{\rm a} - \mathbf{v}_{\rm b}\right)\cdot \mathbf{r}_{\rm ab}}{\rho_{\rm ab}} \nabla_{\rm a} W_{\rm ab} \tag{B.3.1}$$

where $\rho_{\rm ab} = (\rho_{\rm a} + \rho_{\rm b})/2$. The signal speed $v_{\rm sig}$ refers to the maximum signal speed between a particle pair and for hydrodynamics is

$$v_{\rm sig} = \begin{cases} \frac{1}{2}\left[c_{\rm s,a} + c_{\rm s,b} - \beta^{\rm AV}\mathbf{v}_{\rm ab}\cdot\mathbf{r}_{\rm ab}\right]; & \mathbf{v}_{\rm ab}\cdot\mathbf{r}_{\rm ab} \leq 0; \\ 0; & \mathbf{v}_{\rm ab}\cdot\mathbf{r}_{\rm ab} > 0\,. \end{cases} \tag{B.3.2}$$

where $\beta^{\rm AV}$ provides a non-linear term that was originally introduced to prevent particle penetration in high Mach number shocks. The dissipation term in the total energy also contains a term involving $(u_{\rm a} - u_{\rm b})$ that acts to smooth jumps in the thermal energy.

In PHANTOM, dissipation can be turned on only in the presence of shocks, when $\mathbf{v}_{\rm ab}\cdot\mathbf{r}_{\rm ab} \leq 0$, through the Morris & Monaghan (1997) switch. According to this switch the parameter $\alpha^{\rm AV}$ is evolved according to a source and decay equation

$$\frac{d\alpha^{\rm AV}}{dt} = -\frac{\alpha^{\rm AV} - \alpha^{\rm AV}_{\rm min}}{\tau} + S, \;\; \tau = h/(\sigma c_{\rm s}) \tag{B.3.3}$$

where $\sigma = 0.1$, $S = \max(0, -\nabla\cdot\mathbf{v})$, $\alpha^{\rm AV}_{\rm min} = 0.005$ and in general one would enforce $\alpha^{\rm AV}_{\rm max} = 1.0$.

In order to use the AV to represent the Shakura & Sunyaev (1973) disc viscosity, some assumptions are required (Lodato & Price, 2010). The viscosity should be applied to both approaching and receding particles, the signal velocity should be $c_{\rm s}$, the term $v_{\rm sig}$ should be multiplied by a factor $h/|r_{\rm ab}|$ (similar to the Monaghan 1992 AV scheme) and finally the switch should not be used. The artificial $\alpha^{\rm AV}$ and physical α (Shakura & Sunyaev, 1973) viscosity can then be related through

$$\alpha \approx \frac{1}{10}\alpha^{\rm AV}\frac{\langle h\rangle}{H}\,. \tag{B.3.4}$$

where here $\langle h\rangle$ is azimuthally averaged. It is worth noticing that since the smoothing length is inversely proportional to the density, the physical viscosity grows as density decreases. This means that it is not a wise choice to use artificial viscosity to simulate the physical one in low density regions. The disadvantage of using the AV term to represent physical viscosity is that one inevitably ends up with a large and unwanted coefficient of bulk viscosity (Lodato & Price, 2010). For a disc simulation, in general $\nabla\cdot\mathbf{v}$ is not large thus, even if the bulk viscosity coefficient is large, this is multiplied by a small value.

Bibliography

Abbott B. P., et al., 2016, Physical Review Letters, 116, 061102

Abramowicz M. A., Kluźniak W., 2001, A&A, 374, L19

Abramowicz M. A., Czerny B., Lasota J. P., Szuszkiewicz E., 1988, ApJ, 332, 646

Abramowicz M. A., Kluzniak W., Stuchlik Z., Torok G., 2004, ArXiv Astrophysics e-prints,

Alexander T., 2012, in European Physical Journal Web of Conferences. p. 05001 (arXiv:1210.0582), doi:10.1051/epjconf/20123905001

Auchettl K., Guillochon J., Ramirez-Ruiz E., 2017, ApJ, 838, 149

Balbus S. A., Hawley J. F., 1991, ApJ, 376, 214

Bardeen J. M., Petterson J. A., 1975, ApJ, 195, L65

Bardeen J. M., Press W. H., Teukolsky S. A., 1972, ApJ, 178, 347

Bate M. R., Bonnell I. A., Clarke C. J., Lubow S. H., Ogilvie G. I., Pringle J. E., Tout C. A., 2000, MNRAS, 317, 773

Beer M. E., Podsiadlowski P., 2002, MNRAS, 331, 351

Begelman M. C., McKee C. F., Shields G. A., 1983, ApJ, 271, 70

Begelman M. C., King A. R., Pringle J. E., 2006, MNRAS, 370, 399

Begelman M. C., Rossi E. M., Armitage P. J., 2008, MNRAS, 387, 1649

Belloni T., 2005, Interacting Binaries: Accretion, Evolution, and Outcomes, AIP Conference Proceedings, Volume 797, pp. 197-204, 797, 197

Belloni T. M., 2010, Lecture Notes in Physics, Springer-Verlag Berlin Heidelberg, Volume 794, p. 53. ISBN 978-3-540-76936-1., 794, 53

Belloni T., Hasinger G., 1990, A&A, 230, 103

Belloni T. M., Motta S. E., 2016, in Bambi C., ed., Astrophysics and Space Science Library Vol. 440, Astrophysics of Black Holes: From Fundamental Aspects to Latest Developments. p. 61 (arXiv:1603.07872), doi:10.1007/978-3-662-52859-4˙2

Belloni T., Psaltis D., van der Klis M., 2002, ApJ, 572, 392

Belloni T. M., Motta S. E., Muñoz-Darias T., 2011, Bulletin of the Astronomical Society of India, 39, 409

Belloni T. M., Sanna A., Méndez M., 2012, MNRAS, 426, 1701

Bloom J. S., et al., 2011, Science, 333, 203

Bonnerot C., Rossi E. M., Lodato G., Price D. J., 2016, MNRAS, 455, 2253

Bonnerot C., Rossi E. M., Lodato G., 2017, MNRAS, 464, 2816

Brocksopp C., et al., 2002, MNRAS, 331, 765
Broderick A. E., Loeb A., Narayan R., 2009, ApJ, 701, 1357
Burrows D. N., et al., 2011, Nature, 476, 421
Cabanac C., Henri G., Petrucci P.-O., Malzac J., Ferreira J., Belloni T. M., 2010, MNRAS, 404, 738
Cannizzo J. K., Lee H. M., Goodman J., 1990, ApJ, 351, 38
Capitanio F., Belloni T., Del Santo M., Ubertini P., 2009, MNRAS, 398, 1194
Casares J., Jonker P. G., 2014, Space Sci. Rev., 183, 223
Casella P., Belloni T., Homan J., Stella L., 2004, A&A, 426, 587
Casella P., Belloni T., Stella L., 2005, ApJ, 629, 403
Cenko S. B., et al., 2012, ApJ, 753, 77
Coughlin E. R., Nixon C., 2015, ApJ, 808, L11
Cummings J. R., et al., 2011, GRB Coordinates Network, 11823
Czerny M., King A. R., 1989a, MNRAS, 236, 843
Czerny M., King A. R., 1989b, MNRAS, 241, 839
Demianski M., Ivanov P. B., 1997, A&A, 324, 829
Devecchi B., Volonteri M., 2009, ApJ, 694, 302
Donato D., et al., 2014, ApJ, 781, 59
Done C., Kubota A., 2006, MNRAS, 371, 1216
Done C., Gierlinski M., Kubota A., 2007, A&A, 15, 1
Doğan S., Nixon C., King A., Price D. J., 2015, MNRAS, 449, 1251
Dunn R. J. H., Fender R. P., Körding E. G., Belloni T., Cabanac C., 2010, MNRAS, 403, 61
Eisenstein D. J., Loeb A., 1995, ApJ, 443, 11
Esin A. A., McClintock J. E., Narayan R., 1997, ApJ, 489, 865
Esquej P., et al., 2008, A&A, 489, 543
Evans C. R., Kochanek C. S., 1989, ApJ, 346, L13
Facchini S., Lodato G., Price D. J., 2013, MNRAS, 433, 2142
Fan X., et al., 2004, AJ, 128, 515
Fan X., et al., 2006, AJ, 131, 1203
Fender R., Belloni T., 2012, Science, 337, 540
Fender R., Gallo E., 2014, Space Sci. Rev., 183, 323
Fender R., Muñoz-Darias T., 2016, in Haardt F., Gorini V., Moschella U., Treves A., Colpi M., eds, Lecture Notes in Physics, Berlin Springer Verlag Vol. 905, Lecture Notes in Physics, Berlin Springer Verlag. p. 65 (arXiv:1505.03526), doi:10.1007/978-3-319-19416-5˙3
Fender R. P., Belloni T. M., Gallo E., 2004, MNRAS, 355, 1105
Fender R. P., Homan J., Belloni T. M., 2009, MNRAS, 396, 1370
Fender R. P., Gallo E., Russell D., 2010, MNRAS, 406, 1425
Ferrarese L., Merritt D., 2000, ApJ, 539, L9
Foucart F., Lai D., 2014, MNRAS, 445, 1731
Fragile P. C., Anninos P., 2005, ApJ, 623, 347
Fragile P. C., Blaes O. M., Anninos P., Salmonson J. D., 2007, ApJ, 668, 417
Fragos T., McClintock J. E., 2015, ApJ, 800, 17
Franchini A., Lodato G., Facchini S., 2016, MNRAS, 455, 1946

Franchini A., Motta S. E., Lodato G., 2017, MNRAS, 467, 145
Frank J., 1978, MNRAS, 184, 87
Frank J., King A., Raine D., 1992, Accretion power in astrophysics.
Gafton E., Rosswog S., 2011, MNRAS, 418, 770
Galeev A. A., Rosner R., Vaiana G. S., 1979, ApJ, 229, 318
Gallo E., Fender R. P., Pooley G. G., 2003, MNRAS, 344, 60
Gezari S., et al., 2006, ApJ, 653, L25
Gezari S., et al., 2008, ApJ, 676, 944
Gezari S., et al., 2009, ApJ, 698, 1367
Gezari S., et al., 2012, Nature, 485, 217
Ghez A. M., et al., 2008, ApJ, 689, 1044
Gierliński M., Zdziarski A. A., Poutanen J., Coppi P. S., Ebisawa K., Johnson W. N., 1999, MNRAS, 309, 496
Greenhill L. J., Gwinn C. R., Antonucci R., Barvainis R., 1996, ApJ, 472, L21
Greiner J., Schwarz R., Zharikov S., Orio M., 2000, A&A, 362, L25
Grupe D., Thomas H.-C., Leighly K. M., 1999, A&A, 350, L31
Guillochon J., Ramirez-Ruiz E., 2013, ApJ, 767, 25
Haardt F., Maraschi L., 1993, ApJ, 413, 507
Hayasaki K., Stone N., Loeb A., 2013, MNRAS, 434, 909
Hills J. G., 1975, Nature, 254, 295
Hirose S., Krolik J. H., Blaes O., 2009, ApJ, 691, 16
Holoien T. W.-S., et al., 2014, MNRAS, 445, 3263
Holoien T. W.-S., et al., 2016a, MNRAS, 455, 2918
Holoien T. W.-S., et al., 2016b, MNRAS, 463, 3813
Homan J., Belloni T., 2005, Ap&SS, 300, 107
Homan J., Wijnands R., van der Klis M., Belloni T., van Paradijs J., Klein-Wolt M., Fender R., Méndez M., 2001, ApJS, 132, 377
Homan J., Buxton M., Markoff S., Bailyn C. D., Nespoli E., Belloni T., 2005, ApJ, 624, 295
Hynes R. I., Steeghs D., Casares J., Charles P. A., O'Brien K., 2003, ApJ, 583, L95
Ichimaru S., 1977, ApJ, 214, 840
Ingram A., Done C., 2011, MNRAS, 415, 2323
Ingram A., Done C., 2012, MNRAS, 419, 2369
Ingram A., Motta S., 2014, MNRAS, 444, 2065
Ingram A., van der Klis M. v. d., 2013, MNRAS, 434, 1476
Ingram A., Done C., Fragile P. C., 2009, MNRAS, 397, L101
Ingram A., van der Klis M., Middleton M., Done C., Altamirano D., Heil L., Uttley P., Axelsson M., 2016, preprint, (`arXiv:1607.02866`)
Ivanov P. B., Illarionov A. F., 1997, MNRAS, 285, 394
Joinet A., Kalemci E., Senziani F., 2008, ApJ, 679, 655
Kalamkar M., Homan J., Altamirano D., van der Klis M., Casella P., Linares M., 2011, ApJ, 731, L2+
Kato S., 1990, PASJ, 42, 99
Kato S., 2004a, PASJ, 56, 559
Kato S., 2004b, PASJ, 56, 905

Kato S., 2005a, PASJ, 57, 679
Kato S., 2005b, PASJ, 57, L17
Kesden M., 2012, Phys. Rev. D, 85, 024037
King A., 2003, ApJ, 596, L27
King A. R., 2009, MNRAS, 393, L41
King A. R., Kolb U., 1999, MNRAS, 305, 654
King A., Lasota J.-P., 2016, MNRAS, 458, L10
King A. R., Pringle J. E., 2006, MNRAS, 373, L90
King A. R., Ritter H., 1998, MNRAS, 293, L42
King A. R., Kolb U., Burderi L., 1996, ApJ, 464, L127
King A. R., Davies M. B., Ward M. J., Fabbiano G., Elvis M., 2001, ApJ, 552, L109
King A. R., Lubow S. H., Ogilvie G. I., Pringle J. E., 2005, MNRAS, 363, 49
King A. L., et al., 2014, ApJ, 784, L2
Kluzniak W., Abramowicz M. A., 2001, ArXiv Astrophysics e-prints,
Kobayashi S., Hainick Y., Sari R., Rossi E. M., 2012, ApJ, 748, 105
Koliopanos F., Vasilopoulos G., Godet O., Bachetti M., Webb N. A., Barret D., 2017, preprint, (arXiv:1710.04953)
Komossa S., 2015, Journal of High Energy Astrophysics, 7, 148
Komossa S., Bade N., 1999, A&A, 343, 775
Komossa S., Greiner J., 1999, A&A, 349, L45
Komossa S., Halpern J., Schartel N., Hasinger G., Santos-Lleo M., Predehl P., 2004, ApJ, 603, L17
Koushiappas S. M., Bullock J. S., Dekel A., 2004, MNRAS, 354, 292
Kratter K., Lodato G., 2016, ARA&A, 54, 271
Krolik J. H., Hawley J. F., 2015, ApJ, 806, 141
Kruskal M. D., 1960, Physical Review, 119, 1743
Kubota A., Done C., 2004, MNRAS, 353, 980
Kumar S., Pringle J. E., 1985, MNRAS, 213, 435
Larwood J. D., Papaloizou J. C. B., 1997, MNRAS, 285, 288
Larwood J. D., Nelson R. P., Papaloizou J. C. B., Terquem C., 1996, MNRAS, 282, 597
Lasota J.-P., 2001, New Astron. Rev., 45, 449
Lattanzio J. C., Monaghan J. J., Pongracic H., Schwarz M. P., 1986, doi:https://doi.org/10.1137/0907039, 7, 591
Leahy D. A., Elsner R. F., Weisskopf M. C., 1983, ApJ, 272, 256
Lei W.-H., Zhang B., Gao H., 2013, ApJ, 762, 98
Leloudas G., Fraser M., Stone N. C., van Velzen S. e. a., 2016, Nature Astronomy, 1, 0002
Lense J., Thirring H., 1918, Physikalische Zeitschrift, 19, 156
Liang E. P. T., 1977, ApJ, 211, L67
Lightman A. P., Eardley D. M., 1974, ApJ, 187, L1
Liska M., Hesp C., Tchekhovskoy A., Ingram A., van der Klis M., Markoff S., 2017, preprint, (arXiv:1707.06619)
Lodato G., 2007, Nuovo Cimento Rivista Serie, 30
Lodato G., 2008, New Astron. Rev., 52, 21
Lodato G., Facchini S., 2013a, MNRAS, 433, 2157

Lodato G., Facchini S., 2013b, MNRAS, 433, 2157
Lodato G., Natarajan P., 2006, MNRAS, 371, 1813
Lodato G., Natarajan P., 2007, MNRAS, 377, L64
Lodato G., Price D. J., 2010, MNRAS, 405, 1212
Lodato G., Pringle J. E., 2006, MNRAS, 368, 1196
Lodato G., Pringle J. E., 2007, MNRAS, 381, 1287
Lodato G., Rossi E. M., 2011, MNRAS, 410, 359
Lodato G., King A. R., Pringle J. E., 2009, MNRAS, 392, 332
Loeb A., Rasio F. A., 1994, ApJ, 432, 52
Lovelace R. V. E., Li H., Colgate S. A., Nelson A. F., 1999, ApJ, 513, 805
Lubow S. H., Ogilvie G. I., 2000, ApJ, 538, 326
Lubow S. H., Ogilvie G. I., Pringle J. E., 2002, MNRAS, 337, 706
Lynden-Bell D., 1969, Nature, 223, 690
Lynden-Bell D., Pringle J. E., 1974, MNRAS, 168, 603
Maccarone T. J., Coppi P. S., 2003, MNRAS, 338, 189
Madau P., Rees M. J., 2001, ApJ, 551, L27
Magorrian J., Tremaine S., 1999, MNRAS, 309, 447
Markoff S., Falcke H., Fender R., 2001, A&A, 372, L25
Markwardt C. B., Swank J. H., 2005, The Astronomer's Telegram, 414, 1
Mayer M., Pringle J. E., 2007, MNRAS, 376, 435
Mayer L., Kazantzidis S., Escala A., Callegari S., 2010, Nature, 466, 1082
McClintock J. E., et al., 2011, Classical and Quantum Gravity, 28, 114009
McClintock J. E., Narayan R., Steiner J. F., 2014, Space Sci. Rev., 183, 295
McKinney J. C., Tchekhovskoy A., Sadowski A., Narayan R., 2014, MNRAS, 441, 3177
Meyer F., Meyer-Hofmeister E., 1994, A&A, 288, 175
Migliari S., et al., 2007, ApJ, 670, 610
Miller J. M., 2007, ARA&A, 45, 441
Miller J. M., Fabian A. C., in't Zand J. J. M., Reynolds C. S., Wijnands R., Nowak M. A., Lewin W. H. G., 2002, ApJ, 577, L15
Miller J. M., Reynolds C. S., Fabian A. C., Miniutti G., Gallo L. C., 2009, ApJ, 697, 900
Miyamoto S., Kitamoto S., Iga S., Negoro H., Terada K., 1992, ApJ, 391, L21
Miyoshi M., Moran J., Herrnstein J., Greenhill L., Nakai N., Diamond P., Inoue M., 1995, Nature, 373, 127
Monaghan J. J., 1992, ARA&A, 30, 543
Monaghan J. J., 1997, Journal of Computational Physics, 136, 298
Monaghan J. J., 2002, MNRAS, 335, 843
Monaghan J. J., 2005, Reports on Progress in Physics, 68, 1703
Morgan E. H., Remillard R. A., Greiner J., 1997, ApJ, 482, 993
Morningstar W. R., Miller J. M., 2014, ApJ, 793, L33
Morris J. P., Monaghan J. J., 1997, Journal of Computational Physics, 136, 41
Motta S. E., 2016, Astronomische Nachrichten, 337, 398
Motta S., Belloni T. M., 2010, X-ray Astronomy 2009; Present Status, Multi-Wavelength Approach and Future Perspectives, 1248, 185
Motta S., Belloni T., Homan J., 2009, MNRAS, 400, 1603
Motta S., Muñoz-Darias T., Casella P., Belloni T., Homan J., 2011, MNRAS, 418, 2292

Motta S., Homan J., Muñoz Darias T., Casella P., Belloni T. M., Hiemstra B., Méndez M., 2012, MNRAS, 427, 595

Motta S. E., Muñoz-Darias T., Sanna A., Fender R., Belloni T., Stella L., 2014a, MNRAS,

Motta S. E., Belloni T. M., Stella L., Muñoz-Darias T., Fender R., 2014b, MNRAS, 437, 2554

Motta S. E., Casella P., Henze M., Muñoz-Darias T., Sanna A., Fender R., Belloni T., 2015, MNRAS, 447, 2059

Muñoz-Darias T., Casares J., Martínez-Pais I. G., 2008, MNRAS, 385, 2205

Muñoz Darias T., Stiele H., Belloni T., Motta S., 2010, The Astronomer's Telegram, 2999, 1

Muñoz-Darias T., Motta S., Belloni T. M., 2011, MNRAS, 410, 679

Nealon R., Price D. J., Nixon C. J., 2015, MNRAS, 448, 1526

Nelson R. P., Papaloizou J. C. B., 2000, MNRAS, 315, 570

Nixon C., 2015, MNRAS, 450, 2459

Nixon C., King A., 2016, in Haardt F., Gorini V., Moschella U., Treves A., Colpi M., eds, Lecture Notes in Physics, Berlin Springer Verlag Vol. 905, Lecture Notes in Physics, Berlin Springer Verlag. p. 45 (`arXiv:1505.07827`), doi:10.1007/978-3-319-19416-5˙2

Nixon C. J., Pringle J. E., 2010, MNRAS, 403, 1887

Nixon C., King A., Price D., Frank J., 2012, ApJ, 757, L24

Nixon C., King A., Price D., 2013, MNRAS, 434, 1946

Nixon C., Franchini A., Lodato G., King A., 2016, in prep

Novikov I. D., Thorne K. S., 1973, in Dewitt C., Dewitt B. S., eds, Black Holes (Les Astres Occlus). pp 343–450

Ogilvie G. I., 1999, MNRAS, 304, 557

Ogilvie G. I., Latter H. N., 2013, MNRAS, 433, 2403

Ohsuga K., Mineshige S., 2007, ApJ, 670, 1283

Orosz J. A., Steiner J. F., McClintock J. E., Torres M. A. P., Remillard R. A., Bailyn C. D., Miller J. M., 2011, ApJ, 730, 75

Papaloizou J. C. B., Lin D. N. C., 1995, ApJ, 438, 841

Papaloizou J. C. B., Pringle J. E., 1983, MNRAS, 202, 1181

Papaloizou J. C. B., Pringle J. E., 1985, MNRAS, 213, 799

Phinney E. S., 1989, in Morris M., ed., IAU Symposium Vol. 136, The Center of the Galaxy. p. 543

Plant D. S., O'Brien K., Fender R. P., 2014, preprint, (`arXiv:1411.7411`)

Plant D. S., Fender R. P., Ponti G., Muñoz-Darias T., Coriat M., 2015, A&A, 573, A120

Podsiadlowski P., Rappaport S., Han Z., 2003, MNRAS, 341, 385

Polko P., McKinney J. C., 2017, MNRAS, 464, 2660

Poutanen J., Krolik J. H., Ryde F., 1997, MNRAS, 292, L21

Poutanen J., Lipunova G., Fabrika S., Butkevich A. G., Abolmasov P., 2007, MNRAS, 377, 1187

Price D. J., 2004, PhD thesis, Institute of Astronomy, Madingley Rd, Cambridge, CB2 0HA, UK ¡EMAIL¿dprice@cantab.net¡/EMAIL¿

Price D. J., 2012, Journal of Computational Physics, 231, 759

Price D. J., Federrath C., 2010, MNRAS, 406, 1659

Price D. J., Monaghan J. J., 2007, MNRAS, 374, 1347

Price D. J., et al., 2017, preprint, (arXiv:1702.03930)
Pringle J. E., 1992, MNRAS, 258, 811
Psaltis D., Norman C., 2000, ArXiv Astrophysics e-prints,
Rees M. J., 1988, Nature, 333, 523
Reid M. J., McClintock J. E., Steiner J. F., Steeghs D., Remillard R. A., Dhawan V., Narayan R., 2014, ApJ, 796, 2
Reis R. C., Fabian A. C., Ross R. R., Miniutti G., Miller J. M., Reynolds C., 2008, MNRAS, 387, 1489
Reis R. C., Fabian A. C., Miller J. M., 2010, MNRAS, 402, 836
Reis R. C., et al., 2011, MNRAS, 410, 2497
Reynolds C. S., 2013, Space Sci. Rev.,
Różańska A., Malzac J., Belmont R., Czerny B., Petrucci P.-O., 2015, A&A, 580, A77
Russell D. M., Fender R. P., Hynes R. I., Brocksopp C., Homan J., Jonker P. G., Buxton M. M., 2006, MNRAS, 371, 1334
Saito K., Homan J., Yamaoka K., Fukuyama M., Miyakawa T. G., Yoshida A., 2007, ArXiv Astrophysics e-prints,
Saxton R. D., Read A. M., Esquej P., Komossa S., Dougherty S., Rodriguez-Pascual P., Barrado D., 2012, A&A, 541, A106
Saxton R. D., Motta S. E., Komossa S., Read A. M., 2015, MNRAS, 454, 2798
Sądowski A., Bursa M., Abramowicz M., Kluźniak W., Lasota J.-P., Moderski R., Safarzadeh M., 2011, A&A, 532, A41
Scheuer P. A. G., Feiler R., 1996, MNRAS, 282, 291
Schnittman J. D., Homan J., Miller J. M., 2006, ApJ, 642, 420
Schwarzschild K., 1916, Abh. Konigl. Preuss. Akad. Wissenschaften Jahre 1906,92, Berlin,1907, 1916, 189
Shafee R., McClintock J. E., Narayan R., Davis S. W., Li L.-X., Remillard R. A., 2006, ApJ, 636, L113
Shafee R., McKinney J. C., Narayan R., Tchekhovskoy A., Gammie C. F., McClintock J. E., 2008, ApJ, 687, L25
Shakura N. I., Sunyaev R. A., 1973, A&A, 24, 337
Shappee B. J., Prieto J. L., Grupe e. a., 2014, ApJ, 788, 48
Shen R.-F., Matzner C. D., 2014, ApJ, 784, 87
Shiokawa H., Krolik J. H., Cheng R. M., Piran T., Noble S. C., 2015, ApJ, 804, 85
Sobolewska M. A., Życki P. T., 2006, MNRAS, 370, 405
Soleri P., et al., 2013, MNRAS, 429, 1244
Soltan A., 1982, MNRAS, 200, 115
Sorathia K. A., Krolik J. H., Hawley J. F., 2013a, ApJ, 768, 133
Sorathia K. A., Krolik J. H., Hawley J. F., 2013b, ApJ, 777, 21
Steiner J. F., McClintock J. E., Remillard R. A., Gou L., Yamada S., Narayan R., 2010, ApJ, 718, L117
Steiner J. F., et al., 2011, MNRAS, 416, 941
Steiner J. F., et al., 2012, MNRAS, 427, 2552
Stella L., Vietri M., 1998, ApJ, 492, L59+
Stella L., Vietri M., Morsink S. M., 1999, ApJ, 524, L63
Stone N., Loeb A., 2012, Physical Review Letters, 108, 061302

Stone N. C., Metzger B. D., 2016, MNRAS, 455, 859
Stone N., Loeb A., Berger E., 2013, Phys. Rev. D, 87, 084053
Strohmayer T. E., 2001, ApJ, 552, L49
Strubbe L. E., Quataert E., 2009, MNRAS, 400, 2070
Sunyaev R. A., Shakura N. I., 1975, Pisma v Astronomicheskii Zhurnal, 1, 6
Sunyaev R. A., Titarchuk L. G., 1980, A&A, 86, 121
Tagger M., Pellat R., 1999, A&A, 349, 1003
Tanaka Y., Lewin W. H. G., 1995, X-ray Binaries, pp 126–174
Tejeda E., Rosswog S., 2013, MNRAS, 433, 1930
Titarchuk L., Fiorito R., 2004, ApJ, 612, 988
Torricelli-Ciamponi G., Pietrini P., Orr A., 2005, A&A, 438, 55
Ulmer A., 1999, ApJ, 514, 180
Varnière P., Tagger M., 2002, A&A, 394, 329
Varnière P., Tagger M., Rodriguez J., 2012, A&A, 545, A40
Veledina A., Poutanen J., Ingram A., 2013, ApJ, 778, 165
Verlet L., 1967, Phys. Rev., 159, 98
Volonteri M., Rees M. J., 2005, ApJ, 633, 624
Wang J., Merritt D., 2004, ApJ, 600, 149
White N. E., Holt S. S., 1982, ApJ, 257, 318
Wijnands R., Homan J., van der Klis M., 1999, ApJ, 526, L33
Zauderer B. A., et al., 2011, Nature, 476, 425
Zauderer B. A., Berger E., Margutti R., Pooley G. G., Sari R., Soderberg A. M., Brunthaler A., Bietenholz M. F., 2013, ApJ, 767, 152
Zdziarski A. A., Lubiński P., Gilfanov M., Revnivtsev M., 2003, MNRAS, 342, 355
Zhang S. N., et al., 2016, preprint, (`arXiv:1607.08823`)
van Paradijs J., 1996, ApJ, 464, L139
van Velzen S., Farrar G. R., 2014, ApJ, 792, 53
van Velzen S., et al., 2011, ApJ, 741, 73
van den Eijnden J., Ingram A., Uttley P., 2016, MNRAS, 458, 3655
van der Klis M., 2004, Advances in Space Research, 34, 2646
van der Klis M., 2006, Advances in Space Research, 38, 2675

List of Publications

Referred publications

Franchini, Alessia, Lodato, Giuseppe & Facchini, Stefano, *Lense-Thirring precession around supermassive black holes during tidal disruption events* , published in Monthly Notices of the Royal Astronomical Society, 455, 1946, 2016 (**Chapter 5**)

Franchini, Alessia, Motta, Sara Elisa & Lodato, Giuseppe, *Constraining black hole spins with low-frequency quasi-periodic oscillations in soft states*, published in Monthly Notices of the Royal Astronomical Society, 467, 145, 2017 (**Chapter 7**)

Motta, Sara Elisa, **Franchini, Alessia**, Lodato, Giuseppe & Guglielmo Mastroserio, *On the different flavours of Lense-Thirring precession around accreting stellar mass black holes*, accepted for publication in Monthly Notices of the Royal Astronomical Society (**Chapter 8**)

Publications in conference proceedings

Lodato, Giuseppe, **Franchini, Alessia**, Bonnerot, Clement, Rossi, Elena Maria, *Recent developments in the theory of tidal disruption events*, published in the Journal of High Energy Astrophysics, 7, 158, 2015

Acknowledgments

..Don't worry about the future. Or worry, but know that worrying is as effective as trying to solve an algebra equation by chewing bubblegum. The real troubles in your life are apt to be things that never crossed your worried mind, the kind that blindside you at 4 pm on some idle Tuesday. Do one thing every day that scares you. Sing. Don't be reckless with other people's hearts, don't put up with people who are reckless with yours. Floss. Don't waste your time on jealousy. Sometimes you're ahead, sometimes you're behind. The race is long, and in the end, it's only with yourself. Remember compliments you receive, forget the insults; if you succeed in doing this, tell me how...

The Big Kahuna
Mary Schmich

Eventually it comes the time to thank the people who allowed me to pursue this path and to get to where I am today.

I would like to thank my supervisor Giuseppe Lodato for introducing me to the fascinating world of astrophysics since my master studies. His passion inspired me to follow the path of astrophysical research and I will always be thankful for that. Giuseppe always pushed me to deepen my knowledge and understanding of things, allowing me to build a strong physics background. He tought me how to be a good researcher and not to limit myself to the subject I was working on but to broaden my interest to other topics as well.

I would also like to thank Sara Motta for providing me with a precious look at the observational side of astrophysics. She helped me understand the great importance of data analysis in the matter of modelling astrophysical systems. I also thank her for the kind hospitality during my stay at the University of Oxford.

Special thanks go also to the other collaborators I have worked with during my PhD. Finally, I am also grateful to both the referees of this thesis, Adam Ingram and Chris Nixon, for providing very useful comments that allowed me to improve the quality and completeness of this manuscript.

Grazie a tutte le persone che mi hanno sempre sostenuto e supportato nella vita di tutti i giorni e senza le quali non so come avrei fatto ad arrivare dove sono oggi.

Innanzitutto un grazie dal piú profondo del cuore va ai miei genitori. Grazie per essere cosí come siete, per avermi sostenuta sempre nelle mie scelte e per avermi dato la spinta (e la testa) per sviluppare e portare avanti i miei ideali.

Un grazie immenso alle mie amiche, per esserci sempre. Grazie, per non avermi mai fatta sentire sola, per avermi sostenuta e sopportata anche nei periodi di crisi. Mi avete fatto sorridere anche quando non vedevo una ragione per farlo. Grazie agli amici "lambratesi" per le cene, le birre, le risate e tutti i momenti passati insieme.

Grazie ai miei Astroffice mates che mi sopportano tutti i giorni, tra una battuta, un tarallo e un caffè. Non potevo desiderare colleghi migliori.

Grazie a tutti i miei amici fisici, lontani e vicini, che hanno condiviso con me gioie e dolori dell'essere un fisico.

E infine, last but not least, grazie a te, per essere stato al mio fianco quest'ultimo anno e per avermi resa felice. Grazie P.